

Some pages of this thesis may have been removed for copyright restrictions.

If you have discovered material in AURA which is unlawful e.g. breaches copyright, (either yours or that of a third party) or any other law, including but not limited to those relating to patent, trademark, confidentiality, data protection, obscenity, defamation, libel, then please read our [Takedown Policy](#) and [contact the service](#) immediately

Causality and Synchronisation in Complex Systems with applications to neuroscience

ERIK CASAGRANDE

Doctor Of Philosophy



– ASTON UNIVERSITY –

March 2010

This copy of the thesis has been supplied on condition that anyone who consults it is understood to recognise that its copyright rests with its author and that no quotation from the thesis and no information derived from it may be published without proper acknowledgement.

Abstract

This thesis presents an investigation, of synchronisation and causality, motivated by problems in computational neuroscience. The thesis addresses both theoretical and practical signal processing issues regarding the estimation of interdependence from a set of multivariate data generated by a complex underlying dynamical system.

This topic is driven by a series of problems in neuroscience, which represents the principal background motive behind the material in this work. The underlying system is the human brain and the generative process of the data is based on modern electromagnetic neuroimaging methods. In this thesis, the underlying functional of the brain mechanisms are derived from the recent mathematical formalism of dynamical systems in complex networks. This is justified principally on the grounds of the complex hierarchical and multiscale nature of the brain and it offers new methods of analysis to model its emergent phenomena. A fundamental approach to study the neural activity is to investigate the connectivity pattern developed by the brain's complex network. Three types of connectivity are important to study: 1) anatomical connectivity referring to the physical links forming the topology of the brain network; 2) effective connectivity concerning with the way the neural elements communicate with each other using the brain's anatomical structure, through phenomena of synchronisation and information transfer; 3) functional connectivity, presenting an epistemic concept which alludes to the interdependence between data measured from the brain network.

The main contribution of this thesis is to present, apply and discuss novel algorithms of functional connectivities, which are designed to extract different specific aspects of interaction between the underlying generators of the data. Firstly, a univariate statistic is developed to allow for indirect assessment of synchronisation in the local network from a single time series. This approach is useful in inferring the coupling as in a local cortical area as observed by a single measurement electrode. Secondly, different existing methods of phase synchronisation are considered from the perspective of experimental data analysis and inference of coupling from observed data. These methods are designed to address the estimation of medium to long range connectivity and their differences are particularly relevant in the context of volume conduction, that is known to produce spurious detections of connectivity. Finally, an asymmetric temporal metric is introduced in order to detect the direction of the coupling between different regions of the brain. The method developed in this thesis is based on a machine learning extensions of the well known concept of Granger causality.

The thesis discussion is developed alongside examples of synthetic and experimental real data. The synthetic data are simulations of complex dynamical systems with the intention to mimic the behaviour of simple cortical neural assemblies. They are helpful to test the techniques developed in this thesis. The real datasets are provided to illustrate the problem of brain connectivity in the case of important neurological disorders such as Epilepsy and Parkinson's disease. The methods of functional connectivity in this thesis are applied to intracranial EEG recordings in order to extract features, which characterize underlying spatiotemporal dynamics before during and after an epileptic seizure and predict seizure location and onset prior to conventional electrographic signs. The methodology is also applied to a MEG dataset containing healthy, Parkinson's and dementia subjects with the scope of distinguishing patterns of pathological from physiological connectivity.

Contents

1	Introduction	12
1.0.1	Content of the thesis	13
1.1	Modelling Framework: Dynamical systems in complex networks	15
1.1.1	Brain state space model	15
1.1.2	Modelling brain dynamics	16
1.1.3	Connectivity in complex networks	19
1.1.4	Emergent network phenomena	20
1.2	Methods: functional connectivity	22
1.2.1	Assessing local synchronisation using univariate statistics	23
1.2.2	Multivariate statistics	23
1.3	Overview of the thesis	26
2	Neuroscience background materials	29
2.1	Neocortex modular architecture	29
2.2	Electromagnetic techniques	32
2.2.1	Brain imaging	32
2.2.2	Electromagnetic observational paradigm	34
2.2.3	The problem of volume conduction	35
2.3	Materials: Pathological brain datasets	37
2.3.1	Intracranial EEG datasets	37
2.3.2	MEG Parkinson's related Dementia study	41
2.3.3	Photic EEG dataset	44
2.4	Summary	44
3	Single channel assessment of local synchronisation in neural systems	46
3.1	Introduction	47
3.2	Synthetic example	48
3.2.1	Description	48
3.2.2	Simulation	50
3.2.3	Discussion	52
3.3	State Space Reconstruction	53

3.4	Manifold learning	55
3.5	Feature extraction	60
3.5.1	Dimension approach	60
3.5.2	Complexity approach	65
3.5.3	Entropy-MDL approach	67
3.5.4	Discussion	70
3.6	Summary	72
4	Analogues-RBF Granger causality metric	74
4.1	Introduction	74
4.2	Analogues-RBF Granger causality	76
4.2.1	Training and test sets	77
4.2.2	Single predictor	77
4.2.3	Mutual Predictor	80
4.2.4	Interdependence Granger metric	82
4.2.5	Optimisation	85
4.3	Simulations	87
4.3.1	Discrete maps: Coupled Hénon Oscillators	87
4.3.2	Chaotic dynamical systems: Coupled Lorenz oscillators	93
4.3.3	Stochastic autoregressive systems	95
4.4	Summary and discussion	97
5	Univariate Synchronisation in Anomalous Brain Activity	100
5.1	Preprocessing	101
5.2	Data analysis	101
5.2.1	MEG Data	101
5.2.2	Intracranial EEG dataset A	106
5.2.3	Intracranial EEG dataset B	112
5.3	Summary	118
6	Bivariate Functional Connectivity in Anomalous Brain Activity	120
6.1	Multivariate functional connectivity analysis	121
6.1.1	Intracranial dataset A	122
6.1.2	Intracranial dataset B	127
6.1.3	Photic epilepsy dataset	130
6.2	Preliminary investigation of the problem of volume conduction	132
6.2.1	MEG dataset	133
6.3	Summary	137

7 Conclusion	138
7.1 General overview	138
7.1.1 Dynamical systems in complex network applied to neuroscience	139
7.1.2 Assessing local synchronisation using single EM channel	140
7.1.3 Functional synchronisation	141
7.1.4 Analogues-RBF Granger causality	142
7.2 Discussions and future developments	143
7.3 Final consideration	146
A Phase Synchronisation	147
A.1 Instantaneous phase	148
A.2 Mean Phase Coherence	149
A.3 Phase Lag Index	150

List of Figures

1.1	Schematic representation of the analysis problems in this thesis.	27
2.1	Important parts of the brain organisation.	31
2.2	Profile of part of brain with the MEG and EEG scalp recordings.	33
2.3	Schematic representation of the problem of volume conduction.	36
2.4	Snapshot of the intracranial EEG dataset A.	40
2.5	Snapshot of the intracranial EEG dataset B.	41
2.6	Regions of the brain as structured by the MEG channels available.	43
2.7	Portion of an EEG recording that shows Photosensitive Epilepsy.	45
3.1	Conceptual structure of the algorithm presented in this chapter based on state space reconstruction	48
3.2	Lattice of coupled non-identical Rössler Oscillators as a model for local (mesoscopic) neocortical dynamics	49
3.3	Simulation of 3 clusters of synchronisation in the Rössler lattice with $\varepsilon = 2.5$ and $\delta = 0.009$	51
3.4	Simulation of 7 clusters of synchronisation in the Rössler system with $\varepsilon = 2.5$ and $\delta = 0.009$	52
3.5	Sketch of the state space reconstruction	54
3.6	Example of the singular spectrum taken from the iEEG dataset A.	58
3.7	Plots of the singular spectrum for different clustering scenarios of the Rössler system. . . .	59
3.8	Plots showing the value of the cut-off M^* as a function of the window length τ_w for different clustering regimes and for different value of the parameter λ	63
3.9	Plots of the singular spectrum for different clustering scenarios superimposed with the cut-off values as function of the parameter λ	64
3.10	Plots of the C_e and C_f with varying embedding dimension and for different clustering regimes	68
3.11	The C_e and M^* indexes for $\tau_w = 150$ as a function of the variance of a Gaussian additive noise source ξ superimposed to $O(t)$	69
3.12	The spectral entropy index in combination with the MDL algorithm as a function of the Gaussian noise source ξ for $\tau_w = 150$	71
3.13	Plots showing the performance of C_{eM} with a source of additive AR(1) coloured noise . . .	72
4.1	The Radial basis function network model which is an extension of the Lorentz's method of Analogues.	79

4.2	The mutual predictor model used in this thesis.	81
4.3	Graphical comparison between two other possible approaches considered in this thesis. . .	83
4.4	The circular block bootstrapping method to produce the surrogate data.	84
4.5	Diagram of the structure of the synthetic models as discussed in the following sections. . .	88
4.6	Hénon map synchronisation patterns x vs y for identical systems, i.e. $B = 0.3$	89
4.7	An example of a realisation of 500 points of the variable y of the identical Hénon WCDS .	90
4.8	Tuning of the embedding dimension using cross-validation based on the prediction errors of e_x and e_y	91
4.9	Example of tuning the number of nearest neighbours ζ	91
4.10	Example of tuning the number of radial basis functions	92
4.11	Estimation of the Analogues-RBF Granger metric for the WCDS Hénon system.	94
4.12	Analogues-RBF Granger causality for the case of a WCDS Lorenz systems.	96
4.13	Tuning of the neighbours for the linear AR model.	97
4.14	Estimation of the Analogues-RBF Granger metric for the stochastic AR models	98
5.1	Distribution of the single channel synchronisation index for different eyes conditions and for all the MEG sensors	102
5.2	Median values and the 25 th and 75 th percentiles (errorbars) of C_{eM} of the distributions in Figure 5.1 for different eyes conditions	103
5.3	Mean value of the distributions of C_{eM} in different regions of the MEG sensor space	105
5.4	Distributions of C_{eM} in the case of the frontal and occipital lobes	106
5.5	The median of the complexity of the global C_{eM} as a function of the window length τ_w . .	106
5.6	Plot of singular spectrum entropy for the dataset A	108
5.7	This figure shows a snapshot of C_{eM} computed in some channels of the iEEG grid	110
5.8	Average across channels of the indices C_{eM} in the left and the signal power in the right . .	110
5.9	Normalized plot of the C_{eM} using a Z-score statistic with selected snapshots of the grid at different times	111
5.10	Plot of the normalized power similar to Figure 5.9	112
5.11	Plot of singular spectrum entropy for the dataset B	113
5.12	The right plot shows the graphical set up of a simulation of a synthetic time series produced by a Rössler lattice having two regimes of synchronisation	114
5.13	Average of the complexity index around each of the 33 seizures of the dataset	116
5.14	Average of the power around each of the 33 seizures of the dataset	116
5.15	Grid of the dataset B during selected time instants from Figure 5.13	117
5.16	Grid of the dataset B during selected time instants from Figure 5.14	118
6.1	Conceptual structure of the data analysis protocol presented in this thesis	121
6.2	Analysis of synchronisation for the iEEG dataset A.	124
6.3	Causality directions in the iEEG A grid	126
6.4	Analysis of synchronisation for the iEEG dataset B.	128

6.5	Average of the MPC index μ_{MPC} for two different parts of the grid	129
6.6	Causality directions in the iEEG A grid	130
6.7	Analysis of the photic epileptic dataset	132
6.8	Plots that shows the analysis of MEG datasets for the eyes closed condition using the MPC index.	134
6.9	Plots showing the performance of the PLI in the MEG dataset	136

List of Tables

3.1	Simulation values of the Rössler system parameters and correspondent number of cluster found in the lattice	50
5.1	Summary of some statistics relative to the distribution of the complexity measures	102
5.2	Comparison of the median for the distribution of complexity measures in each group of patients in the case of the selected areas	104

To Ermando, Fabio, Genoveffa and Teresa

Acknowledgements

At the end of this journey, this thesis could not have been written without the help of many people. I foremost would like to thank my supervisors Prof. David Lowe and Dr. Avgis Hadjipapas for the inspiration and the guidance I received pursuing this project. I am grateful to Prof. Lowe for the theoretical discussions we had, the extraordinary help and the useful directions he gave me to complete this work. His teaching are going beyond this thesis. I am really grateful to have worked with Dr. Hadjipapas. I have met really few people in my life with his dedication, his passion and his incredible "optimism" for the neuroscience research. His support was essential for me to understand this mystique field, helping me many times not to be discouraged by its quite often complications.

I would like to thanks all the member of the NCRG group for the academic assistance I received through seminars and caffeine break discussions. A particular thanks to Vicky for the administrative and logistic help she provided and Alex for solving most of my hardware and all the "penguin" problems. I would like to thank all the people I met at the Aston Vision Science. In particular, Arjan, Gareth, Ian, Stefano for the human and technical support for the analysis of the brain.

I have met many many friends and colleagues during this long journey. Their psychological and concrete support was essential to complete this work. The list is too long to mention all. Thanks to the guys of the "Lowe team": Thomas, Raji, Michel, Ming. Thanks to Mike, George, Manos and all the greeks for improving my geographical, historical and vocabulary skills. Thanks to Jan and Jim to show me that to hit a simple ball I need to stay calm. Thanks to Jack and Chris for technical, non-technical and nonsense discussion. Thanks for all the guys from the PG rota for the nice nights I spent looking at the stars (mostly the cloud), Paul, Robin, Ahmed, Joobe, Elaine..... Thanks the Italian community in Birmingham, Luigi, Camillo, Daniela, Tiziana and Maria Teresa for making feel at home, feeding me with good food and helping me with the data analysis.

A special thank to Dr. Stephanie Feiereisen for the love and the support she gave me during all this time. More, thanks to the infinite patience she had in the darkest part of this experience. I had great time with you, Dr. Steffy.

I would like to thank my parents and my sister for the help I received in the many good and especially in the many bad periods. While being "a vagabondo" I have never lack of anything anywhere in the world this journey was taking me.

At last, I need to acknowledge and dedicate this piece of work to my grandparents. Through their simplicity they showed me many important virtues which include hard work, dedication and commitment. This thesis was not possible without their life teachings.

1

Introduction

This thesis addresses the general problem of *extracting spatio-temporal information of interdependence within an underlying system from a set of its observations*. This estimation task has become an important part of the general field of multivariate data analysis whose applications are widespread in many modern social, engineering and scientific fields. While the methods developed in this work can be generally used in many of the previous fields, this thesis focuses, in particular, to questions posed in neuroimaging: *the underlying system is the human brain in which neural activity is measured with the help of the latest electromagnetic (EM) imaging techniques [7; 106; 64]: electroencephalography (EEG) and magnetoencephalography (MEG)*.

In the neuroimaging field, the most recent imaging technologies are able to sample the underlying brain substrate with greater spatio-temporal precision and accuracy [7]. This higher level of detail, unscrambled by these new measurement approaches, have offered a new view of some of the underlying structures of the brain: *complexity and its properties such as self-organisation, adaptation and emergent phenomena* [19; 22; 84; 29]. At this level of description, in fact, the complex nature of the brain has been shown to be due to the mutual interaction of many weakly coupled neural subsystems which are linked together into a complicated hierarchical structure. Analysis of connectivity, interdependence and interrelationship between and within complex systems such as the brain is thus fundamental to understand its internal mechanism of functioning [114].

As emphasized in this thesis, two fundamental types of interdependence, connectivity patterns or emergent phenomena, which occur among inner elements of the complex brain system, are important to study:

Causality and *Synchronisation* relationships. The former is related to a phenomenon of information transfer between different part of the brain (drive-response relationships). The latter, instead, describes the system's ability to correlate their internal mechanisms on time and it is believed to be the main form of neural coding of brain information [44; 45; 46; 59].

1.0.1 Content of the thesis

Motivated by the previous general considerations, the following main topics are specifically considered in this thesis:

Feature extraction of functional connectivity. The investigation of brain connectivity in this thesis, i.e. synchronisation and causality phenomena, is based only on the time series provided by EM techniques. We call this situation a *model-free scenario* which emphasizes that one does not have any other structural information about the brain apart from the observable data. This lack of knowledge of the underlying brain model dynamics is a typical case in neuroimaging since a detailed model is too complex. Only dynamics at the microscopic level are in fact understood while the general behaviour of the brain at the global level is yet to be discovered. In practice, the processing of EM signals belongs in this project to an exploratory type of analysis.

Following the the recent framework of *dynamical systems in complex networks* [136; 5; 147] as reported in this introduction, this thesis specifically discusses and implements exploratory analysis techniques of functional brain connectivity. Functional connectivity refers to the generic concept of estimating the inner synchronisation and causality brain phenomena, which is instead called effective connectivity, from the set of EM data [43; 92]. In practice, *functional connectivity is the interdependence between the EM observable time series while effective connectivity is the more important relationships between the neural sources.*

The following functional connectivity problems are particularly discussed in this work:

- A novel method to *assess synchronisation at the local level* in the neural complex network using a single channel EM recording is analysed in Chapter 3: *Entropy-MDL complexity index*.
- A novel *measure of causality* between two distinct points of the brain using a Radial Basis Function (RBF) network [96; 10] is implemented in Chapter 4: *Analogues-RBF Granger causality metric*.
- Two existing measures of bivariate synchronisation are considered: the Mean Phase Coherence (MPC) [116] index and the Phase Lag Index (PLI) [135], as formalized in the Appendix A. They are employed in this thesis to provide a measure of synchronisation in the data analysis and to bring about experimentally an important issue in functional connectivity: the problem of volume conduction [106; 108; 107; 135] in Chapter 2.

These three previous aspects belong to a general framework of interdependence analysis, which are important for the estimation of different features of the underlying neural network connectivity: local interactions, medium to short range interactions, directional interactions.

Examples of data analysis. Some specific neurophysiological datasets are presented to show possible applications where these feature extraction methods can be applied and their strength. The specific data used in this thesis are

- *MEG data relative to Parkinson disease.* The data consists of labelled EM time series coming from three types of population: Control, Parkinson's and Parkinson's Dementia subjects which are recorded during the resting state [14]. This pathology has been recently linked to the degeneration of the anatomical effective connectivity of the brain for affected patients with respect to normal healthy subjects [14; 134]. For this reason, the dataset is considered as a good example for the material of this thesis. The purpose of the analysis of this dataset is twofold: firstly, it helps to provide a tool which is able to find differences in the pattern of functional connectivity between the population of patients and understand its clinical significance. This tool can be useful for the automatic procedure of screening as well as understanding the deficiencies of the disease. Secondly, this dataset is useful to bring about the problem of volume conduction which affects the computation of functional connectivity for the case of scalp electromagnetic techniques such as MEG.
- *EEG examples of epileptic activity.* During epilepsy there is a transition from a pathological but idle state to a massive synchronisation of the brain, either regional or global [73]. The methods in this thesis can help to study this phenomenon: when and where an epileptic seizure starts and how it spreads, i.e. causality, and synchronized over the time. In practice, *the main aim is to study the spatiotemporal occurrence of a seizure.* Estimation of the state of the functional connectivity with these methods, if relevant, provides useful information for further signal processing stages such as seizure detection, localisation and prediction. Two intracranial EEG recordings have been extensively used during the analysis of the methods proposed by the framework of analysis in this thesis. An extra small scalp EEG datasets was employed during the initial stages of this work.

It is not in the main goal of this project to provide new knowledge and novel insights in order to solve these disorders. These datasets have been employed to test and to discuss the methodological part of the thesis. Therefore, they can be considered as pilot studies for future more complete investigations.

Following the previous topic description, this thesis is conceptually divided in three parts: Chapter 1 and Chapter 2 present the introduction and background on the materials, methods and modelling strategies of the brain. Chapter 3 and Chapter 4 discuss in more details novel methods of electromagnetic interdependence signal processing. Chapter 5 and Chapter 6 carry out the specific analysis of the pathological datasets. The descriptions of these datasets are presented in Chapter 2. In Chapter 3 and Chapter 4, during the theoretical part of the thesis synthetic datasets constructed to explore nonlinear dynamics in complex networks are used to support the validity of the methods developed.

1.1 Modelling Framework: Dynamical systems in complex networks

Neuroscience is a field interested in the study of the brain nervous system and its direct role to important human functions such as cognition, emotions, intelligence. The brain is one the most cited and exciting examples of complex systems since it is the central processing unit of the human organism. Its functioning is probably one of the greatest unsolved problems which has concerned generations of thinkers in many scientific fields. The challenges of the understanding of the brain is encoded in the following foremost question which the modern field of neuroscience is attempting to answer [61; 122]:

Problem 1. Binding Problem: *How the unity of conscious perception is brought about by the distributed activities of the central nervous system*

In other terms, how the dynamics of single elements of the complex neural network integrates their behaviour with each other to bring about decision, action, perception or similar higher cognitive concepts. The latter capacities are seriously compromised in neurological disorders such as Epilepsy and Parkinson's. Therefore, the other side of the binding problem is: *how and why does the failure of neural integration produce these pathologies?*

1.1.1 Brain state space model

The solution of the binding problem has been addressed in the last three decades using the developments of the theory of dynamical systems applied to the brain [22]. Following this part of the literature, the most general neuroscience problem studied in this work can be stated mathematically as follows: an unknown underlying system, i.e. the whole human brain or part of it, is observed using a measurement approach which samples regularly its internal state and generates a set of electromagnetic data. The following generic *State Space* representation is used in this thesis to model the brain-EM system \mathcal{X}

$$\mathcal{X} \begin{cases} \frac{d\mathbf{X}(t)}{dt} = \mathbf{f}(\mathbf{X}(t), \theta_{\mathbf{X}}, \mathbf{u}(t)) + \xi, \\ \mathbf{x}(t) = \mathbf{h}(\mathbf{X}(t)) + \eta, \end{cases} \quad (1.1)$$

where $\mathbf{x}(t) \in \mathbb{R}^m$ is a continuous vector variable which represents the observations at the m electromagnetic sensors level and $\mathbf{X}(t) \in \mathbb{R}^n$ is the state of the latent n neural sources level at time t . \mathbf{x} is also referred as the sensor space while \mathbf{X} the source space. Each of the n components of $\mathbf{X}(t)$ represents some defined physiological quantities of the neocortex, i.e. the part of the brain where these neural sources are situated. For instance, $\mathbf{X}(t)$ can be associated with the biochemical state of each neuron and the magnitude of n is of the order of 10^{11} [22]. In practice, as discussed in Chapter 2, $\mathbf{X}(t)$ can be better defined as the descriptor of an ensemble of neurons called a *Macrocolumn* [105; 18]. The latter are considered as the fundamental computational units of the brain with numbers n that may vary between 10^4 to 3×10^3 [105].

The terms ξ and η are generic random variables which are usually included in the state space representation to model internal sources of randomness and external disturbances, respectively. They can be

generally considered as identically distributed, additive, zero mean Gaussian random variables which thus can be decoupled from $\mathbf{f}(\cdot)$ and $\mathbf{h}(\cdot)$.

The function $\mathbf{f}(\cdot) : \mathbb{R}^n \rightarrow \mathbb{R}^n$ is the vector field or *flow* of the differential equation in Eq. 1.1. $\mathbf{f}(\cdot)$ which is unknown with current knowledge, is a generic function which models the physiological behaviour and histological connectivity of the brain system [18]. $\theta_{\mathbf{x}}$ is the set of *control parameters* which are constant (or slowly changing compared to the time scale of the observations) and in general may define the topology and the biochemical properties of the brain as explained later in this thesis. $\mathbf{u}(t)$ is an optional argument which represents a set of external input functions. In practice, the brain is an open system and $\mathbf{u}(t)$ is designed to model the external somatosensory stimuli provided by the receptive fields neurons. This term is dropped during the development of this thesis since we are directly studying stimuli-related experiments.

The function $\mathbf{h}(\cdot) : \mathbb{R}^n \rightarrow \mathbb{R}^m$ models the technical characteristic of the electromagnetic techniques which are expected to measure some of the inner features of the underlying brain. While the single neuron cannot yet be observed in vivo using these technologies, specific brain modules, aggregates of populations of neurons may be accessible. The recent improvement of these techniques such as EEG, MEG but also functional imaging such as fMRI [42], have in fact opened the analysis of the human brain to an increasing level of accuracy both in the spatial and in the temporal domain. Nevertheless, the function $\mathbf{h}(\cdot)$ still mixes the true latent \mathbf{X} which makes \mathbf{x} only a macro aggregate signal. The current inability to know exactly the underlying structure of the brain and the impossibility to measure perfectly each of its single factors drives the analysis into an ill-posed inverse problem. A unique solution cannot be found that relates \mathbf{x} to \mathbf{X} . The description of $\mathbf{h}(\cdot)$ is left for further explanation in Chapter 2 where the EM techniques used in this thesis are reviewed.

The EM data available for analysis $\mathbf{x}(t)$ can be considered in the format of a finite vector valued multivariate time series $\{\mathbf{x}_i\}_{i=1}^L = \{\mathbf{x}_1, \mathbf{x}_2, \mathbf{x}_3, \dots, \mathbf{x}_L\}$. The latter is sampled from $\mathbf{x}(t)$ at discrete intervals τ_s between $t_0 = 0$ and $t_L = L\tau_s$. In this perspective, in order to facilitate the discussion of Eq 1.1, the discretisation of the signals may also apply to the vector field $\mathbf{f}(\cdot)$. In this case, $\mathbf{f}(\cdot) : \mathbb{R}^n \rightarrow \mathbb{R}^n$ is known as a *Map* which updates at discrete intervals τ_s the state of the brain $\{\mathbf{X}_i\}_{i=1}^L$.

1.1.2 Modelling brain dynamics

What is the nature of the function $\mathbf{f}(\cdot)$? The brain is a composite organ since it is a conglomeration of millions of neurons functioning in unison as better described in Section 2.1. It is established that single neurons do not act independently to each other but instead they are connected into populations with a hierarchical and modular scale of coupling [18]. Anatomical studies in neurophysiology have in fact shown different levels of this structure: at the microscopic level localized modules made by dense aggregations of neurons are responsible for the processing of specific basic features [132] such as sensorimotor stimuli. At a mesoscopic level, other more specialized and specific modules (for instance the macrocolumns) composed by the cooperation of the previous subsystems have been observed to exchange information by using a sparser form of connectivity. At the macro and global level, further higher structures account for the regulation of cognitive activities and finally, human consciousness [61].

This brain hierarchical structure gives a few important indications in order to understand the brain and directions to model its description function $\mathbf{f}(\cdot)$. In particular, the latter micro-meso-macro description levels are both reason and cause of the nonlinearity, complexity and *the principle of segregation and integration* of the brain as emphasized in the specialized literature [131]: localized brain modules, at some points of the hierarchical scale, coordinate their internal functioning, enabling the formation of a global self-organized pattern but without allowing their own dynamics to be compromised. In other words, these modules can continue to be responsible for more specialized tasks (segregation), while still be part of the functioning of the whole brain process (integration): brain modules are quasi-independent elements which are weakly coupled with each other.

These findings and theories have led the research community in the last three decades to exploit new methods and areas from the fields of nonlinear analysis in order to offer better modelling tools as well as to allow the study of its EM signals. Two approaches, in particular, need to be mentioned here as subjects of investigation in this thesis: *Nonlinear dynamics and deterministic chaos* and the recent theory of *dynamical systems in complex networks* [3; 5; 136].

The first area of research is based on the geometrical framework of dynamical systems where the brain (or a specific part under investigation), is simplified by a reductionist approach which uses a mean field or lumped models to simulate the dynamics of a large populations of neural elements [98]. These models are deterministic, nonlinear, dissipative and interesting concepts such as attractors, bifurcation phenomena and chaos have been used to study brain signals employed since the middle of the 1980's [135].

The concept of an attractor, important using this deterministic framework, is often reported during the development of the thesis: when $\xi = 0$ (determinism), the state $\mathbf{X}(t)$ is considered as a multidimensional point belonging to the phase space \mathbf{X} . If $\mathbf{f}(\cdot)$ is Lipschitz continuous a unique solution $\varphi(t)$ to the initial value problem can be found. The curve $\varphi(t)$ defines a trajectory in the state space which starts from an initial condition point $\mathbf{X}(t=0) \triangleq \mathbf{X}_0$ to the attractor of the differential equation. The latter is defined as the set \mathbf{A} of state space points invariant under $\mathbf{f}(\cdot)$, i.e. $\mathbf{f}(\mathbf{A}) \subseteq \mathbf{A}$, such that there is a *basin of attraction* $\mathbf{B}(\mathbf{A})$

$$\mathbf{B}(\mathbf{A}) = \{\mathbf{X} | \omega(\mathbf{X}_0) \subseteq \mathbf{A}\}, \quad (1.2)$$

with $\omega(\mathbf{X}_0)$ the ω -limit sets of $\mathbf{f}(\cdot)$ defined as

$$\omega(\mathbf{X}_0) = \bigcap_{T>0} \text{cl} \left(\bigcup_{t>T} \{\mathbf{f}^t(\mathbf{X}_0)\} \right). \quad (1.3)$$

where $\mathbf{f}^t(\cdot)$ is the evolution operator of $\mathbf{f}(\cdot)$ after time t , $T > 0$ is a generic large time instant and $\text{cl}(\cdot)$ is the operation of closure of a set.

In practice, at each hierarchical scale of the brain neural network, the integration of quasi-independent modules reduces the degree of freedom of the global brain aggregate $\mathbf{f}(\cdot)$: the state space trajectory of $\mathbf{f}(\cdot)$ is

unlikely to span the full space, i.e. \mathbb{R}^n , but settle down to a lower dimensional subspace due to the effective degree of freedom of the system, i.e. the attractor. Depending on which part of the brain hierarchy is under study, different types of models $\mathbf{f}(\cdot)$ and consequently attractors with distinct topological properties can be obtained: for instance *fixed point attractors*, *limit cycles* or *strange attractors*. Fixed point attractors are the simplest invariant limit sets and are typically found in linear and stable systems. This is probably not the case in the brain which is considered having a nonlinear behaviour. At the microscopic level, for instance, the behaviour of single neurons may be formulated using Hodgkin-Huxley, Morris-Lecar, Hindmarsh-Rose or other realistic neuronal models [74] which in general lead to limit cycle type of attractors. At an higher hierarchical scale, the coupling of populations of these nonlinear simpler models may result in more complicated topological structures such as strange attractors, which are limit sets that can be found in the basin of attraction of chaotic dynamical systems. Simulation studies and experimental findings have shown, the occurrence of these sets at the level of small populations of neurons [36; 86]. More importantly, these results have boosted the interest and excitement in the 1990's for using chaos and dynamical systems theoretical tools to study brain dynamics also at the global hierarchical level.

However, no conclusive evidence of chaos has been found at the medium-large brain level during the last decade and, recently, several early discoveries have been criticized and re-evaluated [134]: Surrogate testing has shown that misinterpretation of methods from chaos theory can occur if the system behind the data is not chaotic [82]; Lower deterministic chaos is likely to occur in particular situations such as during epileptic seizures but not during normal brain functioning [98]; higher chaotic phenomena such as intermittency and itinerancy [82], that can occur during normal brain rhythms, are not yet well understood and are difficult to be discerned from randomness.

For these reasons, the focus of recent literature has shifted from the study of lumped deterministic chaotic systems to the more realistic study of nonlinear interactions. From a mathematical perspective, this new area of nonlinear time series analysis research is based on the theory of complex dynamical networks and it offers a new modelling framework to study $\mathbf{f}(\cdot)$ and the mechanisms in the brain.

Within this framework, the modelling of the brain is decomposed into aggregates of quasi-independent and communicating dynamical systems which better describe its complex hierarchical structure: *Weakly Coupled Dynamical Systems (WCDS)* [116]. These new tools may embody aggregate nonlinear and chaotic lumped models and they allow the study of nonstationary, stochastic and high dimensional phenomena which are more likely to be found in the brain. Importantly for this thesis, the understanding of the brain system and its data analysis is performed through the estimation of its internal connectivities. As discussed in the following sections, the notion of connectivity can be associated with different aspects of a complex dynamical system network and thus to the brain organisation [71]: *Anatomical*, *Effective* and *Functional Connectivity* [43] respectively, are terms which have been discussed in the neuroscience literature in order to discern this particular dichotomy [92; 37]. The former two types of connectivities are intrinsic properties of the underlying complex dynamical system while the latter instead, is a data-dependent concept.

The thesis main contribution is to discuss some methods and problems of functional connectivity analysis whose results can be use to understand the underlying effective or anatomical connectivities.

1.1.3 Connectivity in complex networks

Anatomical Connectivity

Anatomical connectivity is given by the structural physical links which form the concrete pathways and the topology for exchanging information between elements of the system [132]. It denotes what materials and pieces the system \mathcal{X} is built from and how they are assembled.

In mathematical terms [5], *anatomical connectivity can be abstractly represented by a graph $\mathcal{G}(\mathbf{V}, \mathbf{E})$* where \mathbf{V} is a collection of vertices or nodes and \mathbf{E} is a set of edges. From a neurophysiological perspective, \mathbf{E} represents brain fibres such as axons or synapse which are the medium which joins the nodes. \mathbf{V} refers to elements of the brain such as single neurons or clusters or populations of neurons depending on which hierarchical scale of the brain one wishes to consider as better explained in Section 2.1.

The graph \mathcal{G} can be also expressed in matrix form by an adjacency matrix \mathbf{A} which has entries $a_{ij} = 1$ if a direct link exists from j to i and 0 otherwise. If $a_{ij} \in \mathbb{R}$, i.e. the values a_{ij} can assume any real values, then \mathcal{G} is known as a weighted graph. The latter type of graph, for instance can contain further information about the underlying topology, i.e. distances between nodes.

Anatomical connectivity is not the direct subject of the investigation in this thesis. Its estimation usually requires data and procedures which are not considered in this work. For instance, Diffusion Tensor Imaging (DTI) [9] is a recent magnetic resonance method that can display the internal physical interconnection between neurons by tracking the diffusion of water in the brain fibrous structure. While not available in this thesis, knowing the brain anatomical connectivity is important because its topological information may give plausible constraints on the dynamical (and globally unknown) part of the model in Eq. 1.1 [92].

Effective Connectivity

Effective connectivity is defined as the influence that one neural system exerts over another either at a synaptic or a population level [43]. In practice, it describes how the internal model of the system communicates, functions and exchanges information instead of how it is hard wired by the system's anatomical connectivity.

From a mathematical point of view, the notion of effective connectivity is better associated with the decomposition of $\mathbf{f}(\cdot)$ in Eq. 1.1 over the complex anatomical structure of \mathcal{G} . This decomposition links $\mathbf{f}(\cdot)$ to the family of weakly coupled dynamical systems. In this thesis we consider the following formalism

$$\frac{d\mathbf{X}^{(j)}(t)}{dt} = \mathbf{f}_j \left(\mathbf{X}^{(j)}(t), \theta_{\mathbf{f}_j} \right) + C_{ij} \sum_{i \neq j} \mathbf{f}_{ij} \left(\mathbf{X}^{(i)}(t), \mathbf{X}^{(j)}(t), \theta_{\mathbf{f}_{ij}} \right) + \xi, \quad (1.4)$$

where we consider a partition of the state $\mathbf{X} = (X_1, X_2, \dots, X_n)^T$ given by

$$\mathbf{P} = (\mathbf{X}^{(1)}, \mathbf{X}^{(2)}, \dots, \mathbf{X}^{(M)})^T, \quad (1.5)$$

with

$$\mathbf{X}^{(j)} = (X_{j_1}, X_{j_2}, \dots, X_{j_{k_j}})^T, \quad j = 1, 2, \dots, M, \quad (1.6)$$

and $\mathbf{J} = [j_1, j_2, \dots, j_{k_j}]$ is called the partitioning vector of \mathbf{P} , such that the condition $\sum_i^M k_j = n, M \leq n$ is satisfied.

In practice, the partition function \mathbf{P} associates each subsystem $\mathbf{X}^{(j)}$ to each node j of the anatomical graph \mathcal{G} . The functions $\mathbf{f}_j(\cdot)$ are the dynamical descriptions of each of the nodes, i.e. the models of the brain modules at some points of its hierarchical structure. The $\mathbf{f}_{ij}(\cdot)$ are the functions which establish the coupling between brain modules. This coupling is further regulated by the parameters C_{ij} which in the case of Eq. 1.4 is an entry of the coupling matrix \mathbf{C} . C_{ij} can be considered a function of the previous adjacency matrix, i.e. $C_{ij} = \alpha_{ij} a_{ij}$ for some weighting terms α_{ij} . The coupling C_{ij} is thus dependent on the existence of the correspondent edge a_{ij} in the topology of \mathcal{G} .

Eq. 1.4 is a special case of the family of WCDS but can be further generalized for nonlinear and time dependent coupling and for discrete spatiotemporal systems. The latter are known in the literature as *Coupled Map Lattices (CML)* [80].

WCDS are important tools for modelling and analysing the brain since they are the contact point between structural (anatomical) and dynamical (effective) properties of the underlying neural system. In Chapters 3 and 4 we are interested to simulate medium-large brain dynamics as seen from EM measurements. Some WCDS models are thus considered in order to check the validity of the methods developed. Although, no medium-large brain model is currently available and these synthetic examples are only an oversimplification of the underlying complex dynamics, they still offer several advantages to simulate some characteristics of a simple brain behaviour as explained in Chapters 3 and 4. More importantly, as described next, within the framework of WCDS it is possible to address formally the definition of synchronisation and causality as the emergence relationships between elements of the network.

1.1.4 Emergent network phenomena

Synchronisation

Synchronisation is a complex dynamical relationship of effective connectivity. In the colloquial English, synchronisation means correlated in time behaviour between different processes [21], to occur at the same time or happen at the same time [69]. In practice, a more precise mathematical definition depends on the nature of this relationship and what is actually measured. In fact, while generally related for historical reasons to the interdependence of phases between harmonic oscillators, in the last decades new different types of synchronisation have been formalized [12]: identical synchronisation, lag synchronisation, generalized synchronisation, chaos synchronisation. The inclusion of a larger ontology of methods have blurred a precise concept of synchronisation and have proven to be an obstacle to a unified and precise definition.

From a complex network perspective, synchronisation is defined as a complex dynamical process that results in an adjustment of rhythms of oscillating objects due to their weak interactions [116]. Given the previous decomposition in Eq. 1.4, synchronisation is a relationship of time correlation between the subsystems $\mathbf{X}^{(1)}$ due to the weak coupling \mathbf{C} . More specifically, following the the unified synchronisation scheme in [21] we have that

Definition 1. Given a WCDS \mathcal{Z} as in Eq. 1.4 which is decomposed in two subsystems \mathcal{X} and \mathcal{Y} we say \mathcal{X} and \mathcal{Y} are synchronized on the trajectory $\varphi(t)$ of the global \mathcal{Z} with initial condition $\mathbf{Z}_0 = [\mathbf{X}_0, \mathbf{Y}_0]$, with respect to the properties $\mathbf{g}_\mathcal{X}$ and $\mathbf{g}_\mathcal{Y}$, if there is a time independent mapping $\Theta(\cdot)$ such as

$$\|\Theta(\mathbf{g}_\mathcal{X}, \mathbf{g}_\mathcal{Y})\| = 0, \quad (1.7)$$

where $\mathbf{g}_\mathcal{X}$ and $\mathbf{g}_\mathcal{Y}$ are defined as properties of the system, $\Theta(\cdot)$ is a generic function employed to compare the two properties and $\|\cdot\|$ is any norm function. In the previous definition, we have considered two subsystems \mathcal{X} and \mathcal{Y} of the global WCDS replacing the previous notation in Eq. 1.4, i.e. $\mathbf{X}^{(i)}$ and $\mathbf{X}^{(j)}$. Both $\Theta(\cdot)$ and $\mathbf{g}_\mathcal{X}$ and $\mathbf{g}_\mathcal{Y}$ define the particular type of synchronisation. For instance, $\mathbf{g}_\mathcal{X}$ may be a property of phase, frequency of oscillations, amplitudes, state of the system. We refer to [21; 12] for a more complete technical account of this unification scheme, a few examples of synchronisation and further details. Most importantly for the purpose of this thesis, Eq. 1.7 defines a distance metric between two elements of the WCDS. This concept of distance is later similarly re-proposed at the sensor level when we discuss functional connectivity using as the phase of the signals as a suitable property $\mathbf{g}_\mathcal{X}$ and $\mathbf{g}_\mathcal{Y}$.

Moreover, from a classical dynamical system perspective, instead, synchronisation can be also related to the concept of a *Synchronisation Manifold* [116; 12; 18]. This geometrical entity can be defined as the points in the phase space where Eq. 1.7 is satisfied. In practice, when some of the inner variables of the system \mathcal{X} become synchronized, the system loses some of its degrees of freedom and the trajectory $\varphi(t)$ lies in a sub-manifold of the whole phase space: the synchronisation manifold is thus a special type of attractor as described in Section 1.1.2. In the nonlinear dynamics field the basin of attraction and the stability of the synchronisation manifold is a topic of active research. In this thesis, as discussed in the next section, this estimation of the dimension of this manifold is the major ingredient for the theoretical development in Chapter 3.

Causality

Defining, estimating and reasoning with the concept of causality has proven to be a formidable problem which has brought about several centuries of debate from a philosophical and more recently scientific and statistical perspective. For space reasons and not to be engaged in any of these lengthy debates, we refer to [112] for a comprehensive scientific account to the topic. Citing Clive Granger in [57]: *Causality is a concept whose definition people know what they do not like but few know what they do like*. This statement from an expert in the field emphasizes the vagueness of the concept and thus the difficulty in dealing with it.

From an effective connectivity point of view and thus rigorously, following the same reasoning of [40] and taking advantage of the dynamical system model in Eq. 1.1, causality can be better defined as a problem of inverse system identification: Taking the first order linear approximation of $\mathbf{f}(\cdot)$ and let the state point $\mathbf{X}_0 \in \mathbb{R}^n$ and $\mathbf{f}(\cdot)$ be differentiable at \mathbf{X}_0 we have

$$\mathbf{f}(\mathbf{X}) = \mathbf{f}(\mathbf{X}_0) + \mathbf{J}_{\mathbf{X}_0}(\mathbf{X} - \mathbf{X}_0) + o(|\mathbf{X} - \mathbf{X}_0|^2), \quad (1.8)$$

where the matrix $\mathbf{J}_{\mathbf{X}_0}$ is the Jacobian of the vector field $\mathbf{f}(\cdot)$ at \mathbf{X}_0 which is given by

$$\mathbf{J}_{\mathbf{X}_0} = \left[\frac{\partial f_i}{\partial X_j} \right]_{\mathbf{X}_0}. \quad (1.9)$$

The differential elements in $\mathbf{J}_{\mathbf{X}_0}$, i.e. $v_{ij} = \frac{\partial f_i}{\partial X_j}$, represent the *causal links* or the effective causal constraint between \mathbf{X}_i and \mathbf{X}_j at \mathbf{X}_0 . In practice, the coefficient v_{ij} is responsible for the variation of the effect on \mathbf{X}_i , i.e. $\frac{d\mathbf{X}_i(t)}{dt}$, given the cause \mathbf{X}_j . In the same manner, using the paradigm of WCDS in Eq. 1.4, it is easy to see after a derivation that $v_{ij} = C_{ij}$. Therefore, estimating causality in a complex linear network is equivalent to estimate the coupling matrix \mathbf{C} and in the more general case the entries of the Jacobian \mathbf{J} along the trajectory of the underlying dynamical system.

In a model free scenario, the system of differential equations $\mathbf{f}(\cdot)$ is not known a priori and from the data $\{\mathbf{x}_i\}_{i=1}^L$ alone the value of C_{ij} and J_{ij} cannot uniquely be retrieved. In this thesis, therefore, a different perspective is considered in order to estimate information flow in the brain from a functional connectivity point of view: Granger causality. This approach, we can argue, is a weaker form of causality, nevertheless it allows algorithmic implementation and thus computability.

1.2 Methods: functional connectivity

Functional connectivity is defined as temporal correlation between measurable spatially remote neurophysiological events which deviates from statistical independence [43; 132]. In other words, functional connectivity is specified as a generic pattern of interdependence that can be extracted from the time series $\{\mathbf{x}_i\}_{i=1}^L$. It has a major role in the recent neuroscience literature, as emphasized in [62], where the fundamental problem faced by modern non-invasive techniques such as EEG/MEG can be stated as

Problem 2. [Observational problem] *Can we observe collective neuronal activities from macroscopic aggregate signals?*

Collective activities stand for patterns of effective connectivity emerging between neural elements which regulates the functioning of the brain. What can neuroimaging techniques tell us about the brain distributed circuitry? [47]

As a mathematical problem, given an underlying complex dynamical network, *can we observe the intrinsic dynamical mechanisms of this network from its observable* $\{\mathbf{x}_i\}_{i=1}^L$? Being the latter, the only source of information available in a model-free scenario, functional connectivity is thus the only computable form of interdependence and is the main aim of this thesis: novel machine learning and signal processing techniques are tested in the following chapters against synthetic and real datasets in order to discuss Problem 2. What do the time series $\{\mathbf{x}_i\}_{i=1}^L$ tell us about the emergent phenomena of the underlying complex dynamical system? The next few topics describe some solutions to answer the previous questions.

1.2.1 Assessing local synchronisation using univariate statistics

Univariate statistics have been successfully applied for several years to analyse neurophysiological data. Strictly speaking, these methods cannot be considered as a tool of functional connectivity analysis since they are based on single time series. However, in this thesis we consider a single channel statistic because of the following reasons:

- It estimates a local measure of synchronisation, i.e. above the area which is produced by the single electromagnetic time series $\{\mathbf{x}_i\}_{i=1}^L$.
- Multivariate functional measures produce complex patterns of interdependence which explode combinatorically with the number of time series. A single sensor measure is simple and its outcome is easy to visualize .

We study this statistic in Chapter 3, based on an information criterion which looks at the dimension, at the shape and at the complexity of the local synchronisation manifold. As described previously, when the underlying system is synchronized, it reduces its degree of freedom and the trajectory in state space lies in a lower dimensional manifold than in the case of no synchronized state. We do not have direct information about this manifold since it is latent. However firstly, due to theoretical results in dynamical systems theory, it is possible to reconstruct an equivalent version $\hat{\mathbf{X}}$ of the synchronisation manifold. Secondly, it is possible to extract from $\hat{\mathbf{X}}$ an estimate of dimension, shape and complexity of the original manifold. These quantities are invariants of \mathbf{X} and $\hat{\mathbf{X}}$.

Therefore, we consider an information theoretic method which uses this insight in order to assess synchronisation from a single time series: *Spectral Singular Entropy*. This method was previously discussed in [146; 97; 49]. In this thesis this method is further improved, discussed from a point of view of complex network as in [62] and subsequently applied to the pathological electromagnetic datasets.

1.2.2 Multivariate statistics

In geometrical terms, we can consider each of the observable time series $\mathbf{x} = \{\mathbf{x}_i\}_{i=1}^L$ as a point in a multidimensional m data space. Functional connectivity is explored by computing the statistical relationship between these points defining a distance metric $d(\mathbf{x}, \mathbf{y})$, with $\mathbf{y} = \{\mathbf{y}_i\}_{i=1}^L$ a second signal from a different electrode, which needs to be estimated from the data.

Functional Synchronisation

Synchronisation in functional terms is a possible metric $d_S(\cdot, \cdot)$ in the space of the observable time series which can be generally designed following the definition in Eq. 1.7. In this equation, however, we need to take into account two important points:

- \mathbf{g}_X is the underlying property being measured which needs to be substituted in Eq. 1.7 by $\mathbf{g}(\mathbf{x})$, the property measured at the sensor level [21], which may include the contribution of noise.
- the presence of the random terms ξ and η suggests that Eq. 1.7 needs to be formulated in a probabilistic fashion.

An important question comes naturally at this point: What property of \mathbf{g} needs to be employed to extract the synchronisation metric of functional connectivity from the EM signals? There is no unique answer for this question. Several comparison studies in synthetic (chaotic models) and physiological datasets in the recent literature have taken into account different metrics [87; 121] showing similar results. These metrics include for instance, linear correlation, coherence in frequency domain, mutual information, phase synchronisation, state space synchronisation, event synchronisation ([114] for a comprehensive review). The main message is that a pragmatic choice should be taken according to the quality and the type of data and different metrics need to be employed [87]: for a complete exploratory study over a particular datasets, many methods should be employed and compared [22].

It is not this thesis' purpose to further compare different methods and perform a complete exploratory analysis of the epilepsy and the Parkinson's datasets available. Instead, the contribution of this thesis to debate is to consider two typologies of synchronisation measures based on phase relationships: the Mean Phase Coherence (MPC) [116; 87; 114] and the Phase Lag Index (PLI) [136].

The MPC index is one of the typical techniques in order to extract synchronisation in real data and it is specifically described in Appendix A. This index is computed using the Hilbert transform which is one of the possible approaches which retrieves phase information from broadband signals. Phase interdependence has been intensely used with success to study synchronisation in oscillatory systems such as the brain. The MPC is thus used alongside the univariate measure of synchronisation and the causality algorithm to support the extraction of features of functional connectivity in the epilepsy data in Chapter 6.

The PLI has been recently defined in order to cope with the problem of the EM observation function $\mathbf{h}(\cdot)$ in scalp EEG/MEG, and specifically volume conduction and active reference electrodes which are known as well as *the problem of common sources* [135]. The observation function, in fact, $\mathbf{h}(\cdot)$ mixes the true sources of brain activity and typically produces highly correlated EM signals as better explained in Chapter 2. For this reason spurious synchronisation between sensors may appear when phase relationships are computed using the standard MPC index invalidating the analysis. This is a typical problem with scalp EEG and MEG techniques where the EM sensors are not placed close to the brain cortex. The PLI developed to cope with this problem is specifically discussed in Chapter 6.

Functional Causality

As described previously, in mathematical terms, the estimation of causality is a problem of inverse system identification. This estimation process requires strong prior information about the structure of the underlying system we do not have: in a model-free scenario, the observable time series $\{\mathbf{x}_i\}_{i=1}^L$ are typically the only sources of knowledge. In this model-free scenario, the literature suggests that hints of causal relationships need to resort to the principle of temporal precedence [92]: *if activity in area A occurs prior to activity in area B, then activity in A "might" cause activity in B.* "Might" is emphasized since the condition is necessary but not sufficient for causality (spurious causality [112]).

Given two univariate time series $\mathbf{x} = \{x_i\}_{i=1}^L$ and $\mathbf{y} = \{y_i\}_{i=1}^L$, the previous statement indicate that to seek

a causal relationship it is necessary to look at their temporal coupled asymmetries. Therefore, a possible solution is to employ an asymmetric distance measure, i.e. $d(\mathbf{x}, \mathbf{y}) \neq d(\mathbf{y}, \mathbf{x})$ which can explore the asymmetry in time as well. In this respect, different asymmetric distance metrics such as mutual information, state space synchronisation, synchronisation likelihood have been designed in the literature. However, as shown in [120], asymmetry in the metric can be due to differences in the degree of freedom of the systems underlying the time series rather than a genuine relationship of causality. A similar argument is taken in [128] as a criticism to mutual information as a measure of causality.

A different approach, suggested by Granger [56], considers a plausible definition of causality which follows the principle of temporal preference:

Definition 2. [Granger Causality] Given two observable univariate time series $\mathbf{x} = \{x_i\}_{i=1}^L$ and $\mathbf{y} = \{y_i\}_{i=1}^L$ from an underlying WCDS \mathcal{X} , if the k -step ahead predictor of \mathbf{x} using the past observables of \mathbf{x} and \mathbf{y} together increases the predictability likelihood over a predictor using only \mathbf{x} , then we can say that \mathbf{x} and \mathbf{y} are causally related.

In practice, with this definition, causality asymmetries are tested using predictability across time. From a more general point of view, we can express the same concept in a probabilistic way:

$$\text{If } P(x_{i+k}|x_i^-, y_i^-) \neq P(x_{i+k}|x_i^-) \quad \text{then } \mathbf{y} \text{ causes } \mathbf{x} \quad (1.10)$$

where $\mathbf{x}_i^- = \{x_s\}_{s=1}^i$ and $\mathbf{y}_i^- = \{y_s\}_{s=1}^i$ are the time series point prior of the time i (past) x_{i+k} is the k -step ahead predictor. Eq. 1.10 is defined in [128] as the *measure of deviance from the Markov property*.

In Chapter 4, we propose a novel metric of directional functional interaction which is driven by the concept of Granger causality and is implemented to estimate the metric in Eq. 1.10. A nonlinear mutual prediction algorithm in state space which has roots in the Lorentz method of analogues is considered. The latter is the simplest predictor which belongs to the family of nearest neighbour methods. A novel version of this predictor is studied here to account firstly to keep the simplicity and computational advantage of the Lorenz approach. Secondly, to implement an adaptive technique of regression in machine learning given by a radial basis function neural network (RBF) in order to design a data-driven approach to causality. The prediction error, as considered in Granger's work, is a useful measure of dynamical interdependence which can be employed to estimate directionality of the coupling as well as its strength in neurophysiological data.

Functional Network Analysis

The previous two sections discussed the problem of measuring interactions using two conceptual distance metrics (one symmetric and the other one temporal asymmetric) between elements in the space of the observable data, i.e. time series,. In practice, these measures provide useful statistics in order to address *the problem of functional interdependence between two points of the brain at medium to large range connectivity*. Local connectivity is addressed instead by looking at the single channel measure.

The outcome of computing these metric in all the sensor space is a pattern of global interaction which may be expressed in matrix form (similarity matrix) or by a graph. An important and recent body of the

complex network research applied to neuroscience is therefore involved with the analysis, the processing and the significance of this global connectivity. The latter becomes more intricate the more nodes the measurement system has and, for this reason, several statistics from graph, spectral and clustering theory have been employed to provide some summarising information about the underlying complex mechanism [136; 6].

In particular, the interest of the neuroscience community in using these statistics have been boosted by several recent studies which has related anatomical, effective and functional connectivity to *Small-World* types of network [8; 133]. In mathematical terms, this kind of network has the well known property of *sparse connectivity, locally highly clustered areas and few long ranges connections* [144]. In practice, "small-worldness", firstly, fits the hierarchical structure described by the integration and segregation paradigm of the brain. Secondly, this hypothesis is supported by experimental anatomical findings, simulations of synthetic biological networks and by studies of functional connectivity analysis (for a review see [136]).

The study of the global pattern of interaction is not part of the main core of this thesis: the principal subject of the discussion is centered on the problem of the metric; studying the global pattern will involve a series of more detailed discussions and mathematical tools which would enlarge the body of this thesis. Further specific links to functional network analysis will be discussed during the conclusion chapters.

1.3 Overview of the thesis

The brain is a complex and complicated brain organ formed by a network of neurons with a multiscale architecture which recent theories in computational neuroscience have considered studying with the framework of dynamical system in complex networks. Within these theories, it is possible to describe emergent phenomena such as synchronisation and causality between neocortical elements as the processes responsible for the functioning of the brain. As described in Figure 1.1, these relationships are called effective connectivities while the topology of the brain network is referred to as anatomical connectivity. The main aim of this thesis is to extract these underlying quantities using novel methods of functional connectivity, i.e. the interdependence patterns of the electromagnetic signals generated from the brain complex system. The thesis is divided into the following chapters:

- **Chapter 1** is providing the context for this thesis introduction.
- **Chapter 2** introduces further conceptual background of recent relevant research in neuroscience. In particular: we discuss some more details about the physiological reasons of using complex networks and WCDS in this thesis. Secondly, we consider the observation part of the state space model in Equation 1.1: electromagnetic techniques are optimal tools to measure dynamical processes in the brain as well as functional connectivity. These techniques may be affected by the problem of volume conduction which is further explained in this chapter. A possible solution to this problem is the Phase Lag Index (PLI), a novel approach of functional connectivity appeared recently in the literature.

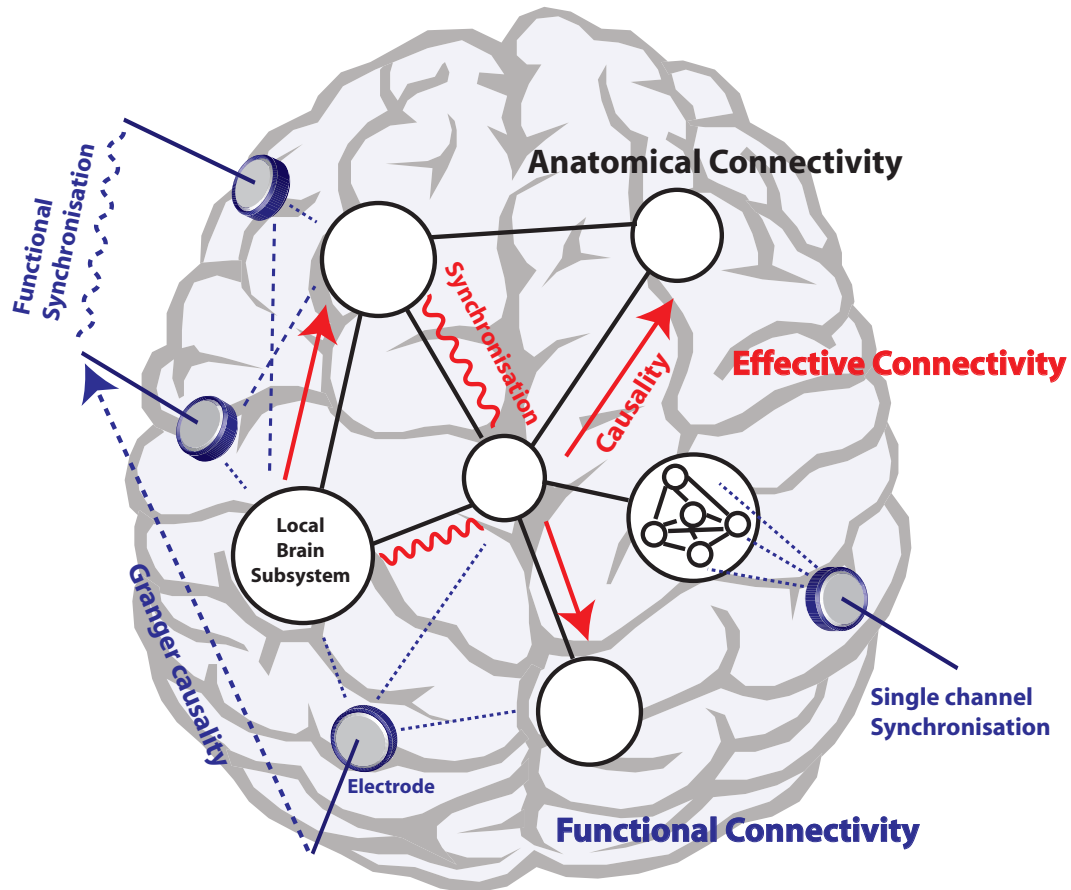


Figure 1.1: Schematic representation of the analysis problems in this thesis. The underlying anatomical and effective connectivities are estimate at the electromagnetic sensor level by their functional counterparts. This thesis consider some problems for single channel synchronisation, bivariate synchronisation and bivariate causality.

Finally, we also presents the description of the physiological datasets which are analysed to test the methods introduced in this thesis.

- **Chapter 3** has the main aim of discussing how to characterize the degree of local synchronisation underlying a single electromagnetic channel. We develop a novel method of analysis extending previous solutions which are discussed in this chapter. These methods will be tested successfully against a synthetic WCDS we specifically constructed for this purpose. This example aims to simulate one of the simplest possible networks which mimics fundamental features of a cortical neural assembly.
- **Chapter 4** explains the new perspective we introduced to measure directional interaction in neurophysiological systems based on Granger causality. We explore a novel and computational efficient machine learning method for causality discovery: the Analogues-RBF Granger causality. This method is tested, as in the previous chapter, using exemplary synthetic datasets. These simulations will show the efficiency of the method proposed and explain some details of the algorithm.
- **Chapter 5** shows the analysis of local synchronisation in the MEG and intracranial EEG datasets. The results will be seen to support our approach of single channel complexity measures as method to detect anomalous brain activity.

- **Chapter 6** displays the experimental findings for the analysis of multivariate functional connectivity in the pathological datasets. The results firstly further support the Analogues-RBF Granger causality approach in the case of real patients datasets. Secondly, this chapter discusses an important open issues the problem of volume conduction during the analysis of functional synchronisation.
- **Chapter 7** concludes the thesis summarizing the main advances and indicating directions and potential applications to be considered in the future.

2

Neuroscience background materials

In the previous chapter the motivations, the theoretical foundations and the methods of investigation of this thesis were introduced using the framework of dynamical complex networks. The main aim of this chapter is to describe further background materials of this thesis: the neocortex and its modular structure is discussed in Section 2.1 as the support for the theoretical models reviewed in the introduction; electromagnetic measurement techniques are the optimal means to extract information about the underlying brain activity and its functional connectivity as described in Section 2.2; pathological datasets are presented in Section 2.3 as examples to support the methods of this project and their possible future and more complete applications.

2.1 Neocortex modular architecture

The human brain can be divided in different functional and anatomical parts (Figure 2.1). In [106] for instance, three main organs are considered: the *brainstem*, the *cerebellum* and the *cerebrum*. The brainstem is the lower part of the brain and it is the structure directly connected to the spinal cord. The cerebellum is believed to be the centre of integration of sensory information and motor control. The cerebrum or *forebrain* is the largest part of the human brain and is divided in two almost equal hemispheres separated by the longitudinal fissure. The outer part of the cerebrum is the cerebral cortex or *neocortex* which is a folded layered sheet of grey tissue on top of white matter which comprises 80 percent of the human brain overall. It has an area of roughly 1600 to 4000 cm² and a thickness of 2 to 5 mm [106]. The white

matter, is mostly composed of axons which are fibres that have the purpose to connect different parts of the neocortex at middle and long range (1cm to 15cm). The neocortex contains about 10^{11} neurons which are interconnected by $2 \cdot 10^{14}$ synapses [22]. More importantly, *the neocortex is the most relevant part of the brain in this thesis* for two reasons:

- It is thought that cognitive functions in humans are generated in this area as well as pathological activity such as epilepsy and Parkinsons' [19].
- The cortex is believed to produce most of the electric potential which can be detected by electromagnetic techniques [106].

In fact, both brainstem and cerebellum contain deeper sources and are not the object of investigation in this thesis. Therefore, this thesis investigation focused on the modelling and the analysis of connectivity of the neocortex.

Neocortical structures

From a top-to-bottom description, the neocortex is partitioned in hemispheres, divided in four lobes by the Rolandic and Sylvian fissures, i.e. Occipital, Parietal, Temporal and Frontal lobes [85], which are further split in regions (Broadman regions [105]). While these areas and specific brain function are in general not related, it is possible to associate some gross functions [85]. For instance, the occipital lobes contain the part of the neocortex which process visual information. This is an established fact which is further considered, for instance, during the analysis of the MEG dataset where difference between patients using occipital brain signals can be detected by the methods developed in this thesis.

From a bottom-to-top description, an important feature of the anatomy of the neocortex is that it has shown to be organized as a neural network with a complex multiscale and modular architecture [17; 106], supporting the use of models such as complex networks and WCDS as described in Chapter 1.

At the microscopic anatomical level the neuron is considered the minimal discrete element of the brain and its biochemical state can be considered as one of the entries of the vector $\mathbf{X}(t)$. This theory is well known as the "neuron hypothesis" and it is now universally accepted [85]. The basic modules, however, which are the effective units of operation of the neocortex are conjectured to be given by assemblies of neurons called cortical structures: *microcolumns* and *macrocolumns* [102; 79; 105; 18]. Microcolumns, which contains 80 – 100 neurons, can be found at a scale of 40 – 50 μ m and are considered as the irreducibly smallest unit of the neocortex [105]. Macrocolumns, instead, can be found the scale of 0.2 – 3mm and are assemblies of 10^5 to 10^6 neurons interconnected by 10^{10} synapses [105; 18]. They are regarded as the fundamental unit for the brain organisation and function [18]. Metaphorically, macrocolumns can be thought of as fundamental subcircuits of the whole network while microcolumns, instead, can be associated to their irreducible inner components (resistors of these subcircuits for instance) [105].

Macrocolumns form the so called mesoscopic level of description and are important from a modelling perspective in this thesis [18] [105]:

- Inside cortical structures, the neurons form an intense connectivity network which can be described by a mean field or all-to-all sort of topology. Outside, instead, the connectivity has shown to be more

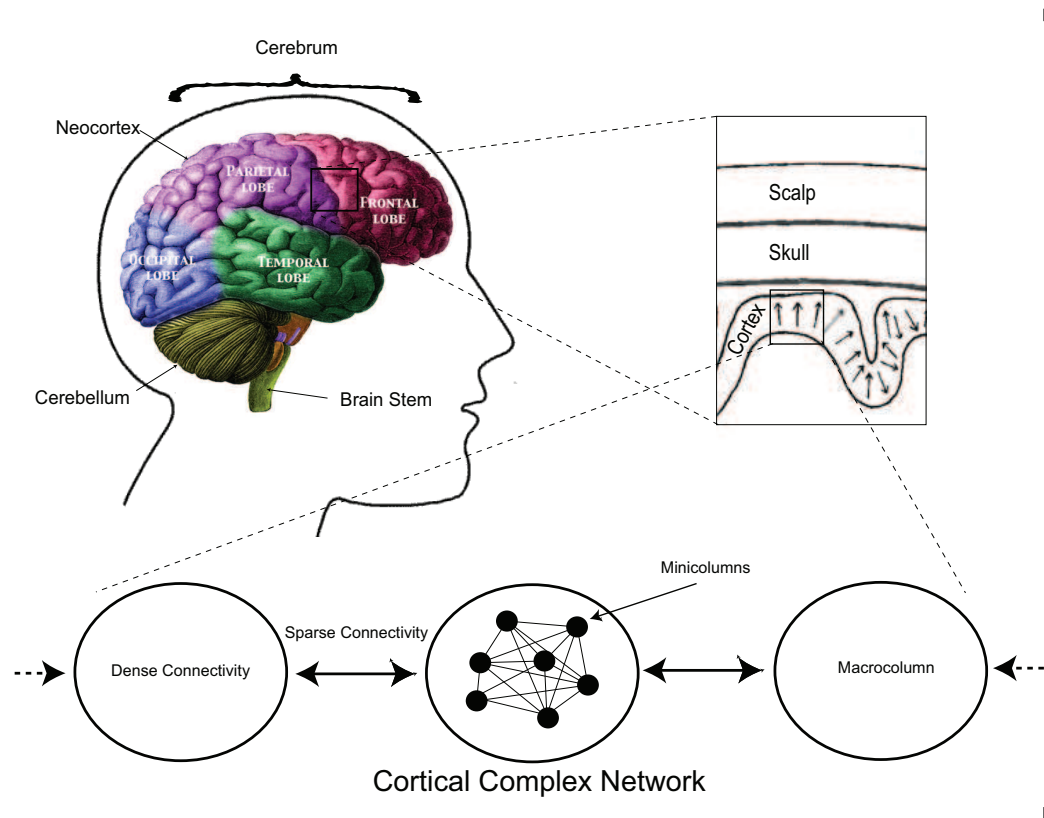


Figure 2.1: Important parts of the brain organisation. The top left corner shows the profile of the human head, as explained in the text. The highly folded human cortex contains the sources of the brain activity. Macrocolumns are the fundamental unit of computation the neocortical neural network and responsible for the electrical brain activity. They can be further decomposed in more basic atomic components (microcolumns).

sparse, with a sequential step decay consistent with this cortical columns physical extension.

- Dynamical correlation between neural activity inside the columns have been shown to be stronger than outside.
- For the previous two points, neurons belonging to these assemblies are more likely to be collectively excited by the same stimuli (shown in the visual cortex for instance).

Therefore, while neurons can be considered as the atomic nodes \mathbf{V}_a of the neocortical graph \mathcal{G} , macrocolumns can be specified as the network's minimal functional nodes \mathbf{V} . If one is interested to model medium to large brain dynamics, as in the case of this thesis, *macrocolumns can be better taken as the minimal latent graph variable of the neocortical network*. Using macrocolumns as modelling blocks have been used for instance in [106]. As discussed in the introduction, the dynamics of these nodes \mathbf{V} may be represented by the partitions functions $\mathbf{f}_i(\cdot)$ which define the biochemical state of the macrocolumns. In the literature, the $\mathbf{f}_i(\cdot)$ are often modelled by nonlinear functions due to the coupling of assemblies of neurons which can give rise to complex and eventually chaotic behaviour (for instance as discussed in [18]).

In the next chapters, for these reasons, the simulations of WCDS with nonlinear and chaotic units in order to model macrocolumns aggregate that can be taken as support for studying medium to large brain dynamics. The main aim of these models, while they cannot realistically be taken as valid brain models,

they can still mimic some aspect of the brain dynamics. More importantly, they are used in support of the feature extraction techniques developed in this thesis.

2.2 Electromagnetic techniques

2.2.1 Brain imaging

The process of measurement of the sources of the brain activity and their interaction is addressed in this thesis using electromagnetic techniques [22; 106]. This family of methods has the property to achieve a greater level of temporal precision in measuring brain signals which is also the reason why EM methods are optimal tools for the investigation of the dynamical properties. This is often compared with techniques of structural and functional imaging because they have higher spatial resolution.

Functional/Structural imaging

Briefly, this category of techniques provides directly or indirectly a tomographic image of the brain anatomy and its physiological activity. Structural imaging refers to techniques such as Computed Tomography Scan (CAT) or Magnetic Resonance Imaging (MRI) which extract static images that can describe only the anatomical property of the brain. Functional imaging instead, refers to approaches such as Positron Emission Tomography (PET) and Functional Magnetic Resonance Imaging (fMRI) [42] which are able to detect also dynamic changes of brain activity.

Nevertheless, while the strength of fMRI is the high spatial resolution, it offers a poor temporal resolution which is due to the slow dynamics of the haemodynamic blood response [42] they estimate. This metabolic activity has in fact a latency of approximately 1s [7]. Moreover, the coupling of the neural activity and the haemodynamic blood response is not well understood yet (?). For this reason, they are not considered the best tools to investigate dynamical interdependency even if recent works have addressed this problem with advanced time series analysis techniques such as dynamical causal models [40].

EEG/MEG

Ionic currents which flow inside the neurons have been shown to produce a measurable electromagnetic field [64]. Electroencephalography (EEG) [106] and Magnetoencephalography (MEG) [64] are the two most important ways to measure neural activity from this field.

EEG analysis was launched in 1929 when H.Berger measured the first electrical brain activity of neural mechanisms inside a living organism [7]. EEG measures the neuronal activity of the brain captured by the electric potential between pairs of electrodes placed directly on the scalp. It is the most common among the imaging techniques since it is a cheap technology and for this reason is widely used as a tool of clinical investigation. MEG is a relatively recent method of imaging since it was introduced in the late 1960's by Zimmerman who invented the SQUID device [64]. SQUID (Superconducting QUantum Interference Device) are sensitive magnetometers which measure the magnetic flux coming from the brain. These magnetometers are placed outside the scalp since the magnetic field emerges from the skull without much

dispersion. This magnetic field, however, is extremely weak and for this reason highly sensitive to external noise comparing to EEG. In order to detect the brain signals, MEG recordings have to be measured in a shielded room and the magnetometers are placed in a large cone containing liquid helium. The adoption of this technology makes the MEG device more expensive than EEG which is the main reason for its restricted use.

EEG and MEG are complementary techniques since the electric and magnetic field are related by Maxwell's equation [106]. As described in Fig. 2.2, MEG and EEG are sensitive to EM activities produced by different neural sources. These neural sources can be considered to be given by macrocolumns which tessellate the neocortex as discussed previously. EEG measures the activity of radial neural sources which are typically found in the sulcus. MEG instead is more influenced by components that are tangential to the surface which are found in the gyri. For this reason, these techniques are supposed to observe distinct types of neural activity and the morphological structure of the EM signals may be different.

A particular advantage of MEG compared to EEG is that the latter is sensitive to current dispersion over the skull whose effect is known as volume conduction [64]. As described in the following subsection, MEG is sensitive only to primary currents which are generated directly from the ionic flows coming from the neurons. For this reason, MEG has an higher spatial resolution (3mm) compare to EEG (1cm) because in the latter, the signal is smoothed out by scalp conductivity effects. This property has allowed MEG to be used, together with techniques of inverse identification, for problems of source localisation [7].



Figure 2.2: Profile of part of brain with the MEG and EEG scalp recordings. The MEG is more sensitive to correlated dipole in the sulcus(cfl) while the EEG is more sensitive to dipoles that are placed in the gyri (bdeghjkm)(picture taken from [106]).

iEEG

EEG/MEG have superior performances in terms of temporal sampling with respect to the previous functional imaging techniques. The electromagnetic field is measured with temporal resolution of tens of milliseconds which is considered enough to capture the faster oscillations of the brain: $\approx 100\text{Hz}$ [7]. However, as discussed, the measurement sensors of the previous techniques are positioned outside the brain and so can only capture a macro aggregate of the real neuronal activity and they are sensitive to any further interference such as external noise and volume conduction. EEG/MEG are in fact non-invasive imaging methods which for this reason have boosted clinical and academical research. The neuronal brain tissues are not directly contacted using these technologies and in theory a neurological experiment can be applied as many times as necessary. This is especially important with studies of healthy normal subjects which for ethical reasons they cannot undergo any submissive surgical operation.

Alternative measurement technologies are placed directly inside the cerebral cortex in order to study the finer spatiotemporal description of the brain at the neuronal level. Typical electromagnetic techniques in this class are called intracranial EEG (**iEEG**), comprising Electrocorticography (**ECoG**), subdural EEG (**SD-EEG**), Stereotaxic depth electrodes [106][22]. They are techniques usually applied either to animals, i.e. monkeys and rats, for research purposes or to humans subjected to chronic neurological diseases for clinical motives such as epilepsy. For the latter, normal extracranial imaging methods are not always sufficient to extract, with the required precision, either the location or the reason of such deficiency and the only hope is to surgically implant internal probes. This is the situation for some of the datasets in this thesis which were recorded using iEEG prior to a surgical operation in order to know the position of the epileptogenic region. Therefore, it is possible to take advantage of this technique, previously recorded for pure clinical purposes, in order:

- To get access to artefact free brain signal.
- To come closer to the level of the effective connectivity of the neocortex.
- To know more about the pathology and provide tools to deal with it.

2.2.2 Electromagnetic observational paradigm

The basis of the electromagnetic activity of the brain is due the electrochemical reactions inside the neuron [64; 106]. It is not possible to measure the single neural activity for living patients due to the limitation in the spatial accuracy of today's equipment. However, the synchronized firing of a large population of neurons, i.e. macrocolumns, gives rise to an average field which can be monitored by electromagnetic techniques, EEG and MEG as discussed before. The relationship between macro aggregate neural sources and the magnetic field \mathbf{B} and the electric potential V retrieved from the EM recording sensors is completely described by the well known Maxwell's partial differential equations [106]. Since the range of frequencies adopted for the analysis of the brain activity is below 100Hz (cellular activity may contain frequencies below 1KHz [64]) the EM signals can be considered in the *Quasi-Stationarity* regime [7]¹As in . For this reason,

¹As in [64], the assumption of quasi-stationarity is valid for $2f\epsilon/\sigma \ll 1$. For the brain tissue, $\epsilon = 10^5\epsilon_0$ and $\sigma = 0.3\Omega^{-1}m^{-1}$. For $f = 100\text{Hz}$ we have that $2f\epsilon/\sigma = 2 \cdot 10^3 \ll 1$

the magnetic and electric field are decoupled, they can be retrieved independently. A general formulation of mapping the neural activity to the EM is given by the nonlinear observation function in Equation 1.1 and can be rewritten by:

$$\mathbf{x}(\mathbf{r}) = \mathbf{h}(\mathbf{r}, \mathbf{J}^P(\mathbf{r}')) + \eta, \quad (2.1)$$

where $\mathbf{J}^P(\mathbf{r}')$ is the primary current flow at the spatial location \mathbf{r}' . $\mathbf{x}(\mathbf{r})$ is either the magnetic field \mathbf{B} or the electric potential V measured at the sensors level with spatial coordinate \mathbf{r} and η is an additive random noise factor which affect the measurements.

The solution of the Equation (2.1) as a function of the current density $\mathbf{J}^P(\mathbf{r}')$ is called *the Forward Model* and it is analytically computable only in a few special cases. It is generally a function of two parameters: the model of the sources of the neural activity and the geometry of the head. In the particular case of dipolar sources, $\mathbf{J}^P(\mathbf{r}') = q\delta(\mathbf{r}' - \mathbf{r}_q)$ where q is the amplitude of the dipole centred at \mathbf{r}_q and $\delta(\cdot)$ is the Dirac delta function. Furthermore, in the case where the head model is spherical, it is possible to obtain the following approximation of Equation (2.1):

$$\mathbf{x}(\mathbf{r}) = \mathbf{h}(\mathbf{r}, \mathbf{r}_q, \Theta)\mathbf{q}^T + \eta, \quad (2.2)$$

where $\mathbf{q} = (q_1, q_2, \dots, q_n)$ is the vector of n neural source amplitudes and $\mathbf{h}(\cdot)$ is a nonlinear function of the dipole position \mathbf{r}_q and orientation Θ . If one considers that the dipoles have fixed orientation, Equation 2.1 becomes linear and it can be rewritten as [64]:

$$\mathbf{x}(\mathbf{r}) = \int \mathcal{L}(\mathbf{r}, \mathbf{r}')\mathbf{J}^P(\mathbf{r}')d\mathbf{v}, \quad (2.3)$$

where $\mathcal{L}(\mathbf{r}, \mathbf{r}')$ is called the lead field which represents some construction characteristics of the EEG/MEG sensors and \mathbf{v} the volume of neural tissue where the dipoles are situated. In particular, Equation 2.1 can be also approximated and rewritten in matrix form as:

$$\mathbf{x}(t) = \mathbf{H}\mathbf{X}(t) + \eta, \quad (2.4)$$

where $\mathbf{X}(t)$ is now the vector of the general dynamical system of the brain. $\mathbf{X}(t)$ thus represents the amplitude of the neural activity of n elements in the brain, i.e. $\mathbf{X} = \mathbf{q}$. The important message, here, is that \mathbf{x} is a linear function of \mathbf{X} in first approximation and thus possible nonlinear dynamics in observations are due to phenomena inside the brain.

2.2.3 The problem of volume conduction

While the linear Equation 2.4 is only a coarse simplification of Maxwell's laws, it is enough to show the problem of volume conduction which typically influences EM techniques. In practice, the matrix \mathbf{H} can be seen as a *spatial filter*. A single observable time series \mathbf{x} , is dependent on a weighted combination of the underlying neighbouring sources as depicted in Figure 2.3. In particular, the signal of a single source can propagate its effects to different neighbour electrodes: *any measure of synchronisation computed between*

these neighbour electrodes would be correlated by the presence of this common mode and spurious functional connectivity may arise. This effect is particularly remarked on in few studies, which we mention, based on coherence as measure of interaction where it is experimentally discussed [108][107].

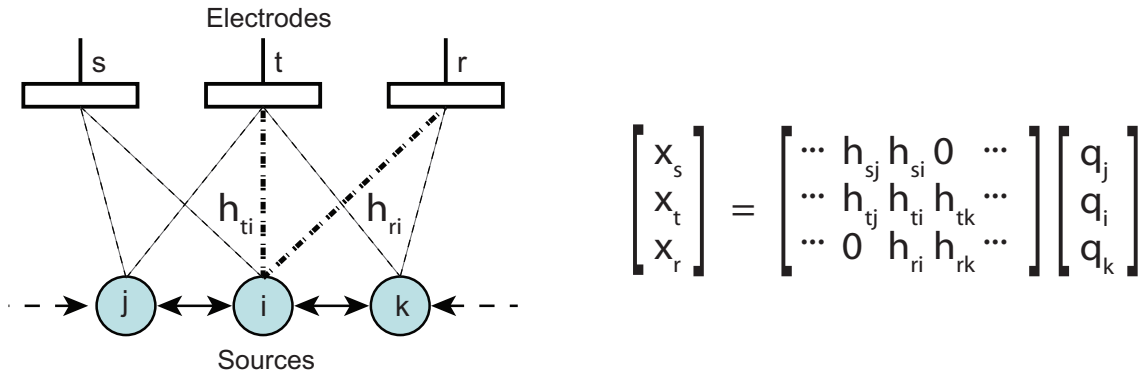


Figure 2.3: Schematic representation of the problem of volume conduction. Electromagnetic waves from single sources can propagate their effects to neighbouring electrodes. They are responsible for spurious correlations between these electrodes.

The volume conduction has been known for many years [106], however, only recently has it become a serious problem when analysis of functional connectivity became the key paradigm for brain understanding. The estimated connectivity pattern may be in fact due to spurious correlation at the scalp level and not given by the genuine interaction between sources. In practice, this problem may influence the ability of functional connectivity to estimate the real effective connectivity.

As described in [135] there are two classes of methodologies one can currently resort to cope with the estimation of functional connectivity in the case of volume conduction:

- The first one consists of *extracting functional connectivity at the source level*: an algorithm of source reconstruction is firstly needed to solve the inverse problem [7]; Secondly, interdependence between these sources can be computed [63]. As described in [135], this approach however suffers from the ill-posed nature of the inverse problem: No unique choice of the source model can and the procedure of source reconstruction can influence the interdependence pattern [63].
- The other alternative is to *apply a measure of interaction directly on the signals at sensor level which is not influenced by the problem of volume conduction*. Methods such as the partial coherence [108; 107] and the imaginary part of coherence [104] were shown to be effective against this spurious effects. Another possible method of the same family that has been recently proposed is the Phase Lag Index (PLI) [135]. The main idea behind the PLI is that common signals due to the volume conduction would propagate at the same instant on two different electrodes. This phenomenon would correlate at zero lag the signals in these two channels. Therefore, PLI penalized zero lag correlation (and thus synchronisation) searching for asymmetry in measuring synchronisation. Further mathematical details for the PLI are left in Appendix A where the standard Mean Phase Coherence is also treated.

The problem of volume conduction is further discussed in this thesis experimentally during the analysis of functional phase synchronisation on real patients data and remain an open issue. It is not in the main

aim to solve this problem but it is important to remark on its existence during any functional connectivity analysis of EM data. While there has been a recent explosion of studies of EM brain data using functional connectivity complex network techniques, their findings need to be reported back to this important problem: *To what extent the propagation of EM signals influences functional connectivity in estimating the true effective connectivity of the brain?*

To conclude this section, it is important to mention, that the univariate functional connectivity analysis described in Chapter 3 is possible only because of a volume conduction effect. In fact, multiple local sources propagate their electromagnetic effects to the single electromagnetic channel above their locations. Therefore, the algorithm in Chapter 3 takes advantage in a positive way the problem of volume conduction detected from a single time series when these multiple local sources become mutually synchronised.

2.3 Materials: Pathological brain datasets

While the most challenging question in neuroscience consists of understanding the mechanisms of the normal and healthy brain, the datasets provided here comprise a typology of problems which are often encountered during clinical research. They are examples of pathological brain activity which are taken in this thesis firstly to support the validity of the studied methods and secondly to demonstrate their possible clinical use. In this respect, the main aim is to produce a qualitative analysis of each pathological case. We are not in the position to make any general quantitative examination as for instance in the case of epilepsy one dataset is not sufficient. The material of this thesis can be thus considered as exemplary or pilot studies. Further and more detailed analysis are needed for a complete and deeper investigation of each single disorder.

2.3.1 Intracranial EEG datasets

Epilepsy

Epilepsy is a disorder of the central nervous system of the brain which is caused by a sudden burst of excess electrical activity that interferes with the normal neural activity and causes mental and physical dysfunction. It is an important disease since about 1% to 3% of the world population are affected while 10% can experience at least one seizure during their lifetime [129]. Generally, epilepsy can affect at any age but it has been reported that it develops more often during childhood and in the elderly [73]. A formal definition of this disease can be found in [38] (another source of definition can be found in [35]) by defining the meaning of the following concepts:

- An *epileptic seizure* is a transient occurrence of signs and/or symptoms due to abnormal excessive or synchronous neuronal activity of the brain.
- *Epilepsy* is a disorder of the brain characterized by an enduring predisposition to generate epileptic seizure and by the neurobiotic, cognitive, psychological and social consequences of this condition. The definition of epilepsy requires the occurrence of at least one epileptic seizure.

A seizure is a clear demarcation in time with a start and a finish [38]. It produces a clinical manifestation giving rise to signs and symptoms. Most importantly for the goal of this thesis a seizure is caused by an abnormal enhanced synchrony of neurons. In an epileptic brain, in fact, a massive widespread synchronous activity takes place [95]. The exact mechanism of why a seizure occurs and how, at the present time, remains unknown [73]. Dynamical theories of the brain have thus been proposed to understand the cause of this disorder which have led to the interests of nonlinear time series analysis and chaos modelling techniques in the last three decades [134][100].

Using the framework of dynamical systems, in [94][95] the authors have given two possible scenarios in which a seizure can occur. In the first one the differential laws of the underlying network provides two basins of attraction compatible with *interictal* and *ictal* states. The interictal state is characterized by a brain activity which seems normal. The ictal state is instead represented by the occurrence of the seizure. The latter one is typically represented by a low dimensional manifold which represents the higher level of synchronisation (few degrees of freedom in the neural system). In the former, i.e. interictal state, this manifold instead is highly complex. While in healthy subjects the trajectory remains stable around the interictal attractor, an abrupt change takes place prior to the seizure from one to the other in epilepsy patients. The second scenario assumes that the attractor is only one. However, some changes can occur in the set of control parameters which govern the neural system. The attractor gradually changes and it deforms its shape from interictal to ictal in epilepsy patients.

The transition interictal to ictal can be exogenous, endogenous or due to random noise [94]. In the first case some external stimuli cause the seizure to be triggered. This common type of epilepsy is called *reflexive* and it can be addressed in an experimental analysis (for instance using photic stimulation[77] as described later). In the endogenous case, the route to epilepsy may be due to a gradual change in the underlying brain control parameters. Identification and tracking of these parameters may be important to detect pathological changes prior to the seizure. In the last case, random fluctuation of the phase space trajectory can initiate the switch between basins of attraction and an abrupt transition would occur. The route to the occurrence of a seizure, in this case, may be impossible to detect.

From a complex network perspective, epilepsy is assumed to be caused by abnormal discharge in the so called *burster neurons* [100]. These neurons initiate the seizure when they entrain their neighbours to reach a critical mass of pathological firing patterns. The process of entrainment can be driven by a pathological synchronisation, a loss of inhibition or due to the lowering of the threshold of excitation of the neurons. In any case, this causes, the widespread pathological global synchronisation which characterizes epilepsy.

Dataset description

We obtained relevant data on patients from the Birmingham Childrens Hospital on intracranial epileptic events to submit to the data analysis stage. Two subjects with symptomatic focal epilepsy were studied. While the hospital database contained clinical records of several other patients, these two subjects were the

only ones selected after manually screening their EEGs. Clinical recordings of other patients were available but not suitable for the analysis in this thesis since their data was of poor quality, i.e. it contained high level of noise, it had not sufficiently long time series or it contained too many external artifacts. The recording of this data was intended and it was sufficient for clinical reasons but not suitable for further signal processing.

The diagnosis of focal epilepsy was made according to the classification scheme published by the Commission on Classification and Terminology of the International League Against Epilepsy in 2001 [35]. The two patients had a previous detailed neurologic examination and prolonged video-EEG (electroencephalography) monitoring with scalp electrodes placed according to the International 10-20 system. Moreover, high-resolution magnetic resonance imaging (MRI) was performed with a Siemens 1.5 Tesla SP system (Siemens, Erlangen, Germany) using a standardized epilepsy protocol that included high-resolution T1-weighted volume acquisition, T2-weighted, and fluid attenuated inversion recovery (FLAIR) sequences. Subdural electrodes (SDEs) were implanted thereafter in the two patients to confirm the scalp EEG and MRI data about the epileptic focus before proceeding to the surgical operation. Both patients underwent surgery after the recording. The resection comprised the area localized using the information obtained by the EEG recording and the neuroradiological data and the outcome was good.

The first subject was 15 years old at the time of the recording. From the age of 8 she presented stereotyped seizures pattern consistent with an onset in the somatosensory area quickly spreading to the motor cortex with clinical features involving the supplementary motor cortex and secondary generalisation. At the time of the evaluation the patient was treated with Carbamazepine and Levitiracetam without a good control of the seizures. The EEG pattern was characterized by an interictal slow-wave activity with superimposed sharp transient in the parietal regions and during sleep by almost continuous spikes, polyspikes and spike and slow wave. The neuroradiological finding showed a DNET (acronym in the literature of the dysembryoplastic neuroepithelial tumor) in the left centro parietal area. The EEG was recorded using grid contacts over the left centro-parietal area (A01-40) with a separate strip of 4 in the medial area (B01-04). In this study we consider the A contacts only. Electrode array A01 to A08 was placed in the anterior-posterior direction with contact A01 being more posterior and lateral. Contacts A07, A15, A23, A31 were mapped to correspond to primary sensory cortex. The contact A03 was not considered since it was not recording properly. Therefore, 39 iEEG electrodes were left for the analysis.

During the recording, the patient presented several clinical seizures associated to a spread of activity on the full grid contacts. The dataset used in this thesis contains one clear event which was selected because long interictal and ictal periods were available and the signals have no artefacts. The dataset is referred to *Intracranial EEG dataset A*. In Figure 2.4, part of the recording submitted to the analysis is shown. An expert confirmed the presence of early bursts of spike and fast rhythmic discharges in the contacts about A17-A20. The presence of a global epileptic event is clearly displayed.

The second subject was 12 years old at the time of the recording. From the age of 6 he presented clinical episodes characterized by subjective somatosensory symptoms (numbness down the right arm followed by shaking of the ipsilateral arm) followed by generalized tonic-clonic seizures. The patient was treated with

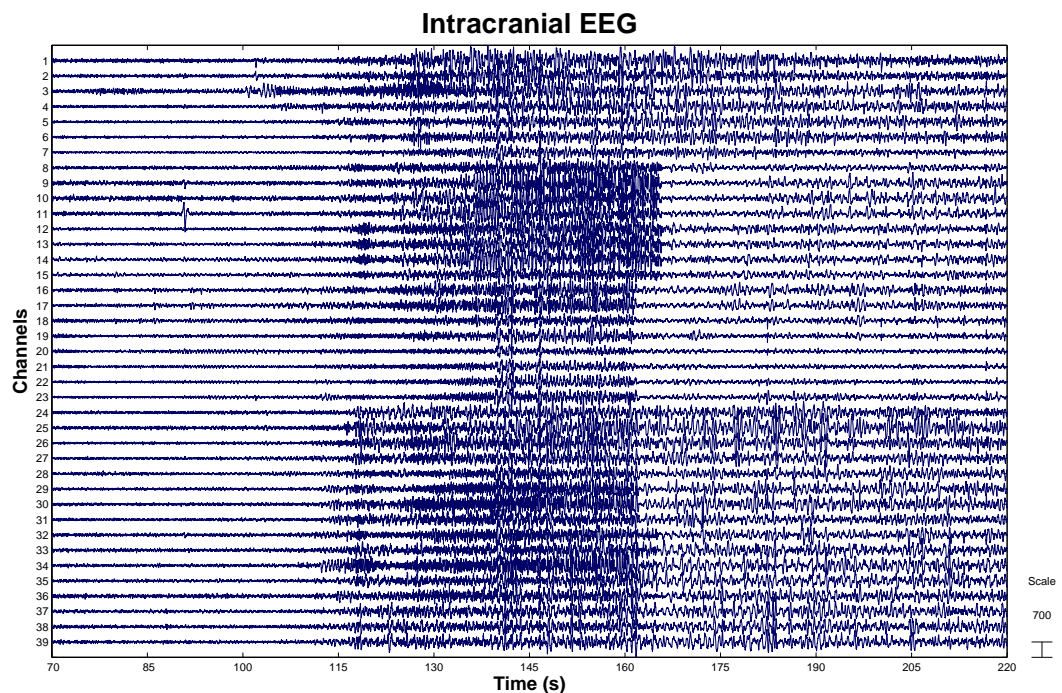


Figure 2.4: Snapshot of the intracranial EEG dataset A where period of apparently interictal activity is followed by an ictal one which is spread all across the grid.

carbamazepine with a partial improvement of the seizures and the addition of Levitiracetam allowed an attenuation of the clonic component of the seizures but he never became seizure free. The EEG pattern was characterized by rhythmic theta and sharp activity in the left parietal region. The neuroradiological findings showed the presence of a cortical dysplasia just posterior to the post-central gyrus of the left parietal lobe. The EEG was recorded using a 32-channel subdural grid placed directly over the left parietal lesion. Contacts 8, 16, 24 and 32 were along the medial aspect of the grid and contacts 1, 9, 17 and 25 were along the lateral aspect.

During the recording the patient presented numerous seizures associated with the clinical signs previously described. These seizures were associated with prolonged bursts of spike and fast rhythmic discharges mostly localized on contact 20, 21, 28, 29. A snapshot of one of these activities is shown in Figure 2.5. In total 33 epileptic bursts were counted in the recording considered. The dataset is referred to as *Intracranial EEG dataset B*. Interestingly, from a signal processing point of view and in contrast with the previous patient, these events suddenly occur and do not propagate globally to all the grid.

Data analysis

The main purpose of analysing these iEEG datasets is to address the problem of characterizing the spatiotemporal evolution of an epileptic seizure. In this respect, the data processing is performed using a sliding windows methodology which extracts over the time measures of functional connectivity. The different stages of the framework of analysis of this thesis are important because:

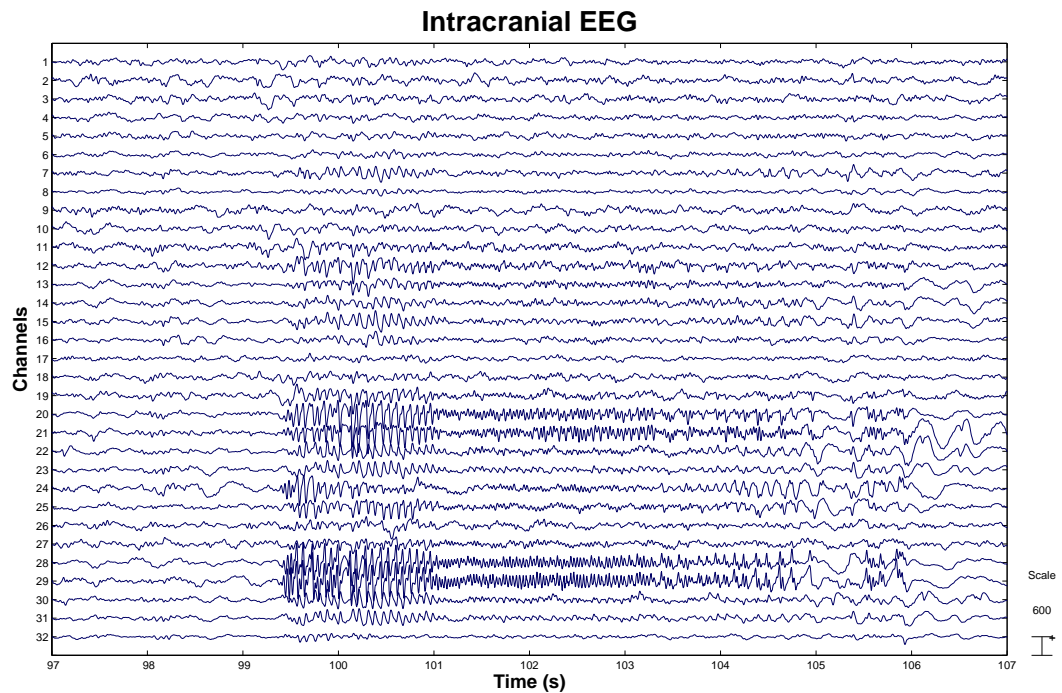


Figure 2.5: Snapshot of the intracranial EEG dataset B. In some contacts there is evidence of pathological epileptic activity.

- the single channel measure of synchronisation provides the first stage of analysis. It is designed to spot abnormal synchrony beneath each electrode and find the position where the seizure starts (positions of the burster neurons).
- The multivariate synchronisation measure is intended to spot abnormality at medium and large connectivity range. It further establishes the state of the pathological process measuring the strength of the coupling among electrodes.
- A directional dynamical interdependence measure detects the local spread of pathological synchronisation to the global scale looking at changes of the information flow between electrodes.

2.3.2 MEG Parkinson's related Dementia study

Parkinson's and Parkinson's related dementia diseases are complex neurological disorders which are known to cause several behavioural dysfunction and quality of life impairment [14; 16; 15; 139; 138]. Parkinson's affects ten million people worldwide while dementia has been shown to develop from the latter with a rate of 60% [15]. Parkinson's patients show subtle executive dysfunctions, tremor at rest, poverty of movement and postural instability. Dementia patients have further cognitive impairments which affect memory, attention and cognition [14].

Similar to other neurological disorders such as Alzheimer's disease (AD), the underlying mechanisms of these disturbances and their differences are far from being elucidated [134]. In terms of pathological

mechanisms, it has been shown (references in [138]) that these disorders are generally related to progressive degeneration of different neural structures of the brain. Lesions were observed in the cortex which may indicate serious damage in the anatomical connectivity of the pathological brain. These lesions, in the context of Parkinson's, have shown to be more advanced with a specific signature for dementia patients compared to normal Parkinson's. We refer to [14] for a more detailed explanation of clinical causes and recent findings from a neurophysiological perspective.

Importantly for the purpose of this thesis, the evidence of anatomical damage, including AD, are in fact compatible with *loss of dynamical complexity* of the brain activities and pattern of *functional disconnectivity* between different areas [134]. For this reason, different studies look for patterns of functional connectivity to identify abnormal neural activities.

Dataset description

Three groups of subjects participated in this study. The data was collected and previously reported in [14] which are provided here for completeness. In [14] a full detailed description and further particular analysis can be found. The groups have the following composition: 13 Dementia (8♂, 5♀, 74.38 ± 4.9 years), 13 Parkinson's without dementia (6♂, 7♀, 71.69 ± 5.1 years) and 13 healthy, elderly control (8♂, 5♀, 71.69 ± 5.9 years). It was reported in [14] that there are no significant differences in age or gender distribution between the groups as assessed by univariate analysis of variance (ANOVA).

All of the patients had undergone a series of physical, neurological and cognitive examinations. Parkinson's patients fulfilled the criteria of "Parkinsonism" using the United Kingdom Parkinson's Disease Society Brain Bank (UK-PDSBB) clinical diagnostic criteria. Dementia fulfilled the DSM-IV criteria from the American Psychiatric Association for dementia. Controls had no evidence of neurological or psychiatric disease in their clinical history and they had no difficulty with cognitive functions in their everyday life. Cognitive abilities were assessed using the Mini Mental State Examination (MMSE) [39] and the CAMCOG [123]. Dementia patients had MMSE scores of 24 or less (out of 30), whereas Parkinson's and control participants scored 28 or above. Using the CAMCOG there were significant differences (ANOVA) between dementia subjects (71.5 ± 12) and the other groups while no significant difference between Parkinson's (96.0 ± 5) and controls (99.5 ± 4). Further exclusion criteria for the subject groups and the medical treatment of the patients can be found in [14].

The study protocol was approved by the medical ethical committee of the Amsterdam University Medical Centre and all subjects gave written informed consent.

MEG data were acquired using a 151-channel whole-head MEG system (CTF Systems Inc., Port Coquitlam, BC, Canada) in a magnetically shielded room (Vacuum-schmelze GmbH, Hanau, Germany). MEG recordings were acquired in the morning and all patients had been asked to not take their medication before coming to the experiment. The registration in these conditions is generally defined as OFF-state.

The MEG was recorded in eyes close resting state condition and eyes open resting state condition. The MEG data was recorded at 312.5Hz band passed at 0 – 125Hz. A 3rd order software gradient was applied

to the data [143]. The data selected for this thesis study are 5s which are long artefact free and furthermore DC corrected from an external investigator ($L = 1562$ time samples).

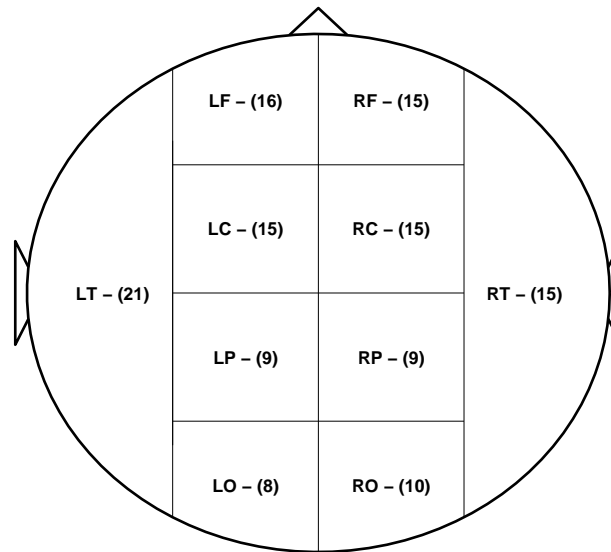


Figure 2.6: Regions of the brain as labelled by the channels available (L=left, R=right, O=occipital, C=central, F=frontal, P=parietal, T=temporal). The number inside the brackets indicates the number of each channels available for each scalp area.

From the previous study [14], out of the the total 151 channels, the datasets are reduced to 141 channels in order to take into account faulty and noisy channels in common to all patients. The selected channels can be divided in regions of interest which are depicted in Figure 2.6. The middle line region (channels labelled with a "Z") were considered during the global investigation but are not belonging to any local area and thus not shown in the partition of .

For each patient and for both eyes closed and eyes open conditions a series of trials were undertaken. From the datasets we have, it is noticed that the number of trials are unevenly distributed across patients due to the removal of possible artefacts. For each group the global dataset has 342 trials for the controls, 329 for the Parkinson's patients and 322 for the dementia patients in one of the 2 eyes conditions. In total, the dataset size used during the following study is given by: $2 \times (322 + 329 + 342) \times 141$ time series of length 1562 samples.

Data analysis

Differently to the previous iEEG datasets, where the functional connectivity analysis investigates the dynamics of a seizure, for this MEG dataset the purpose of the investigation is to extract structural differences among the group of subjects. The data processing is an event related type:

- The single channel technique, as in the case of the previous epilepsy datasets is important for an exploratory type of analysis because is a local measure of coupling and it does not suffer of the problem of interpretation of bivariate similarity matrix.

- The multivariate synchronisation measure is intended in this dataset, to show how scalp measurements such as MEG are affected by common sources problems and how spurious synchronisation may occur.
- The analysis of this dataset is not intended for the causality analysis. Firstly, there are no physiological reasons to consider such an investigation. In the case of epilepsy, a measure of directional interdependence is specifically intended to spot the spreading of the pathological activity due to the occurrence of a seizure. Currently, there are not hypotheses which support difference of information flow between group's of subjects with this paradigm and diseases. Secondly, it is not clear what is the effect of volume conduction on a causality investigation. The Granger causality metric in Chapter 4 does not take into account this problem.

2.3.3 Photic EEG dataset

During the initial stage of this project, a scalp EEG dataset was considered as recorded in a previous study from the Birmingham Children Hospital. This dataset is an example from a photic epilepsy patient.

Photosensitive epilepsy (PSE) [78] is a common type of epilepsy that appears in a significant proportion (10%) of the epileptic population. It is a common stimulus-induced epilepsy that can be triggered by everyday life devices such as television or videogames consoles. The underlying mechanism is still unknown as for the rest of the epilepsy family. In a clinical setting the PSE is generated in the patient by using an intermittent photic stimulation such as complex video patterns or intermittent flash stimulation. These stimuli are usually controlled by changing the frequency of the trigger.

In this thesis, the dataset available is a noninvasive scalp EEG recording from a subset of 19 electrodes of the standard 10/20 system. In Figure 2.7, for instance, a portion of the recording, which shows an abnormal EEG activity, is displayed. In this figure is also present the additional channel that registers the external Intermittent Photic Stimulation (IPS). This channel is important because when epilepsy is triggered by the appropriate frequency the pathological activity is clearly visible in the EEG trace.

The data analysis of this dataset is discussed in Chapter 6 as part of the causality investigation reported in [24]. As in the case of the MEG, volume conduction may influence multivariate connectivity and the effect on the causality estimation is not clear and left for future study. More importantly, while the results of causality can be successfully interpreted showing the validity of the causality algorithm, the reason to pursue this type of analysis does not seem to help the study of this particular kind of pathology. Previous works have rather focused on of synchronisation analysis [78].

2.4 Summary

The objective of this chapter was to present further relevant medical background details in order to complete the introductory part of this thesis.

In particular, it was discussed that the neocortex is the portion of the brain which contains the sources of neural activity observable using electromagnetic techniques. This activity can be modelled by approximating the hierarchical and multiscale anatomical architecture of the neocortex as a complex dynamical

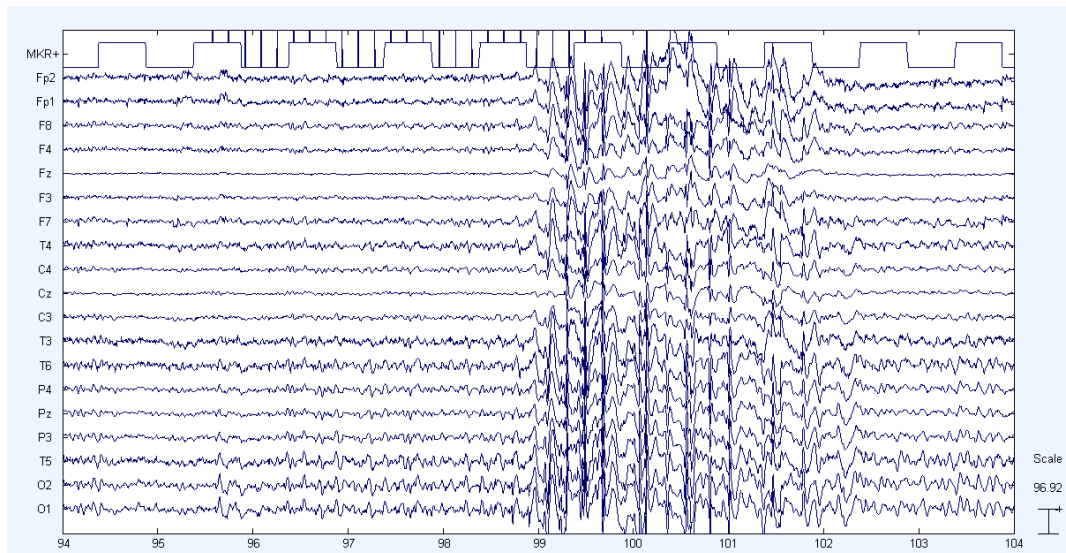


Figure 2.7: Portion of an EEG recording that shows Photosensitive Epilepsy. The first channel contains the stimuli.

network at its mesoscopic level of description. Macrocolumns are the nodes of this network as well as the fundamental computational blocks in the brain.

Electromagnetic techniques produce highly sampled multivariate time series which are shown to be tools to infer dynamical processes in this network. In this chapter, it was discussed that these time series can be approximated by a linear mixing function of the amplitude of the nonlinear activity in the neocortex. For this reason, the estimation of functional connectivity at the sensor level is biased towards the volume conduction problems.

This chapter introduced the description of a few pathological datasets related to epilepsy and Parkinson's diseases. They are common neurological disorders where the effective connectivity of the brain is seriously compromised. They are examples of MEG and EEG techniques. They therefore offer a possible representative illustration of the use of the methods developed in this thesis and later analysed.

3

Single channel assessment of local synchronisation in neural systems

In the introduction, in analogy to the typical brain mapping inverse problem, an additional important question was addressed: Can collective properties (system interdependence) of the neural system be retrieved by the macro aggregate signals from EEG/MEG?.

The main goal of this chapter is to address the previous question when the macro aggregate signal is a single time series localized to a particular brain region. A set of complexity feature extraction methods are proposed and compared based on a state space reconstruction approach using singular spectrum analysis. These techniques are checked in this chapter against a simulation study of a synthetic weakly coupled dynamical system. It serves the purpose to model the plausible dynamics of a local neural network. Application and further discussions of these methods to real electromagnetic data are left to Chapter 5 and Chapter 6.

This part of the thesis is based on the work discussed in [62]. In this chapter further analysis is proposed to extend this work.

3.1 Introduction

As discussed in Chapter 2, synchronisation patterns are due to the biochemical and topological properties of the neuronal networks in the neocortex which constrain the solution of its dynamics to evolve in a lower dimensional subspace than its potential degrees of freedom (number of neocortical elements). This invariant orbit in state space is coincident with the notions of attractor and synchronisation manifold. The dimensionality of this subspace and its geometry (complexity) may play an important role in order to assess different degrees of coupling of the underlying neural network. From the measurements side, methods exist to reliably localize brain activity using non-invasive measurements and extract time series of high signal-to-noise ratio (SNR) comparable with invasive measurements [62]. For this reason, the dimensionality and the complexity of the underlying system subspace can be explored which helps to inform two fundamental questions in this thesis: the functional role of synchronisation and desynchronisation phenomena at the local level and the discrimination of patients subjected to neurological pathologies.

Different univariate time series analysis methods, as suggested in the literature, can be employed to extract discriminatory statistics. Linear methods based on autocorrelation function, power spectrum and autoregressive modelling have been successfully applied for both normal and pathological brain activities ([106] and reference therein). However, in the last two decades, nonlinear statistics started to gain more interest and more applications [134; 114]. The use of these methods is justified by the intrinsic nonlinear nature of the brain as presented in Chapter 2. Techniques such as the largest Lyapunov exponents (L1), correlation dimension (D2) [82] and various entropic based measures [81] have been exploited to investigate complexity of nonlinear EM time series. In particular, some of these methods have been originally designed to analyse low dimensional chaotic models before being applied to brain research as well [134].

However, while the nonlinear analysis of the electromagnetic signals was largely explored in the last 20 years, the hypothesis of a low dimensional attractor to explain the brain dynamics did not provide enough evidence to support chaotic behaviour [134]. Firstly, some strong grounds have been found only at the neuronal level but failed at larger scale [36; 86]. Secondly, at a macroscopic scale, due to the intrinsic presence of a noise term, randomness can be confused with deterministic chaotic behaviour. In [82], for instance, the authors warn of the use of chaotic tools when the underlying system is not chaotic. Thirdly, the electromagnetic observations may mix the basic neural signals and destroy our capability to identify true low dimensional chaos [62].

On the basis of the previous argument, a methodology it is considered here that firstly accepts the presence of nonlinear brain dynamics, without assuming the existence of chaos in the data. A complexity measure based on entropy is designed to fulfill this purpose. Secondly, an automatic data driven procedure is proposed which results in a simple algorithm. Thirdly, this method rejects observational sources of noise at the sensor level which may limit the ability to discern subtle changes in the underlying synchronisation process.

The following three steps which are graphically shown in Figure 3.1 presents the structure of this chapter idea:

State Space Reconstruction which provides a preprocessing procedure to the time series $\{\mathbf{x}_i\}_{i=1}^L$ to retrieve the hidden space which describes the nonlinear brain dynamics. This approach is based on the

geometrical framework of the delay embeddings and Taken's theorem.

Manifold learning which is designed to fulfil two roles: to tune the choice of the method of delay embeddings. Secondly, to explore the reconstructed space quantifying its geometry. In this thesis, this stage is implemented using Singular Spectrum Analysis (SSA) which provides the singular spectrum $\{\sigma_i\}_{i=1}^N$ as its output.

Feature extraction in order to assess univariate synchronisation statistic based on the singular spectrum. Two families of methods, i.e. dimensionality and complexity, have been proposed in the literature to examine the reconstructed manifold. The combination of the two are considered to extract the local synchronisation and to reject observational noise.

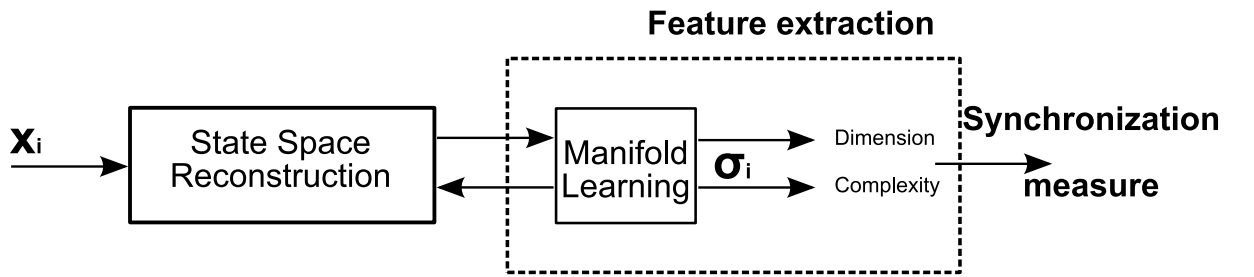


Figure 3.1: Conceptual structure of the algorithm presented in this chapter based on state space reconstruction.

3.2 Synthetic example

3.2.1 Description

This chapter uses a synthetic model which emulates the possible behaviour of the underlying neuronal assemblies in the cortex as described by the weakly coupled dynamical system paradigm in Chapter 1 and Chapter 2. The main aim of this model is to *test that proposed single channel measures can recover different degrees of collective behaviour*. The model chosen for this purpose is a chain of coupled non-identical Rössler Oscillators, as described in Figure 3.2 which fits our basic requirement: it is a WCDS which previous studies in the literature [109; 61] have shown provides clustering of synchronisation among its elements for a specific range of control parameters.

The mathematical formulation of this lattice is described by the following coupled differential equations:

$$\begin{cases} \dot{x}_i &= -\omega_i y_i - z_i, \\ \dot{y}_i &= \omega_i x_i + a y_i + \epsilon(y_{i+1} - 2y_i + y_{i-1}), \\ \dot{z}_i &= b + z_i(x_i - c), \end{cases} \quad (3.1)$$

where x_i, y_i, z_i for $i = 1, \dots, n$ are the $3i$ state variables of the individual Rössler system, a, b, c are parameters of the lattice which define the topology of each oscillator, ω_i are the natural frequencies of each oscillators and ϵ is the coupling strength between neighbouring systems. The number of oscillators is given by $N = 50$.

This synthetic example mimics a plausible pattern formation among cortical networks as suggested in Chapter 2. From this perspective, it is important to emphasize that while the Rössler system itself cannot be taken as a precise model of the biological nature of the underlying neural network, it can still offer an abstract representation of the neocortical dynamics [62]. In this simulation $a = 0.15, b = 0.4, c = 8.3$ are fixed during the simulation following the numerical investigation of the lattice in [109]. This choice of parameters has been shown to produce at the level of the single Rössler system a dynamic which can be approximated by a nonlinear phase coherent oscillator with ω_i natural frequency. Complex oscillatory behaviour of populations of neurons have been shown to be a fundamental ingredient of the brain rhythms. Thus, the individual Rössler can then be taken as a simple representation for the microscopic level of a typical neural assembly. In practice, they offer a model of the mesoscopic nodes of the neocortex, i.e. the macrocolumns.

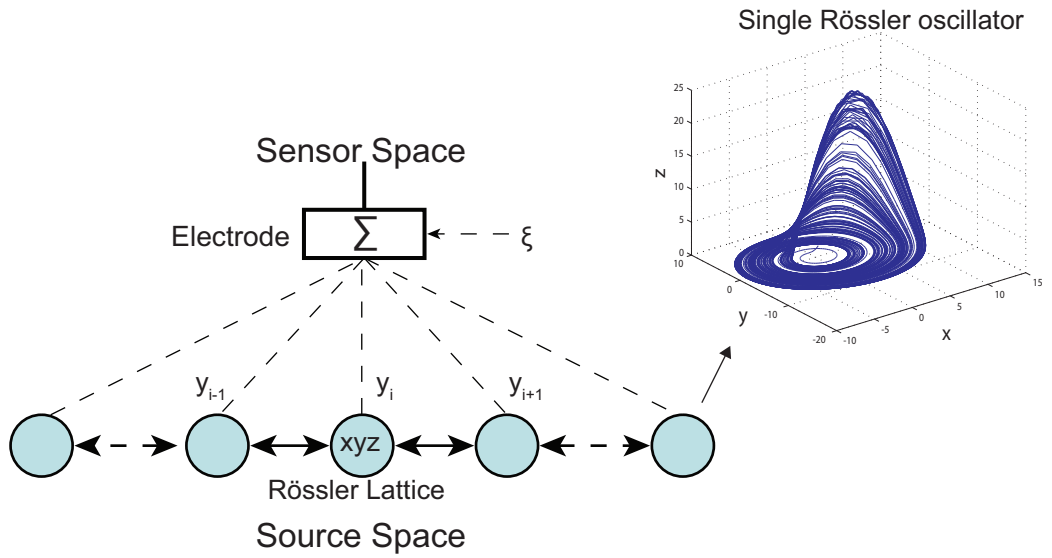


Figure 3.2: Lattice of coupled non-identical Rössler Oscillators as a model for local (mesoscopic) neocortical dynamics. The single Rössler system is described by three variables x_i, y_i, z_i which trajectory is drawn by its classical attractor shape. The virtual electrode captures a weighted sum of the variable y_i plus an additive random term ξ .

At the global level, the Rössler network is regulated through two parameters: ϵ and δ . The ϵ accounts for the strength of a nearest neighbours diffusive type of coupling, i.e. $(y_{i+1} - 2y_i + y_{i-1})$. The first $i = 1$ and the last $i = 50$ oscillators are coupled to remove the boundary effects. The further collective term δ introduces a set of frequencies mismatch between the individual units of the network. The Rössler system in this synthetic example is studied using a linear distribution of the natural frequencies as follow

$$\omega_i = \omega_1 + \delta(i - 1), \quad (3.2)$$

where $\omega_1 = 1 \text{ rad/s}$ is the characteristic frequency of the first element $i = 1$ of the lattice. The parameters ϵ and δ are designed to simulate the concept of functional integration and segregation which is at the basis of the complexity behaviour of the brain dynamics as introduced in Chapter 2. The coupling strength ϵ contributes to merge the dynamics of each single oscillator while the frequency mismatch δ tends to keep them apart. This property is indeed a common feature to weakly coupled dynamical systems which

emphasizes the interest they received in the last few years to model brain rhythms.

The macroscopic aggregate $O(t)$ at the mean field level is designated as the superposition of the signal of each Rössler. This quantity is measured by the electromagnetic electrodes and is given as follows

$$O(t) = \frac{1}{n} \sum_{i=1}^n y_i(t) + \xi(t), \tag{3.3}$$

where $\xi(t)$ is a source of additive white noise which simulates the common external disturbance of EEG/MEG sensors. The choice of the variable y_i is considered to form the aggregate signal because this coordinate has been shown [1] to better capture the degrees of freedom of the underlying system. The single Rössler system is thus more observable from y_i than from x_i or z_i .

3.2.2 Simulation

Following the numerical analysis of this chain [62; 109], the frequency mismatch is fixed at $\delta = 0.009$ during the simulation. The coupling strength is varied with $\epsilon = 4, 2.5, 1.1, 0.6, 0.4$ in order to obtain a pattern of respectively 2, 3, 5, 6, 7 clusters. These values have been set manually since a minimum variability of ϵ destroys the structure. The parameters chosen during the simulation are summarized in Table 3.1. The numerical integration is performed in Matlab using the Runge-Kutta Ode45 routine. The simulation was computed from 0 to 2.5×10^4 s using a step of 0.1s. However $O(t)$ is subsampled at 1s to prevent consecutive time points of the mean field becoming too correlated. As described in the following section, this procedure is necessary to avoid the window of analysis becoming too large. Therefore, the total number of points available for the simulation is $2.5 \cdot 10^4$. The first 5000 points which may contain the initial transient effects are discarded (the burn-in samples). The data available during the investigation thus contains 20000 time points. An observational noise component ξ is added to the data which is sampled from a zero mean Gaussian distribution with standard deviation equal to the 5% standard deviation of $O(t)$.

Rössler simulation			
Fixed Parameters	Detuning	Coupling	No. Clusters
$a = 0.15$	$\delta = 0.009$	$\epsilon = 4$	2
		$\epsilon = 2.5$	3
$\epsilon = 1.1$		5	
$\epsilon = 0.6$		6	
$\epsilon = 0.4$		7	
$\epsilon = 0$		No Cluster	
$b = 0.4$			
$c = 8.3$			

Table 3.1: Simulation values of the Rössler system parameters and correspondent number of cluster found in the lattice.

In Figure 3.3, the numerical analysis of the Rössler system is presented after setting $\epsilon = 2.5$. In this figure it is possible to notice the emergence of 3 macro clusters of synchronisation. This is shown by its similarity matrix computed using a measure of bivariate phase synchronisation between all the possible combination of Rössler systems: the Mean Phase Coherence (MPC), as shown in the Appendix A. The

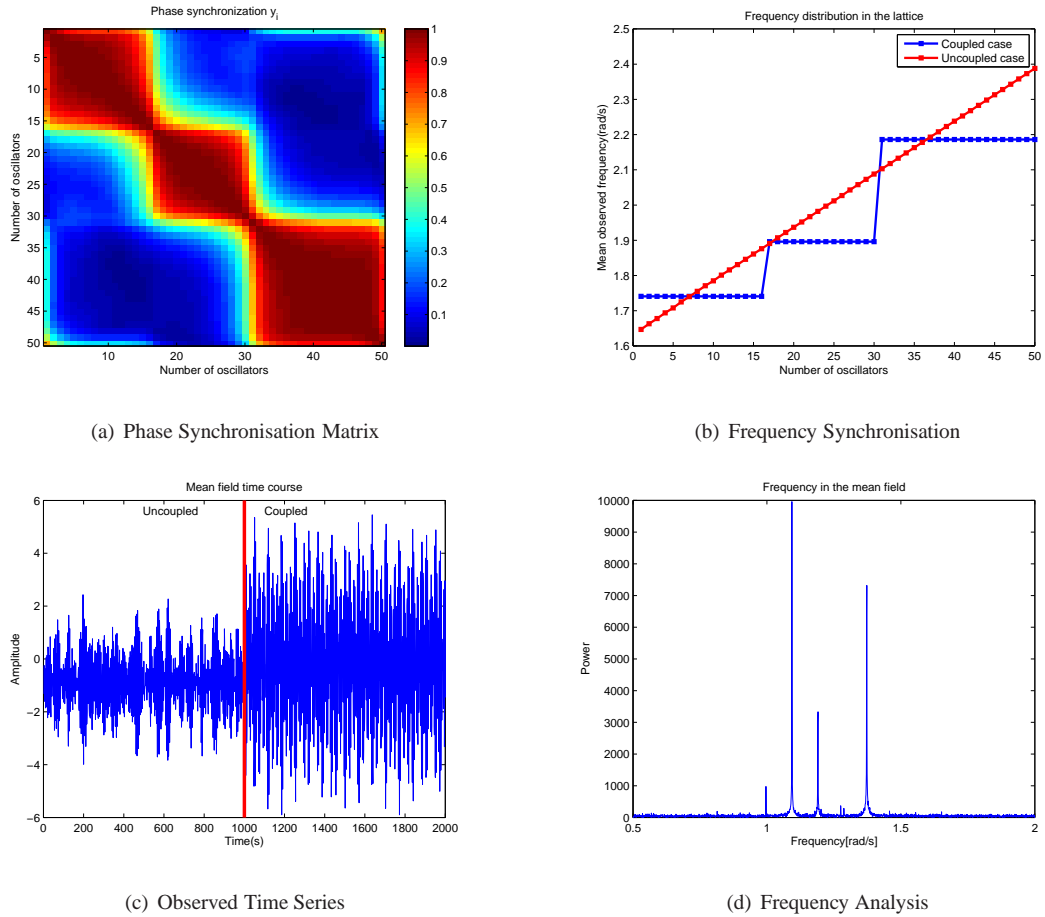


Figure 3.3: Simulation of 3 clusters of synchronisation in the Rössler lattice with $\varepsilon = 2.5$ and $\delta = 0.009$. The analysis is based on 20000 time samples without the effect of the transient. The measure of mean phase coherence (MPC) shows that the 3 clusters are locally coupled in the top left figure. In the top right figure three frequency plateaus are found in the system and plotted against the uncoupled case. The bottom right graphs represent the mean field of the system using the Equation 3.3. The coupled case and the uncoupled case are plotted against each other which shows difference in amplitudes due to the mean field coupling. In the bottom right picture it is shown the frequency contents of the mean field. 3 main peaks are clearly visible due to the clustering of frequencies of the underlying network.

similarity matrix reveals that the synchronisation happens between nearest neighbour elements as shown by the interdependency pattern along the main diagonal. This was expected by the initial topology of the lattice. In Figure 3.3(b), 3 plateaus of frequency locking are estimated from each oscillator and they are plotted against the uncoupled scenario, i.e. $\varepsilon = 0$. As in the plot of the phases, this plot shows frequency specificity at local level. In the bottom figures, the plots of the aggregate signals are presented. The left figure, shows the comparison between the mean field due to clustering and the one given by uncoupling. The right figure shows the frequency content of the simulated coupled system.

In Figure 3.4 a similar plot to Figure 3.3 with $\varepsilon = 2.5$ shows the emergence of 7 clusters of synchronisation using a coupling value $\varepsilon = 0.4$.

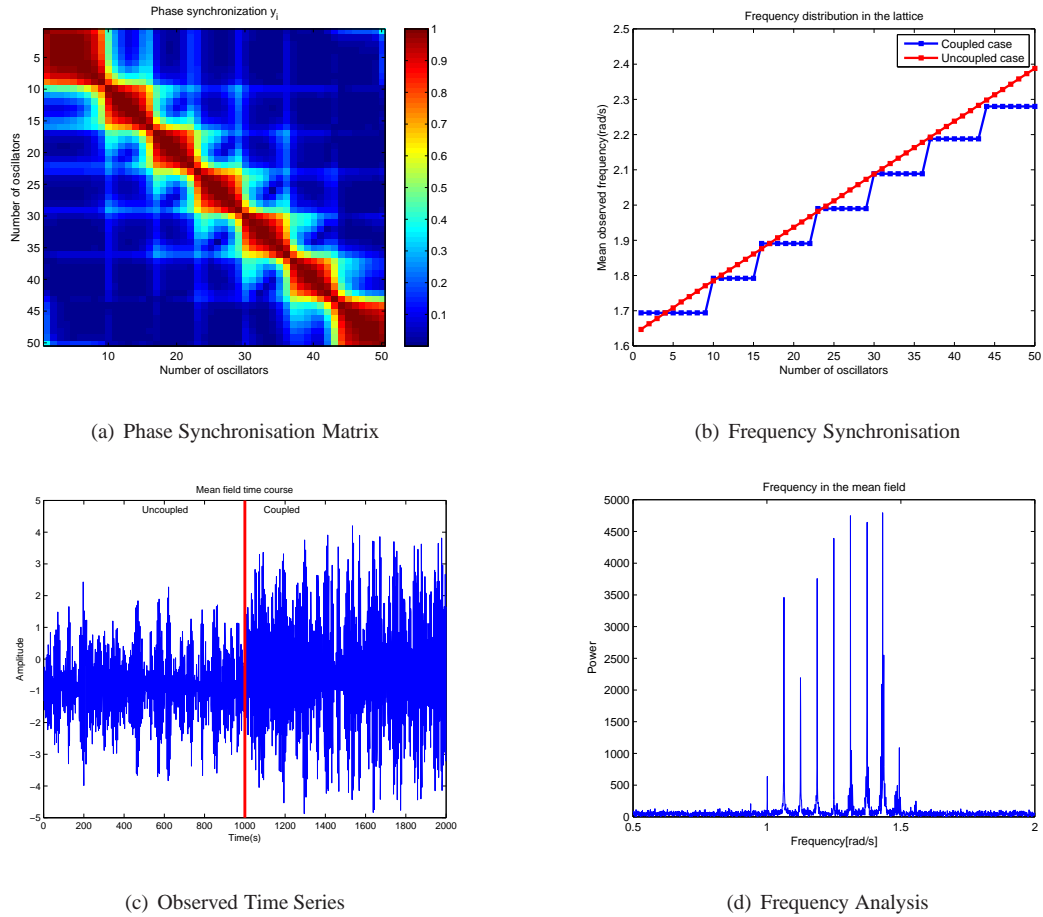


Figure 3.4: Simulation of 7 clusters of synchronisation in the Rössler system with $\epsilon = 2.5$ and $\delta = 0.009$. The plots shows similar properties than the one in Figure 3.3 which is referred to for an explanation.

3.2.3 Discussion

From the bottom plots in Figure 3.3 and Figure 3.4, it is possible to notice two important points: the power of the signal increases with the coupling and three and seven main peaks are clearly emergent in the frequency spectrum. Therefore, both characteristics can be taken as measures to discriminate the underlying synchronisation. However, the simulated system described here is only the best case scenario for these measures.

Clustering in frequencies can be taken as a measure of interdependence only in this particular case which is difficult to find in real signals. As discussed in [62], the Rössler system with the previous setting consists of phase-coherent oscillators which normally presents sharp phase-locking at different frequencies [117]. Real cortical models are consistent with non-phase-coherent oscillators, instead [62]. Therefore, it is possible that a more complex profile of the frequency spectrum of the electromagnetic recordings emerges which is normally the case in real data.

In the power case, as shown in [61] in simulation, the power-synchronisation relationship may be more complicated due to the underlying coupling and to the observation function. Global power decrease has been shown during the increase of the coupling for different choices of the parameters in Equation 3.1 [61]. It is possible that the increase of the power happened instead in specific frequency bands. Thus, it may be

possible that there is no direct mapping between global power increase and synchronisation. Nevertheless, it is a general conviction that power and synchronisation are generally proportional at the mean field level and several works have considered power as a measure of coupling ([115] and reference therein). We are not aware if the latter point has been rigorously proven.

A measure based on dimensionality and complexity, instead, is designed here to capture linearity, measured by spectral methods, as well as nonlinear coupling. Non-phase-coherent oscillators can, in fact, give rise to phenomena of generalized synchronisation [124]. The trajectories of the system are thus attracted to the synchronisation manifold, the dimensionality of which, can be estimated by the methods proposed in this thesis. Therefore, while with this simulation linear methods based on power and frequency spectrum can be employed to characterize synchronisation, it is expected that methods using state space reconstruction are more generally applicable.

3.3 State Space Reconstruction

The WCDS Rössler system in Equation 3.1 and Equation 3.3 is a particular type of state space model as described in Equation 1.1. It is proposed again using the same notation:

$$\begin{cases} \frac{d\mathbf{X}(t)}{dt} = \mathbf{f}(\mathbf{X}(t), \theta_{\mathbf{f}}) + \xi, \\ \mathbf{x}(t) = \mathbf{h}(\mathbf{X}(t)) + \eta. \end{cases} \quad (3.4)$$

The general purpose of a state space reconstruction approach consists in extracting information from an underlying dynamical system using its observable sample data $\{\mathbf{x}_i\}_{i=1}^L$. It is thus designed to solve an inverse problem of system identification in a model-free scenario.

The main step and the core of SSR consists in building a reconstructed space $\hat{\mathbf{X}}$ which is equivalent to \mathbf{X} such that some of the properties of \mathbf{X} are in common and can be estimated using $\hat{\mathbf{X}}$. The mathematical significance is associated with the existence of a function $\Phi(\cdot)$ which relates \mathbf{X} to $\hat{\mathbf{X}}$, i.e. $\hat{\mathbf{X}} = \Phi(\mathbf{X})$. In particular, it is convenient that this transformation function is an *Embedding* which means that $\Phi(\cdot)$ is locally differentiable and so is its inverse. If this condition is satisfied, it guarantees that it is possible to extract some property of the original space dynamics using only the reconstructed spaces. These features are known in the literature as *geometrical invariants* of the function $\Phi(\cdot)$ [82]. The dimension of the space \mathbf{X} is an invariant and thus motivates the use of these tools for the goal of this thesis [82].

The problem of connecting the dynamics of the original state space with its observations is addressed in this thesis using a particular instance of the *method of delay embedding* (for a general review see [82]). It is the most common approach of state space reconstruction in order to choose observable points to build the space $\hat{\mathbf{X}}$. In [111] it was shown numerically that given a scalar time series $\{x_i\}_{i=1}^L$, it is possible to reconstruct an equivalent multidimensional state space of its original attractor. A simple procedure considers a set of vectors as follow

$$\mathbf{v}_i = (x_i, x_{i+\tau}, \dots, x_{i+(M-1)\tau}) \quad (3.5)$$

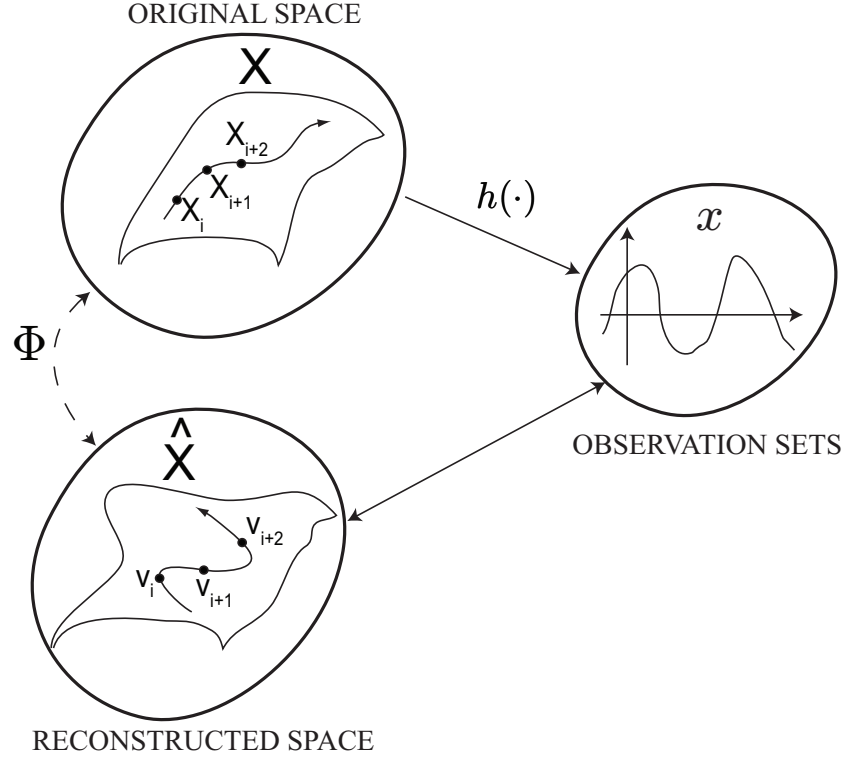


Figure 3.5: Sketch of the state space reconstruction.

where M is known in the literature as the *Embedding dimension* and τ is the *Time delay*. For continuous systems with sampling time τ_s , the time delay is defined as $\tau = \rho\tau_s$ with $\rho \in \mathbb{N}$. The composition of the time series segments $\{\mathbf{v}_i\}_{i=1}^K$ is iterated along $\{x_i\}_{i=1}^L$. This set of vectors can be combined in the following trajectory matrix

$$\mathbf{V} = \begin{bmatrix} v_i & v_{i+\tau} & \cdots & v_{i+K} \\ v_{i+\tau} & v_{i+2\tau} & \cdots & v_{i+(K+1)} \\ \vdots & \vdots & \vdots & \vdots \\ v_{i+(M-1)\tau} & v_{i+M\tau} & \cdots & v_{i+K+(M-1)\tau} \end{bmatrix} \quad (3.6)$$

where $K = L - (M - 1)\tau$ is the number of delay vectors in \mathbf{V} . The trajectory matrix \mathbf{V} represents the discretisation of reconstructed space $\hat{\mathbf{X}}$ as seen by its scalar observations. The relationship of equivalence between \mathbf{X} and $\hat{\mathbf{X}}$ using \mathbf{V} was demonstrated in the last few decades, in the context of dynamical systems by Takens [140] who show that for a generic choice of delay coordinate, a system attractor with D dimensions can be embedded in \mathbb{R}^{2D+1} . In this condition there exists a function $\Phi(\cdot)$ between these two spaces which is a diffeomorphism. In [125], another important result extended the previous result for dimension D which is fractal. As stated in the introductory part of this chapter, the hypothesis of low-dimensional chaos explaining the brain has been revealed as too simple [134] and therefore, Takens' result is enough for the purpose of reconstruction of a general dynamical system.

By construction, the method of delays is developed using a single channel time series which is consistent with the task of this chapter. However, it is important to emphasize that the success of the method of delay is subject to an observability condition [93; 1]: the single channel time series $\{x_i\}_{i=1}^L$ needs to sample all

the degrees of freedom of the underlying brain dynamics. This property is specified in Takens' theorem by the term "generic choice of the delay coordinates" [125]. In practice, many time series contain several difficulties which may destroy this assumption such as finite precision of the data and noise. The above theorems do not take into account these factors because they are only existence proofs [113]. Therefore, the assumption that the underlying neural activity is observable from the electromagnetic sensor chosen needs to be confirmed. As stated in Section 3.2, the variable y_i for the Rössler system, is consistent with the previous assumption.

3.4 Manifold learning

The stage of manifold learning consists of the parameterisation of the state space $\hat{\mathbf{X}}$. This operation involves the choice of the triplet $\theta_{SSR} = (M, \tau, L)$ which is also known as the procedure of *tuning the embedding*.

Takens' theorem guarantees a lower bound on the attractor dimension but it does not give any indication how to choose this bound. More importantly, as discussed previously, the theorem is only an existence proof. Since the development of Takens' theorem, the main aim of the state space reconstruction research has been focused on finding suitable methods. As discussed in [113], there is still not a universal answer to the best choice of parameters and most of the methods rely on heuristic approaches and advices. In this work the SSA approach to space reconstruction is considered because:

- It is a simple approach of tuning the embedding in presence of real data.
- It is a particular case of delay embedding which has been shown to be optimal for short a noisy time series.
- It provides information about the decomposition of the space for the feature extraction stage.

SSA is initially based on setting the time delay $\tau = 1$. The trajectory matrix $\tilde{\mathbf{V}}$, in this case, is built by choosing consecutive time points from the data:

$$\tilde{\mathbf{v}}_{\mathbf{k}} = (x_i, x_{i+1}, \dots, x_{i+(M-1)}). \quad (3.7)$$

Interestingly, with SSA, the dimension M becomes the only parameter to be varied which initially reduces the degrees of freedom of the tuning procedure. As shown in [53; 89], the SSA approach and the traditional method of delays are equivalent because they are related by the product $(M-1)\tau$ which defines the *Window Length* τ_w of the embedding[20], i.e. $\tau_w = (M-1)\tau$. This means that the two methods are equivalent for constant values of τ_w [89] according to [89]. However, in order to keep constant the product $(M-1)\tau$, the length M using SSA needs to be very long which make the delay vectors highly correlated and thus the reconstructed space $\hat{\mathbf{X}}$ redundant ($M \gg 2D+1$). In practice, SSA is thus consists of the following stages:

- Embedding the time series as described in Equation 3.7. This step involves, as discussed, the only tuning of the parameter $\tau_w \doteq M$ and the length of the segment L .

- Factor the reconstructed space $\hat{\mathbf{X}}$ with singular value decomposition (SVD), and search for the lower dimensional subspace $\tilde{\mathbf{X}}$. This procedure involves estimating the effective dimensions of $\tilde{\mathbf{X}}$ which is a characteristic considered in the next feature extraction stage.

Window length

The window length τ_w is equal to the dimension of embedding M when $\tau = 1$. In [88], the author shows that the right choice for τ_w is to set it as the mean orbital period τ_p if the system is continuous. This quantity represents the distance between two successive visits of a neighbour in state space. If the time series is oscillatory, as in the electromagnetic data, τ_p represents also the distance between two main peaks of the main oscillation. A visual inspection of the trace can be helpful to extract this measure if the main oscillation is clear enough to be captured. This measure as stated by the authors in [88] is a straightforward and easy solution if used with real data. As described in [97], the previous condition on τ_p can be derived in the frequency domain using the SSA approach in order to obtain the following lower bound

$$M \geq \frac{f_s}{f_{Low}}, \quad \tau = 1, \quad (3.8)$$

where $f_s = 1/\tau_s$ is the sampling frequency and f_{Low} is the lowest frequency of interest. In the previous Rössler system it is possible to use this method using the frequency content of the signal.

Segment length

In the dynamical systems literature the parameter L (or equivalently K) has a secondary importance with respect to M and τ because studies on synthetic chaotic data consider datasets as long as 10^5 points ($K \gg M$) [82]. However, for real data and in the SSA literature short time series are often evaluated and this parameter influences the choice of the embedding. The following advice are considered:

- A first condition is given by the relationships with the window length τ_w . It is meaningless to take τ_w longer than half the length of the time series L [54]. This assumption in fact ensures that the matrix \mathbf{V} is full rank. It is interesting to notice that increasing the time series length would automatically increase the bound on the choice of τ_w .
- Another important requirement is set by the oscillatory nature of the electromagnetic signal. As discussed above an optimal choice for the window length is given by $\tau_w = \tau_p$. The sliding window, thus, needs to contain at least one oscillation to impose this assumption. In practice, it is important to assume that L contains more oscillations of interest. The ratio τ_w/L has to be as large as possible in order to assure an higher degree of statistical confidence [52].
- The analysis of the brain is intrinsically non-stationary, i.e. epileptic activity. Taking K too large would cause different dynamics to be averaged and important features or changing points can be lost. It is difficult in this case to have a golden standard method to optimize K and it is useful to proceed with a trial and error paradigm.

Singular value decomposition

In order to study the reconstructed space $\tilde{\mathbf{X}}$, the trajectory matrix \mathbf{V} which results from Equation 3.6 is decomposed using singular value decomposition.

$$\frac{1}{\sqrt{K}}\mathbf{V} = \mathbf{U}\mathbf{\Sigma}\mathbf{Z}^T \quad (3.9)$$

where $\mathbf{\Sigma} = \text{diag}(\sigma_1, \dots, \sigma_M)$ is the diagonal matrix $M \times M$ of the singular values σ_i . \mathbf{Z} is the matrix $M \times K$ of the eigenvectors or right singular vectors. \mathbf{U} is the matrix $K \times M$ of left singular vectors. The SVD transformation describes the space spanned by the embedding vectors in \mathbf{V} . It can be shown that \mathbf{Z} are the eigenvectors of the estimated covariance matrix \mathbf{C} and \mathbf{U} are the eigenvectors of the estimated structure matrix $\tilde{\mathbf{C}}$ defined as

$$\mathbf{C}_V = \frac{1}{\sqrt{K}}\mathbf{V}\mathbf{V}^T \quad (3.10)$$

$$\tilde{\mathbf{C}}_V = \frac{1}{\sqrt{K}}\mathbf{V}^T\mathbf{V} \quad (3.11)$$

The singular values σ_i are the square roots of the eigenvalues of both \mathbf{C}_V and $\tilde{\mathbf{C}}_V$. As discussed for instance in [28; 20], the SVD approach to find the eigenstructure of the embedding space is less sensitive and more robust to noise than the traditional covariance matrix approach. For this reason, SVD is considered in the rest of the thesis.

The set of singular values σ_i gives the variances of the reconstructed space $\hat{\mathbf{X}}$ when embedded in a euclidean box of dimension M . This structure can be inspected graphically using the *Scree Plot*. This graph is represented by plotting the singular values of \mathbf{V} in decreasing order of magnitude ($\sigma_1 \geq \sigma_2 \geq \dots \geq 0$). Alternatively, the eigenvalues σ_i^2 or $\log \sigma_i^2$ can be used to build the scree plot in the same manner [75].

An example of a singular spectrum is shown in Figure 3.6 after extracting an appropriate trajectory matrix from one of the real datasets available (iEEG dataset A). It is possible to notice two distinct parts of this graph which is characteristic of this kind of plot: a first part which is specified by a progressive drop of the singular values magnitude and a second part in which successive σ_i are similar in value and the graph flattens out.

At the limit of infinite data ($L \rightarrow \infty$), in the case of the time series is a stationary random process and if the model of the noise is additive, the matrix \mathbf{C}_V has the Toeplitz form $\rho(|i-j|\tau_s)$ where $\rho(\cdot)$ is the autocorrelation function of the process and $i, j = 1, \dots, M$. In this situation, it is possible to factorise the trajectory matrix as follows

$$\frac{1}{\sqrt{K}}\mathbf{V} = \begin{bmatrix} \mathbf{U}_s & \mathbf{U}_n \end{bmatrix} \begin{bmatrix} \mathbf{\Sigma}_s & 0 \\ 0 & \mathbf{\Sigma}_n \end{bmatrix} \begin{bmatrix} \mathbf{Z}_s & \mathbf{Z}_n \end{bmatrix}^T \quad (3.12)$$

where the decomposition $\{\mathbf{U}_s, \mathbf{\Sigma}_s, \mathbf{Z}_s\}$ and $\{\mathbf{U}_n, \mathbf{\Sigma}_n, \mathbf{Z}_n\}$ defines the *Signal subspace* and the *Noise subspace* respectively. In particular $\mathbf{\Sigma}_s = \text{diag}(\sigma_1, \dots, \sigma_{M^*})$ and $\mathbf{\Sigma}_n = \text{diag}(\sigma_{M^*}, \dots, \sigma_M)$ where the index M^* is referred here as the Signal-to-Noise (SNR) cut-off point.

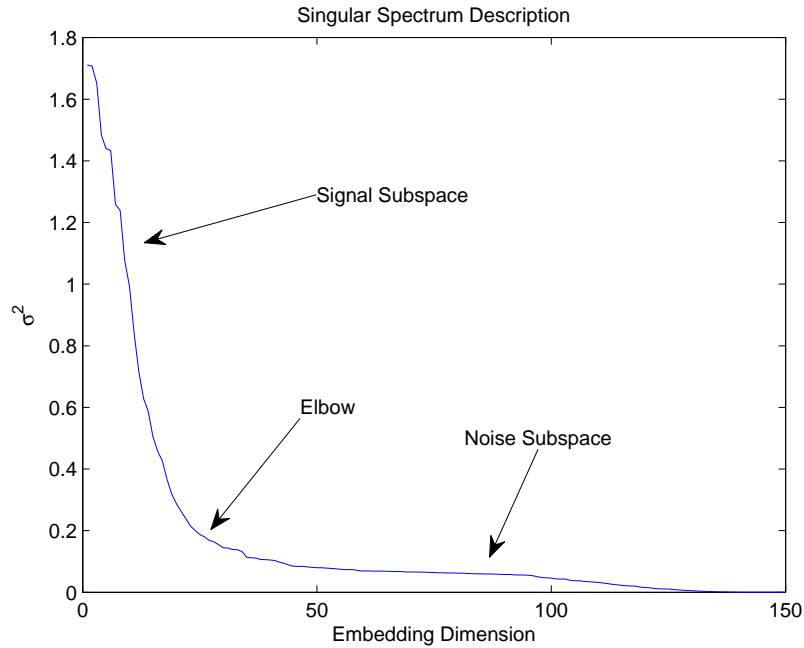


Figure 3.6: Example of the singular spectrum taken from the iEEG dataset A. For this plot an embedding dimension $M = 150$ and $\tau = 1$ is considered (read the following section for a discussion about this choice). The two parts of the plot, i.e. signal subspace and noise subspace are shown. The Signal-to-Noise cut off point can be distinguished by the characteristic "elbow" shape of the singular spectrum

The problem of estimating the value of M^* is discussed and reviewed in the following section of feature extraction. Here, it is important to emphasize that computing the SNR cut-off point M^* is equivalent to find an effective time lag $\tau^* = \tau_w/M^*$. Therefore, while reducing the degree of freedom in the choice of embedding parameters to only τ_w , the method of SSA introduces into the problem of tuning the correct embedding the value of the SNR cut-off point M^* . Although the SSA and method of delays, i.e. tuning M and τ , have been shown to be equivalent, in [89] the author concludes that SSA has better performance for short and noisy time series respectively. This opinion is shared in the standard literature of SSA (for instance [52; 54]). For this reason, SSA seems to fit better the study of electromagnetic signals because firstly they are intrinsically affected by noise and they contains artefacts. Secondly, their analysis needs typically to handle finite size length time series.

In Figure 3.7, the normalized singular spectrum relative to the different clustering regimes in the case of the Rössler system is shown. The analysis is performed taking the last $L = 1500$ points of the simulation and using an embedding dimension of $\tau_w = 200$ as discussed previously. The choice of L is considered to simulate the typical amount of time points used during the analysis of real electromagnetic data. The sampling rate is around $\tau_s = 256\text{Hz}$ and the segment length is 4-6 seconds. From these plots is possible to notice a qualitative and mild difference in structure of the singular values which the feature extraction approaches in the next section intend to give a quantitative estimation of these differences.

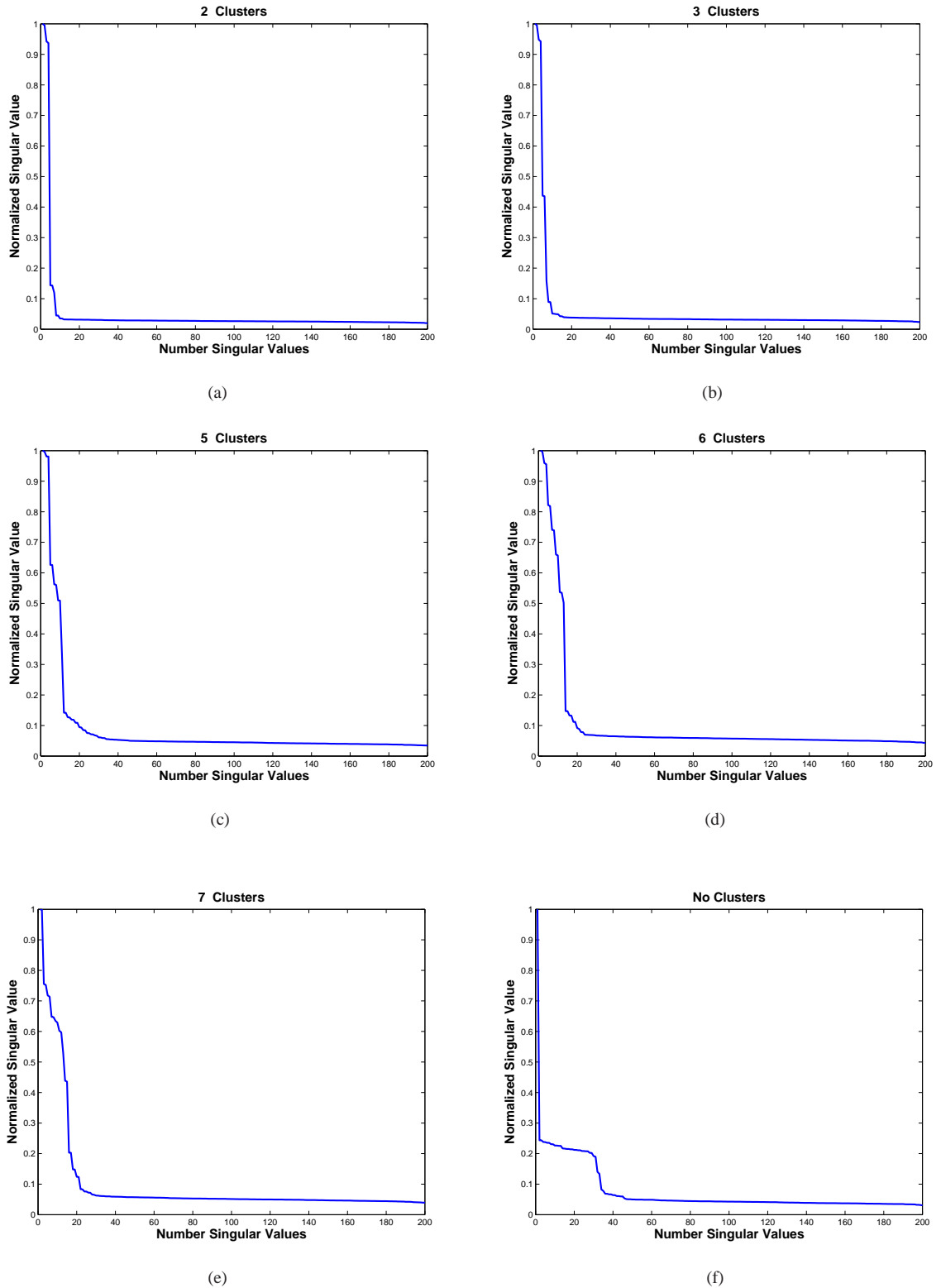


Figure 3.7: Plots of the singular spectrum for different clustering scenarios of the Rössler system. In these figures is possible to notice a small qualitative visual difference in the elbow point of these spectra. The elbow point is moving forward to a larger value if the number of cluster in the Rössler system increases. Therefore, the following feature extraction stage is designed to compute a statistic which expressed this difference and thus identify the underlying change of the system synchronisation.

3.5 Feature extraction

In Section 3.3, it was discussed that under generic conditions it is possible to build an equivalent state space $\hat{\mathbf{X}}$ of the underlying brain dynamical system \mathbf{X} . SSA is used to compose $\hat{\mathbf{X}}$ together with a suitable SVD decomposition of this space. In Section 3.4, a qualitative inspection of the singular spectrum of the toy model discriminates different underlying synchronisation regimes. Therefore, in this section, *we consider the task of extracting features in order to help to characterize this difference in synchronisation regimes, quantitatively.*

Two families of approaches reported in the literature may be considered: firstly, a set of methods addressing directly the problem of finding the dimension cut-off point M^* where the singular spectrum levels which divide the signal to the noise subspace; secondly, a family of information theoretical methods based on the distribution of the singular spectrum is employed [97; 146; 49]. The following sections investigate them both.

3.5.1 Dimension approach

The Signal/Noise cut off (S/N) is an important parameter which is generally related to the problem of dimensionality reduction in data analysis [11]. It is common to deal with high M dimensional datasets for which elements exist close to a much smaller M^* dimensional manifold ($M^* \ll M$). Principal component analysis (PCA) [28; 75] is one the most common techniques which searches for M^* directions in the space spanned by the M dimensional data that contribute the most to its variances. The projection of the original data to the M^* dimensional subspace its maximized. While this transformation reduces dimensionality of the data, it retains most of the information: the distance between the original and the projected data is minimal. In practice, the problem of the cut-off point in this thesis is a particular case of PCA since it considers the covariance structure of the \mathbf{C}_V trajectory matrix.

Visual inspection of the scree plot is the simplest method to find the cut off [75]. One needs to look for the elbow as in Figure 3.6: the demarcation point between the signal/noise subspace. However, firstly the demarcation point using visual inspection can be a subjective measure especially in the case where there is a smooth transition between signal and noise subspaces. Secondly, an automatic algorithm [148] is required which is needed when the dataset is big, as in the case of the MEG data, or when a moving windows analysis is performed, as for the iEEG in Chapter 5. We refer to [75] for a complete survey of the most common recent techniques. Some of the possible methods considered in this work are:

Percentage Ratio One of the most straightforward solution is to decide a priori a threshold based on the total energy of the singular spectrum. For this purpose in this section a different normalisation scheme than Equation 3.24 is considered which is given by

$$\hat{\sigma}_i = \frac{\sigma_i}{\max(\sigma_i)}, \quad \text{for } i = 1, \dots, M \quad (3.13)$$

From the properties of the singular spectrum, trivially $\{\max \sigma_i\}_{i=1}^M = \sigma_1$. Given the following:

$$\frac{\sigma_1 + \sigma_2 + \dots + \sigma_{M^*}}{\sigma_1 + \sigma_2 + \dots + \sigma_M} \geq \gamma_p, \quad (3.14)$$

where the threshold quantity γ_p is a value between 0 and 1. In particular, a common threshold is chosen between 0.7 to 0.99 depending on the structure of the signal [75]. Given γ_p , the value of M^* is chosen in order to satisfy the above inequality.

Gradient Cut-Off In [62], we used a simple alternative method which aims specifically to find the elbow of the singular spectrum. This approach looks for the difference between sequential values of σ_i in order to estimate the point M^* where the singular spectrum starts to level off. In particular, the statistic is given by

$$\sigma_{n-1} - \sigma_n \leq \sigma_{max} \gamma_g, \quad (3.15)$$

where σ_{max} is the maximum difference of the gradient across the spectrum and γ_g is the predetermined threshold for this method. If the normalisation scheme in Equation 3.13 is used, then $\sigma_{max} = 1$. In [62], γ_g is set to 5% of σ_{max} . In order to avoid problems with eventual flat plateaux belonging to the signal subspace, the search for the cut off is backwards, i.e. it starts from the least significant singular values.

Surrogate Data This method is based on the production of an appropriate surrogate dataset based on the null distribution σ_i^0 . For instance, a Monte Carlo scheme can be considered after the estimation of the noise processing [52]. The point where the σ_i exceeds 95% of the distribution σ_i^0 is retained as the estimate of M^* . Alternatively, without a model of the noise, it is possible to resample the data using the method of bootstrapping [149].

The previous techniques have some drawbacks considering the objective of this thesis. The first two approaches contain a subjective threshold to be set which is thus dependent on the signals analysed. The third family of approaches would require a computational intensive procedure of surrogates. Moreover, the last procedure would be advantageous if the noise of the model is known a priori. The noise level if not accessible from the data available and its estimation would need to be addressed during the experiments. This would require a parametrisation of the noise model [52].

In [62], we already developed the second method in the list which we referred to. In this thesis, the main approach which automates the process of estimation of M^* is based on information theory. This approach is model free and is derived from the problem of model order selection in regression analysis. Given some data, one needs to find the model that gives the best generalisation property. The order of the free parameters needs to satisfy a trade off between the fit the model can obtain and its effective complexity [10]. Information criteria (IC) have been used for this purpose in order to penalize the bias of the maximum likelihood of the data adding an extra penalisation term. Considering the terminology used for space reconstruction a general IC is given by

$$IC(M^*) = \log P(\mathbf{v}_1, \mathbf{v}_2, \dots | \hat{\Theta}) + C(M^*) \quad (3.16)$$

where $P(\mathbf{v}_1, \mathbf{v}_2, \dots | \hat{\Theta})$ is the family of probability distributions parameterised by the maximum likelihood estimate $\hat{\Theta}$ of Θ . $C(M^*)$ is a function of the adjustable free parameters of the model. In [28], for instance, two choices of $C(M^*)$ are considered which account for two well known information indices *Akaike's Information Criteria* (AIC) and *Maximum Description Length* (MDL).

$$AIC(M^*) = -2 \log (P(\mathbf{v}_1, \mathbf{v}_2, \dots | \hat{\Theta})) + 2M^*, \quad (3.17)$$

and

$$MDL(M^*) = -\log (P(\mathbf{v}_1, \mathbf{v}_2, \dots | \hat{\Theta})) + \frac{1}{2} \log M^*. \quad (3.18)$$

Since the main goal of this thesis is not to compare the different choices of the penalty function, the method based on MDL is adopted a priori. In this context, as discussed in [28], a closed form of $MDL(M^*)$ can be found only if $\{\mathbf{v}_i\}_{i=1}^K$ are considered i.i.d Gaussian distributed random variables.

$$MDL(M^*) = -K(M^* - M) \log \psi(N) + \frac{1}{2} (2M - M^*) \log M^*, \quad (3.19)$$

where

$$\psi(M^*) = \frac{(\hat{\sigma}_{M^*+1} \hat{\sigma}_{M^*+2} \dots \hat{\sigma}_M)^{\frac{1}{M-M^*}}}{\frac{1}{M-M^*} (\hat{\sigma}_{M^*+1} + \hat{\sigma}_{M^*+2} + \dots + \hat{\sigma}_M)}, \quad (3.20)$$

where $\{\hat{\sigma}_i\}_{i=1}^M$ is the normalized spectrum as defined in Equation 3.13. The present method has been used in the problem of Blind Source Separation (BSS) to estimate the number of underlying sources. While it has been shown to be a suboptimal estimate due to the previous Gaussian approximation [28], it has also demonstrated good performance in retrieving the degrees of freedom of the underlying system. However, as discussed in [28], if the $\{\hat{\sigma}_i\}_{i=M^*}^M$ of the noise subspace are close to zero the formula can present numerical problems. Therefore, in the following analysis, a regularisation term added to the normalized singular spectrum is introduced,

$$\tilde{\sigma}_i = \hat{\sigma}_i + \lambda, \quad \text{for } i = 1, \dots, M. \quad (3.21)$$

where λ is set in this thesis to assume a value simulating an ideal random noise term which is added to the original signal. Practically, λ adds an extra parameter to the method for which a further heuristic is needed to be tuned. In the following analysis, the impact of λ to the automatic computation of the cut off is considered.

Analysis

The first part of the analysis intends to verify that the measures identify the correct number of clusters during different values of the Rössler system coupling. The mean field $O(t)$ is computed firstly as described in Section 3.2 with a mild amount of noise ξ (5% of the standard deviation of the signal). The analysis considers a segment of length $L = 1500$ which results in the plots in Figure 3.7. Figure 3.8 shows the behaviour of the M^* with different parameters of the numerical regularisation λ . A qualitative inspection of Figure 3.7 suggests that the regularisation term is necessary since there are a large portion of the singular

values close to zero which can lead to an instability of the MDL algorithm. The analysis of M^* is shown as a function of the window length τ_w from 0 to 150. A second Figure 3.9, shows more closely the performance of the MDL algorithm: Figure 3.7 is reproduced including the value of the cut off point M^* at $\tau_w = 150$, superimposed.

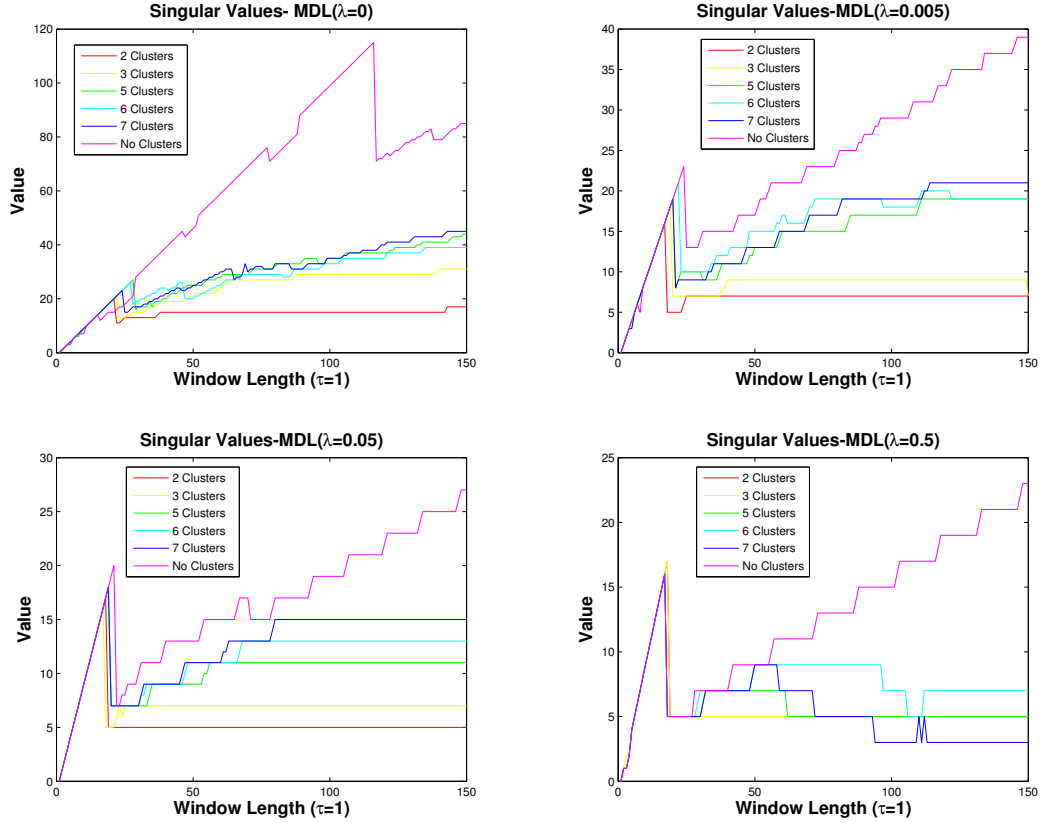


Figure 3.8: The plots shows the value of the cut-off M^* as a function of the window length τ_w for different clustering regimes and for different value of the parameter λ . Only in the case (c), with the value of $\lambda = 0.05$, the clustering regimes can be distinguished between each other when the value of $\tau_w \gtrsim 90$, i.e. no overlap between the number of singular values estimated. In the other cases the discrimination is not possible since the number of singular values overlap. This figures shows the dependency of the MDL algorithm on the parameter λ . See the text for further explanation.

In Figure 3.8(a), we start by considering $\lambda = 0$. Firstly, from this parameter choice, the different clustering regimes (apart from the *No Clusters* and the *2 Clusters*) cannot be distinguished. Secondly, from a qualitative inspection of Figure 3.9, this value of λ seems not to correctly estimate the elbow of the singular spectrum. A better result seems to be achieved using a small nonzero value of $\lambda = 0.005$: in Figure 3.9 this value of λ produces a cut-off point close to the elbow of the singular spectrum while slightly overestimating it. In Figure 3.8(b), however, this setting still fails to discriminate between the clustering regimes. With $\lambda = 0.05$, as shown in Figure 3.8(c), the MDL algorithm seems to be able to distinguish the different synchronisation regimes when $\tau_w \gtrsim 90$. After the latter value of the window length, M^* converges to an horizontal estimate. From an inspection of Figure 3.9, moreover, this choice of regularisation is consistent in most of the figures with the big drop in the singular spectrum. Finally, Figure 3.8(d) considers the case of $\lambda = 1$ which is shown to be too high and tends to further penalize the value of M^* . In particular Figure 3.9 does not result in a correct discrimination of the underlying synchronisation.

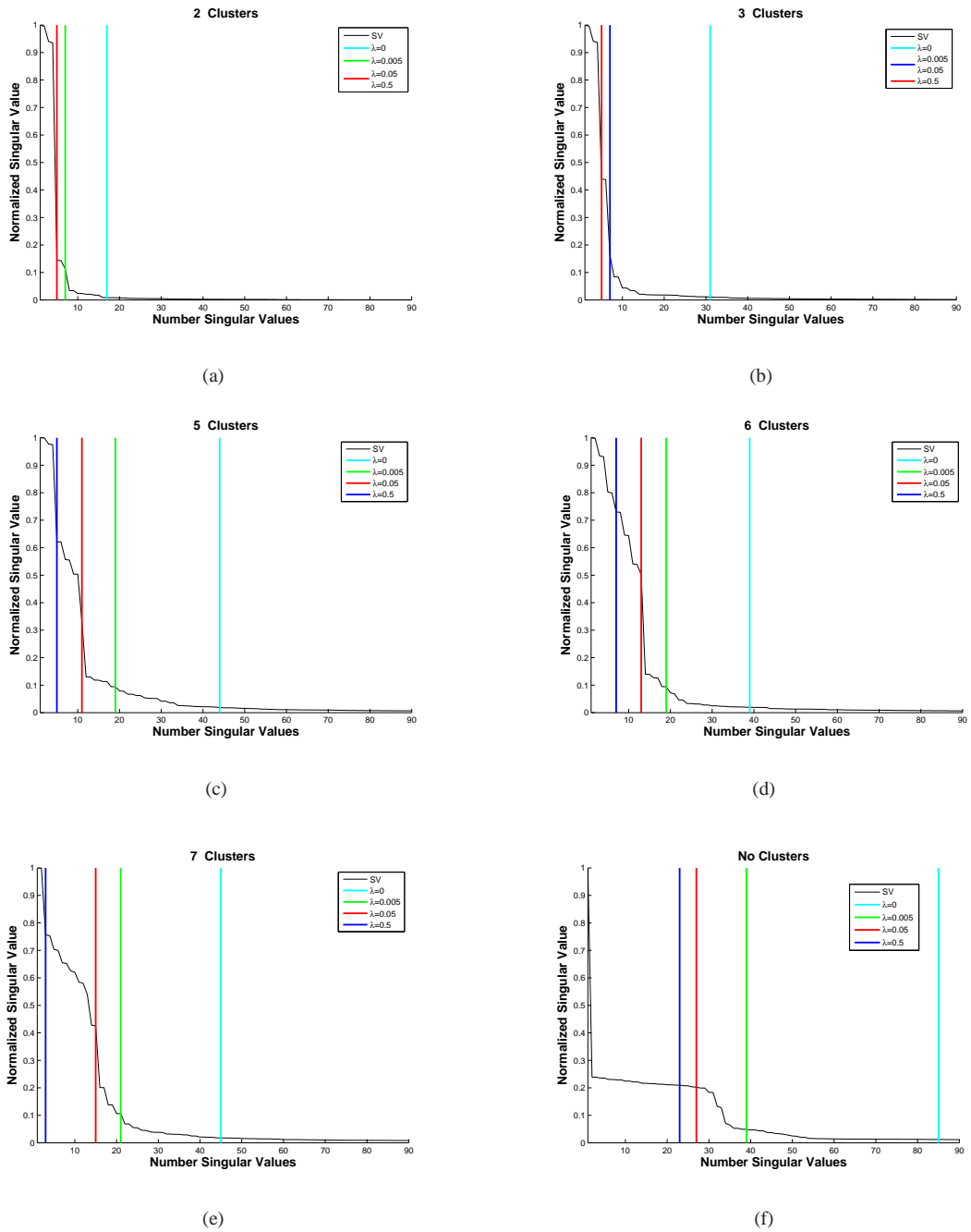


Figure 3.9: Plots of the singular spectrum for different clustering scenarios superimposed with the cut-off values as a function of the parameter λ . These plots show the cut-offs computed in Figure 3.8 in the case of $\tau_w = 150$. See the text for further explanation.

It is interesting to mention that for low values of the window length ($\tau_w < 30$), the algorithm in all the λ cases presents some numerical instability probably due to the small values of the singular spectrum. In this range of the window length, neither values of λ seem to be able to regularize the solution sufficiently since no discrimination of clustering regimes is possible. In practice, this is not a problem because values of $\tau_w < 30$ are unlikely to be a valid embedding.

To summarize, while the MDL algorithm aims for the automation of the signal-to-noise cut off point, in practice it requires the tuning of a small parameter to achieve a good discriminatory performance in the

case the signal subspace is low dimensional.

3.5.2 Complexity approach

In previous studies, the concept of complexity of the system underlying the observable data linked the singular spectrum to the analysis of electromagnetic signals [97; 146]. Consistent with the discussion in this thesis, in [97], the authors considered the distribution and the shape of the singular values, and not only the cut-off point, in the reconstructed space as possible extra information in order to estimate the degree of complexity of the underlying neural system. In this thesis, two solutions based on information theory were designed to look for a simple description of disorder of the distribution of the singular spectrum:

Singular Spectral Entropy Entropy is a well known information theory concept which measures the degree of disorder of a system [31]. Given a probability function $p(x)$ sampled from this system, Shannon's entropy is given as follow

$$H(x) = -E[\log(p(x))] = - \int_{-\infty}^{\infty} p(x) \log(p(x)) dx. \quad (3.22)$$

The main point considered in this section is to use the normalized singular spectrum $\{\hat{\sigma}_i\}_{i=1}^M$ as *pseudo probability distribution*. In fact, the distributions of the singular values in the spectrum shows the directions in the embedding spaces where the SVD find the variance which explain the data the most. From the inspection of Figure 3.7 the singular values tends to be more distributed around the first part of the plot when the system is more synchronized, i.e. the system is less complex. Consistent with [97], a measure of entropy is employed to evaluate the peakiness of the singular spectrum. The measure of C_e can be thus given by

$$C_e = - \sum_{i=1}^M \hat{\sigma}_i \log(\hat{\sigma}_i), \quad (3.23)$$

The spectrum $\{\hat{\sigma}_i\}_{i=1}^M$ is normalized as:

$$\hat{\sigma}_i = \frac{\sigma_i}{\sum(\sigma_i)}, \quad \text{for } i = 1, \dots, M. \quad (3.24)$$

Singular Spectral Fisher Information An alternative concept in information theory is given by the Fisher information which is defined as follows

$$C_f(\theta) = E \left[\left(\frac{\partial \log P(\theta)}{\partial \theta} \right)^2 \right], \quad (3.25)$$

where $P(\theta)$ is the likelihood function associated to the the parameter θ , $I(\theta)$ is the information of θ associated to a sample of M observation which is averaged by the expectation operator $E[\cdot]$. Using the discretisation of the θ domain it is possible to show that

$$C_f(\theta) = \sum_{i=1}^M \frac{(P(\theta_{i+1}) - P(\theta_i))^2}{P(\theta_i)}. \quad (3.26)$$

If one considers $P(\theta_i) = \sigma_i$ the expression in Equation 3.26 can be used for the normalized singular spectrum $\{\hat{\sigma}_i\}_{i=1}^M$ as for the case of the C_E . The C_f , as shown in Equation 3.26, gives a method to investigate the differential properties of the singular spectrum. The C_e instead is an integrative method as defined by the sum in Equation 3.23. For this reason, it is expected that C_f can detect finer changes of the spectrum than the C_e .

In this thesis, the case of the spectral singular entropy only is considered, based on previous results [146; 49] where a qualitative difference between the two methods on EEG and MEG data was performed and our investigation in the next section. In [49], these measures were used to discriminate patterns of EEG relative to patients subjected to different mental tasks. In [146], analysis of MEG signals showed that complexity is able to characterize an experiment based on a visual paradigm. In all these previous investigations, both C_e and C_f were shown to provide the same qualitative information about the underlying complexity. However, these works have also shown some drawbacks in the case of the Fisher index in the case of noisy signals. In practice, the computation of the derivatives in Equation 3.26 has shown to be sensitive to noise making therefore C_f poorly suited to real signals. This problem was addressed in [49] where computation of these derivatives based on spline interpolation was performed. Nevertheless, the author, found still better performance for C_e than C_f in his experimental investigation of an EEG case of study

Analysis

In Figure 3.10 the analysis of C_e is shown as a function of the window length τ_w . In Figure 3.8 to check the previous investigations about the Fisher index, C_f is plotted as well. These pictures are produced with the same parameters as before: ξ at 5% of the standard deviation of the signal and $L = 1500$. In Figure 3.10, a dashed line is added to the plot which shows the bound of the theoretical maximum entropy. Given $\{\hat{\sigma}_i\}_{i=1}^M$ and using the normalisation scheme in 3.24, the upper bound of C_e is given by

$$\{C_e\}_{max} = - \sum_{i=1}^M \frac{1}{M} \log\left(\frac{1}{M}\right) \equiv \log M. \quad (3.27)$$

The value $\{C_e\}_{max}$ is met when the singular spectrum is flat, i.e. $\{\hat{\sigma}_i\}_{i=1}^M = \frac{1}{M}$. This specific case occurs when the reconstructed space has the same variance across all directions. At the limit of infinite data ($L \rightarrow \infty$) the case of $\{C_e\}_{max}$ is the result of an embedding of white noise in M dimension. With the same arguments, $\{C_f\}_{min} = 0$ since the gradient of a flat singular spectrum is zero.

The first most important point to notice is that for a relatively high embedding both measures can capture the different degrees of synchronisation using the mean field $O(t)$. The opposite behaviour of the C_e and C_f metrics is also noticed, i.e. for high complexity and low synchronisation the entropy increases while the Fisher index decreases. However, the C_f seems to perform less well than the entropy index when the system synchronisation increases (signal more complex and the 6 clusters C_f partially overlap the 7 cluster case). Furthermore, the C_f during the tuning of τ_w is more noisy than C_e .

As in the case of Figure 3.8, in the clustering regimes, both C_e and C_f level off to an horizontal estimate before $\tau_w = 150$ when the underlying system has clustered. This result is consistent with the convergent property of the reconstructed space as described in [20] to the attractor of the system after a determinate

value of τ_w is correctly embedded as described by Takens' theorem. Further dimensions would make no difference for the signal subspace. The singular spectrum and thus any statistic based on it, such as C_e and C_f , would be stationary after the signal is correctly embedded. In practice, this property is interesting because it can use, as a further tuning option, the window length τ_w : when the complexity indices become stationary the space is correctly embedded. This convergence property of the singular spectrum is used in [146] to find the optimal choice of τ_w during an MEG case of study.

In Figure 3.10, in the case of no clusters, the C_e and C_f do not seem to level off. The arguable reason for this situation is given by the fact that the observable signal tends to become more Gaussian when it is made by an higher number of complex components i.e. single uncoupled Rössler oscillators (large number law). In practice, when the signal contains random terms or is highly complex (in the Rössler example both situations are present since of the term ξ) the singular spectrum possesses an higher number of nonzero singular values that do not vanish for a low dimensional embedding operation. In the extreme case, when the signal is Gaussian random noise, the procedure of embedding is given by the expression in Equation 3.27 in which C_e correspond to the curve Max-SSE in Figure 3.10. In the case of 2 to 7 clusters, the amount of noise injected into the signal, i.e. 5%, is not enough to undermine the low dimensional nature of the macroaggregate which therefore presents a horizon plateau estimate. Since the random component ξ is present in the macroaggregate signal, also these curves do not exactly level off if one takes a closer look.

For this last reason, a method of tuning based on the convergence of C_e may not be work for brain signals. It is in fact reasonable to expect the synchronized activity in the underlying neural network is not as simple as in the case drawn by this Rössler lattice.

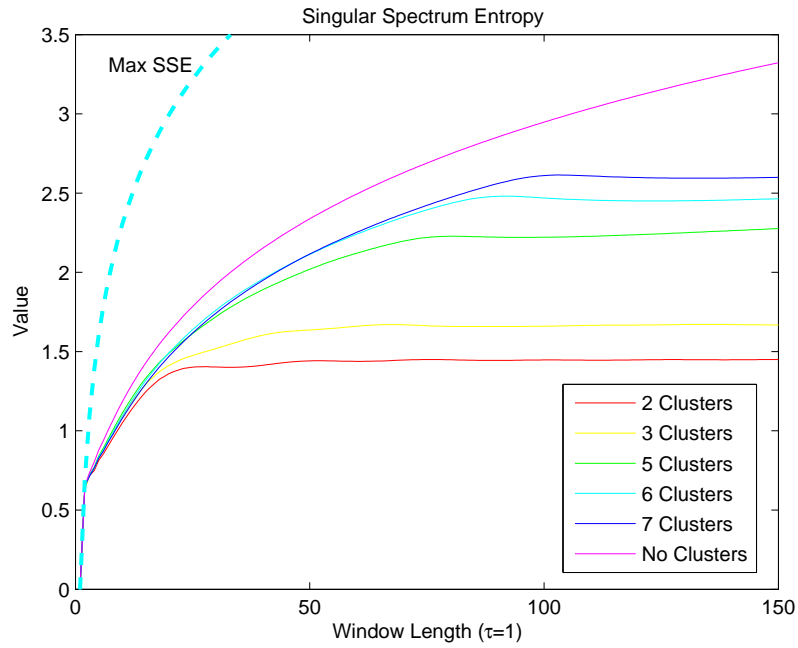
Therefore, to summarize, the findings of this simulation suggests that C_e and C_f can both be taken as discriminatory statistics of the underlying synchronisation state. However, the slightly worse performance of the C_f and difficulty with the computation of the derivatives weights more our choice to use C_e than C_f for real data. This is consistent with the previous works in [146; 49].

3.5.3 Entropy-MDL approach

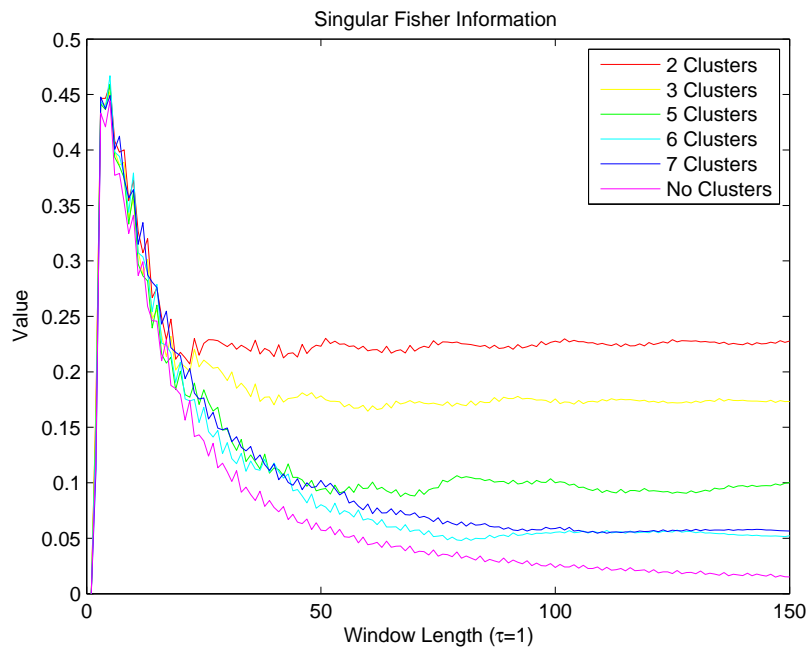
Noise analysis

The previous methods of complexity and dimensionality are able to discriminate different underlying synchronisation regimes for relatively noiseless signals (ξ at the 5% level). In this section, it is investigated and discussed the effect of the observational noise ξ on the quality of these estimations. As above ξ is considered to be sampled from a source of white noise, i.e. $\xi \in \mathcal{N}(0, \sigma_\xi^2)$. The σ_ξ^2 is progressively varied during this analysis as the percentage of the standard deviation of the original noiseless signal. As reported in the literature [20], the addition of the white noise ξ into the mean field $O(t)$ results in an increase of the noise floor of the singular spectrum.

The value of the noise injected into the signal is considered between 0 and the maximum peak value of the signal itself (100%). This range is not directly related to the real amount of noise found in EM signals but is to provide an argument for the stability of the synthetic examples. Realistically, in general, the percentage of noise into the signal is complex and may depend on the type of brain activity, the frequency



(a)



(b)

Figure 3.10: Plots of the C_e and C_f with varying embedding dimension and for different clustering regimes. The plots shows that without any regularisation parameters the C_e statistic is able to discriminate the underlying synchronisation of the Rössler system for increasing value of the window length. For C_f , the plots are noisier and there are problems for discriminating 7 to 6 clusters.

band of interest, the source of the noise and the measurements techniques adopted, i.e EEG/MEG/iEEG (for discussions, references and more details in [126; 72]). Normal brain activity have signals that can go from few μV for some auditory and visual event-related potentials(ERP) and rise up to $50\mu V$ for spontaneous α -

rhythms [126]. The noise can be generated within the human body, (spontaneous activity, muscular artifact...) or from the environment (electrode contact, measurement amplifier, AC power...). In [126], the noise from the amplifier of a scalp EEG has been observed to reach $4\mu\text{V}$ but only for frequencies above the 100Hz. The noise from electrode contact in some cases can reach $10\mu\text{V}$ and can thus create some problems for weaker signal [72] since the noise can be stronger of the signal itself. We refer to the previous references for further details.

Figure 3.11 shows the results for the C_e and M^* over the segment of $L = 1500$ with a window length of $\tau_w = 150$. The analysis is reproduced 100 times with different samples from the distribution of ξ in order to provide error bars. C_e is affected by this increment as shown in Figure 3.11. Both measures detect an increase of the complexity of the underlying system which was expected by the intrinsic nature of the white noise ξ . In terms of discrimination, when the level of noise is known C_e can still intercept the difference between synchronisation regimes. The presence of noise, however, reduces this difference. M^* becomes stable for a large range of noise levels when $\lambda = 0.05$ is set to provide the correct amount of regularisation. In the other cases, when $\lambda < 0.05$ the M^* changes with varying ξ while for $\lambda > 0.05$ the MDL is over penalized as for the noiseless case.

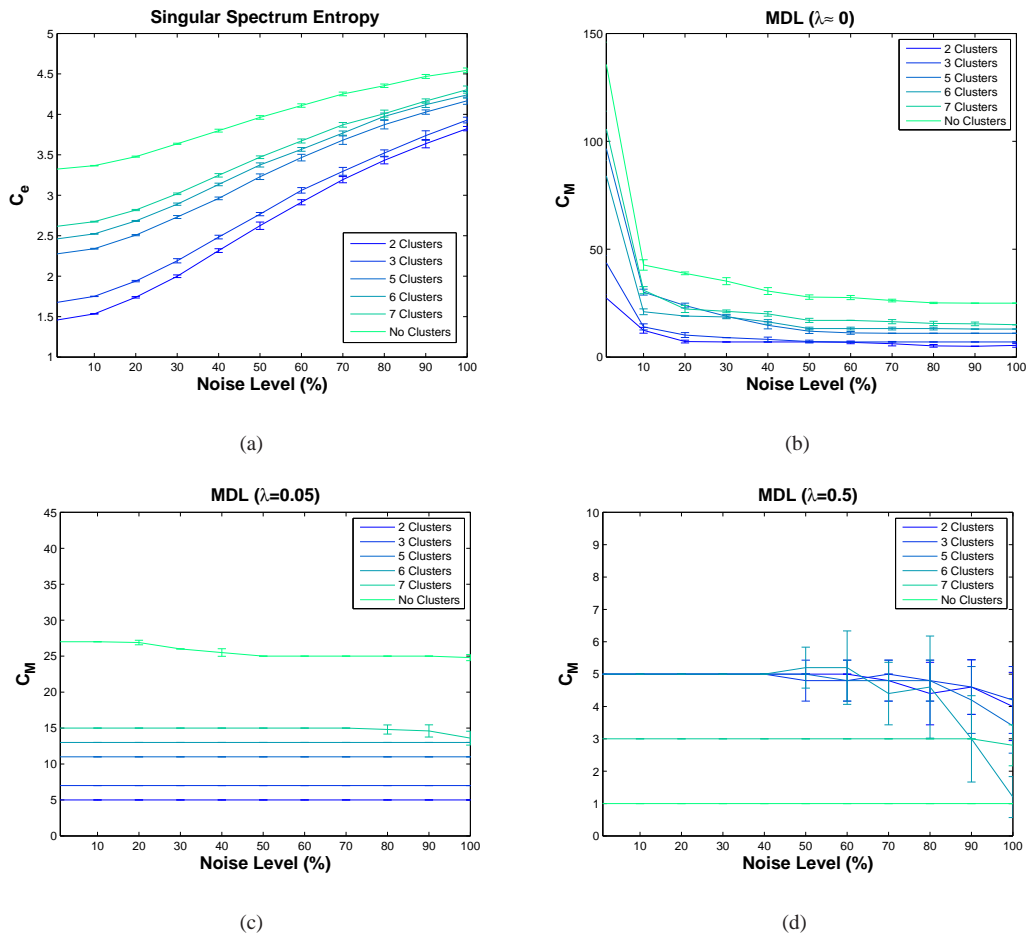


Figure 3.11: The C_e and M^* indexes using $\tau_w = 150$ as a function of the variance of a Gaussian additive noise source ξ superimposed to $O(t)$ in the x axes. The error bars indicates the standard deviation of an ensemble of simulations for each clustering regimes. The figures shows that the entropy index C_e is dependent on the amount of noise introduced as its values increase for increasing noise. The M^* found with the MDL algorithm is however independent on the noise if the right choice of λ is considered, i.e. case (c).

Index Combination

In order to fully use the advantages of both dimensionality and complexity methods, finally their combination is considered: firstly, the cut off point is used to eliminate part of the noise subspace and secondly, the complexity measure is applied over the signal subspace. This results in a complexity index $C_eM(\lambda)$ based on entropy, where λ as before is the regularisation parameter of the MDL. The main idea is to use the stability to noise of the MDL with the quantitative characterisation of the complexity of the previous entropy index. In [146], the entropy was computed after cutting the singular spectrum at a subjective dimension. $C_eM(\lambda)$ can perform the same task automatically.

In Figure 3.12, the study of this new measure is repeated for different values of the observational noise and for different values of the regularisation term. As shown in Figure 3.12, the new measure $C_eM(\lambda)$ is stable for the all ranges of noise level added to the system. More importantly, the figures show that the index is not sensitive to the choice of λ . In fact, for the range previously studied of $\lambda < 0.5$ the plots in Figure 3.12 do not differentiate and they provide the same rejection to noise as $\lambda = 0$. In practice, when the choice of $\lambda > 0.5$, the MDL algorithm removes too many singular values and the value of $C_eM(\lambda)$ does not discriminate different clustering regimes.

Different sources of noise

Another experiment considered applies a source of coloured random noise to the mean field observations. In this case a simple autoregressive AR(1) noise model is employed:

$$\xi_{AR}(t) = \alpha \xi_{AR}(t-1) + \xi_0, \quad (3.28)$$

where ξ_0 is the previous white noise source. In Figure 3.13 the results are shown for two different choices of $\alpha = \{0.3, 0.7\}$ and for two different choices of $\lambda = \{0, 0.05\}$. In practice, the plots show that the source of coloured observational noise may influence the new complexity index C_eM . This is particularly shown with the higher level of $\alpha = 0.7$ while a mild influence is observed for $\alpha = 0.3$. The parameter λ seems to correct this disturbance. However, including λ into the algorithm would result as before in a tuning empirical procedure. In this thesis, the effect of coloured observational noise is not considered further but instead, while emphasizing its existence is left for future research. During the practical investigation with real datasets, the assumption of random Gaussian noise (or a mild deviation from this condition) in the measurement system is usually considered acceptable in the literature.

3.5.4 Discussion

There is an interesting consideration to be made concerning the use of a metric independent from the level of the noise. We discussed in Section 3.2.3 that an increase of the power of the observable signal can be taken as a measure of the rise of the underlying system synchronisation. As explained, this point needs to be further elucidated since the power-synchronisation relationship in a complex neural system may not be so simple.

Changes in the power of the aggregate signal will result in an increase of the Signal-to-Noise ratio if

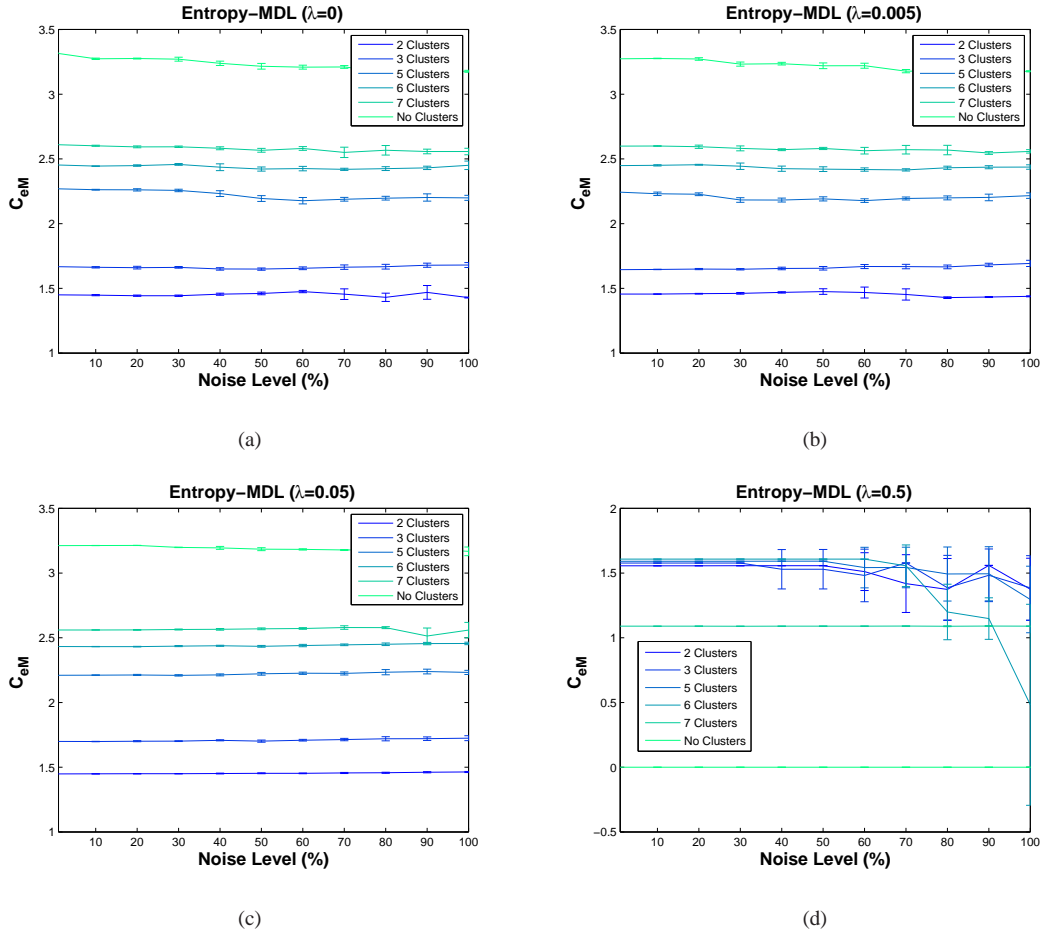


Figure 3.12: The spectral entropy index in combination with the MDL algorithm as a function of the Gaussian noise source ξ on the x axis for $\tau_w = 150$. The plots show that C_{eM} is insensitive to the noise since for varying amount of noise the C_{eM} results constant and can discriminate the synchronisation regimes of the underlying system.. More importantly, C_{eM} is independent from the regularisation parameter λ if the latter is sufficiently small. For a larger value of λ in (d), there is not discrimination between the clustering regimes.

the variance of the observational noise is stationary during this variation. In practice, changes in power can affect the noise level and thus the measure of synchronisation as shown in Figure 3.11 if the C_e and the M^* without regularisation are employed. Using a metric which is independent of SNR variations, such as the C_{eM} , discharges this possibility: variations or differences between the values of the single channel statistic is a genuine measure of the underlying synchronisation. As discussed in Section 3.5.3, this point is true only if the model of the observational noise is Gaussian. With coloured random sources the C_{eM} was shown to be influenced by SNR variations. Currently, during the data analysis, the assumption of the whiteness of the observational noise is taken. Therefore, as future plans, the following points are left open:

- The nature of the power-synchronisation relationship needs to be clarified from experimental and/or simulated data.
- A measure of single channel synchronisation, in order to avoid problems with complex power-synchronisation relationships, needs to be independent of any source of observational noise.

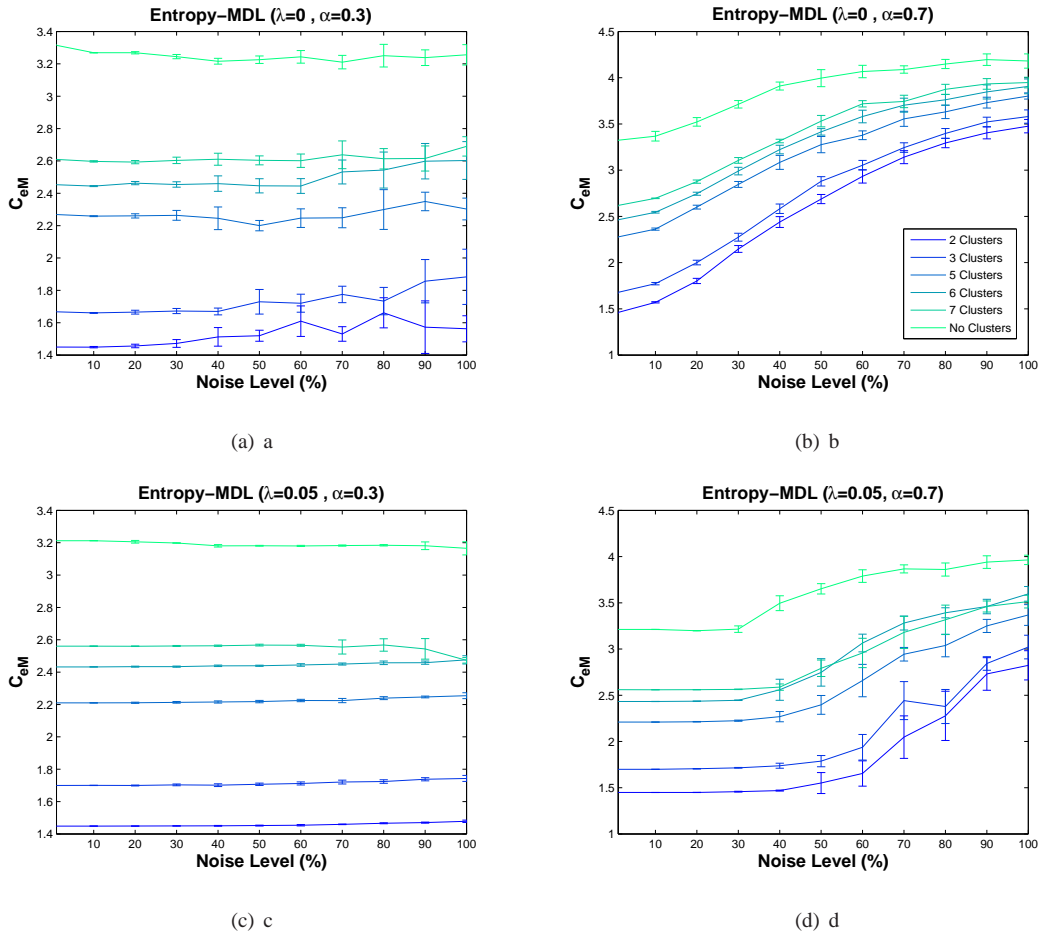


Figure 3.13: The plots show the performance of C_{eM} with a source of additive AR(1) coloured noise. For a small level of α in the plots (a) and (c), i.e. more Gaussian, C_{eM} can still be considered insensitive to noise and independent of the regularisation parameter λ . The values of C_{eM} are in fact constant. With a source of strong coloured noise, i.e. case (b) and (d), C_{eM} is not independent anymore to the variance of the noise but C_{eM} varies with it. Therefore a source of non Gaussian noise can destroy the independence of the C_{eM} .

3.6 Summary

In this chapter a synthetic model of a lattice of Rössler Oscillators was considered which serves as an example of local neural assemblies in the cortex. This model is justified by the weakly coupled dynamical system paradigm as described in the previous chapters. The main objective of this model is to test some univariate statistics which are designed to measure the degrees of synchronisation of the underlying Rössler system from a single channel EM signal.

Within this aim, a few possible techniques based on state space reconstruction and singular spectrum analysis were investigated: An empirical measure which computes the complexity of the underlying local system based on an information theoretical principle; A statistic which extracts the degree of freedom and the dimensionality of the underlying system looking at the signal-to-noise cut off point.

During the analysis of the Rössler system it was found that the combination of complexity and dimensionality can be used to provide a suitable method to perform the discrimination of different regimes of neural local synchronisation in the Rössler lattice. Moreover, this statistic rejects the problem of SNR variations for white and mild coloured sources of observational noise. The experimental relevance of the new

measure C_{eM} is further investigated in Chapter 5 on real data.

4

Analogues-RBF Granger causality metric

The main aim of this chapter is to discuss the problem of developing a metric of functional connectivity in order to estimate directional dynamical interaction. This technique is based on the concept of Granger causality and is implemented by a nonlinear prediction algorithm in state space which is derived by the original Lorentz method of analogues. In this chapter a novel extension of this method is investigated using a neural radial basis function network.

After a general introduction and references in Section 4.1, the algorithm and its theoretical description is presented in Section 4.2. Some numerical simulations using unidirectional coupled systems are performed to test the algorithm in Section 4.3. The experimental use and findings of the techniques presented here are left for further consideration in Chapter 6 during the analysis of intracranial EEG data.

This part of the thesis is based on integration of the work discuss in [25] and [24].

4.1 Introduction

As presented in the introduction, causality is a type of relationship of effective connectivity which can be defined by the coupling parameters of the underlying model (the entries of the Jacobian metric in Equation 1.9 of the WCDS). In a model free scenario, i.e. using the observable data only, these quantities cannot be uniquely estimated because they are solutions of an ill-posed inverse problem. Granger (collection of

his paper in [58]) proposed a weaker definition of causality (*prima-facie causality* [57]), as enunciated in Definition 2, in data space based on a principle of predictability. This approach results into a practical statistical method for causality estimation which can lead, as a general formalism, to the following *deviation to Markov property* [128]:

$$\text{If } P(x_{i+k}|\mathbf{x}_i^-, \mathbf{y}_i^-) \neq P(x_{i+k}|\mathbf{x}_i^-), \quad \text{then } \mathbf{y} \text{ causes } \mathbf{x}. \quad (4.1)$$

As discussed in [128; 68] within the previous expression, causality can be understood as a *flow of information* among processes underlying the two time series \mathbf{x} and \mathbf{y} . Therefore, the Equation 4.1 defines a time asymmetric metric $d_c(\mathbf{x}, \mathbf{y})$ and this chapter methodology, as a main aim, attempts to address the estimation of $d_c(\mathbf{x}, \mathbf{y})$ from data.

The Granger paradigm has been employed in many data analysis domains including for instance, econometrics and finance [130; 70; 50; 110], climatology [142] and recently neuroscience [92; 55; 114; 34]. Using a linear stochastic system, a totally admissible algorithmic choice implemented initially by Granger [56] uses the conditional variance of the prediction error: the terms in Equation 4.1 becomes $\sigma(x_{i+k}|\mathbf{x}_i^-, \mathbf{y}_i^-)$ and $\sigma(x_{i+k}|\mathbf{x}_i^-)$. Since for a linear system the autocorrelation and Fourier spectrum are related by the Wiener-Khinchin theorem, the literature has produced several implementation of causality measures based on coherence [56].

With the increasing interest on dynamical systems and complexity, in the last decade, several works have considered the problem of extending the causality metric in order to address nonlinear phenomena. Two main classes of approaches have been used to tackle this problem. A first important class of methods is based on nonlinear predictor modelling [26; 4; 41]. These methods are natural extensions of the ARMA classical approach to Granger causality. They are relevant literature in this thesis because the Analogues-RBF method developed in this chapter belongs to the same class of techniques: *Maximum likelihood estimation*. Secondly, from a different perspective, other popular methods for nonlinear Granger causality have employed nonparametric estimation (for a general review in [68]). These techniques are based on estimators of correlation integrals, nonparametric probability distributions and entropy. In practice, they address the estimation of Equation 4.1 from an *Information theoretical* point of view. While have been considered for neurophysiology analysis [27], these methods they often required a high number of data points in order to obtain a statistical significant estimate of the information flow.

Granger maximum likelihood estimation

Different approaches have been proposed to measure the inequality in Equation 4.1. The method proposed by Granger, and considered in this thesis, can be regarded as *a maximum likelihood type of estimator of the Markov property*. The two sides of Eq. 4.1 are modelled by the following regression equations:

$$\tilde{x}_{i+k} = \hat{\mathbf{F}}_{\mathbf{S}}(\mathbf{x}_i^-; \mathbf{w}_{\mathbf{x}}) + e_x, \quad \tilde{x}_{i+k} = \hat{\mathbf{F}}_{\mathbf{M}}(\mathbf{x}_i^- \mathbf{y}_i^-; \mathbf{w}_{\mathbf{xy}}) + e_{xy}, \quad (4.2)$$

where the functions $\hat{\mathbf{F}}_{\mathbf{S}}(\cdot)$ and $\hat{\mathbf{F}}_{\mathbf{M}}(\cdot)$ implement respectively the *single predictor* and the *mutual predictor* and x_{i+k} is the k-step ahead predictor of \mathbf{x} at time i . The e_x and e_{xy} are error terms i.i.d. random processes which are assumed to be additive. $\mathbf{w}_{\mathbf{x}}$ and $\mathbf{w}_{\mathbf{xy}}$ are the free parameters of these models which a

learning strategy based on maximum likelihood minimisation needs to estimate. The Granger algorithm for the estimation of Equation 4.1 is divided into the following conceptual stages:

- Divide the observable data \mathbf{x} and \mathbf{y} into a training set and a test set.
- Learn the regression models in Eq. 4.2 from the training dataset.
- Compute an estimate of the prediction errors \tilde{e}_{xy} and \tilde{e}_x in the test set, i.e. *out-of-sample prediction errors*.
- Check the expression in Eq. 4.1 using a *Granger statistic* $G(\tilde{e}_x, \tilde{e}_{xy})$ based on the previous prediction errors. The Granger statistic, in practice, is the causality distance metric which needs to be computed: $d_c(\mathbf{x}, \mathbf{y}) = G(\tilde{e}_x, \tilde{e}_{xy})^1$
- Assess the statistical significance of Eq. 4.1.

The last step of the previous stages, strictly speaking, does not belong to the definition of the directional metric but it is a common practice during the data analysis to ask for the statistical significance of its value. It is thus an optional step which is considered in this thesis using a bootstrapping technique.

4.2 Analogues-RBF Granger causality

This section explores a novel method in order to estimate the metric of dynamical interdependence $d_c(\cdot, \cdot)$ based on the maximum likelihood Granger methodology. The literature shows that there are many possible solutions to address this problem. The approach of this thesis is motivated by the following points:

- On the basis of the previous chapters a nonlinear metric is necessary to detect directionality in a nonlinear complex system such as the brain.
- $\hat{\mathbf{F}}_S(\cdot)$ and $\hat{\mathbf{F}}_M(\cdot)$ are considered belonging to the family of nearest neighbours methods in state space. They are local predictor techniques which have been shown to be very powerful and simple alternatives to global techniques for forecasting dynamical system [82; 145]. The simplest approach included in this class is known as the Lorentz method of analogues.
- A machine learning extension of the previous class of methods is considered in order to provide a data-driven approach to model nearest neighbours dynamics. A similar technique has been previously used in the context of time series forecasting [66], i.e. modelling $\hat{\mathbf{F}}_S(\cdot)$. In this chapter, therefore, this previous work is studied and embodied in the directional interdependence metric $d_c(\cdot, \cdot)$.

Given the previous motivations, the following subsections introduce the proposed novel metric $d_c(\cdot, \cdot)$ as discussed by the procedure in Section 4.1.

¹ $G_{y \rightarrow x} = \ln \left(\frac{\sigma_x^2}{\sigma_{xy}^2} \right)$ as further discussed in Section 4.2.4. σ_x^2 and σ_{xy}^2 are the variance of the RMS out-of-sample single and mutual error, i.e. \tilde{e}_x and \tilde{e}_{xy} .

4.2.1 Training and test sets

Given a single time series \mathbf{x} , let us consider the database of examples \mathcal{D}_x . It is needed in order to learn the single regression models $\hat{\mathbf{F}}_S(\cdot)$ in Eq. 4.2, generalizing the underlying generator of the data which are sampled according to the state space model in Eq. 1.1 and compute the out-of-sample prediction error which is later used for the causality metric $d_c(\cdot, \cdot)$. Before this operation, the \mathbf{x} is assumed to have been a priori normalized to zero mean and unit standard deviation.

Firstly, the training database for the k -step ahead predictor is given by,

$$\mathcal{D}_x^- = \{(x_{i+k}, \mathbf{x}_i^-)\}_{i=1}^{N^*}, \quad (4.3)$$

where N^* is the number of training examples inside \mathcal{D}_x^- . Secondly the test set is given by

$$\mathcal{D}_x^+ = \{(x_{i+k}, \mathbf{x}_i^+)\}_{i=N^*}^N, \quad (4.4)$$

where N is the total number of examples of the \mathcal{D}_x given by joining \mathcal{D}_x^- and \mathcal{D}_x^+ . In practice, as a common procedure in signal processing, the prediction x_{i+k} is a weighted sum of the previous past points \mathbf{x}_i^- or \mathbf{x}_i^+ (input). \mathcal{D}_x^- provides the examples which are used to learn the function $\hat{\mathbf{F}}_S(\cdot)$. \mathcal{D}_x^+ provides the examples to estimate the prediction error \tilde{e}_x .

There is no need to include the whole past \mathbf{x}_i^- or future \mathbf{x}_i^+ as input to $\hat{\mathbf{F}}_S(\cdot)$ but only a selected set of past points needs to be employed. Using a preprocessing stage based on state space reconstruction this set of points for \mathbf{x}_i^- is given by $\hat{\mathbf{X}}_i$, the embedding vectors at each time point i . Therefore, the database \mathcal{D}_x can be transformed to be

$$\mathcal{D}_x = \{(x_{i+k}, \hat{\mathbf{X}}_i)\}_{i=1}^N. \quad (4.5)$$

As discussed in the previous chapter, approaches such as the method of delay vectors or SSA can be employed to build $\hat{\mathbf{X}}$ accordingly. In order to avoid some problems with the correlation of the data, the normalisation of the embedding $\hat{\mathbf{X}}$ with zero mean and unit standard deviation is further performed before the learning stage [90]. The same procedure, as discussed in this section, can be applied to the training dataset \mathcal{D}_y given the time series \mathbf{y} .

4.2.2 Single predictor

As described in the regression analysis literature, there are many possible solutions in order to build a forecasting model $\hat{\mathbf{F}}_S(\cdot)$ for a single time series. In the field of nonlinear time series analysis, a popular regression approach based on state space reconstruction is given by the *Lorentz's method of Analogues* [82] which is a simple nearest neighbour technique used for prediction. Let us consider, as a first step, the following prediction rule in the space \mathcal{X} : In a first order approximation, close trajectories of the original state space of \mathcal{X} at time i will stay close at $i + \Delta t$ for for the continuous variable Δt sufficiently small, i.e. $\Delta t \ll T_p$ with T_p the characteristic time scale of the underlying model. This condition results in a strong correlation between \mathbf{X}_i and $\mathbf{X}_{i+\Delta t}$. Using this assumption, we consider the set of nearest neighbours \mathcal{U}_ϵ of

\mathbf{X}_i , employing a general distance metric in \mathbf{X} (euclidean for instance), such as $\mathbf{X}_j \in \mathcal{U}_\epsilon$ if $|\mathbf{X}_i - \mathbf{X}_j| \leq \epsilon$. The Lorentz's predictor is then given by,

$$\tilde{\mathbf{X}}_{i+k} = \frac{1}{|\mathcal{U}_\epsilon|} \sum_{\mathbf{X}_j \in \mathcal{U}_\epsilon} \mathbf{X}_{j+k} = \frac{1}{\zeta} \sum_{j=1}^{\zeta} \mathbf{X}_{j+k}, \quad (4.6)$$

where $\tilde{\mathbf{X}}_{i+k}$ and $\tilde{\mathbf{X}}_{j+k}$ are the k -step ahead predictors in the original space of \mathbf{X}_i and \mathbf{X}_j . k is an integer number and need to satisfy the previous first order approximation, i.e. $k\tau_s \approx \Delta t$ with τ_s the time series sampling time. In Equation 4.6 and in the following discussion, it is considered, for simplicity of notation that \mathcal{U}_ϵ contains ζ nearest neighbours. Since \mathbf{X} is the hidden original space, the approximation in Equation 4.6 needs to be translated into the observable time series domain \mathbf{x} where $\hat{\mathbf{F}}_S(\cdot)$ is constructed to generalize the underlying generator of the data. Therefore,

$$\tilde{x}_{i+k} = \frac{1}{\zeta} \sum_{j=1}^{\zeta} x_{j+k}, \quad (4.7)$$

which is explained by a two step procedure using \mathcal{D}_x : firstly, at time i there is a search in $\hat{\mathcal{D}}_x$ the set of ζ -nearest neighbours $\hat{\mathbf{X}}_j \in \hat{\mathcal{U}}_\epsilon$ of $\hat{\mathbf{X}}_i$ such as $|\hat{\mathbf{X}}_i - \hat{\mathbf{X}}_j| \leq \epsilon$. Secondly, a lookup procedure in the database $\hat{\mathcal{D}}_x$ for the correspondent entry x_{j+k} of the nearest neighbours embedding vectors $\hat{\mathbf{X}}_j$ is accomplished. It is important to underline that the the previous first approximation in Equation 4.6 holds in Equation 4.7 due to the diffeomorphic conditions induced by Takens' theorem which relates \mathbf{X} to $\hat{\mathbf{X}}$.

A possible extension for the predictor in Equation 4.7 is to incorporate a weighted sum depending on the manifold shape into a neighbourhood of the time point i . This means that the previous formulation includes a smoothing term which weights each neighbour relative to the distance from the centre $\hat{\mathbf{X}}_i$. It follows that

$$\tilde{x}_{i+k} = \sum_{j=1}^{\zeta} \Phi(\hat{\mathbf{X}}_i, \hat{\mathbf{X}}_j, \mathbf{w}_x) x_{j+k}, \quad (4.8)$$

where the kernel function $\Phi(\hat{\mathbf{X}}_i, \hat{\mathbf{X}}_j, \mathbf{w}_x)$ is imposed to satisfy the summation constraint

$$\sum_{j=1}^{\zeta} \Phi(\hat{\mathbf{X}}_i, \hat{\mathbf{X}}_j, \mathbf{w}_x) = 1, \quad (4.9)$$

with \mathbf{w}_x the free coefficients which parametrise the previous kernel which need to be estimated accordingly. The Equation 4.8 is known in the literature as the *Nadaraya-Watson regression estimator* (NWRE) [65]. If we choose the simplest kernel function as a constant, i.e., $\Phi(\hat{\mathbf{X}}_i, \hat{\mathbf{X}}_j) = 1/\zeta$ if $\hat{\mathbf{X}}_j$ is one of the nearest neighbours of $\hat{\mathbf{X}}_i$ otherwise $w(\hat{\mathbf{X}}_i, \hat{\mathbf{X}}_j) = 0$, the approach is equivalent to Equation 4.7. In the literature, this simplest case with uniform kernel can be referred to as the ζ -nearest neighbour estimate [60] or the *zero-th order* predictor [127]. As described in [60], the use of various kernels can result in different types of predictor such as the kernel estimate and the partitioned estimate.

In this thesis, as suggested by the approach taken in [66], we take an intermediate approach to Equation 4.6 and Equation 4.8. In fact, instead of the kernel $\Phi(\hat{\mathbf{X}}_i, \hat{\mathbf{X}}_j, \mathbf{w}_x)$ in Equation 4.8, which is a function with support in the embedding space, it is here considered as a kernel function with support on the time series domain, i.e. $\Phi(x_i, x_j, \mathbf{w}_x)$. This original approach can be better represented and explained by the neural network forward structure of the predictor $\hat{\mathbf{F}}_S(\cdot)$ as described in Figure. 4.1.

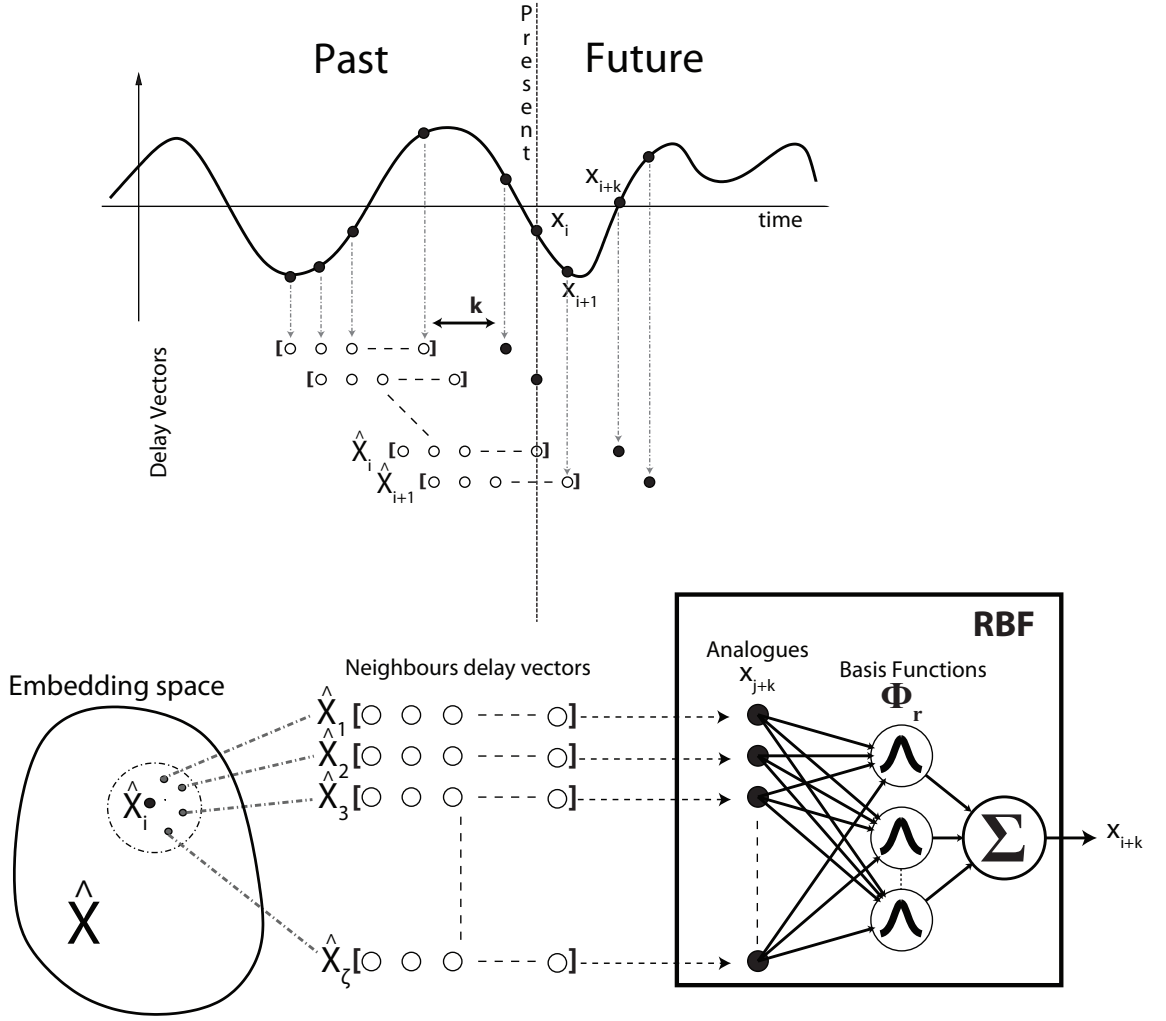


Figure 4.1: The Radial basis function network model which is an extension of the Lorentz's method of Analogues. The variables \hat{X} define the embedding vector space while x_{i+k} is the k -th step ahead predictor.

In practice, after the nearest neighbours search is performed in the embedding space \hat{X} , the corresponding ζ points x_{j+k} in \hat{D}_x are input to a neural network which will generate, as output, the predictor point x_{i+k} . In [66], a feed forward single layer artificial neural network with sigmoidal activation function is used. In this work, a Radial Basis Function (RBF) Neural Network [96] is preferred with a mathematical representation generalizing Equation 4.6 and Equation 4.8 as follows

$$\tilde{x}_{i+k} = \sum_{r=1}^R W_r \Phi_r(\Upsilon) + w_0, \quad (4.10)$$

where W_r and w_0 are the linear output layer weights, $\Phi_r(\cdot)$ are the basis functions with $R \leq N$. The input space of the RBF is the vector $\Upsilon = \{x_{j+k}\}_{j=1}^{\zeta}$ of corresponding projections of the nearest neighbours of \hat{X}_i . In this thesis a classical local Gaussian basis function is used though this is not crucial:

$$\Phi_r(x) = \exp\left(-\frac{\|x - \mu_r\|^2}{2\sigma_r^2}\right), \quad (4.11)$$

with mean μ_r and standard deviation σ_r .

The Analogues-RBF approach just described is a semiparametric variation of *memory-based* methods in the pattern recognition literature [11]. Computationally, memory-based methods such as the Lorenz

analogues are fast in training, since they require only building the database of examples $\hat{\mathcal{D}}_x$, but slow in prediction since they need to seek neighbours at each time i . During the training, the Analogues-RBF version is computationally slower than the Lorenz method since it requires the learning of the RBF network. This step, however, has the advantage of offering a better approximation of the shape of the local neighbourhood. In order to increase the performance of the algorithm for large databases during the neighbour search, it is advisable to develop the structure of the database $\hat{\mathcal{D}}_x$ using K-D trees [30]. The latter solution can compute the neighbours problem in $O(K \log K)$ time comparing to an unstructured solution which requires $O(dK^2)$ time if the pairwise distance of K embedding d dimensional vectors is computed.

Thailer Correction

By construction, the embedding is biased towards the problem of temporal correlations [82; 141]: Consecutive time delay vectors are close in the embedding space because they may include the same time series points and not because of the true geometrical distances in state space. To prevent this bias, the search for nearest neighbours does not take into account the embedding vectors $\hat{\mathbf{X}}_j$ belonging to a window $W_\tau = 2 \times \tau_w$ (Thailer window) around the present time i [141]. Apart from increasing prediction capabilities, this Thailer correction is a typical processing stage in the nonlinear time series literature during the computation of geometrical invariants [82], i.e. correlation dimension, but also used for algorithms of state space synchronisation, i.e. synchronisation likelihood [137].

4.2.3 Mutual Predictor

The second part of the Granger causality algorithm considers modelling the conditional distribution of the right hand side of Equation 4.1. The main problem to address in this section is how to integrate the information from both \mathbf{x} and \mathbf{y} to build a suitable mutual predictor $\hat{\mathbf{F}}_{\mathbf{M}}(\cdot)$ for either \mathbf{x} or \mathbf{y} .

In the context of state space reconstruction, this question can be more generally related to the issue of building a multivariate embedding [82]. While the problem of univariate embedding has been intensively studied in the literature, little has been done to extend it to a fully multivariate method [113]. In theory, the embedding theorems do not put any limitation on the dimensionality of the measurement vectors. The space $\hat{\mathbf{X}}$ can be reconstructed using different time series and even from different types of measurements (even using the haemodynamic blood signal from fMRI, for instance) if one can be assured that they are independently sampled from the underlying brain network [82]. Some methods of distributed embedding have been proposed for dynamical systems [13; 48; 23] and discussed for EM data [91] but still, to our knowledge, they have been poorly applied in practice.

In this thesis, a mutual predictor is considered which avoids the implicit construction of multivariate embeddings by using a variant of the Analogues-RBF neural network forward structure of the previous single predictor. The conceptual framework of this method is shown in Figure 4.2. At each time point i , the set of neighbours $\hat{\mathbf{X}}_j$ of $\hat{\mathbf{X}}_i$ and $\hat{\mathbf{Y}}_j$ of $\hat{\mathbf{Y}}_i$ are computed and the corresponding time series entries in $\hat{\mathcal{D}}_x$ and $\hat{\mathcal{D}}_y$ of these neighbours are employed as inputs of a 'double' RBF neural network. The forward neural network structure that follows, is applied to forecast the output of the RBF based on the set \mathbf{x} or \mathbf{y} . This can be expressed by

$$\tilde{x}_{i+k} = \sum_{r=1}^R W_r \Phi_r(\Upsilon_1) + w_0 \quad (4.12)$$

where $\Upsilon_1 = [\{x_{j+k}\}_{j=1}^{\zeta_x}, \{y_{j+k}\}_{j=1}^{\zeta_y}]$ is the set of nearest neighbours projection as described in Figure 4.2. In this thesis, to reduce the degree of freedom of the method during analysis the choice of $\zeta_x = \zeta_y = 2 \times \zeta$ has been considered.

In practice, this type of mutual predictor re-utilises the computational information about the neighbours of the previous stage and leaves the RBF machine to learn the best mutual forecasting rule. The results section shows, using some synthetic examples, that this method can be successfully employed for the causal metric designed in this thesis.

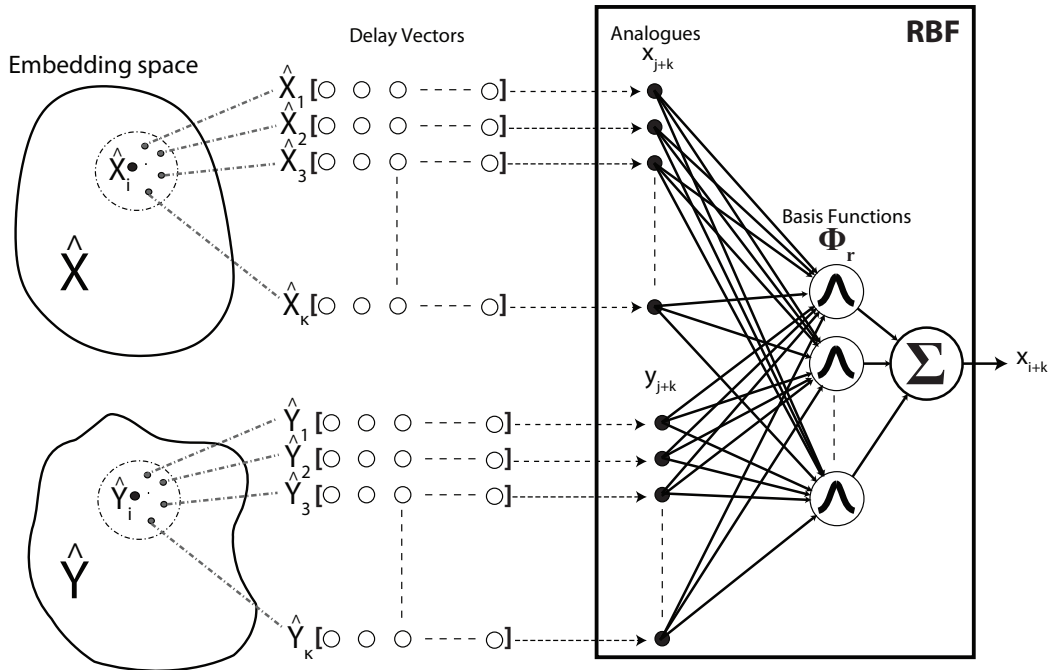


Figure 4.2: The mutual predictor model used in this thesis. The RBF learns the prediction of \tilde{x}_{i+k} given the analogues collected in the \hat{X} and \hat{Y} , separately.

During this project, some other possible solutions were also taken into consideration. (Investigated in [25], initially without the Analogues-RBF interface but not further developed here). Figure 4.3 shows the schematic representations of these cases. A second method, which is referred to here as the *Joint space approach* addresses directly the problem of the multivariate embedding by constructing a new space \hat{Z} and a new database of examples \mathcal{D}_{xy} (the same for \mathcal{D}_{yx}) defined as:

$$\mathcal{D}_{xy} = \{(x_{i+k}, \hat{\mathbf{Z}}_i)\}_{i=1}^{N_e} = \{(x_{i+k}, [\hat{\mathbf{X}}_i, \hat{\mathbf{Y}}_i])\}_{i=1}^{N_e}. \quad (4.13)$$

In practice, the embedding vector $\hat{\mathbf{Z}}_i$ is formed from the concatenation of the two vectors $\hat{\mathbf{X}}_i$ and $\hat{\mathbf{Y}}_i$ at each time i . The latter is a solution which has often been employed for multivariate state space reconstruction [82]. With respect to the previous method, however, this technique is computationally slower and statistically less reliable. In fact, it needs an additional search procedure: firstly, seek for the neighbours vectors ($\hat{\mathbf{Z}}_j$) of the present $\hat{\mathbf{Z}}_i$; secondly, the corresponding entries of $\hat{\mathbf{Z}}_j$ in the database \mathcal{D}_{xy} , i.e. x_{j+k} , are considered as the input of the RBF neural network with output x_{i+k} . Another issue with this method is due to the fact that $\hat{\mathbf{Z}}$ is an higher dimensional space than $\hat{\mathbf{X}}$ or $\hat{\mathbf{Y}}$: more points are required to offer a statistical significant model due to the curse of dimensionality.

A third method, named the *Mutual neighbour approach*, while addressing the problem of directional functional connectivity based on predictability, does not strictly belong to the class of Granger causality techniques and its usage is left for future projects. This method was initially proposed in [127] to detect dynamical interdependence and it is related to the concept of generalized synchronisation [124]: Firstly, it considers the embedding vector $\hat{\mathbf{X}}_i$ at time point i and searches for the corresponding counterpart $\hat{\mathbf{Y}}_i$ in the partner space; Secondly, the nearest neighbours $\hat{\mathbf{Y}}_j$ of $\hat{\mathbf{Y}}_i$ are gathered; Thirdly, the mutual set of neighbours back in the original $\hat{\mathbf{X}}$ space corresponding to the $\hat{\mathbf{Y}}$ -space neighbours $\hat{\mathbf{Y}}_j$ are considered to build the mutual Analogues-RBF predictor. The operation of '*mutual back-projection*' from space to space is a typical procedure of state space synchronisation techniques (for instance Synchronisation Likelihood [137]).

4.2.4 Interdependence Granger metric

The final step of the algorithm consists of building the directional functional distance metric $d_c(\mathbf{x}, \mathbf{y})$ based on the deviation from Markov property in Equation 4.1. By processing the test database \mathcal{D}_x^+ as built in Section 4.2.1 using the previous single and mutual predictors, the following root mean square (RMS) out-of-sample error measure is computed as:

$$e_x = \sqrt{\frac{1}{N^+} \sum_{i=1}^{N^+} (x_{i+k}^+ - \tilde{x}_{i+k})^2}. \quad (4.14)$$

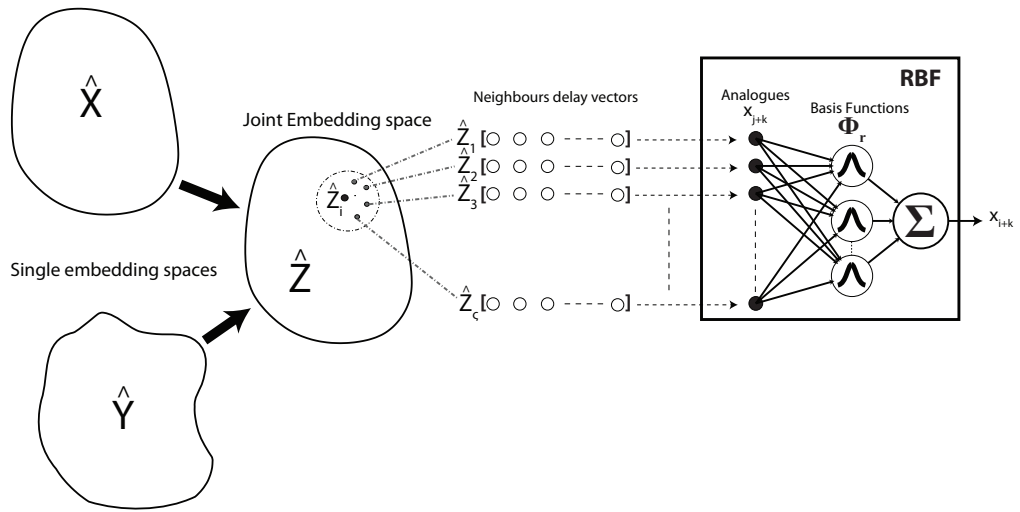
In the same way the corresponding mutual RMS is given by:

$$e_{xy} = \sqrt{\frac{1}{N^+} \sum_{i=1}^{N^+} (x_{i+k}^+ - \tilde{x}y_{i+k})^2}. \quad (4.15)$$

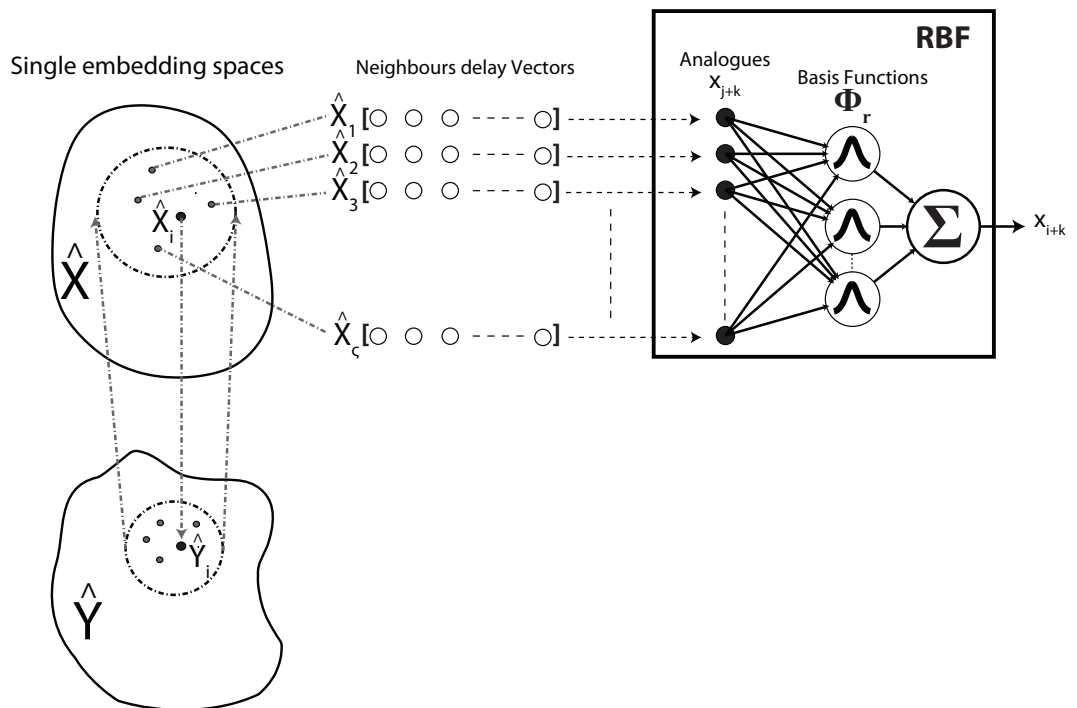
Given the previous two error terms the following directional metric of Granger causality can be computed:

$$G_{y \rightarrow x} = \ln \left(\frac{\sigma_x^2}{\sigma_{xy}^2} \right), \quad (4.16)$$

where σ_x^2 and σ_{xy}^2 are the variance of the RMS out-of-sample single and mutual error respectively. In practice, if the information from the time series \mathbf{y} influences \mathbf{x} the denominator in eq (4.16) will be smaller



(a) Joint Space Approach



(b)

Figure 4.3: Graphical comparison between two other possible approaches considered in this thesis. a) represents the joint space approach while b) the mutual neighbours approach.

than the numerator and $G_{y \rightarrow x}$ will increase. If there is no influence the numerator and denominator will be equal and the measure G will be zero as the variance ratio is transformed by the logarithm. In an equivalent way, it is possible to define the mutual influence $G_{x \rightarrow y}$. Equation 4.16 has been used in other studies [55] and it was originally discussed in [51] for linear stochastic systems.

Significance assessment of causality

It is a practical and important step of the analysis to ask for the significance of the computed causality index in Equation 4.16. A significant value indicates the existence of causal connectivity. Since the underlying distribution of the signals and the Granger metric is not known, a nonparametric approach based on the method of surrogate data better fits the purpose of this thesis rather than employing results from asymptotic distribution theory. The use of asymptotic theory for Granger causality has been reported for instance in [51] for the linear causality (F-test) as well as in [67] for the causality based on correlation integrals.

The method of surrogates, instead, is based on the principle of bootstrapping [149]: new sets of data \mathbf{x}^* and \mathbf{y}^* are resampled from the original \mathbf{x} and \mathbf{y} in order to destroy any causal dependence between the two. In this way, the statistic $G_{y \rightarrow x}$ (or $G_{x \rightarrow y}$) can be tested against the null H_0 distribution $G_{y \rightarrow x}^*$ (or $G_{x \rightarrow y}^*$) computed based on \mathbf{x}^* and \mathbf{y}^* and checked for its significance using an hypothesis testing framework.

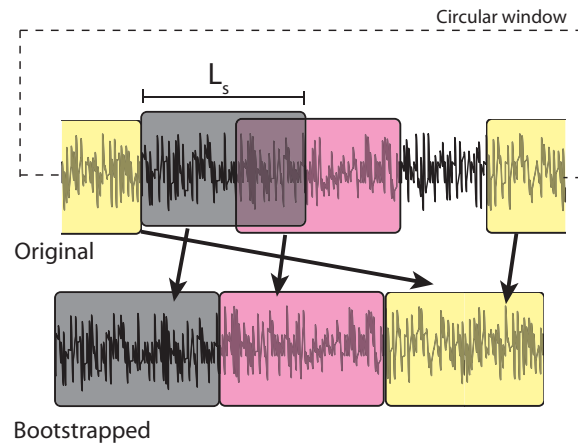


Figure 4.4: The circular block bootstrapping method to produce the surrogate data.

The most simple bootstrapping method consists of randomly shuffling the data points in \mathbf{x} and \mathbf{y} . However, this method is restricted to stationary and i.i.d. data and it is poorly suited to time series. Instead, in order to preserve the temporal structure of the data, a method based on the concept of the *moving block bootstrapping* is better considered for the goal of this chapter [149]. In practice, from a given time series \mathbf{x} , a set of segments of length L_s randomly chosen in \mathbf{x} are concatenated to form the new time series \mathbf{x}^* . The chosen segments of data are allowed to overlap with each other and their time points can be taken in a circular way as schematically shown in Figure 4.4. The latter procedural step is known as circular block bootstrapping, a possible variant of the original moving block technique, which is applied by wrapping the beginning of \mathbf{x} with its end.

The length L_s needs to be chosen to preserve as much as possible the dependence structure of the data but not so large that the number of concatenated blocks become too small [149]. It is a crucial parameter which

has been the subject of intense empirical and theoretical study. Nevertheless, available results have offered little guidance in its selection and applicability to real data [149]. In this thesis, following previous studies concerning Granger causality [32; 27], it has been decided to implement the technique of the *stationary bootstrap* [118] for tuning L_s . In practice, this method is a further variant of the moving and circular block bootstrapping where L_s is not fixed but is instead taken as a random variable drawn by a geometric probability distribution:

$$P(L_s = m) = (1 - p)^{m-1} p, \quad \text{for } m = 1, \dots, \quad (4.17)$$

where p is considered to be small (following [32], in this thesis $p = 0.05$). Within this approach, L_s is computed several times during the bootstrapping from the previous geometrical distribution until the time series \mathbf{x}^* reaches the same length of the original \mathbf{x} .

As investigated and suggested in [32], the method of bootstrapping is better performed in only one of the two signals. Applying this technique to both signals has been shown to introduce bias to the rejection of the null hypothesis. In particular, since the causal metric is asymmetric, the signal to resample is based on the causality statement one wants to test: \mathbf{x} is considered for bootstrapping if testing $G_{x \rightarrow y}$. In practice, the signal to be bootstrapped is the *master* of the causal relationship and not the *slave*. This modus operandi has been shown to increase the power of the hypothesis testing, and useful on neurophysiological data [27].

The probability that the previous indices $G_{x \rightarrow y}$ and $G_{y \rightarrow x}$ are significant is measured by the corresponding P-values computed from the bootstrap null Granger distributions $G_{x \rightarrow y}^*$ and $G_{y \rightarrow x}^*$ using a t-test. A reasonable threshold for the significance of the P-values is set in this thesis to 0.05.

Differential Granger Index

If both $G_{x \rightarrow y}$ and $G_{y \rightarrow x}$ are significant against the surrogate test, feedback processes may take place between \mathbf{x} and \mathbf{y} . In this thesis, we are not interested in feedback processes, i.e. the strength of the separate causal relationships $G_{y \rightarrow x}$ and $G_{x \rightarrow y}$. Instead, an eventual difference between the values of $G_{y \rightarrow x}$ and $G_{x \rightarrow y}$ provides a test for directionality of the overall coupling which is the *differential Granger measure*

$$\Delta G = G_{x \rightarrow y} - G_{y \rightarrow x} \quad (4.18)$$

Another possible index found in the literature is proposed by [4], where for bidirectional coupling $D = \frac{c_2 - c_1}{c_1 + c_2}$ is used with $c_1 = \sigma_x^2 - \sigma_{x|xy}^2$ and $c_2 = \sigma_y^2 - \sigma_{y|xy}^2$.

4.2.5 Optimisation

The causal metric $d_c(\cdot, \cdot)$ is not parameter free: It contains a set of parameters which need to be a priori imposed beforehand or learned from the data. They are the embedding parameters discussed in the previous chapter, i.e. the dimension M , the delay τ and the length of the time series L , and the RBF network parameters, i.e the number of neighbours, the weights W_r and the the number and the specifications of the basis functions $\Phi_r(\cdot)$. In this work, a two stage *Cross-Validation-Procedure*, typical for a maximum likelihood estimation scheme, is considered in order to tune the choice of the causal metric and extract its

value: some parameters are firstly learned using the training set \mathcal{D}_x^- by a function minimisation algorithm; Secondly, since the final purpose of building the predictor is not forecasting, the rest of the parameters can be chosen in order to minimize the out-of-sample prediction errors in the available test set \mathcal{D}_x^+ . The function minimisation algorithm is thus repeated for different choices of these latter parameters until the out-of-sample prediction errors is minimised.

If the predictor is used for forecasting as usually designed, the test set \mathcal{D}_x^+ is not available but it is strictly to be considered as unseen data, i.e data that the build predictor need to forecast. In practice, in this case when only the training dataset is available a third set (validation set) is extracted from the training data in order to tune the choice of the parameters (different methods exists to extract validation set and we refer to [10] for further details).

Radial Basis Function minimisation

The optimisation of the RBF network involves the choice of the weights W_r , the number of basis functions R , their centre locations μ_r and the variances σ_r^2 employing a function minimisation algorithm using the training dataset. The number R of basis function, which indicates the complexity of the neural network, usually needs to be specified before this procedure of minimisation. The latter is an empirical argument which is significantly smaller than the size of the training example [65] and can be addressed by cross-validation using the test set. For the other parameters a two stages RBF learning process based on an optimisation algorithm described in Netlab [103] is considered:

- The first part of the algorithm consists of an unsupervised learning procedure based on the Expectation-Maximisation algorithm [10] in order to train the hidden layer of the RBF (estimate centre locations μ_r and the variances σ_r^2). The centres are chosen by randomised start initial K-means clustering [10] and the variances determined by the maximum distance between the centres as indicated in NetLab.
- In the second part, the layer of the weights W_r are calculated via a linear least square computation based on the result of the $\Phi_r(\cdot)$.

Embedding as a modelling problem

In the previous chapter, the choice of the embedding parameters were discussed using a method based on SSA. As described, the latter technique employs a two stage estimation algorithm which computes firstly the dimension of the embedding m , and secondly the delay parameter τ . A similar modus operandi is found in other classical and popularly used approaches of tuning the embedding [82]. As a reference, alternatively, it is possible to tune the embedding parameters using cross-validation (for a detailed explanation in [76]): The couple dimension-delay $((m, \tau))$ are chosen, within a single step, in order to minimize the out-of-sample prediction error in the test set. As discussed in the literature, an advantage of this method is that there is no need to consider separately M and τ but their values can be found simultaneously. This method need a model of the data on top of the embedding such as our Analogues-RBF approach which computes the prediction error and find the optimal choice of $((m, \tau))$. It is not clear which is the best approach of embedding, as discussed in [113] but with the availability of the predictor we consider using a cross validation technique to seek for the best (M, τ) .

Nearest neighbours

The choice of the number ζ of the nearest neighbours follows the cross validation procedure. The neighbourhood needs to be small enough in order to satisfy the initial assumption of the Lorenz analogues. In practice, using the RBF has the advantage that this assumption may be relaxed since during the learning stage points that are too far away may be penalized. In this case, it is important to avoid overfitting the data and a cross validation stage is necessary.

4.3 Simulations

As for the case of single channel analysis, simulated examples are investigated next, to check the efficiency of this chapter's directional metric. The Rössler lattice of the previous chapter is not taken here as a suitable example because it does not contain any nontrivial directional flow between its elements (its diffusive form of coupling is symmetric). Instead, in this chapter, the ability of the causality metric to estimate directionality in data is tested against dedicated WCDS formed by only two elements as shown in Figure 4.5. This choice is consistent with the following considerations:

- As in the previous chapter, these synthetic examples are not designed to provide a precise representation of the underlying neural system but they mimic possible cortical columns interactions to test the previous causality algorithms.
- These coupled dynamical systems are taken from previous works in the literature where they were considered already as possible toy models for testing causal algorithms used in a second time to detect directional interdependence in the brain.
- The aim of this chapter's discussion is focused on the problem of the causality metric only. Therefore, the global underlying dynamical system uses two elements only to simulate the interaction between two points at the sensor level. The problem of functional network analysis which requires a global multi-elements dynamical systems is left for future investigations.
- The signals at the sensor level are taken directly from the corresponding underlying cortical regions. While the Analogues-RBF metric was initially tested on scalp EEG, the causality metric in this thesis is mostly designed to be used during the analysis of iEEG where volume conduction phenomena are considered to be negligible. The problem of volume conduction and its effects on the functional directional connectivity is another interesting issue which needs to be addressed in future projects before applying it to scalp EM measurements.

4.3.1 Discrete maps: Coupled Hénon Oscillators

Model

The following mathematical model describes the dynamics of two Hénon maps \mathcal{X} and \mathcal{Y} unidirectionally coupled. This model has appeared in several previous works to report properties of algorithms for directional interactions [127; 87; 120].

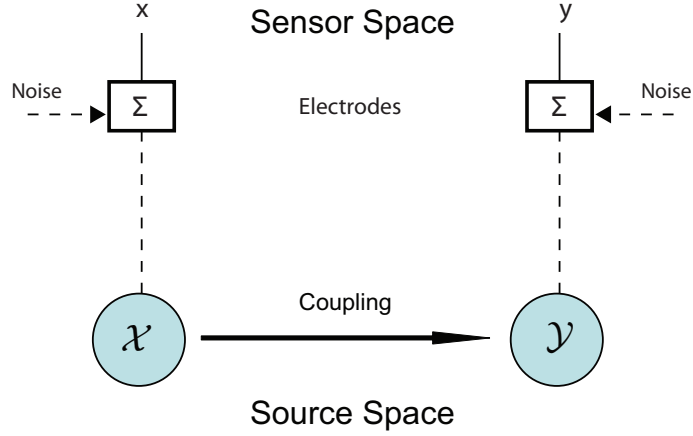


Figure 4.5: Diagram of the structure of the synthetic models as discussed in the following sections.

$$\begin{aligned} \mathcal{X} &= \begin{cases} x_{i+1} &= 1.4 - x_i^2 + 0.3u_i, \\ u_{i+1} &= x_i, \end{cases} \\ \mathcal{Y} &= \begin{cases} y_{i+1} &= 1.4 - (Cx_i + (1-C)y_i)y_i + Bv_i, \\ v_{i+1} &= y_i, \end{cases} \end{aligned} \quad (4.19)$$

where, as used in the literature, the parameter $B = 0.3$ imposes two identical Hénon system while $B = 0.1$ is used for non-identical systems [127]. The parameter C defines the coupling between the two systems with a range considered in this thesis between values of 0 and 1.

The analysis of causality in the Hénon system is performed for the two variables \mathbf{x} and \mathbf{y} of the global WCDS while varying the coupling strength C . During the numerical simulations, the first 10^4 points synthetically generated from initial condition $[x_0 = 0.9, u_0 = 0.5, y_0 = 1.5, v_0 = 1]$ are discarded (the 'burn in' sample). The choice of the initial conditions are taken from the literature in order to avoid numerical instability of the basin of attraction. From the rest of the simulation, a realisation of 1500 points is considered for the analysis of causality. This realisation is moreover contaminated by two sources of white noise \mathbf{v} and ξ for \mathbf{x} and \mathbf{y} , respectively. The noise terms, which account for observational disturbances, are sampled from a zero mean Gaussian distribution with standard deviation set to the 5% standard deviation of the time series. The starting point of this short set of points is randomly chosen after the the burn in period and the generation of the noise was repeated several times in order to check if the causality algorithm is working for different samples. In the following, the results of only one of these realisation is displayed. A different choice has in fact been shown not to change the quantitative discussion of the analysis. From the set of 1500 points, a further subdivision of 1000 and 500 points is considered. The first part accounts for the training set while the second part for the test set.

Figure 4.6 shows as an example, the 2 dimensional state space of the driven system \mathcal{Y} and some synchronisation patterns between \mathbf{x} and \mathbf{y} for some values of the coupling C with $B = 0.3$, i.e. two identical Hénon systems. In the latter figure, it is possible to notice the effect of the coupling in the two underlying systems: \mathbf{x} and \mathbf{y} are uncorrelated in the first left figure, partially synchronised in the second one while they switch to a state of identical or complete synchronisation when $C \simeq 0.7$ in the rightmost figure. Figure (4.7) shows an example of 500 points realisation of the \mathbf{y} time series, showing the oscillatory nature of the system.

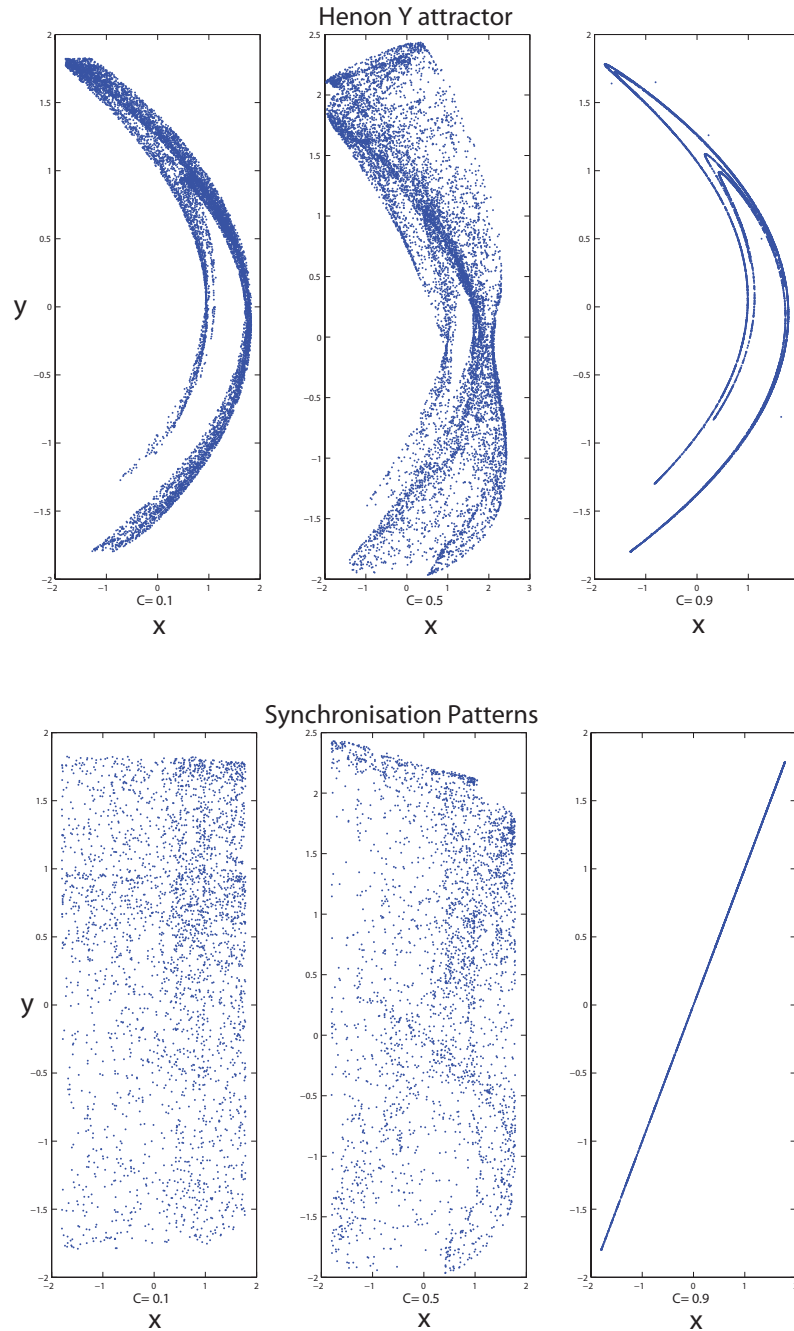


Figure 4.6: Hénon map synchronisation patterns x vs y for identical systems, i.e. $B = 0.3$. The three stages show the route to synchronisation for different values of the coupling

Examples of tuning the Granger metric

As described in the theoretical part, the Analogues-RBF metric contains a set of parameters to choose. While the internal variables of the RBF are optimized by a two stages functional minimisation algorithm, the others need to be either a priori imposed or tuned using a cross-validation procedure. In this section, a few examples are shown of tuning the Granger metric's internal parameters applied to the case of nonidentical Hénon WCDS.

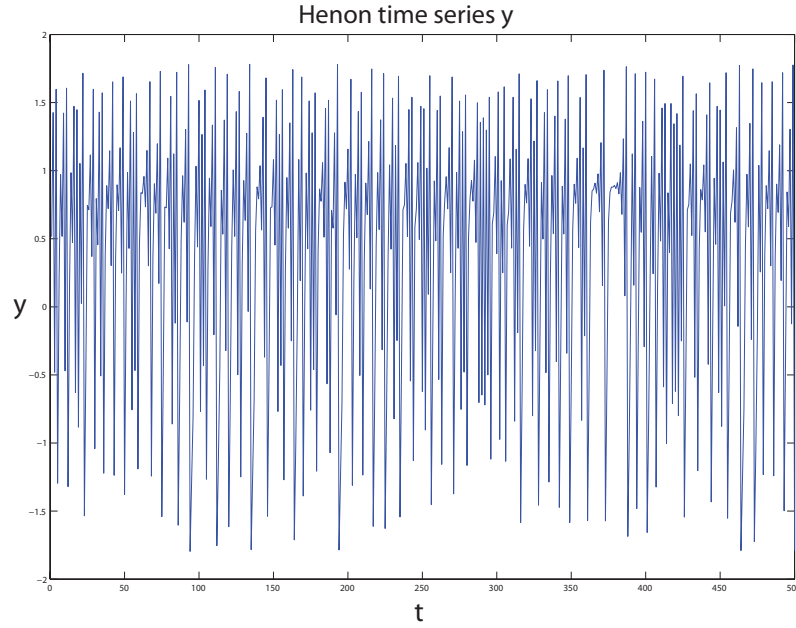


Figure 4.7: An example of a realisation of 500 points of the variable y of the identical Hénon WCDS which shows the oscillatory nature of signal analysed.

Figure 4.8 shows the tuning of the embedding dimension for the case of the two signals x and y and for three values of the coupling C . Firstly, it is possible to notice that for all the coupling regimes there is a minimum of the RMS error in both time series for 3 – 4 dimensions. This value is compatible with the effective embedding dimension for the case of an Hénon system [127]. Secondly, the RMS error for time series y is in general higher than the corresponding x . This effect is consistent with the fact that the time series y is more complex than the x since y is causally driven and thus includes the influence of x .

Figure 4.9 shows the tuning of the number of the nearest neighbours ζ . In this case, with respect of the tuning of embedding dimensions, Figure 4.9 displays the RMS errors for the single predictor (e_y) and the mutual predictor ($e_{y,x}$) based on the driven time series y as an output. Firstly, a difference in these errors, as depicted in all these plots, shows the detection of a causal relationship from x to y . In fact, e_y and $e_{y,x}$ are the components of the Granger index G_{yx} as expressed in Equation 4.16. Secondly, the optimal number of neighbours in both predictors seems to be set to $\zeta = 8$. This choice is important for the low coupling regime $C = 0.1$ since an increase of ζ , knowing that a weak causal relationships exists between x to y , would result in an erroneous difference in the errors ($e_y < e_{y,x}$). For a high value of the coupling strength C (and for a higher causal flow), the choice of the number of neighbours does not seem to influence the difference in the RMS error (and the causality detection). In both central and rightmost subplots of Figure 4.9, however, a minimum of the RMS errors around 8 – 10 are compatible with the ζ of the leftmost figure. Therefore, $\zeta = 8$ is taken as an optimal selection.

To conclude, the number of basis functions for the single and the mutual predictors in the case of the driven time series y are shown in Figure 4.10. Similar considerations discussed for the tuning of the number

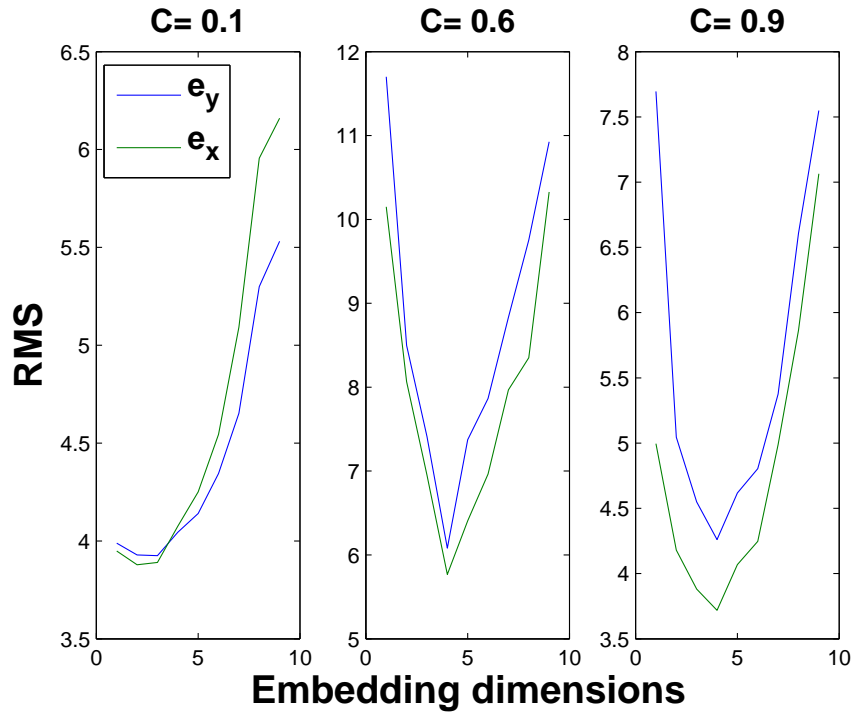


Figure 4.8: Tuning of the embedding dimension using cross-validation based on the prediction errors of e_x and e_y . The time delay is set to $\tau = 1$ since this choice has been seen to give the minimum RMS prediction errors. The other parameters which are taken constant during the analysis of the embedding dimension are: the number of neighbours is $\zeta = 8$ in both single and mutual predictors and the number of basis functions are $R_{single} = 6$ and $R_{mutual} = 12$, respectively.

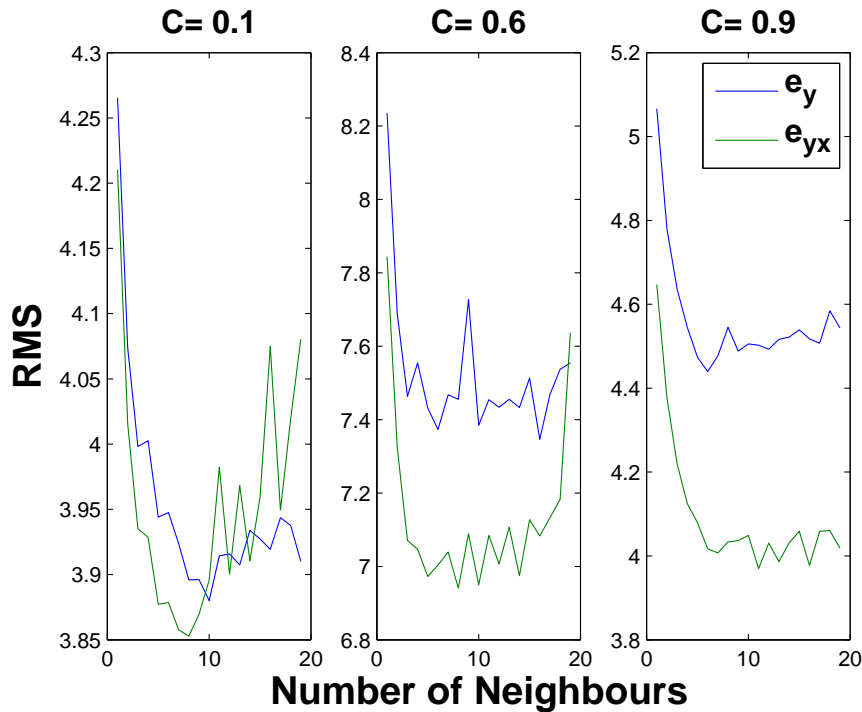


Figure 4.9: Example of tuning the number of nearest neighbours ζ in the case of the single predictor (e_y) and mutual predictor (e_{yx}) for the driven time series y . For this example, the embedding parameters are considered constant to $m_x = m_y = 4$ and $\tau = 1$ and the number of basis function are $R_{single} = 6$ for the single predictor and $R = 12$ for the mutual predictor.

of nearest neighbours may apply to this case. There is a difference between e_y and e_{yx} (visually increasing with the coupling C) which indicates a causal relationship from \mathbf{x} to \mathbf{y} . The RMS errors seem not to reach a minimum yet and the number of basis functions can thus be increased above 20. However, since the difference between e_y and e_{yx} (therefore the causal metric G_{yx}) is already visible, a suboptimal number of basis can be tolerated. A lower number of basis functions, moreover, helps to improve the computational performance of the training stage. If a common number has to be taken constant for all the values of C , in order to emphasize the detection of causality at a lower coupling strength, the number of basis functions for the mutual predictor needs to be higher than in the single case. This is consistent with the difference in input dimensions between the two types of predictors and it is noticeable in the case of $C = 0.1$. A choice of $R_{single} = 6$ and $R_{mutual} = 12$ seems to bring about the difference between the RMS errors e_y and e_{yx} . For higher values of coupling, where the causality should be stronger, both R_{single} and R_{mutual} can be taken with the same value.

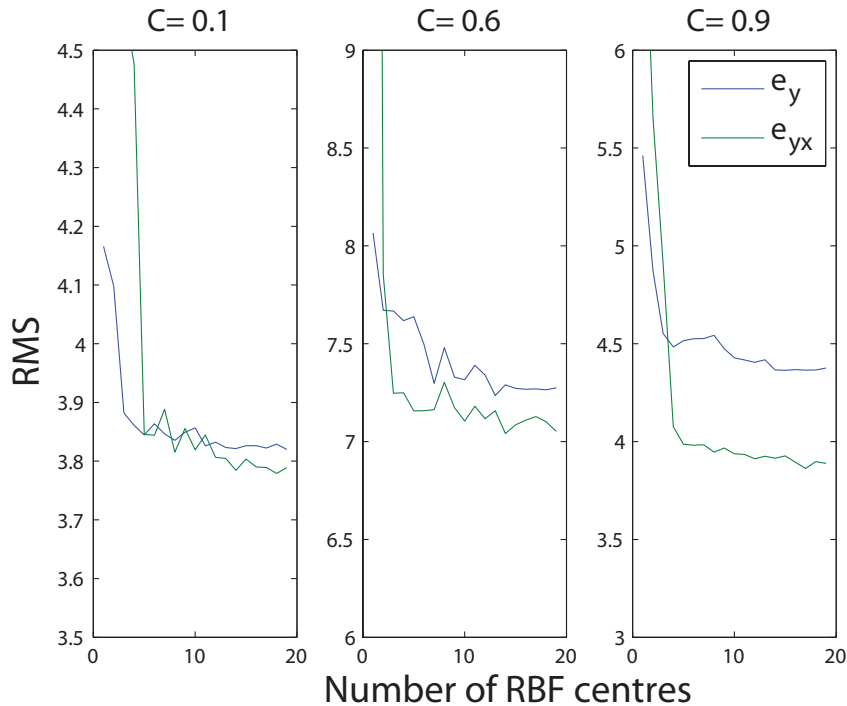


Figure 4.10: Example of tuning the number of radial basis functions in the case of the single predictor (e_y) and mutual predictor (e_{yx}) for the driven time series \mathbf{y} . For this figure, the embedding parameters are considered constant to $m_x = m_y = 4$ and $\tau = 1$ while the number of neighbours are 8 for both single and mutual predictors.

In practice, after this cross-validation analysis, the parameters of the Analogues-RBF metric for the case of the nonidentical Hénon system are set to: $m_x = m_y = 4$, $\tau = 1$, $\zeta = 8$, $R_{single} = 6$ and $R_{mutual} = 12$. The other parameters are left to the optimisation of the RBF training stage. Similar values are shown to be consistent with the study of the identical Hénon system.

Causality metric

Following the tuning of the parameters for the causality metric, Figure 4.11 shows the results of the Analogues-RBF index with varying coupling C for a particular realisation of 1500 points. Figure 4.11(a) depicts the case of identical Hénon maps ($B = 0.3$), while in Figure 4.11(b), the same computation is performed for the case of non-identical oscillators ($B = 0.1$). These plots sketch the behaviour of the two indices G_{xy} and G_{yx} , their corresponding surrogates (errorbars) and the values of the synchronisation between the time series \mathbf{x} and \mathbf{y} using the Mean Phase Coherence index as explained in Appendix A.

Firstly, as expected from a visual inspection of Figure 4.6, the synchronisation increases with the coupling: In the case of identical Hénon maps the underlying system reaches the state of full synchronisation for $C \simeq 0.7$; In the case of non identical oscillators, the coupling increases but the time series \mathbf{x} and \mathbf{y} do not become completely synchronized. Secondly, in both cases, the Analogues-RBF algorithm can retrieve correctly the direction of the flow between the two systems for a certain range of the coupling parameter C . The values of G_{yx} are, in fact, emerging from their set of surrogates.

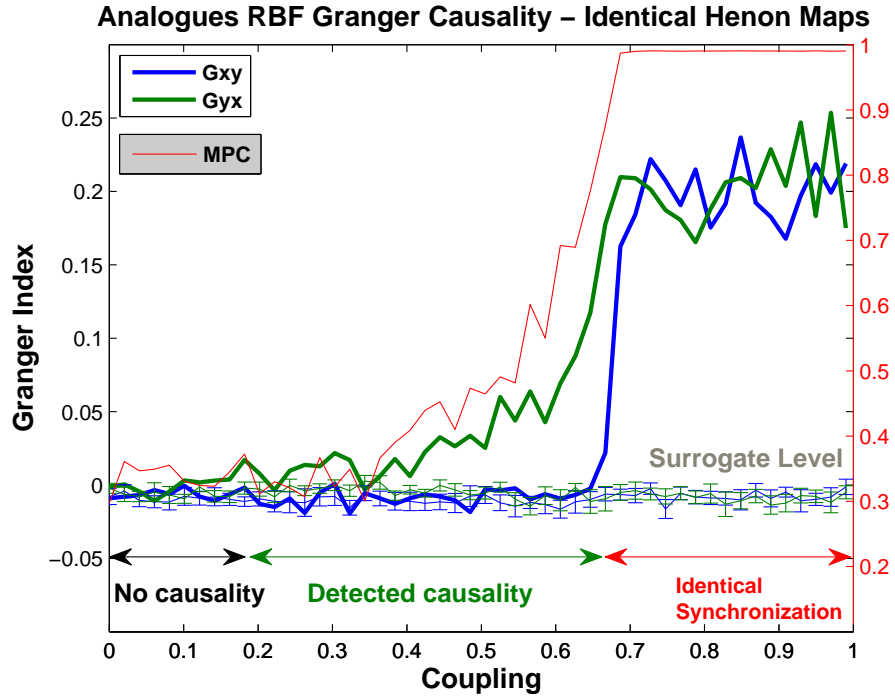
For the identical Hénon WCDS three regimes for the Granger metric can be established. For a low value of coupling, both G_{xy} and G_{yx} cannot be distinguishable from their surrogates and the direction of the information flow is not estimated. For an intermediate strength of coupling, G_{yx} becomes significant and it increases its value correlated with the rise of the synchronisation. G_{xy} remains indistinguishable from its surrogates. Finally when the system becomes fully synchronized both directional measures are significant. In this latter situation, as described visually in Figure 4.6, both time series \mathbf{x} and \mathbf{y} are identical and the algorithm fails to find any directionality even if present. It should be impossible to distinguish any interaction between the systems in this instance, which is intuitively correct.

In the case of nonidentical Hénon maps, the figure shows some similarity with the behaviour of the identical one. However, the directionality of the link can be detected for a larger range of coupling than in the previous case. The two Hénon maps do not become fully synchronized and while for high synchronisation the G_{xy} become slightly statistically significant, the G_{yx} has a greater value. Using the differential Granger index ΔG the directionality of the link can be successfully estimated. This latter nonidentical case is likely to happen in real data, as discussed in Chapter 2 and Chapter 3 for the lattice of Rössler oscillators. In the Rössler example, in fact, the frequency mismatch δ was meant to reproduce the effects of segregation of the neural activity. This phenomenon is considered here by the mismatch between the B parameter.

4.3.2 Chaotic dynamical systems: Coupled Lorenz oscillators

A second example considered is a continuous WCDS implemented using a coupled Lorenz system. This example was included in [87] for a study of synchronisation but not for causality. This WCDS mathematical formulation is given as follows:

$$\mathcal{X} = \begin{cases} \dot{x}_1 &= 10(x_2 - x_1), \\ \dot{x}_2 &= x_1(28 - x_3) - x_2, \\ \dot{x}_3 &= x_1x_2 - \frac{8}{3}x_3, \end{cases} \quad (4.20)$$



Analogues RBF Granger Causality – Not Identical Henon Maps

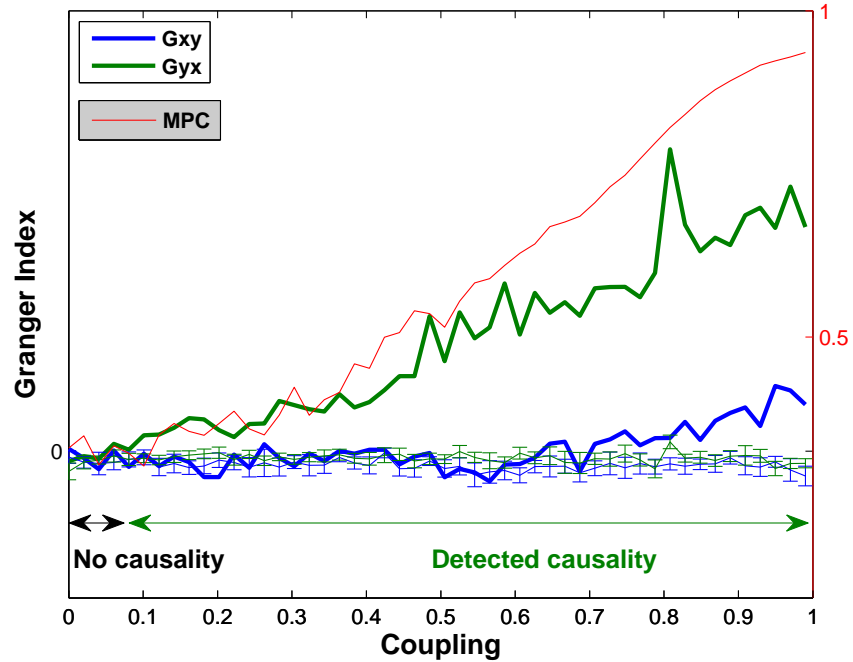


Figure 4.11: Estimation of the Analogues-RBF Granger metric for the identical WCDS Hénon system in a) and the nonidentical system in b). The Analogues-RBF Granger metric successfully detects causality in these systems during a regime of weak coupling. For high values of synchronisation numerical problems can arise and the directionality may disappear.

$$\mathcal{Y} = \begin{cases} \dot{y}_1 = 10(y_2 - y_1), \\ \dot{y}_2 = y_1(28.001 - y_3) - y_2, \\ \dot{y}_3 = y_1 y_2 - \frac{8}{3} y_3 + C(x_3 - y_3). \end{cases} \quad (4.21)$$

The numerical integration was performed in Matlab using the Runge-Kutta Ode45 routine using a step size of 0.001s. The sampling interval for the time series was set to 0.3s. As in the previous simulation of the Hénon WCDS, the first 10^4 points synthetically generated were discarded as the burn in sample. The initial conditions, for this example, were randomly chosen since the stability of the system trajectories were not particularly sensitive to this selection. The time series taken for the causality analysis are x_3 and y_3 . The other two coordinates present some intermittent jumps due to the switching between the wings of the Lorenz attractor. A set of 1500 points, contaminated by Gaussian noise with mean zero and 5% of the time series standard deviations, is considered (divided in 1000 and 500 points for training and test set). The coupling C has range between 0 and 2 following the analysis in [87]. Moreover, there is a mismatch in the second component of the system \mathcal{Y} (28.001 instead of 28) which is used to produce two non identical systems.

As discussed in the previous Hénon example, after the simulation, the internal parameters of the causality metric need to be chosen. The details of this procedure are not displayed here since they have been shown to bring about similar results of the previous example: the embedding parameters are set to $m_x = m_y = 4$ and $\tau = 2$, the number of nearest neighbours are set to 8 for both mutual and single predictor, the number of radial basis function are set to 6 for both the single predictor and 12 for the mutual predictor. Figure 4.12 shows the results of the computation of the Granger metric for the WCDS Lorenz system. This plot depicts, in the same fashion as for the previous Hénon examples, the two Granger indeces and the synchronisation between the oscillators over the coupling strength C . The synchronisation is increasing, as expected by its type and by the range of coupling, to a state of identical synchronisation for $C \simeq 1.35$ [87]. The Analogues-RBF indices successfully identify the direction of the causal link for intermediate values of coupling where the G_{yx} results are significant while G_{xy} not. When the coupling reaches $C \simeq 1.35$, the oscillators reach the state of identical synchronisation. While both measures G_{xy} and G_{yx} are significant after this coupling, the directionality becomes undetectable and not significant.

4.3.3 Stochastic autoregressive systems

Finally, two synthetic models of autoregressive stochastic non chaotic systems are considered. These example are taken from [27] (also in [32]) where they were used as possible toy models for an entropy-based causality investigation. The mathematical formulation, for the case of a simple linear autoregressive model, given by:

$$\mathcal{AR} = \begin{cases} \dot{x}_i &= 0.6x_{i-1} + \omega_x, \\ \dot{y}_i &= 0.6y_{i-1} + Cx_{i-1}\omega_y, \end{cases} \quad (4.22)$$

while for the case of a nonlinear autoregressive model with a nontrivial causal relationship:

$$\mathcal{NAR} = \begin{cases} \dot{x}_i &= 0.7x_{i-1} + \omega_x, \\ \dot{y}_i &= 0.1 + 0.4y_{i-2} + \frac{2.4 - Cy_{i-3}}{1 + e^{-4y_{i-3}}} + \omega_y, \end{cases} \quad (4.23)$$

where ω_x and ω_y are sources of dynamical noise with zero mean Gaussian distribution and unitary standard deviation and the coupling C in both systems is varied between 0 and 1.

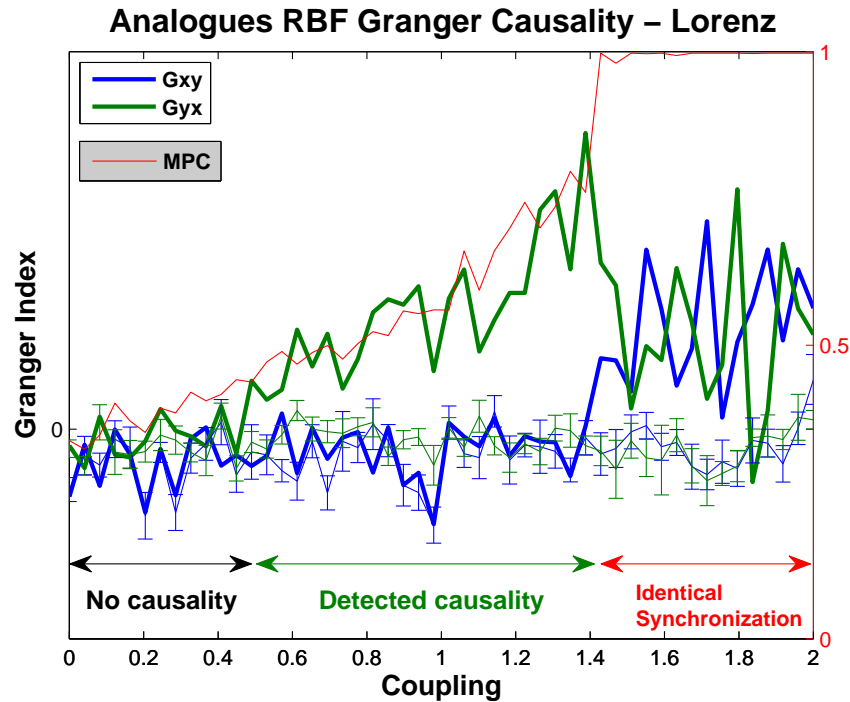


Figure 4.12: Analogues-RBF Granger causality for the case of a WCDS Lorenz systems. As for the previous Hénon maps examples this index identifies correctly the direction of the flow of information for a weakly coupled strength of C .

The same analysis as in the previous examples is applied here. The Analogues-RBF metric is estimated on 1500 point realisations of \mathbf{x} and \mathbf{y} contaminated by the observational noises v and ξ (5% of the time series standard deviations). In Figure 4.14 the results of the computations with varying the coupling C are shown. These plots are produced using the following set of parameters: the embedding parameters are set to $m_x = m_y = 3$ and $\tau = 1$, the number of nearest neighbours are set to 10 for both mutual and single predictor, the number of radial basis functions are set to 4 for both the single predictor and 8 for the mutual predictor. The precise details of this choice reflects the same considerations as in the previous case and not further reported here. It is however interesting to show the behaviour of the single and mutual prediction errors e_y and e_{yx} as shown in Figure 4.13 in the case of the number of neighbours. The RMS errors decrease by increasing the number of neighbours used which is probably due to the fact that the system is stochastic. There is no clear minimum. However, the difference in the value of e_y and e_{yx} can be detected with a small number of neighbours used: the choice of 10 neighbours is seen as a good trade-off between obtaining a good Granger statistic and having good computational performances.

Figure 4.14 shows that in both models the Analogues-RBF metric are correlated with the corresponding MPC synchronisation index and the correct direction of the causality can be found: In the linear AR case, the increase of the parameter C results in an increase of the synchronisation and thus the value of the Granger index is above its surrogate; In the nonlinear model, the decrease of synchronisation due to coupling is detected and correlated with the MPC and by the Analogues-RBF metric. The latter is significant for all the values of coupling.

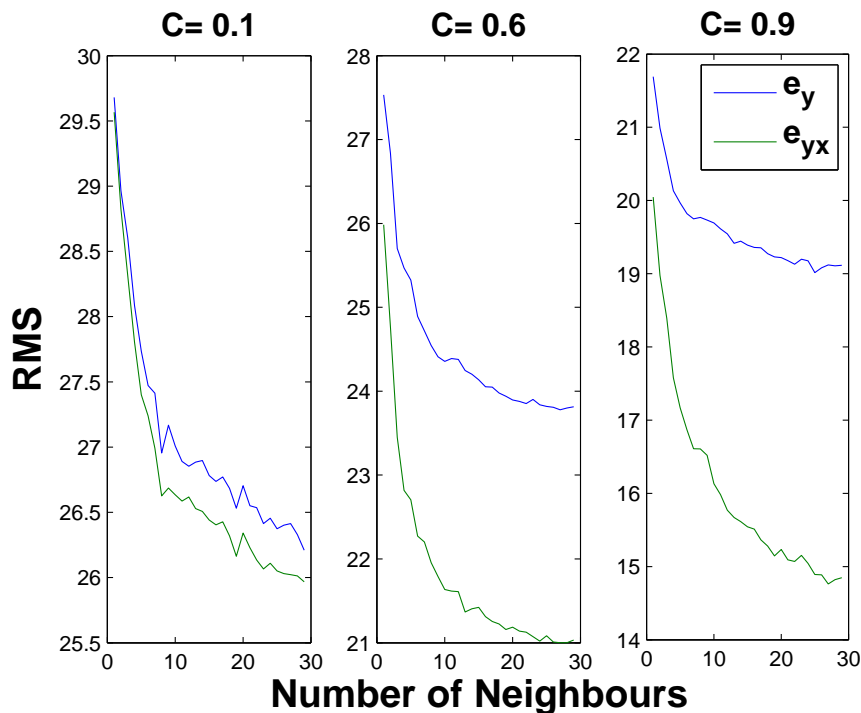


Figure 4.13: Tuning of the neighbours for the linear AR model.

4.4 Summary and discussion

The main goal of this chapter is to develop a measure of causality or information transfer between bivariate time series which can be used to study directional interactions in EM brain data. The outcome of this chapter analysis is a novel causal method which is referred to as an Analogues-RBF Granger metric.

In Section 4.2, the theoretical description of the Analogues-RBF Granger metric is provided. This metric derives from a general formulation of the concept of Granger causality defined by the inequality in Equation 4.1. The latter is known as the deviation from Markov property. The novel method developed in this chapter is a possible maximum likelihood estimator of this inequality which is based on an extension of the Lorenz method of Analogues: It is a simple local non-parametric predictor in state space which is interfaced by a RBF neural network. The latter structure is employed with the intent to provide a data-driven mechanisms of learning to the Analogues-RBF method.

In Section 4.3 a set of synthetic examples were simulated in order to test the validity of the Analogues-RBF Granger metric. These examples were suggested by the specialized literature as possible toy models in order to investigate directional interaction and they were employed in previous studies concerning neurophysiological data analysis. It is important to remark that they are not meant to reproduce a precise representation of the underlying neural system but they mimic possible cortical columns interactions. The following main conclusions were drawn from the results of the simulations.

- The analysis of the data generated by these synthetic examples shows that the Analogues-RBF method successful estimated causal relationships in all the examples when present. Firstly, this chapter metric

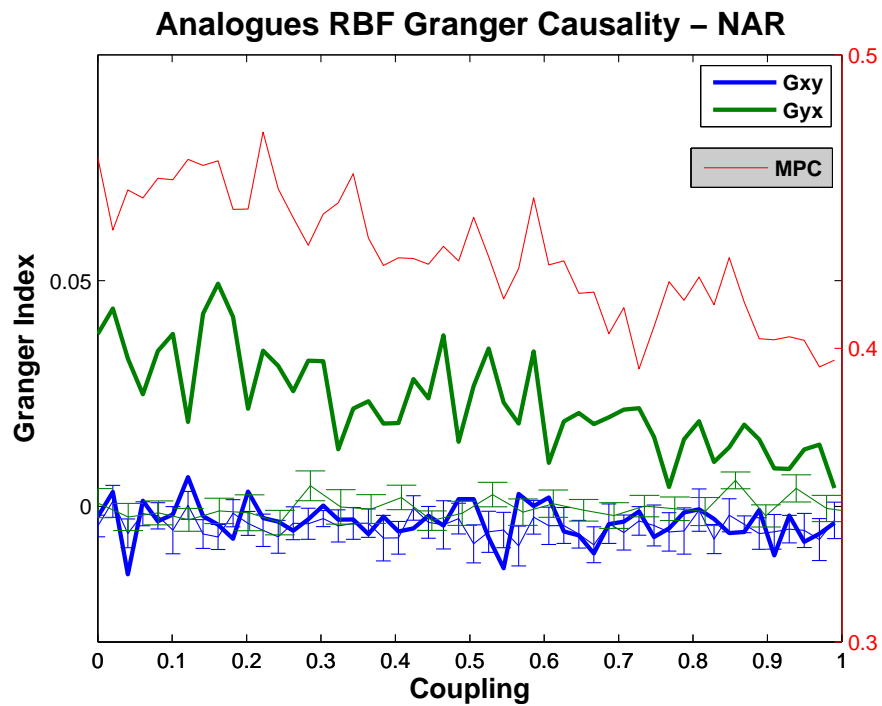
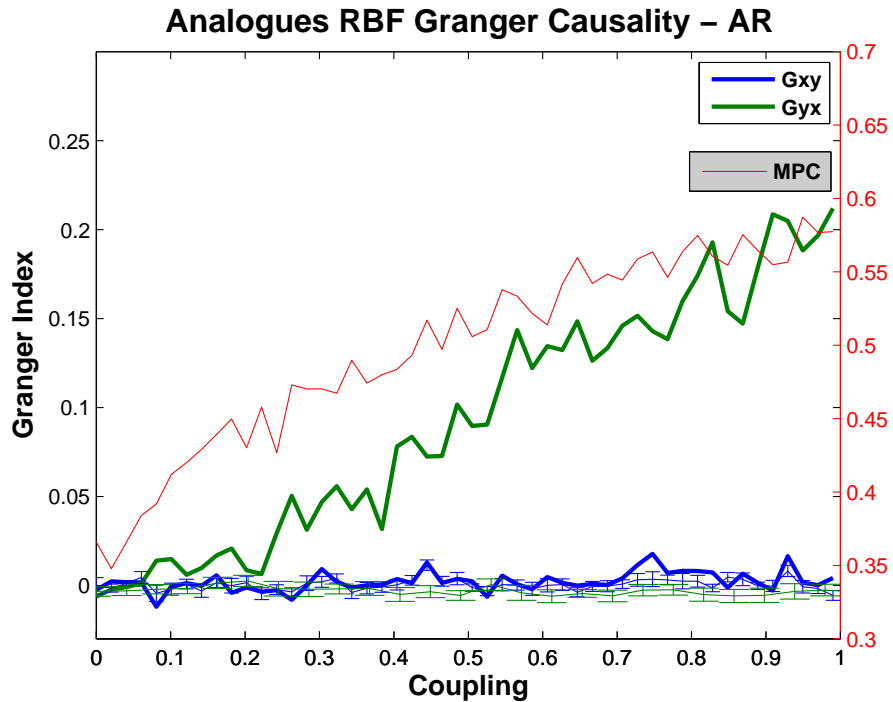


Figure 4.14: Estimation of the Analogues-RBF Granger metric for the stochastic AR models. In a) is shown the linear model while in b) the nonlinear model is shown. Also in this case the Granger causality metric detects coupling and directionality of the underlying information flow.

has shown to be correlated with the behaviour of a measure of phase synchronisation. This result demonstrates that the metric detects the correct strength of the coupling. Secondly, the asymmetric

nature of the metric and a test based on surrogate data further established that the Analogues-RBF technique correctly detects the direction of the information flow.

- The Analogues-RBF Granger metric detects the causality in the data for a regime of weak coupling: when the data are highly synchronised the causal metric may not be able to find the correct direction of the interdependence. This phenomenon is intuitively correct: when the trajectory of the two systems are the same any directional information is lost. It is thus important to check during the data analysis the value of synchronisation in order to give significance to the measure of causality.
- The causal metric is not parameter free and it thus requires an optimisation stage to tune its internal variables. A cross-validation stage is employed during the analysis of the metric as part of the classic maximum-likelihood scheme of the Analogues-RBF method.

Therefore, supported by the previous discussion and synthetic analysis, the Analogues-RBF Granger metric is employed for the analysis of real neurophysiological patients data in Chapter 6.

5

Univariate Synchronisation in Anomalous Brain Activity

In these last two chapters, functional connectivity is investigated experimentally using real patient data: an MEG dataset related to Parkinson's disorder and the intracranial EEG datasets on the epilepsy disease are presented. The main aim of this analysis is to provide some methodological examples to support the approaches of signal processing described previously, to show their practical usages and discuss their problems on real data. It is not the main purpose of this thesis to provide new results for the understanding of these disorders nor to provide specific clinical directions of these pathologies for the subjects whose data were collected. Therefore, these last chapters should be considered as a pilot study from which further and more detailed analysis is left for future examinations.

The two datasets presented in this thesis offer, other than two typical pathological challenging disorders, two types of functional connectivity problems. For the MEG dataset, the methods of feature extraction need to address the problem of finding the pathological functional connectivity from a structural point of view: *What is the difference between the groups of subjects in terms of network analysis.* With epilepsy, instead, the dynamical side of the functional connectivity is explored: *How does the spatiotemporal evolution of the epileptic activity develop?*

This chapter address the problem of local synchronisation using the single channel metric developed in Chapter 3. In Section 5.1, the detail of the data preprocessing is considered. In Section 5.2 the result of the MEG and iEEG analysis are reported. Finally, in Section 6.2 some final consideration about this analysis are drawn.

5.1 Preprocessing

The data processing for all the material in this chapter is applied to broadband signals to reduce the complexity of the analysis. Different frequency bands, as reported in the literature [106], may be associated to distinguishing characteristics of the underlying brain mechanisms. Future and more specific investigation in narrowband signals may be needed to consider in more detail these neurological disorders and to understand better their pathological origins as performed. For instance [14] studies bands in the range of 0.5 – 4Hz (delta), 4 – 8Hz (theta), 8 – 10Hz (low alpha), 10 – 13Hz (high alpha), 13 – 30Hz (beta) and 30 – 48Hz (gamma). The choice of working with broadband signals has shown to be sufficient to bring about the arguments of the thesis and display the practical use of the previous methods.

Therefore, the data in both datasets is filtered between 0.5 – 48Hz using a digital Butterworth filter implemented in Matlab. This choice is derived from the low-pass and high pass limits of the previous MEG study in [14]: the low-pass limit at 0.5Hz is chosen to avoid any problem with the DC levels while components outside the high-pass limit are assumed to be negligible from a neurophysiological perspective to the following investigation. The same applies to the epilepsy data where the high-pass limit avoids the problem of including the effect of the power line at 50Hz (usually a notch filter needs to be implemented if a larger band is considered). In the MEG dataset, the power line was not present in the available time series (pre-filtered by an external expert).

The iEEG was successively under-sampled at $\tau_s = 256\text{Hz}$ from $\tau_s = 512\text{Hz}$. This step is necessary in order to avoid the embedding windows of SSA becoming excessively large due to the strong correlation of the time samples. This effect can be deduced from the bound in Equation 3.8: with the same frequency of interest, the increase of the sampling rate results in an increase of the embedding window. The MEG dataset has a sampling rate of 312Hz which was considered a reasonable value and kept during the analysis (the previous work in [14] analysed the data at this frequency).

5.2 Data analysis

5.2.1 MEG Data

The complexity index $C_eM(\lambda)$ is computed in each of the time series of the datasets. The technical consideration about the tuning of this index and thus the choice of the parameters of SSA is given as follows:

- The value of $\lambda = 0$ is considered. This parameter is not relevant if the observational model of the noise is assumed to be Gaussian distributed as explained in Chapter 3. Changes due to SNR do not influence the C_eM with this hypothesis.
- The segment size L in this study is given by the whole time series length, i.e. 1562 point samples.
- As suggested in Chapter 3, τ_w can be computed using Equation 3.8. Following this bound, since the analysis is performed in broadband, the maximum value of the window length with the minimum frequency of interest available is $\tau_w = 312/0.5 = 512$. This value accounts for all the frequencies above the low-pass filter limit 0.5Hz. However the choice of this embedding may be too large and not

necessary. As discussed in Chapter 3, the larger the windows the more correlated the embedding space and the less the degree of statistical confidence (τ_w/L) is. Considering that important phenomena can happen in the delta band (4 – 8Hz), an initial pragmatic choice of $\tau_w = 150$ is taken which accounts for a frequency of interest roughly in the middle of this band. At the end of this section, this initial choice is further investigated.

Global channels distribution

Figure 5.1 shows the distributions of the complexity measures computed for each group of patients in all the channels available: each histogram is therefore based on 322×141 values of C_{eM} . The statistics of these distributions are summarised in Table 5.1. The distributions are not Gaussian by a visual inspection of Figure 5.1 and by the values of their kurtosis and skewness. Therefore, in Table 5.1 and during this section, the median of these distributions are considered as reported in Table 5.1, since it is less affected by artefact and outliers and is a better indication of their central tendency than the mean.

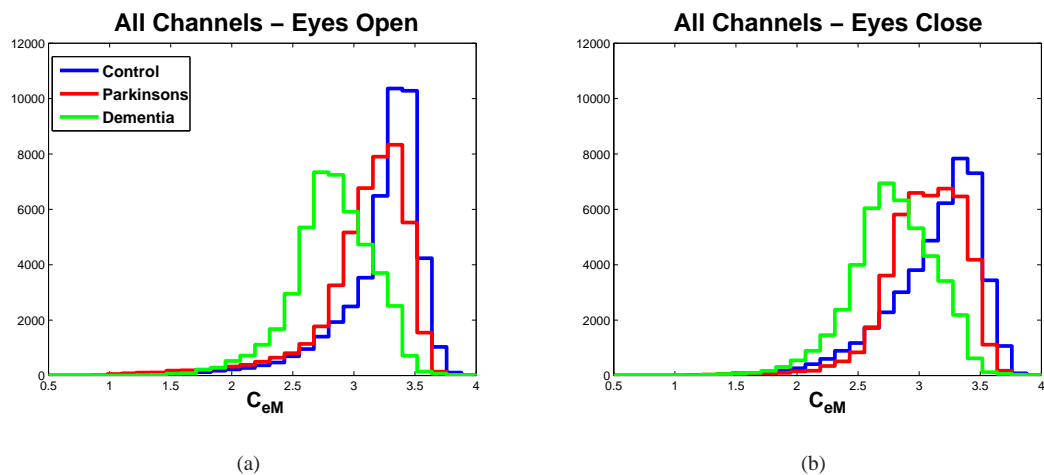


Figure 5.1: Distribution of the single channel synchronisation index for different eyes conditions and for all the MEG sensors. The most relevant point to mention is the drop of the median value of the complexity of these distribution consistent with the different type of the disorder.

Statistics	Eyes Open			Eyes Closed		
	C	PD	PDD	C	PD	PDD
Mean	3.2108	3.0214	2.7617	3.0676	2.9937	2.7217
Standard deviation	0.3589	0.3902	0.3293	0.3793	0.3199	0.3430
Median	3.2532	3.1072	2.7711	3.1601	3.0204	2.7268
Kurtosis	7.4513	7.9904	3.9624	4.6558	6.2176	4.0234
Skewness	-1.8584	-1.9243	-0.5753	-1.1782	-1.1738	-0.5254

Table 5.1: Summary of some statistics relative to the distribution of the complexity measures as shown in Figure 5.1, in each group of patients and in the case of all channels.

The results obtained by the single channel analysis shows interesting points of the connectivity of the

groups at a local level. Firstly, there is a clear drop of the complexity index (or an increase of the local synchronisation as discussed in Chapter 3) between the groups. This drop in C_{eM} is consistent with the different kind of disorders (Dementia < Parkinson's < Control) as pointed out in the literature [138]. This may be the indication that for patients affected by Parkinson's and Dementia disorders, the effective connectivity becomes more synchronous and therefore overly stationary, reducing the cognitive flexibility of the underlying dynamical process [138].

Secondly, as depicted in Figure 5.2 and Table 5.1, another issue to mention is the drop of the median and mean values of the distribution of C_{eM} from the eyes open to the eyes closed conditions. The difference in the eyes conditions is consistent with the literature with a well known result where differences of EM signal characteristics between the eyes open/closed have been the topic of numerous research studies dating back to the early EEG recordings. During eyes open, the visual stimuli entering the brain, have the effect of desynchronizing the activity of a complex brain network. Since the alpha band is usually a relevant component in the power spectrum of the electromagnetic signals [106], it is possible to argue that this effect may be noticeable in broadband, as well.

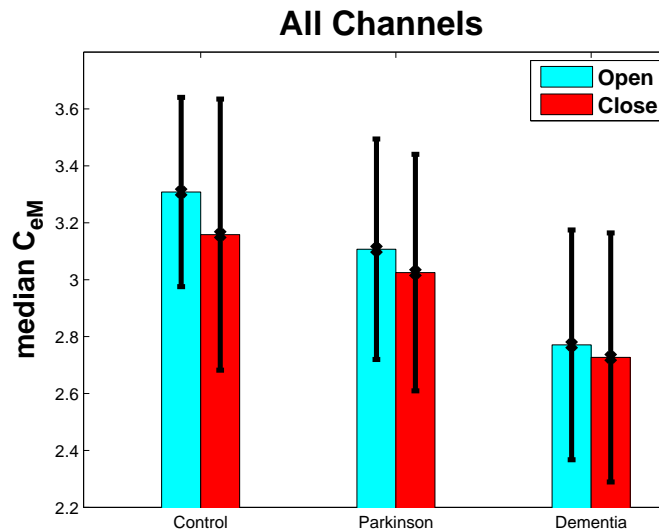


Figure 5.2: Median values and the 25th and 75th percentiles (errorbars) of C_{eM} of the distributions in Figure 5.1 for different eyes conditions. Notice the difference between eyes closed and eyes open is more predominant for the control subjects.

A final remark of this subsection is that the difference between the two eyes conditions seem more evident in the case of control subjects, after a numerical inspection of Table 5.1. This effect can also be noticed in Figure 5.2 where the median and the 25th and 75th percentiles (error bars) of C_{eM} are displayed. A difference between eyes closed and eyes open in the case of the control patients is clearly visible compared to Parkinson's and dementia. These results are significant using the Wilcoxon rank-sum test ($p < 0.001$).

Analysis in different brain areas

Figure 5.3 shows the analysis of single channel synchronisation for different areas of the brain. The areas are partitioned as in Figure 2.6. Figure 5.3 plots the median and the 25th and 75th percentiles statistics of

the distribution of C_{eM} in each of the areas in the same manner as Figure 5.2. The following Table 5.2 summarizes the median of these distributions and indicates the values that are not significant using the Wilcoxon rank-sum test

Task	Eyes Open			Eyes Closed		
	C	PD	PDD	C	PD	PDD
LT	3.1813	3.0102	2.6960	3.0762	2.9138	2.6467
LF	3.1715	3.1457	2.7543‡	3.1301	3.1646	2.7273‡
LC	3.3244	3.2185	2.8302	3.2921	3.1608	2.7823
LP	3.2954	3.0863	2.6809	3.1191	2.8901	2.6397
LO	3.2323	3.0430	2.7377	3.0251	2.8098	2.6697
RT	3.2127	3.0086	2.7110	3.1106	2.9228	2.6603
RF	3.2211	3.1684	2.8479†	3.1927*	3.2024*	2.8499†
RC	3.3251	3.1955	2.8785	3.2973	3.1563	2.8609
RP	3.2948	3.0553	2.7139	3.1132	2.8707	2.6680
RO	3.2525	3.0135	2.7433	2.9925	2.8131	2.7137

Table 5.2: Comparison of the median for the distribution of complexity measures in each group of patients in the case of the selected areas. Some results are not significant using the Wilcoxon rank-sum test: * not significant between control and Parkinson's subjects with eyes closed; † not significant between eyes closed and eyes open for dementia patients; ‡ not significant between eyes closed and eyes open for dementia patients.

These results show a clear decrease of the C_{eM} (Dementia < Parkinson's < Control) for the regions at the back of the head. In the frontal lobe this phenomenon is not so evident as shown in Figure 5.3 where the complexity is higher in Parkinson's than control subjects. In this area, moreover, the complexity of eyes closed for Parkinson's is in general slightly higher than in the eyes open. Since the frontal lobe is not situated above the location of the visual cortex (Occipital and Parietal areas) the difference between the eyes conditions are probably not physiologically significant. In fact, Figure 5.3 shows that the channels on the back of the head have a stronger difference between eyes closed and eyes open, i.e. they are sensitive to the visual stimuli.

Loss of reactivity

Interestingly, as mentioned previously for the global channel distribution, the control subjects show a bigger difference between eyes closed and open for the sensors at the back of the head in Figure 5.3. In this latter figure, this difference is also displayed by the Parkinson's patients. This phenomenon is consistent with some results in the literature (discussed in [14]) where dementia patients do not have a substantial difference between eyes open/close conditions. In [14], the power in the α band was not decreased for dementia patients between the two eyes conditions, in contrast to the other two groups. These particular results were interpreted as *a loss of dynamical brain reactivity*, which is a phenomenon that can also link to patients suffering Alzheimer's disease.

Figure 5.4 shows explicitly the plots of the distributions of C_{eM} for different group and eyes conditions

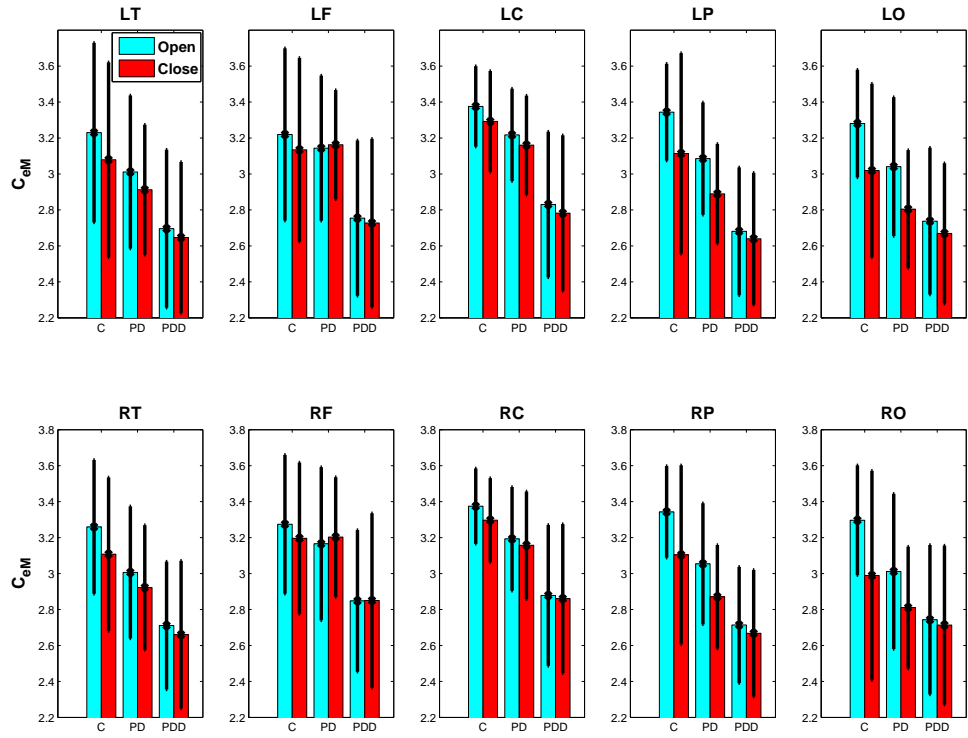


Figure 5.3: Mean value of the distributions of C_{eM} in different regions of the MEG sensor space. (R)ight and (L)eft hemisphere. (T)emporal, (F)rontal, (C)entral, (P)arietal and (O)ccipital lobes. The errorbars are the 25th and 75th percentiles of the C_{eM} .

in the case of the parietal and the occipital areas. In this picture, it is possible to see clearly that there is not much visible difference in the distribution of dementia patients which may suggest the occurrence of the loss in reactivity phenomena.

Window length revisited

In Figure 5.5, the analysis of the index C_{eM} is performed as a function of the window length in order to check the correctness of its initial value, i.e. $\tau_w = 150$. Figure 5.5 shows the median of the distributions as in Figure 5.1 as a function of the window length in the case of eyes closed only (for the eyes open the same conclusion were found).

Firstly, it is possible to notice that the distances and thus the discrimination between groups remain stable for increasing values of the window length, i.e. for the values of $\tau_w \gtrsim 40$. In practice, this means that the discrimination between groups is not sensitive for a sufficiently high value of τ_w . τ_w can actually be reduced without compromising much the discrimination power but increasing the computational speed by reducing the size of the trajectory matrix. Secondly, the curves do not level-off to an horizontal asymptote. As discussed in Chapter 3 this indicates that the MEG signals contain either random components and/or are formed from an aggregate of many complex subsignals. Both situations are possible here: MEG channels are affected by external noise and the electromagnetic sensors are placed at the scalp level and thus are sensitive to the brain activity coming from a large neural region.

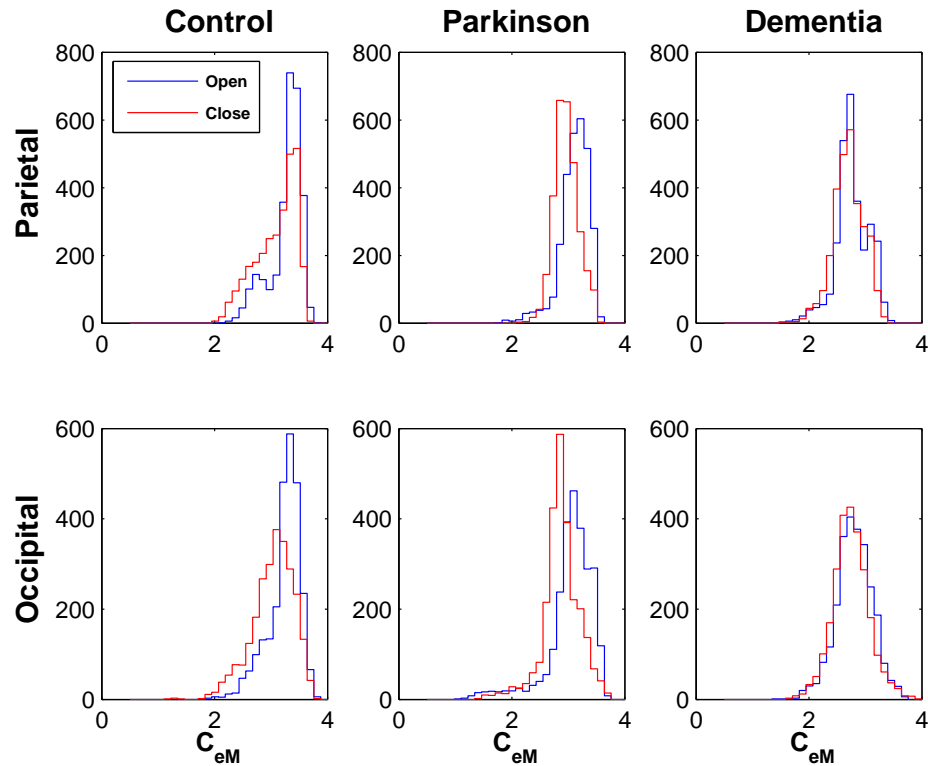


Figure 5.4: Distributions of C_{eM} in the case of the frontal and occipital lobes. A loss of dynamical brain reactivity for the dementia patients is shown as displayed by the no difference in eyes open/close paradigms.

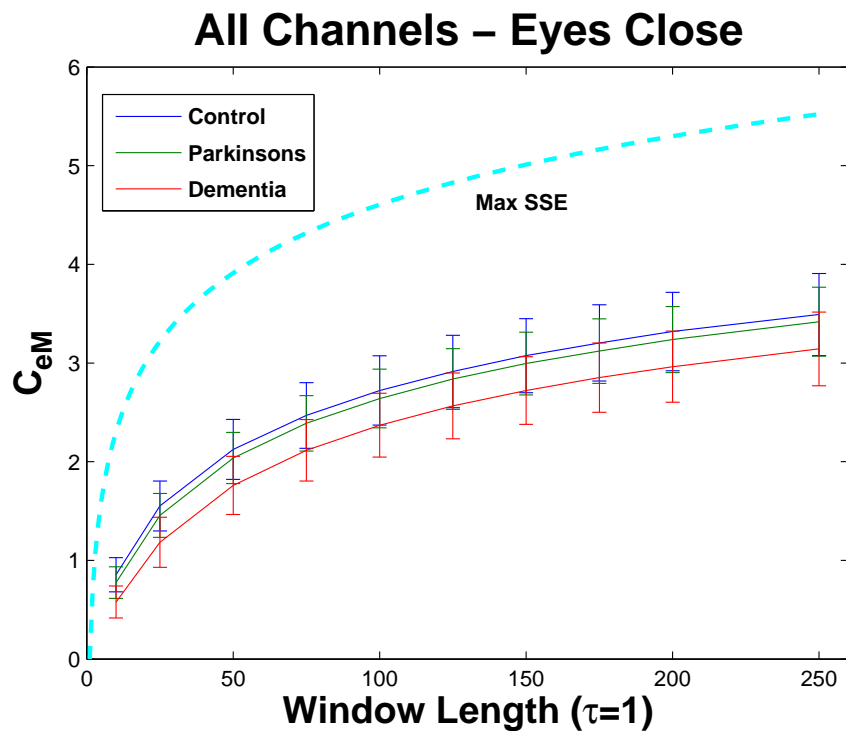


Figure 5.5: The median of the complexity of the global C_{eM} as a function of the window length τ_w . The discrimination between subjects is not sensitive to values of the window length sufficiently big, i.e. $\tau_w \gtrsim 40$.

5.2.2 Intracranial EEG dataset A

The analysis of this epileptic dataset starts by investigating the complexity index $C_{eM}(\lambda)$ using a moving window approach. The following initial points are considered:

- As before, the regularisation parameter is set to $\lambda = 0$ since the assumption of the gaussianity of the observational noise is considered.
- Unlike the previous dataset, the iEEG recording needs to be segmented into overlapping quasi-stationary segments in order to study the dynamics of the seizure over time. The length of the segment size is a difficult parameter to choose since there is not a straightforward procedure to infer it from the data. A pragmatic choice needs to be taken. As discussed in Section 3.4, from a data analysis perspective, it is necessary to choose a trade-off between computing resources, temporal resolution and statistical significance. From a neurophysiological perspective, time scales of 1sec have been considered as the minimum quasi-stationary segments of brain state [83]. In [33] this extreme choice was used but only together with a multi trial procedure of averaging in order to be able to gain sufficient temporal resolution and statistical significance that is not the situation in the datasets used in this thesis since a unique event is considered. Therefore, different values of L between 2s and 6s were tried. As discussed in [146; 49] and from our personal investigation, the choice of L influences the smoothness of the complexity index and the qualitative results achieved in this section are shown not to be particularly affected by this choice. A length $L = 3s$ (750 time samples) with a step size between subsequent segments set to 64 time samples is chosen for the sliding windows in the following experiments.
- τ_w can be computed using the bound in Eq. 3.8. Since the analysis is broadband, $\tau_w = 120$ is considered consistent with the centre of the lowest band of interest of 2Hz (delta) as in the previous section. As shown for a bigger dataset in the previous MEG analysis, the choice of this parameter is not particularly sensitive to the feature extraction capabilities of the index C_{eM} in broadband.
- Prior to the analysis, the data is further pre-processed using a Hamming window to each segment. This operation avoids fringe effects at the edge of the windows and helps to give more importance at the centre of each segment during a sliding window analysis [146].

In Figure 5.6, a complete view of the analysis of C_{eM} is shown over all $N_c = 39$ channels. As explained in chapter 2 a channel was left out of the analysis due to the bad quality of the signal (channel 3 which is not displayed). In the upper graph the value of C_{eM} for each channel is plotted using a colour scale against time. The first important detail which can be seen is the variation of the C_{eM} values in some channels before the moment indicated by an expert as the start of some noticeable changes in the iEEG trace ($\approx 40s$ before). Most importantly these channels are consistent with the area where the focal point is supposedly situated (expert decision), i.e. parietal lobe. In the second, third and fourth rows of Figure 5.6 the C_{eM} , the power and time series of the channel 18 in the parietal lobe are plotted. This particular channel has shown the most interesting variation of the C_{eM} index before the occurrence of the seizure among all the iEEG grid.

Channel 18 – Parietal Lobe

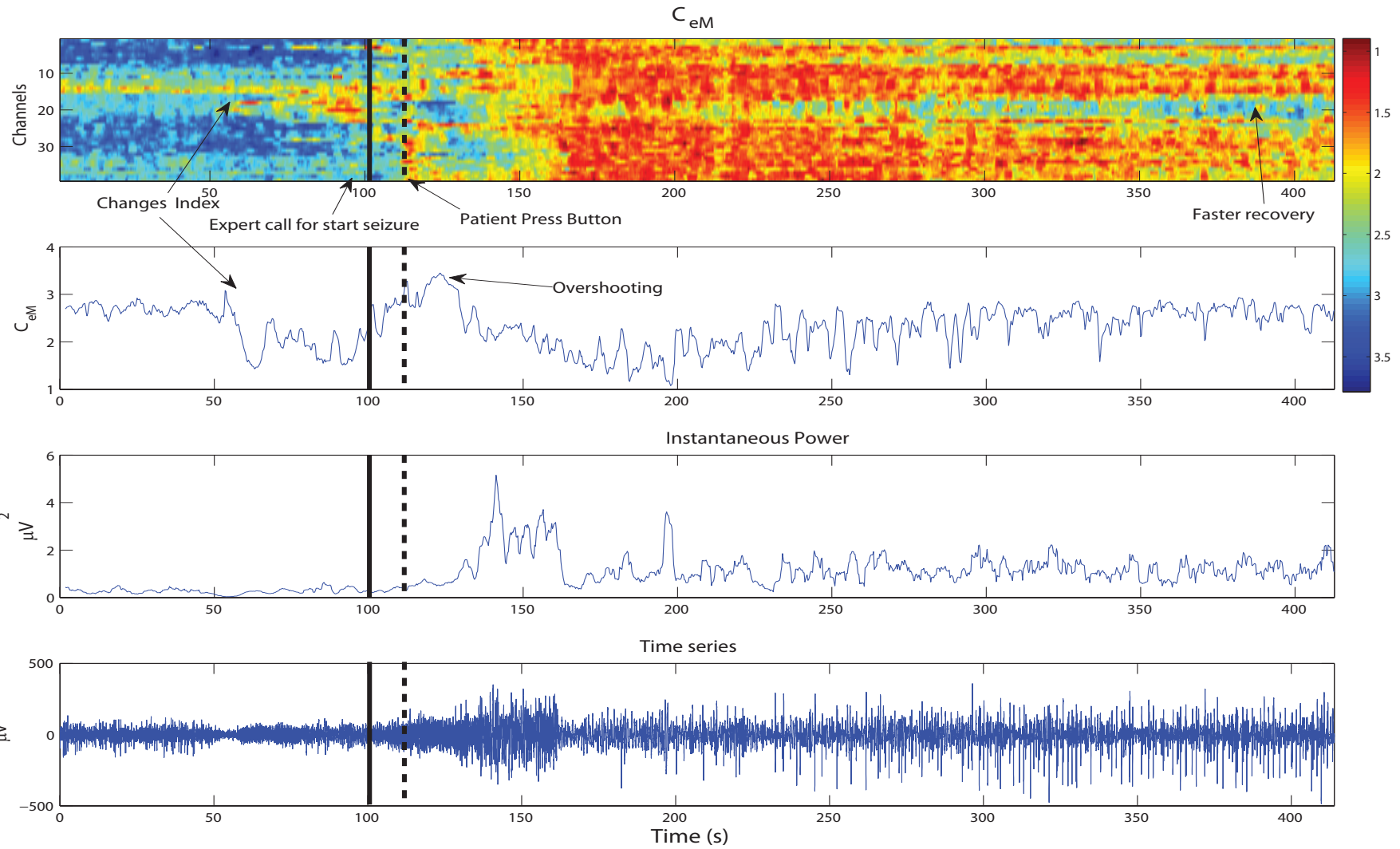


Figure 5.6: Plot of singular spectrum entropy for the dataset A. The first plot shows with a colour scale the behaviour of the C_e index over the time during the epileptic iEEG trace. In the second plot is shown the C_e for the channel 18. This channel is considered because it shows an early change in the C_e pattern. The third plot shows the power of the signal in the channel 18 which is not correlated to the C_e pattern. In the fourth plot the time series of the channel 18 is shown

In the second plot, the drop of the spectral entropy before the seizure may indicate a reduction of complexity and a possible increase of synchronisation which is indicative of epileptic activity. This variation, from a visual inspection seems not to correlate with the power of the signal which remains constant before the seizure starts. Firstly, this point is important since *it indicates the complexity carries a different piece of information than the simple power*. This fact will be emphasized during the following investigation. Secondly, since power and C_{eM} are not correlated, it is possible to argue that this drop is due to a genuine change of the underlying synchronisation and is not affected by SNR variations.

During the seizure, after the expert noticed the pathology in the iEEG trace, there is an increase (overshooting) of the C_{eM} , a subsequent decrease and finally an increase of the complexity of the signal. The overshooting of the SSE is visible only on the few channels in the parietal lobe which may be a characteristic feature of this patient seizure. No particular explanation is offered by this behaviour which needs further investigations. In the same channels, a faster recovery is noticed from the ictal to the interictal level of complexity than is visible in the other channels. This phenomenon may be associated to the resetting of the state of the brain after the epileptic event. The fact that this faster recovery is situated in the location where the complexity first dropped, gives the confirmation that this particular area may have been involved in the epileptic event.

Other channels in the grid are considered in Figure 5.7 for a comparison. The drop of complexity in some channels has a time delay with respect to the channel 18. This reduction occurs after the expert noticed a change in the iEEG trace but before the power of the signal increases due to the ictal brain state. During the ictal period the complexity becomes low all over the grid which may indicate an increase of synchronisation.

Figure 5.8 shows the mean of the C_{eM} and the power across the grid channels. The first interesting detail in these plots is the clear segmentation of the different zones of interest of the seizure captured by the complexity measure. It is possible to notice a pre-seizure period in the first 50s of the iEEG trace where the complexity is stable. The second part of the seizure starts after 50s which is followed by an overall drop of the complexity. In the third part of the trace the complexity rises again. This phenomenon of synchronisation-desynchronisation is consistent with the typical spatiotemporal properties of seizure [134]. The second remarkable detail in these plots consists in the qualitative difference between the power of the signal and the complexity indices. This indicates and supports the difference in the information content captured by the power with respect to the complexity. In fact, the power changes its baseline behaviour following the epileptic electromagnetic discharge only after the expert noticed the iEEG changes.

Grid display

We consider the problem of visualizing this index on the grid to better define the spatial extent of the seizure. During the analysis of this particular dataset, the first plot in Figure 5.6 is normalized against a baseline period. Figure 5.8 shows 50s of interictal pre-seizure period which can be used as a baseline. The baseline captures a time period where the brain activity is in theory normal, not pathological and without any significant variations of the indices. In practice, in an epileptic patient, the EM trace should never be

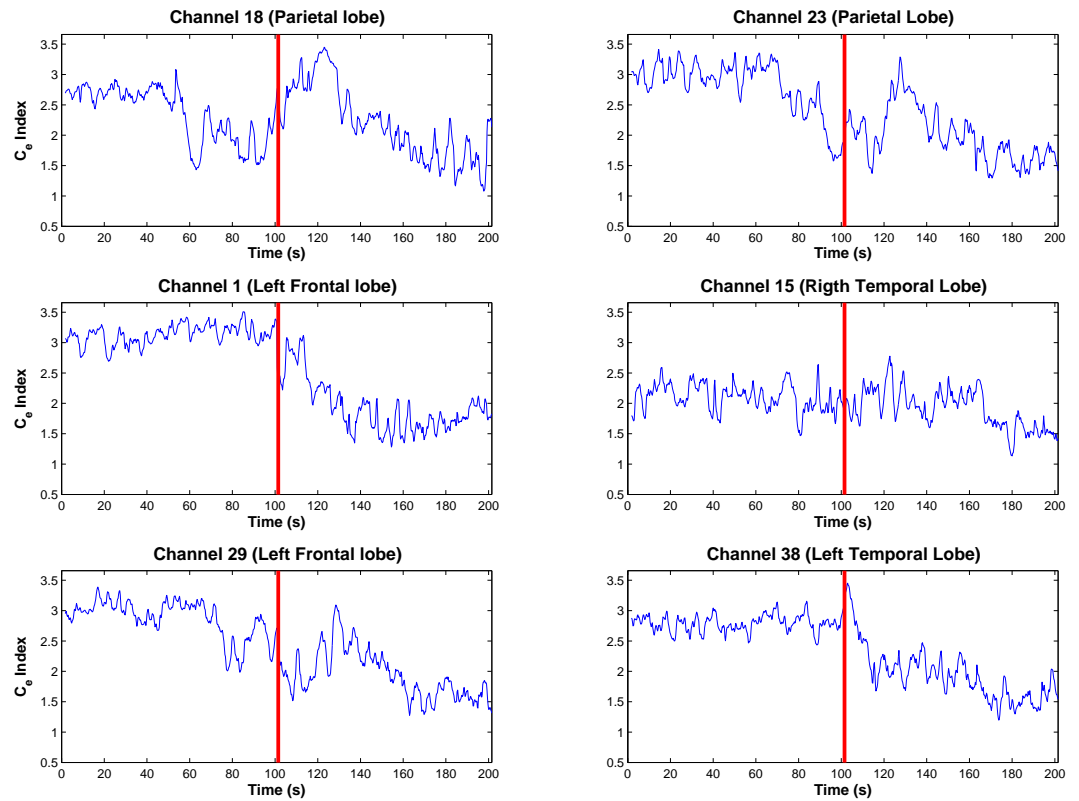


Figure 5.7: This figure shows a snapshot of C_{eM} computed in some channels of the iEEG grid. The plots consider the first part of the seizure (beginning 800 segments). The red line indicates the moment where the expert notices a change on the EM trace. It is possible to notice different time scales of the drop of C_{eM} in other parts of the grid compared to the channel 18.

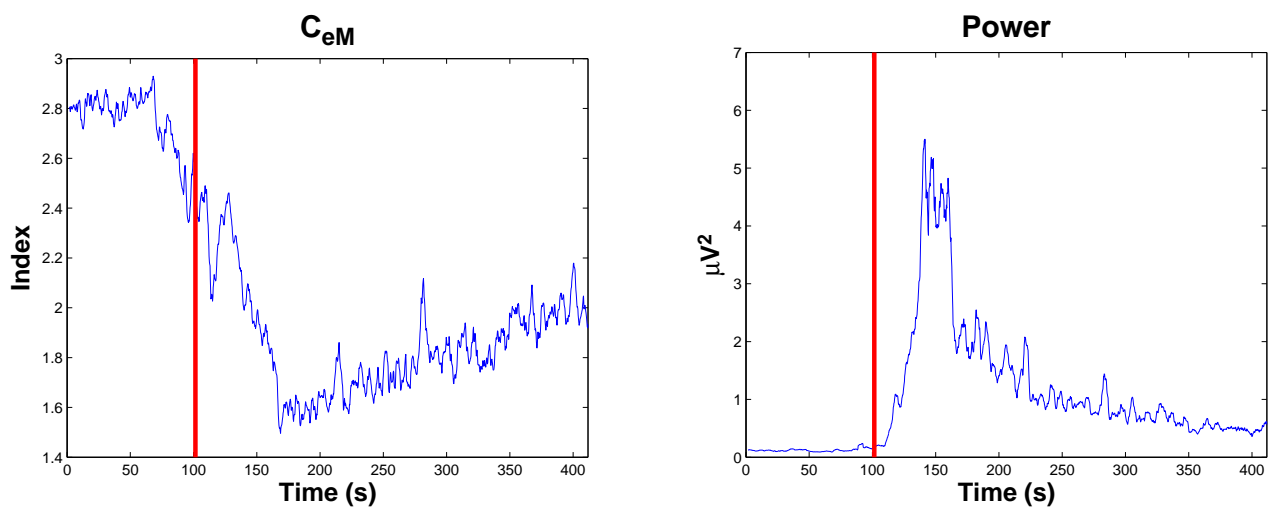


Figure 5.8: Average across channels of the indices C_{eM} in the left and the signal power in the right. The red line indicates the moment in the trace where the expert notices visually some changes in the time series. This plot emphasizes the temporal segmentation of the seizure in three sections: interictal, ictal, postictal. It emphasizes also the different information content of the power with respect to the complexity.

considered not pathological and a sensible choice of baseline needs to be found during the interictal period prior to the seizure. In this experiment, the chosen baseline is supported by the segmentation of the trace in Figure 5.8. Therefore, in order to compare the variation of the indices among different channels, the data is normalized against this period. The main goal is to be able to emphasize the channels where the activity starts to manifest before the others (changing-point problem) and the variation of the index is more evident. The following *Z-score statistic* is applied to each channel

$$Z = \frac{C_{eM} - \hat{\mu}_C}{\hat{\sigma}_C}, \quad (5.1)$$

where $\hat{\mu}_C$ and $\hat{\sigma}_C$ are the estimated mean and standard deviation of the complexity index C_{eM} computed in each channel over the baseline period. Figure 5.9 shows the result of this normalisation procedure where a Gaussian spatial filter is further applied to smooth the edges between channel values for a better visualisation.

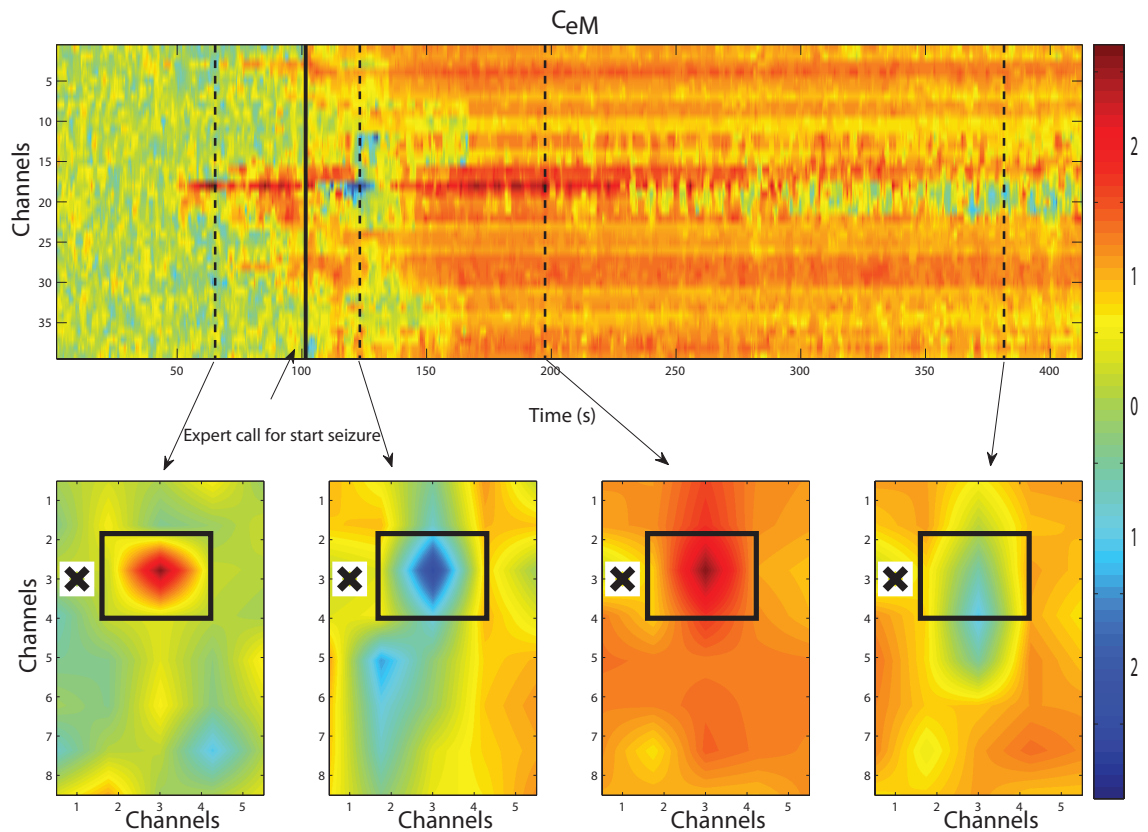


Figure 5.9: Normalized plot of the C_{eM} using a Z-score statistic with selected snapshots of the grid at different times. The source of the pathological activity is clearly emphasized in the top middle of the grid by the rectangular square. The cross indicates the position of the channel not used in the analysis since the signal was too noisy.

From Figure 5.9, it is possible to observe how the Z-score normalisation and the choice of the parameter λ offers a clearer view of the points of interest of the complexity trace. In the second row of the same figure, snapshots of the spatial value of the Z-score on the iEEG grid are shown. Figure 5.9 shows the localized changes of activity for the channels in the parietal lobe where the focus is situated. In this plot, an x on top of the channel is inserted in the grid which has not been analysed due to the poor signal quality and it is not part of the channel numbering.

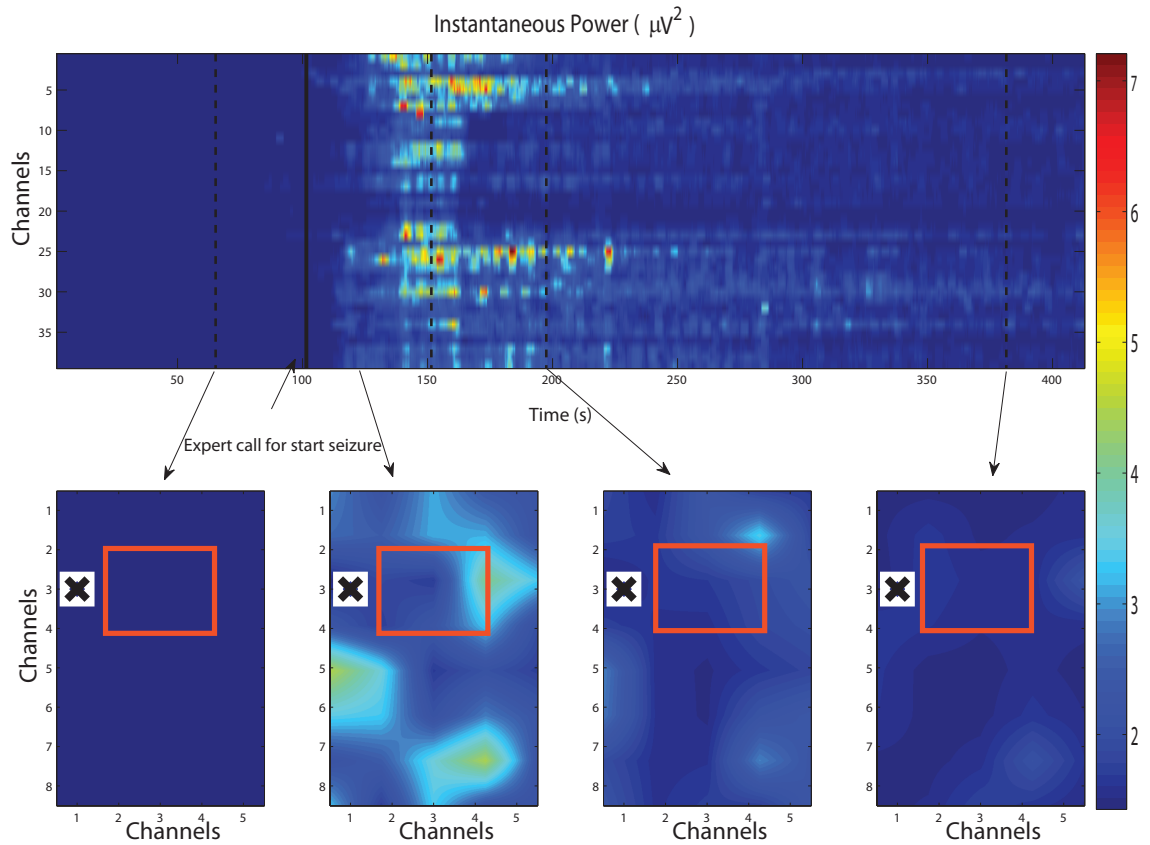


Figure 5.10: Plot of the normalized power similar to Figure 5.9. The power embodies a different view on the dynamic of the seizure and it does not show clearly the changing points as well as the complexity index.

To conclude this section the normalized plot of the power is shown in Figure 5.10. As from its time series, the power seems to contain different information than C_{eM} . It is difficult to visually deduce any useful characteristic from both the top plot and its correspondent grid plots.

5.2.3 Intracranial EEG dataset B

The analysis of local synchronisation for this intracranial EEG dataset is performed following the same initial consideration of the previous example: the complexity index $C_{eM}(\lambda)$ is considered with $\lambda = 0$ and is computed over the time using a sliding overlapping window containing $L = 750$ points with 64 points interspaced. The result of this analysis is shown in Figure 5.11. In the first colourplot, the C_{eM} is displayed for all the channels over time in the same manner as in the previous dataset. From a visual inspection it is possible to notice that some of the channels have a complexity generally lower than the rest (red spot in the colourplot) with some quick spiky events (blue colour). This characteristic is shown more clearly, for instance, in the plots of C_{eM} and in the signal power of the channel 29. The latter is one of the channels for which the complexity metric contains few noticeable spikes emerging from its mean level. These spikes can be correlated in time with the occurrence of all the short abnormal EEG segments present in the whole dataset. For instance, one of these segments is clearly displayed in Figure 2.5. They are clinically identified as occurrences of epileptic activity. While similar spikes are present in the power signal after a visual inspection, these are not clearly distinguishable as in the case of the complexity index.

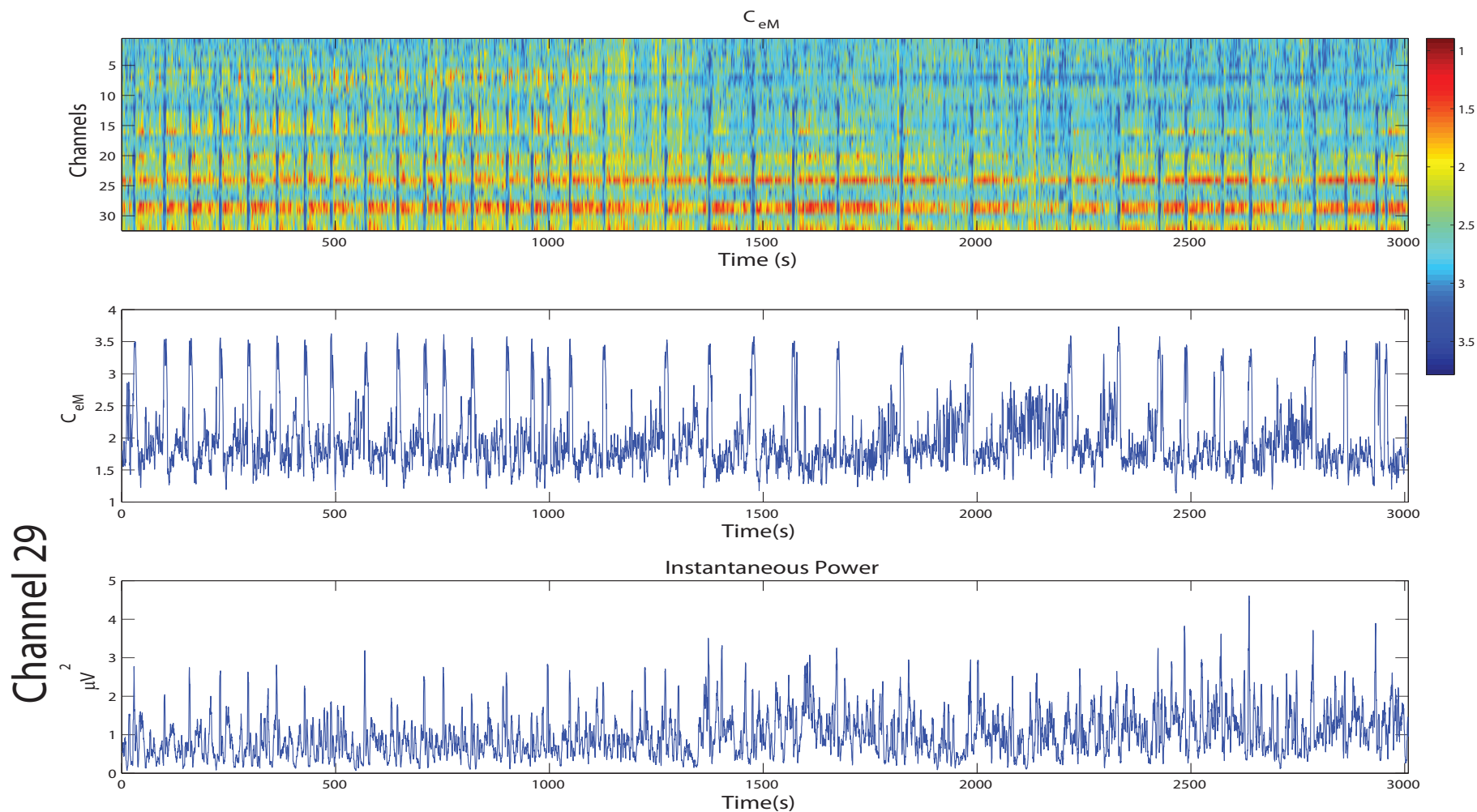


Figure 5.11: Plot of singular spectrum entropy for the dataset B. The first plot shows the image of the overall behaviour of C_{eM} index over the time during the epileptic iEEG trace. Some channels have generally lower complexity (red spots) but with some instantaneous peaks of complexity (blue colour). In the second plot is shown the C_{eM} for the channel 29. This channel is considered because it shows several clear changes in the C_{eM} pattern with respect to the other channels in the grid. The third plot shows the power of the signal in the channel 29. It is difficult to notice from the power visually the peaks presented in C_{eM} .

Figure 5.11 shows that at the onsets of these short seizures, the complexity increases. This phenomenon is counter intuitive since the intrinsic synchronisation should increase during a seizures, i.e. C_{eM} goes down. This characteristic is further investigated using the Rössler lattice within a sliding windows analysis in order to find a possible explanation. Figure 5.12 shows the result of the investigation in the case of two different situations. The red plots refer to the case where during a sliding windows analysis there is an abrupt transition between two regimes: one with 5 clusters ($\varepsilon = 1.1$) and one with 3 clusters ($\varepsilon = 2.5$). The Rössler lattice is simulated by producing a time series of 5000 time points with 2500 taken from the simulated 5 clusters followed by 2500 from the 3 clusters. Observational noise is added to the system as in Chapter 3, i.e. 5% of the standard deviation of the macroaggregate signal $O(t)$. As shown in the diagram in Figure 5.12(b) the sliding windows can be either contained in the zone of regime A or regime B, or can overlap both regions. The red plots, instead, refers to a gradual transition which is imposed during the simulation: the ε is nonstationary and varies between 1.1 to 2.5 in order to produce a time series with the same length as for the blue case, i.e. 5000 time points, but with a gradual varying synchronisation regime. Both red and blue plots are considered also for two situations: $L = 512$ and $L = 1024$ time points.

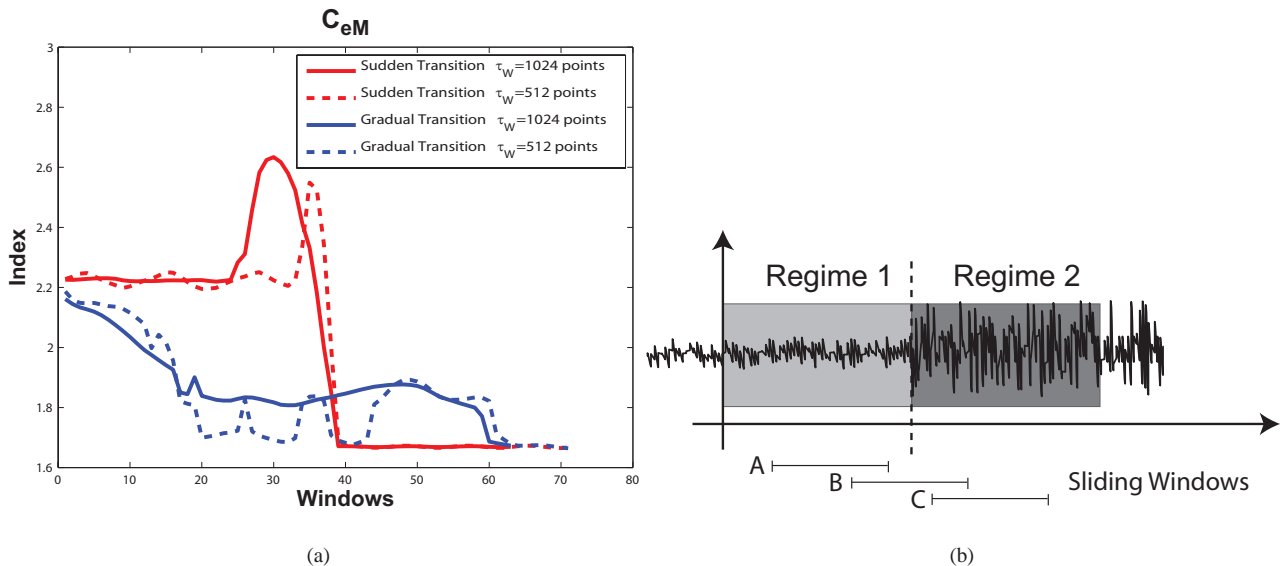


Figure 5.12: The right plot shows the graphical set up of a simulation of a synthetic time series produced by a Rössler lattice having two regimes of synchronisation. A sliding window analysis is performed over this simulation. In the left figure the results show that an abrupt transition can create a spurious peak (see in the text for more explanation).

Figure 5.12(a) shows that the sudden switch between the two dynamical regimes produces a peak in the complexity index C_{eM} while the smooth transition does not. *This peak is in fact a spurious outcome from the algorithm.* When the sliding windows contain the sudden transition, the signal analysed contains two different regimes and thus the C_{eM} algorithm captures a signal which is therefore more complex and nonstationary. Only when the sliding window passes over the transition point does the C_{eM} correctly account for the 3 clusters complexity. The length of the peak depends on the width of sliding window. The red dashed line shows that the peak can in fact be reduced imposing the length L to lower values. At the same time, a lower value has the drawback to produce C_{eM} more dependent on the noise, as shown in Figure 5.12(a). In the case of the blue plots in Figure 5.12(a), no peaks are present but instead a smoother

transition between the two regimes is noticed. Since the system is chaotic, a smooth curve as a function of the coupling parameter could not be found in the latter case which justifies the up and down trend of the simulated complexity index. Therefore, referring back to the epileptic dataset B, it is possible to argue that the behaviour of the complexity index C_{eM} is consistent with the morphology of this particular type of seizure, i.e. an abrupt transition between the ictal and the interictal state as in the red plot of Figure 5.12(a). The dataset A, instead, seems to be more consistent with a gradual transition from the poorly synchronized interictal to the fully synchronize ictal state.

Following the previous considerations, and since many seizures are present in the iEEG recording, this dataset is analyzed by taking an average of the single channel metric around the occurrence of every epileptic event across all the channels. In this way, the average behaviour of the interictal-ictal (region 1-region 2) transition is emphasized. Therefore the following steps are taken into account:

- The time instants of the peaks of C_{eM} for the case of the channel 29, i.e. the channel where the peaks are more distinct, is automatically found.
- A window time of ± 45 s is considered around each of these instants in the recordings. Since the occurrence of these seizure are not regular in time, this value corresponds to the minimum half time interval between two seizures in our dataset.
- The result of these windows is averaged over all the peaks for each channel.

The result of this analysis is shown in Figure 5.13. This figure displays the three stages of the analysis for the epileptic event which matches the simulation in Figure 5.12. The sudden transition between interictal and ictal produces a spurious peak dividing the time before and after the seizure. The width of the peak interval is approximately 6 – 10s. This value accounts roughly to the time of the sliding windows passing over the transition with, i.e. 3s, plus the effect of the averaging.

In Figure 5.13 another two important characteristics need to be mentioned: before the seizure a few channels have a characteristic lower complexity than the others in the grid, i.e. electrodes 24,29 and 28. Secondly, after the seizure, it is possible to notice a general reduction of most of the channels with respect to the moment before, i.e. the interictal state. This reduction, which has a minimum value just after the spurious peak vanished (around 55s in the time scale in Figure 5.13), has a clear increasing trend thereafter. This phenomenon may indicate the tendency of the system to reset its state to the pre-seizure value as discussed in the previous dataset A for the channels around the focus.

Figure 5.14 shows the power computed around the average seizure in the same fashion as Figure 5.13. While there is a clear change of power during the transition from interictal to ictal as indicated by a few distinguishable peaks (the maximum is on the channel 20), the values before and after seem not to carry distinguishable detail as in Figure 5.13. As repeated many times during this chapter, C_{eM} seems to contain a different (and useful) piece of information to the power.

In order to better visualize the location of the epileptic transition interictal-ictal, the index C_{eM} is projected to the respective place in the grid. The plot of C_{eM} is not normalized as did in the previous section. Firstly, there is no need to emphasize the changing point between interictal and ictal (this point is already

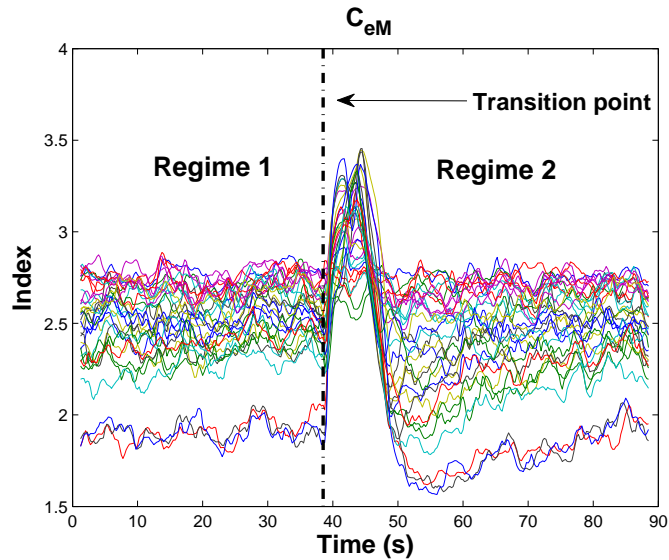


Figure 5.13: Average of the complexity index around each of the 33 seizures of the dataset. The spurious peak divides the interictal (region 1) to the ictal (region 2) state. During the interictal stage a few channels have a clear lower complexity than the others in the grid. During the ictal period and after the spurious peak vanishes, globally, many channels of the grid have lower complexity than during the interictal phase.

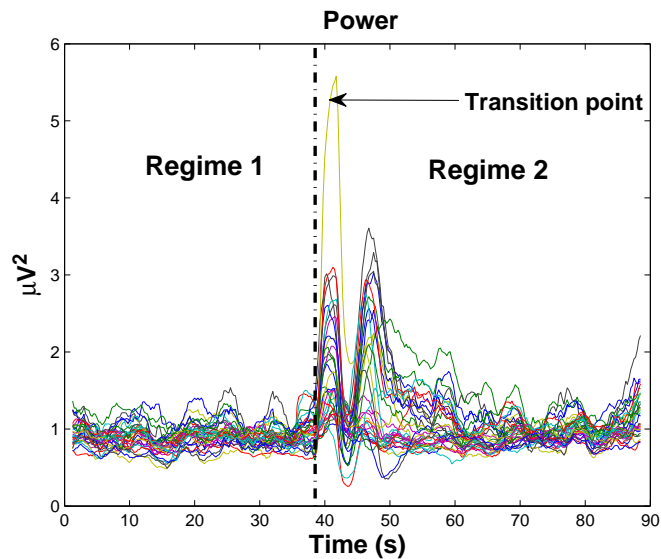


Figure 5.14: Average of the power around each of the 33 seizures of the dataset. The transition interictal-ictal is visible in this plot. During the interictal no channels can be discriminated from the others as in the complexity plot in Figure 5.13.

given by the spurious peak). Secondly, normalizing the values in Figure 5.13 would result in losing the absolute value and thus the difference in complexity value before and after the seizure. Figure 5.15 shows snapshots of the value of C_{eM} in the grid for some time instants selected in Figure 5.13. In the first few images, during regime 1, there are two spots with lower complexity relative to channels 28-29 and 24. Importantly, the region around 20-21 and 28-29 as described in Chapter 2 is considered by experts to be responsible for the seizure. Channel 24, while close to the epileptic region of interest, has not been considered by experts and may be due to this particular recording. Further investigation is needed at this point of the analysis for this channel. During the transition, it is possible to notice that the spurious peak (red spot)

seems to develop in the region close to channels 28-29, i.e. 20-21. This peak is produced by the algorithm and not by a genuine increase of complexity: unfortunately, it may hide some of the interesting dynamics of the C_{eM} . The final images show the reset of the complexity of the grid. This phenomenon is localized in particular, in all regions on the bottom right of the grid. The last image, having a similar pattern to the first one suggests that the pathological activity due to the seizure is going to terminate.

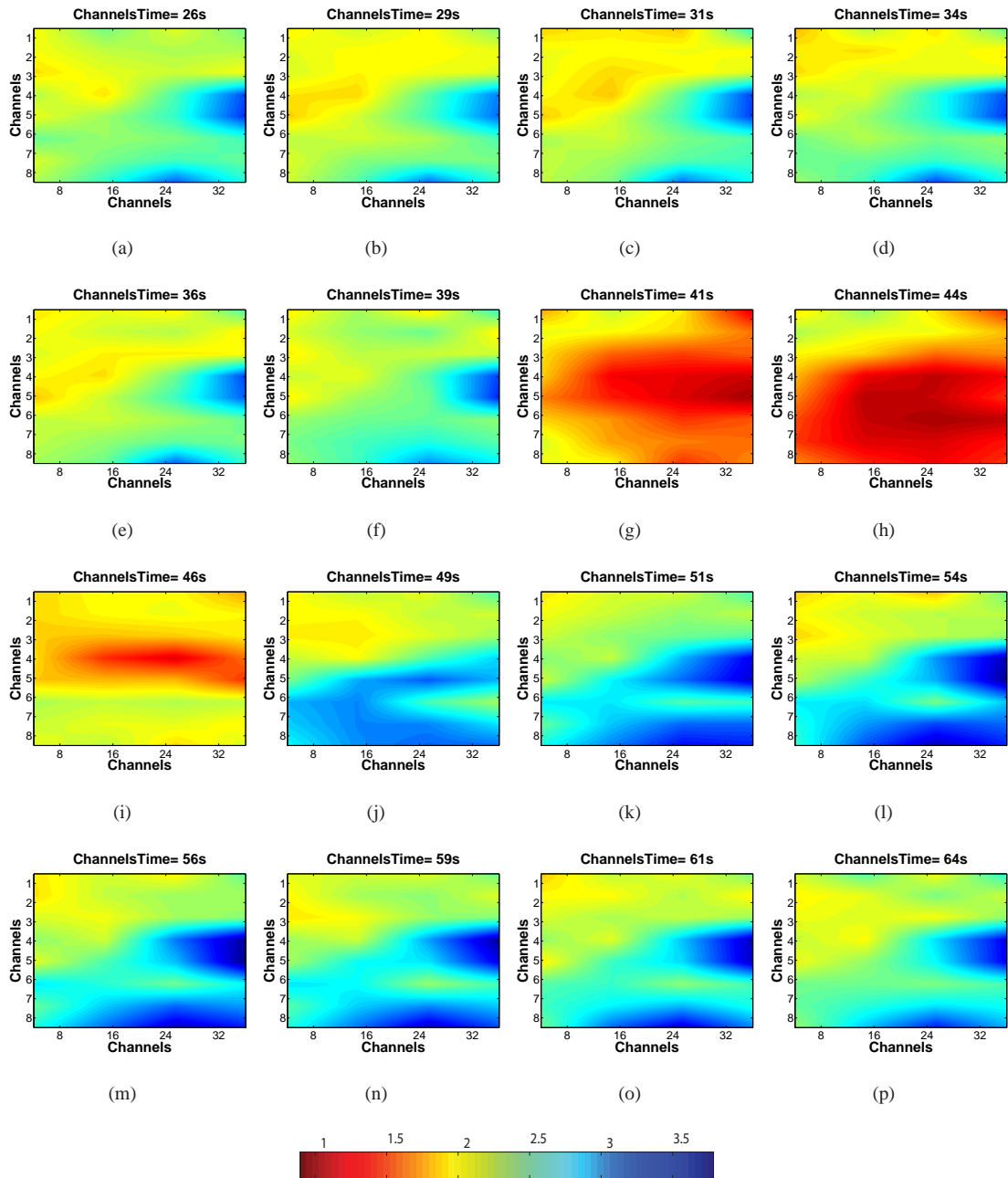


Figure 5.15: Grid of the dataset B during selected time instants from Figure 5.13. Two areas of low complexity are visible in channels 28-29 and 24. During the seizure the appearance of the spurious peak around channels 20-21 is visible. After the transition event the state of the grid resets to the interictal state.

Finally, Figure 5.16 shows the power computed around the average seizure projected on the grid in the same fashion as Figure 5.15. A clear spot is distinguishable in the snapshot in Figure 5.15(g) on the grid in the channel 20 when the seizure initiates.

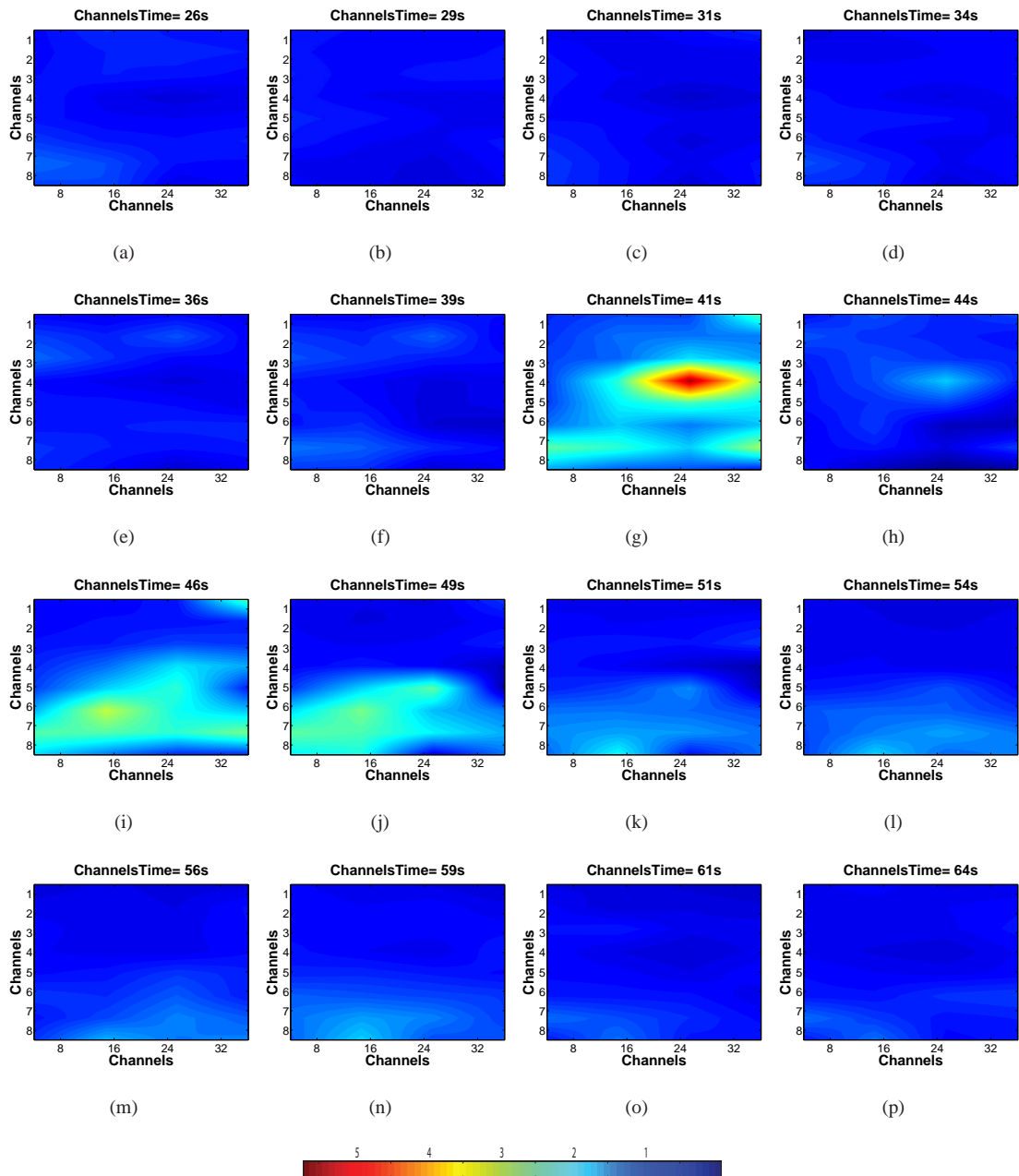


Figure 5.16: Grid of the dataset B during selected time instants from Figure 5.14. The peak in power which can be correlated with the location of the spurious peak in the C_eM plot is clearly visible in (g).

5.3 Summary

The focus of this chapter has been on the analysis of local synchronisation of the MEG and iEEG datasets using the single channel technique developed in Chapter 3. The data processing results have shown to bring about interesting findings in order to explain the underlying functional connectivity of these neurological disorders.

In the MEG dataset, from a data mining perspective, there is a significant difference in functional connectivity among the three groups of subjects. The univariate synchronisation statistic has shown to be straightforward to use and its tuning not particularly sensitive to different choices of its parameters (the

window length τ_w). In particular, the channels at the back of the head (occipital and parietal areas) have shown to be more responsive to this difference using the paradigm eyes open/closed. A future successful applications of data screening should be focused on these channels. In terms of brain understanding, the single channel analysis has shown that there is a decrease of the complexity (increase of synchronisation) at a local level for dementia and Parkinson's patients with respect to the healthy controls. These findings can be correlated to previous research studies in the literature, based on signal power analysis.

In both iEEG datasets, the C_{eM} index was able to detect early epileptic events and their locations which are compatible with the region responsible for the abnormal brain activity as suggested by an expert and by prior neurological analysis. These events could be tracked successfully over the time by the single channel metric, displaying spatiotemporal characteristics typical of the epilepsy disorder. The only problem mentioned during the analysis of the dataset B is due to the sudden transition between interictal-ictal regimes which may result in spurious peaks of complexity. While this problem needs to be sorted in future theoretical developments, the methodology of analysis described in this chapter was able, nevertheless, to detect interesting features of the dynamics of the epilepsy in the second dataset.

To conclude, the single channel metric C_{eM} , after proving its strength over a synthetic dataset, has shown to produce useful experimental results in this chapter. This approach can be therefore used in following and more detailed analysis of neuroscientific problems. In the next chapter, the investigation of these datasets is applied to the multivariate functional connectivity analysis.

6

Bivariate Functional Connectivity in Anomalous Brain Activity

This chapter concludes the experimental part of this thesis addressing and discussing problems of functional connectivity applied to the EM datasets for medium to large scale interactions. In particular, the following two topics are considered here:

- The main purpose of Section 6.1 is to provide a demonstration of the multivariate functional connectivity in the case of the epilepsy data and experimentally support the Analogues-RBF Granger causality metric described in Chapter 4.
- As a preliminary data analysis, Section 6.2 presents some experimental analysis addressed to the problem of volume conduction which typically affects electromagnetic techniques. This part of the thesis is briefly considered as an open problem and for future investigations. The analysis is performed on the MEG dataset.

As remarked in the previous chapter, the clinical examination of the pathological datasets in this part of the thesis is qualitative. It is not the main purpose of this thesis to supply new knowledge for the understanding of these disorders but rather to provide methodological examples for the analytical tools developed.

6.1 Multivariate functional connectivity analysis

Figure 6.1 reports the scheme of this thesis experimental data analysis framework. The focus of this thesis has been the three early stages of exploratory analysis of EM signals. After successfully investigating the coupling of the underlying brain network at a local level in the previous chapter, the framework in Figure 6.1 is completed by two stages of multivariate connectivity analysis. These stages are designed to extract medium to long range neural interaction: a block for the estimation of synchronisation (temporal symmetric relationship) followed by one for causality (temporal asymmetric relationship).

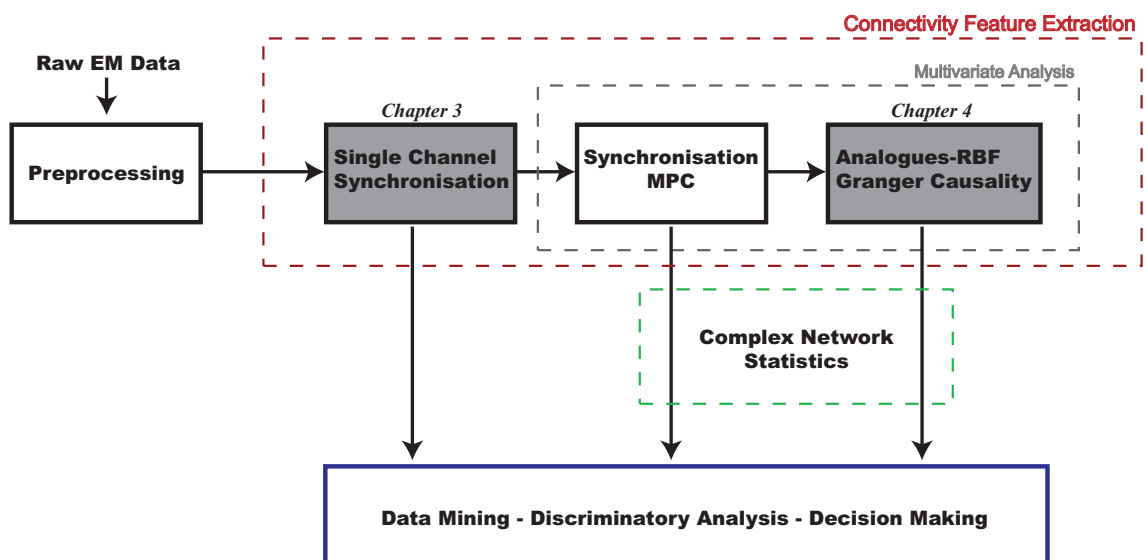


Figure 6.1: Conceptual structure of the data analysis protocol presented in this thesis. The shaded blocks describes the topics discussed in this thesis in Chapter 3 and Chapter 4. Further stages are considered as possible future developments (see text).

The stages of single channel synchronisation and causality estimation are shaded (red) in Figure 6.1 in order to underline the theoretical part of this thesis as reported in Chapter 3 and Chapter 4. Computing the synchronisation between electrodes, using the MPC index (described in Appendix A), is the intermediate stage of the framework in Figure 6.1. This stage is included in this thesis analysis for the following two reasons:

- Firstly, a measure of phase synchronisation such as the MPC, being symmetric and without many internal parameters to tune, can be considered as a reasonable choice for an early exploratory investigation of the connectivity in the brain.
- As shown during the simulation of the Analogues-RBF Granger method in Chapter 4, it is important to check beforehand if the level of synchronisation does not become too high in order to avoid spurious estimations of directional interaction.

In Figure 6.1, the scheme is completed by successive postprocessing stages which are considered part of a future, more detailed and deeper investigation of the data. The last part of the diagram may involve data mining, discriminatory and decision making analysis which are driven by the synchronisation and

causality features extracted in this thesis. As discussed in the previous chapter, for instance for the MEG data, the single channel measure can be used as a possible feature to build a classifier to discriminate patients from different groups; For the epilepsy data a method based on this thesis' feature extraction can be used for prediction of the occurrence of a seizure. Up to now, this task, which is also one of the most important goal in epilepsy, has not been resolved yet [100]. Prior to this part, an intermediate stage of data processing may also be considered between the extraction of the functional connectivity features and their following analysis. Especially in the case of multivariate functional connectivity, it may be important to find further features which help to explain the complicated pattern of multivariate functional connectivity. Since a multivariate synchronisation and causality analysis produce an estimate of the underlying complex neural network connectivity, several graph and spectral methods [6], i.e. shortest path length or clustering coefficient, have served the purpose to provide summarizing statistics to characterised this global patterns. These methods have become popular in the recent neuroscience literature [136], and they may be employed in future applications of this thesis material.

The experimental analysis in this chapter is applied to the epileptic datasets only. Currently, no reason was found to perform an analysis of causality in the MEG dataset. It is difficult by the state of the art of the literature to give an interpretation of the the flow of information in the brain during the resting state for Parkinson's and dementia pathologies. While it is reasonable to think that during the course of Parkinson's pathology not only the strength but also the flow of communications between areas of the brain may be compromised, this particular study is left for future investigation. The MEG data, in this chapter, are considered only in Section 6.2 in the context of volume conduction effects in multivariate functional connectivity. Instead, in the epilepsy datasets, it is possible to assume that during the seizure the spread of synchronised activity is propagating from the focus. The causality algorithm developed in Chapter 4 is intended to estimate this dynamical effect and can contribute to characterize the location of the focus. Epilepsy is therefore the ideal case of study for the framework in Figure 6.1: Single channel synchronisation deals with finding the early detection and the location of the focus; Causality and synchronisation measures detect the long range dynamics, the propagation and the extension of the epileptic seizure over time in a broader region.

6.1.1 Intracranial dataset A

MPC

The extraction of the phase synchronisation is evaluated using the MPC index over the time series as previously investigated by the single channel metric. Therefore, these signals are preprocessed from the raw EEG signals as described in Section 5.1. The MPC is computed using a moving window with $L = 3s$ which is consistent with the length adopted in the previous chapter. Each moving window has finite size, edge effects due to computation of the Hilbert transform which may not be negligible in this specific case [101]. However, in order to avoid this problem, the Hilbert transform is not applied to each single sliding window but is instead computed along the entire trace. For this reason, edge effects are restricted to the first few

samples of the global trace not compromising the analysis in the most interesting part of the recordings (the central part).

Figure 6.2, shows significant analysis of synchronisation applied to the current intracranial dataset. The outcome of this analysis is a similarity matrix $\mathbf{D}(t)$ which contains all the $N_c \times N_c$ ($N_c = 39$) pairwise synchronisation coefficients $d_{ij}(t)$ over the time t . The first two plots of Figure 6.2 are just re-drawn here from the single channel analysis for comparison only: the global C_{eM} analysis, the C_{eM} and the signal power for the 18 channel case. The third plot represents a global synchronisation statistic: the mean value of the synchronisation similarity matrix taken as:

$$\mu_{MPC} = \frac{1}{N_c \cdot N_c} \sum_{i=1}^{N_c} \sum_{j=1}^{N_c} d_{ij}. \quad (6.1)$$

In practice, μ_{MPC} is a possible summarizing statistic as mentioned in Figure 6.1 which has the same role of complex network analysis measure used in the literature [136]: it indicates the state of the intricate pattern of the matrix $\mathbf{D}(t)$ with a single statistic which is otherwise difficult to interpret. In Figure 6.2(b), for instance, some of these patterns are shown as snapshots of $\mathbf{D}(t)$.

The plots in Figure 6.2 show several interesting correlations between the synchronisation mean index, the epileptic event and the previous C_{eM} and signal power values. Firstly, the μ_{MPC} , while simple as a statistic, shows that the global level of synchronisation during and after the epileptic event is on average higher than the baseline (50s). As discussed, this is a well known characteristic during the occurrence of a generalized seizure which is displayed also by the behaviour of the complexity index C_{eM} . Secondly, peaks in Figure 6.2, are occasionally emerging from this mean level which emphasizes moments of the grid with a higher level of global synchronisations. The occurrence of the peaks start just before the expert notices the seizure on the trace but they appear a few seconds after the drop of complexity in channel 18. These peaks increase their amplitudes up to the seizure (maximum at the marked peak **H**) and they decrease thereafter compatible with the interictal-ictal-postictal transition. The maximum in **H** is consistent with the maximum of the power.

A visual inspection of the adjacency matrix during these peaks is reported in the bottom part of Figure 6.2(a). In **B**, **C** and **D**, just before the transition period to the ictal event, we notice a cluster of high synchronisation including the edges connecting channels 17 to 21. These channels are discussed in the univariate synchronisation metric as possible candidates for the location of the focus. They are correlated with changes in the C_{eM} trace prior to the clinical seizure, as described in Figure 6.2. The fact that they can be visually clustered, is a further reason to consider that region as a possible starting point of the neural anomaly. During the highest peak **H** of the seizure, all the channels become synchronized showing the maximum synchronisation point.

Analogues-RBF Granger Causality

The computation of the causality in the iEEG grid for this dataset A employs the sliding window approach as considered in the previous MPC case. However, in order to reduce the higher computational load with respect to the MPC due to the complexity of the Analogues-RBF algorithm, the extraction of the Granger

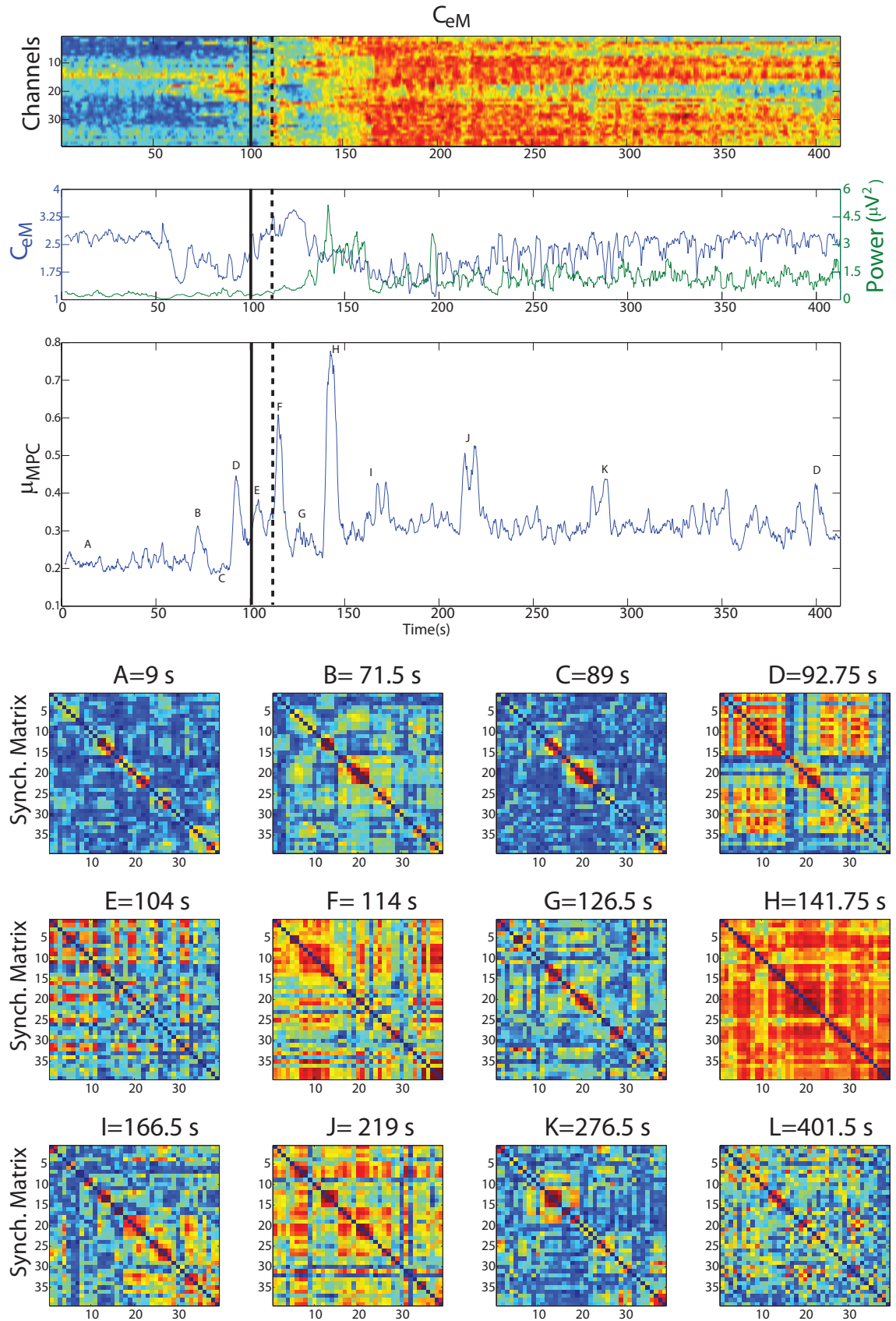


Figure 6.2: Analysis of synchronisation for the Intracranial dataset A. The first two plots report, as in previous figures, the behaviour of the C_{eM} in the whole grid and in the channel 18 together with its power. The third plot shows the average μ_{MPC} across channels of the affinity synchronisation matrix $\mathbf{D}(t)$. The bottom images display the state of the affinity matrix in particular time moments as labelled in the μ_{MPC} plot.

index is considered here in a subset of all the possible combinations of bivariate time series: the analysis was performed between nearest neighbour channels. This choice was shown to be sufficient for the purpose of this section, i.e. to demonstrate that the algorithm correctly identifies the propagation of the seizure outside its focus, as explained later.

Each moving window is $L = 3s$ long, which is chosen to be compatible with the previous MPC and the C_{eM} analysis. Following the Analogues-RBF algorithm, each window needs to be divided in two sets: The first $2s$ is set to be the training set which is used to learn the RBF model while the rest ($1s$) is considered as the test set which calculates the prediction errors and most importantly computes the Granger index. This subdivision is chosen on a subjective basis. It is, nevertheless, a common subdivision in the field of neural network, i.e. training set 70% and test set 30% of the total data [10].

As discussed in Chapter 4, while the Analogues-RBF method is designed with the intention to learn causality relationships automatically from the data, a few parameters still need to be tuned manually: the number of neighbours, the number of basis functions and the embedding dimensions. However, the tuning of the Analogues-RBF algorithm is a hard task to accomplish during the analysis, since the iEEG dataset contains a great number of bivariate time series as well as a large number of sliding window to inspect. It is impractical to check the optimal value of these parameters on each sliding windows with an automatic procedure as performed in Chapter 4. Nevertheless, following the Chapter 4 analysis on the synthetic data, the following considerations can relax the experimental procedure of tuning the causality measure:

- In the case of the embedding dimension, as mentioned in Section 4.2.5, two types of procedure can be employed: either the cross-validation using the out-of-sample prediction error of the Analogues-RBF or, alternatively, using the cut-off point of the singular spectrum using the MDL algorithm. While from different philosophies, both of them are strategies in machine learning for model selection, i.e the dimension of the embedding. In particular, the information from the MDL is already available when computing the index C_{eM} which seems to be a reasonable solution to consider for this experimental analysis instead of the more lengthy cross-validation procedure. Therefore during the computation of the causality between bivariate time series, the embedding dimension in both time series is set as the maximum of their singular spectrum cut-off. This latter condition is necessary in order to ensure that both reconstructed attractors would be unfolded.
- During the simulation in Chapter 4, it was shown that in the presence of an underlying strong causal link, the increasing of the number of neighbours as well as the number of RBF centres would result in an increase in the difference between single and mutual prediction errors. While this fact has shown not to be true for a weak causal link (for example in Figure 4.5), in the following analysis the number of neighbours is set to 20 and the number of RBF centres is set to 15. Slightly varying these two parameters around these two figures has not changed the following interpretation of the results. Therefore, with this choice of parameters, strong causal links can be correctly retrieved while weak links are going to be penalised and not found.

After computing the Granger index, in each sliding window a set of 100 surrogates are calculated via the bootstrapping approach as described in Chapter 4. Therefore, the causal link between two sensors is

signed as significant if and only if the threshold level of the P-values during bootstrapping is above a certain threshold (set to the 0.05 significance level). Moreover, another condition for the significance of the links is given by the MPC as precomputed in the previous section: the synchronisation does not have to exceed the value of 0.8 in order to avoid spurious causality. In the case that both directions between any two channels are tested significant for causality, then the greater of the two is considered as the correct direction.

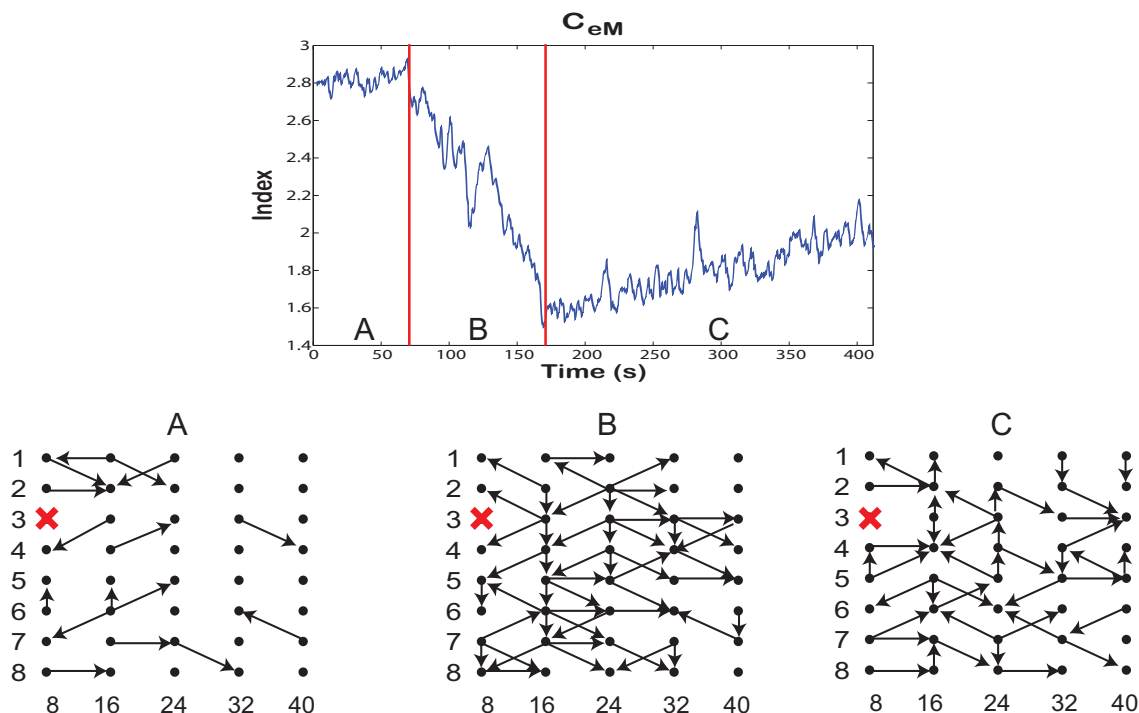


Figure 6.3: Causality directions in the iEEG A grid for three different periods of the recording as segmented by the C_{eM} index. An increase in the number of estimated causality links is found during the ictal period (**B** and **C**) compared to the interictal (**A**). Visually, during (**B**), the links seem to be going out of the region which includes channel 18, where the focus is supposed to be situated. The cross indicates the missing channel.

Figure 6.3 presents the main result of the computation of the Granger index. This figure is divided into three temporal sections of the overall seizure in order to give an informative display of this dataset's analysis: the causal links are computed during the three states of the epileptic activity as segmented by using the single channel analysis (Interictal-Ictal-Postictal). In each of these areas a link is shown in the correspondent place in the grid if at least 30% of the sliding windows in the corresponding period is significant. This threshold percentage was found manually in order to be able to sufficiently populate the plots and to show the possible points of interests, i.e. the casual links from the focal.

The results show, firstly, that there is an increase of causal links during the ictal and postictal phases of the seizure (**B** and **C**) as opposed to the interictal state (**A**). More importantly in the ictal case there are, by visual inspection, few links which are propagating out from the area around channel 18. This finding seems to support positively the intuition of the result retrieved in the previous analysis. In the case of the postictal period, while Figure 6.3 shows an increase of the causal activity with respect to the interictal one, it fails to show a coherent pattern towards or out of the focus of the epilepsy. This may be explained by the fact that the higher state of disorder of the grid after the peak of the synchronisation may interfere with the

estimation of the genuine causality.

It is important to remark that while a subjective threshold is not a good idea because can either emphasise spurious causal connections or hide important ones, this choice was necessary in order to visualize directional information using an arrow-like graph such as in Figure 6.3. With this type of visualisation, in fact, the emergence of a complicated and interlaced pattern of links may soon become a problem because of the exponential growth of the number of the edges present in the graph. Ideally, the data analyst should be equipped with a sliding toolbar to tune interactively the thresholding parameter in order to allow the emergence of interesting patterns (during the selection of the thresholding, we virtually use this type of procedure). In this thesis, for this type of visualization and in the case of the iEEG data, the use of this manual procedure of tuning is justified by the results obtained, i.e. the emergence of a directional flow from the focal. However, in general, when the pattern of causal interactions become difficult to visualize and interpret, a totally different approach is needed which may address as well the issue of subjectivity of the map thresholding (a different visualization tool may not need any thresholding). Further methods, possibly using complex network statistics, are under investigation and are left for future analysis.

To summarize this section: the previous MPC analysis seems to confirm the previous single channel analysis, providing moreover further particulars (sudden peaks of epileptic activity) to help to describe the spatiotemporal dynamics of the seizure. The Analogues-RBF Granger causality analysis seems to find evidence of the propagation of the epileptic activity from the focus (around channel 18). These tools can be used as features for the analysis of this type of seizure.

6.1.2 Intracranial dataset B

MPC

The same analysis of synchronisation described for the dataset A is conducted for this iEEG dataset B. The MPC is computed across 32 channels available and the corresponding matrices $\mathbf{D}(t)$ are defined over the time t . The results of this analysis are reported in Figure 6.4(a) in the same fashion as Figure 6.2(a): the synchronisation mean index μ_{MPC} , the C_{eM} global trace and the C_{eM} and the power signal in channel 29 are shown.

As displayed by Figure 6.4(a), this plot reports a pattern of synchronisation which seems more complex than the previous dataset A. The overall plot of μ_{MPC} seems not to be regularly associated with the occurrence of each of the 33 seizures which can be visually correlated with the peak of the C_{eM} in channel 29. Instead, the plot of μ_{MPC} can be visually divided in two parts: in the first one, until 1100s, the mean level of synchronisation in the grid seems to oscillate around the value of 0.3; In the second part, big peaks of global synchronisation are distributed unevenly above a mean level visually lower than 0.3. From a careful investigation of these dynamics we notice two particular points relative to the occurrence of these peaks in μ_{MPC} . It is difficult to explain the reason of this behaviour in MPC which may be restricted to this particular recording and to this specific patient. However, as for the previous dataset the important point to make here is that the previous synchronisation findings cannot be discovered using only the univariate statistic C_{eM} . In practice, this fact further emphasizes the importance to use both measures, i.e. univariate and bivariate

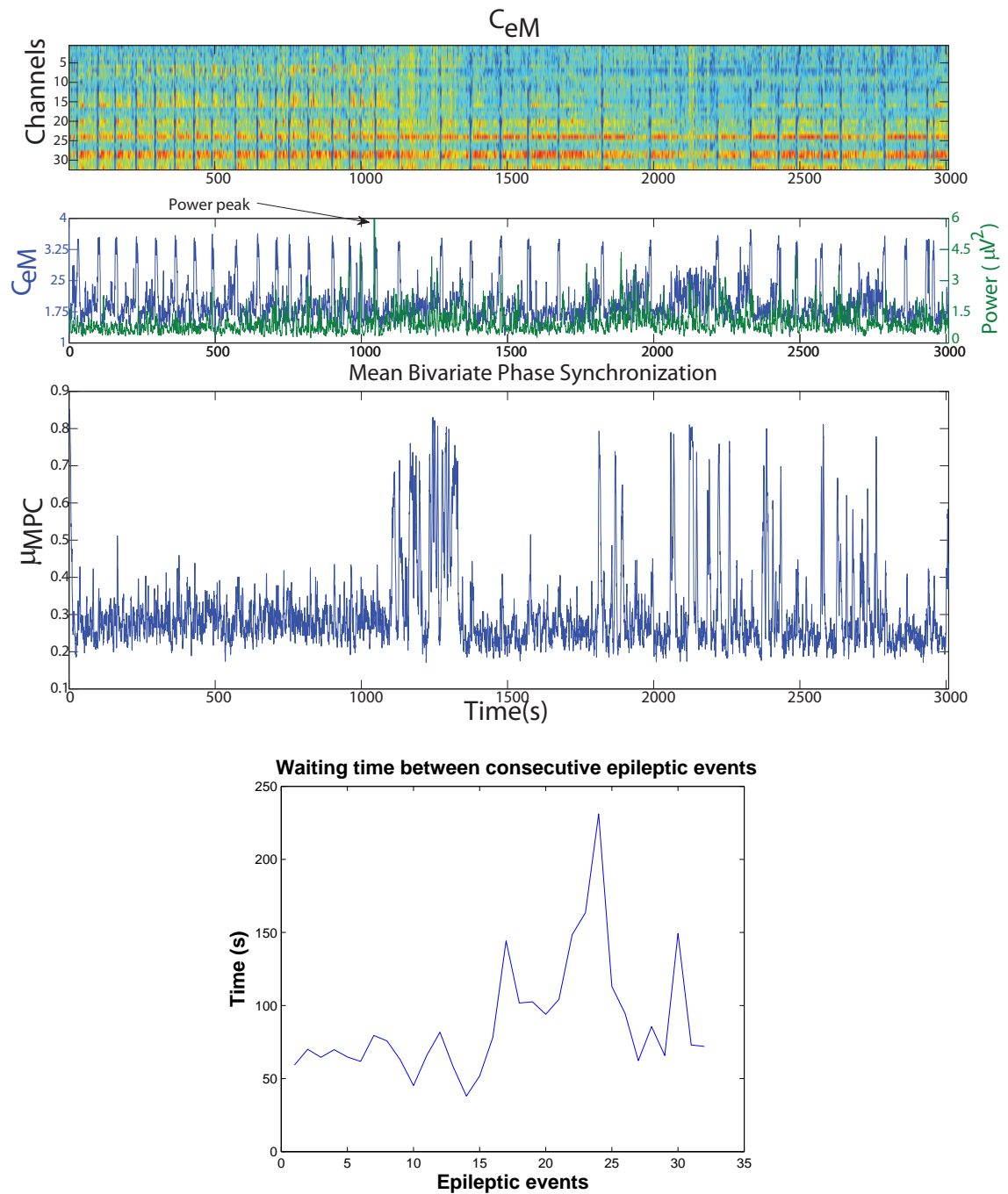


Figure 6.4: Analysis of synchronisation for the iEEG dataset B. The first two plots report, as in Figure 6.2, the behaviour of the C_{eM} in the whole grid and in channel 18 together with its power and the average μMPC across channels. A more complex dynamics of the phase synchronisation is shown in this figure. The bottom plot displays the temporal distance between epileptic events. When the distance become longer the plot of μMPC presents few peaks of complete synchronisation of the grid. This particular regime starts when a sudden peak power as shown in the second plot appears in channel 29. From that instant μMPC oscillates and the waiting time between epileptic events increases.

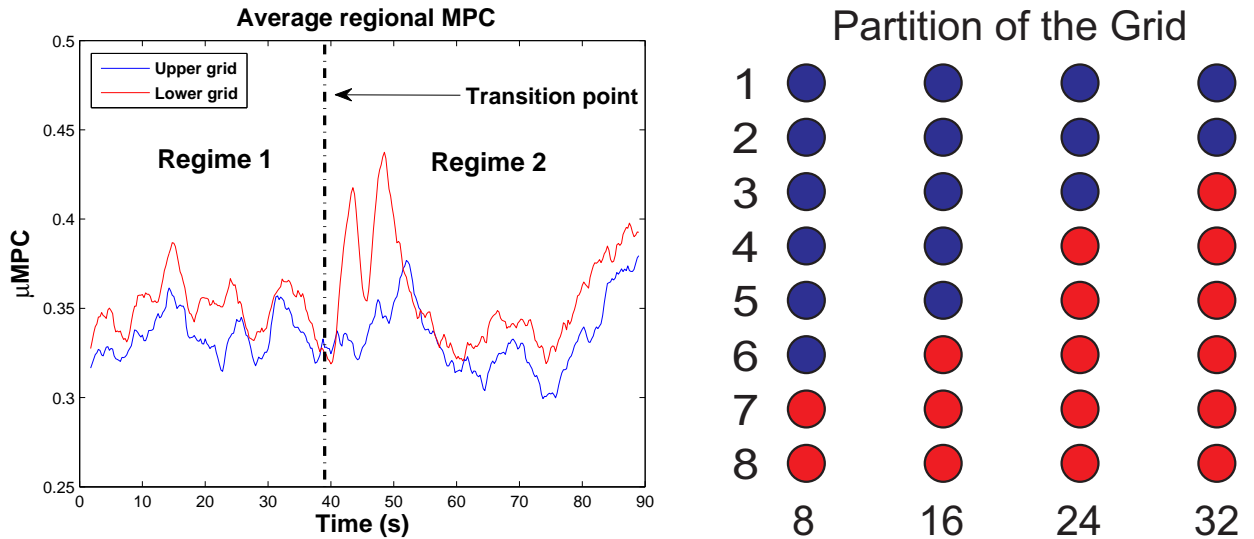


Figure 6.5: Average of the MPC index μ_{MPC} for two different parts of the grid. In the bottom right part (red) of the grid shows a clearer synchronisation change after the occurrence of the epileptic event.

synchronisation statistics, to extract features for studying the spatiotemporal evolution of epileptic seizures. Some interesting points of the figure which are under investigation are: firstly a peak in the signal power, noticeable before the start of peaks of synchronisation which may be the sign of some transition of the underlying dynamical process. Secondly, as shown in Figure 6.4(b) the time occurrence of the epileptic events after this transition seems to be less stable.

As illustrated in the single channel analysis of the iEEG dataset B, we further consider averaging the behaviour of $\mathbf{D}(t)$ around each of the short seizures in the recordings. The average is performed as before, considering the interictal-ictal transition (region 1-region 2) as marked by each peak of the index C_{eM} in channel 29. In Figure 6.5, the results of this computation are shown. Following the suggestion of the previous single channel analysis, we decided to divide the grid in two groups of channels and compute the μ_{MPC} in each of them. It is possible to notice that the upper side (blue channels) is weakly affected by local synchronisation while the lower side (red channels) include the area where the epileptic activity starts and is located. In Figure 6.5 the plots shows that the blue channels have a general lower synchronisation than the red ones and the transition does not change qualitatively its average μ_{MPC} . The red plot, instead, shows an increase of the multivariate synchronisation activity due to the spreading of the activity in the local area.

Analogues-RBF Granger Causality

The same computation of causality described for the dataset A is considered for this iEEG dataset B using the same sliding windows analysis: Each of the 3s sliding windows is divided in 2s of training set and 1s of test set; The Analogues-RBF Granger algorithm is tuned empirically such that the number of neighbours is 20 and the number of basis functions is 15; The embedding dimensions is set as the maximum of the cut-off between each bivariate time series; The Granger index is computed for the subset of bivariate time series where channels are nearest neighbours. Once the Granger index has been extracted, 100 surrogate indices

are resampled using bootstrapping in order to validate the results.

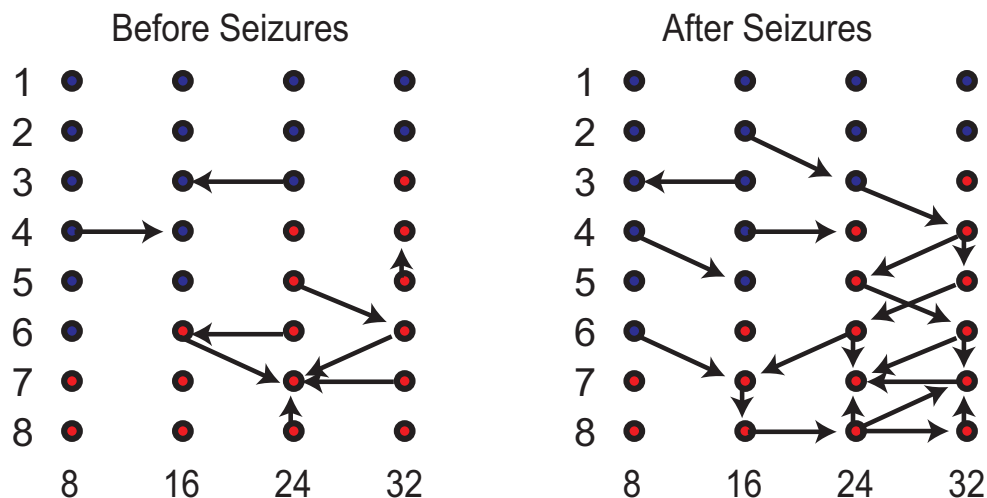


Figure 6.6: Causality directions in the iEEG A grid before and after the 33 occurrences of epileptic activity. The segmentation follows the analysis as discussed in Figure 6.5. From the figure it is possible to notice an increase of causality between the high and the low synchronisation regions as well as the increase between interictal and ictal state. No preferred causality direction was found during the analysis.

Figure 6.6 shows the estimation of the causality linkage for two different states of the grid. These states represent the two average regimes before and after the 33 seizures of the whole recording as described from the segmentation previously shown in Figure 6.5. From a visual inspection of the resulting causal flow, it is possible to notice that there is a weak increase in the number of directional links in the red region of the grid (higher synchronisation) compared to the blue one. An increase can also be noticed in between the two states: the number of causality links after the seizure is higher than before the seizure. This latter finding seems to be compatible with the previous iEEG dataset A where the difference between interictal and ictal state is given by an increase in the number of causal links.

Nevertheless, for this dataset, it was not possible to clearly identify a preferred direction or a source of causality from a visual inspection. Firstly, this result might be justified by the specific type of seizure which fails to propagate on the whole grid as compared to the previous dataset. Similarly, it is possible that the causality algorithm cannot estimate the transition between the interictal to ictal state because this pathological event is too quick to be appreciated. For this reason, using causality, it is not possible to identify through the Analogues-RBF algorithm, channel 29 as a possible source of the epileptic activity. A longer iEEG and further analysis is needed to verify this point.

6.1.3 Photic epilepsy dataset

The photic epileptic dataset was investigated in the early stage of this project as a possible example for testing causality algorithms. In this dataset, it is in fact possible to define a priori the moment and the location of the seizure onset. The seizure occurrence is signed in the recording by the instants after the photic stimulation is turned on (this is true only if the frequency of the lamp correctly triggers the seizure). Secondly, the onset of the epileptic activity should be spatially located in the visual cortex where the neural

system is excited by the photic stimulation. From the visual cortex, the seizure should propagate over the whole EEG scalp since the epilepsy of this dataset is of a generalised type. The Analogues-RBF analysis should estimate this latter causal phenomenon and, more importantly, should also be helpful to confirm the efficiency of this algorithm.

In the recording of this epileptic dataset there are 3 occurrences of the type represented in Figure 2.7, i.e. having the seizure triggered by the photic stimulation with the exact same frequency. The 5s before the stimuli and the successive 5s during the stimuli are taken in all 3 occurrences for the analysis. The analysis is performed over these 3 occurrences considering both the MPC and the Analogues-RBF algorithms. This investigation employs the same methodology as developed in the previous two iEEG datasets, i.e. a sliding windows analysis which is tuned with the same parameters for the MPC and the Granger causality algorithm. While the EM signals are considered at the scalp level, their electrophysical origins are the same as for the intracranial data. At the moment, while a difference might be possible, it is not clear how to take a different methodological and parametrical choice.

The main results of the exploratory analysis of this dataset are shown in Figure 6.7. The first plot considers the analysis of synchronisation (average in all three occurrences), using the mean MPC index across all channels, i.e. the μ_{MPC} . The findings confirm an increase of synchronization during the presence of the stimuli as expected by the seizure activation. Secondly, two plots of the scalp EEG causal network are shown. These plots are computed in the 5 second partition before and during the stimuli. The first thing to notice is the increase in the number of causal links estimated during the stimuli as evidence of the initiation of the seizure. Secondly, in the rightmost plot, it is possible to visually observe the back-to-front direction of the propagation of the 'causal wave' due to the seizure generalisation. Again, this fact can be taken as evidence that the causal algorithm correctly captures the phenomenon of seizure propagation, as stated in the beginning of this section.

While obtaining encouraging results in the analysis of this latter dataset, the focus of the thesis was mainly directed towards the epileptic iEEG cases. The latter offers a more interesting and useful set of problems than the former. In the iEEG datasets, the propagation of the seizure, as estimated by a causality algorithm, is a feature which can be taken as further support for the location of the epileptic focus. In the photic dataset the back to front propagation, since it is a known effect, does not have any specific contribution to this case of study. It is only used here to check the correctness of the Analogues-RBF algorithm.

A second reason is due to the fact that the study of the causality algorithm, as explained in Chapter 4 did not take into account effects of volume conduction. It is well known that volume conduction strongly affects EEG [106]. Nevertheless, since the previous results show evidence of the back to front propagation of the seizure even at scalp level, this may further underline the correct estimation capabilities of the Analogues-RBF causality algorithm. This experimental section was also added to this chapter to emphasise the latter fact.

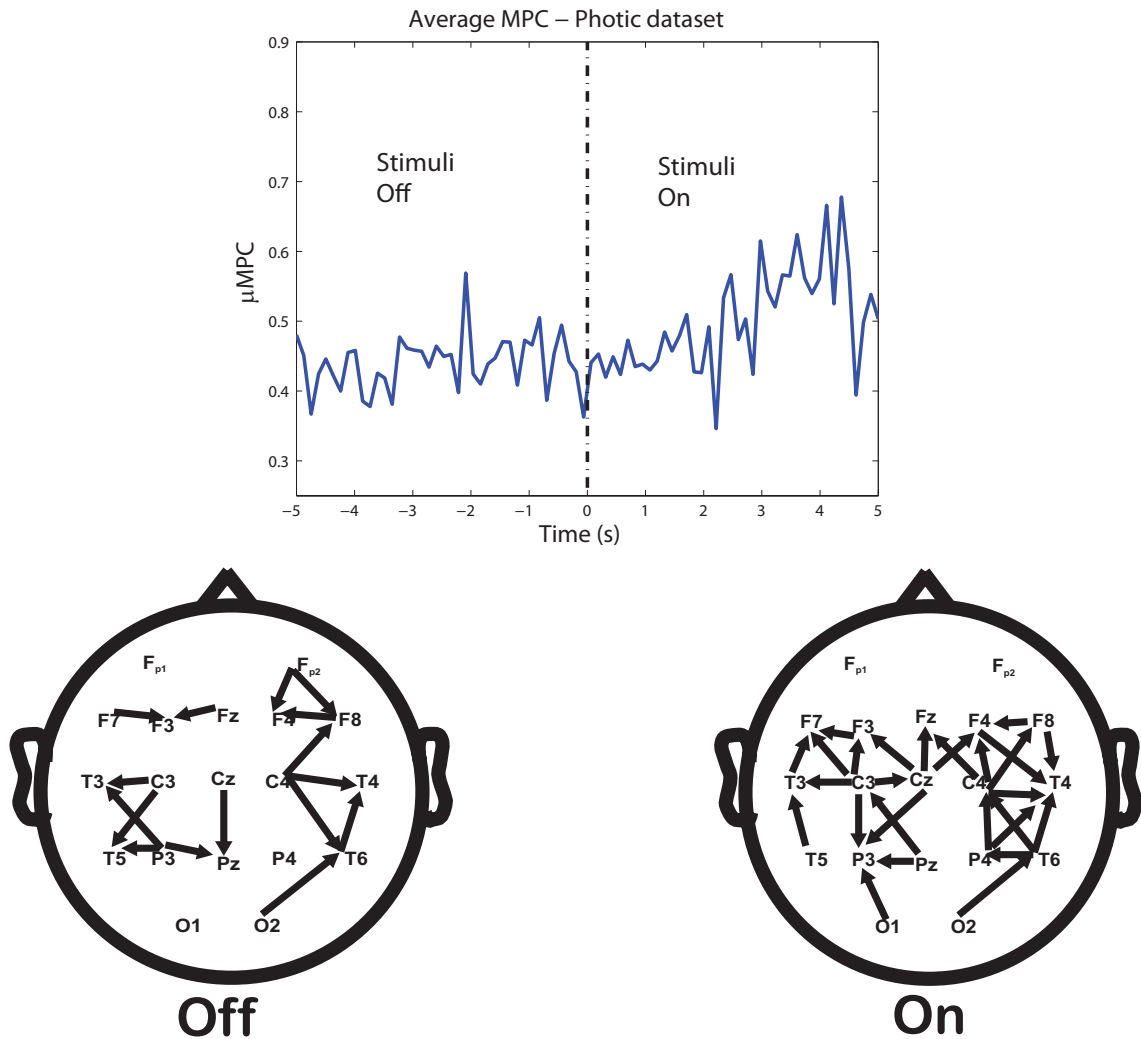


Figure 6.7: Analysis of the photic epileptic dataset. In the topmost figure, the analysis of synchronisation as computed using the μMPC index. As expected the level of synchronisation during the interictal state is lower than after the interictal state. In the bottom figures the pattern of causality shows the back-to-front propagation of the seizure.

6.2 Preliminary investigation of the problem of volume conduction

As discussed in Chapter 2, while the analysis of connectivity using methods from complex systems/networks theory is an established and expanding research topic in neuroscience, the understanding and the interpretation of the multivariate pattern of interaction from EM measurements may be intrinsically biased towards the problem of volume conduction. In this respect, one of the directions which has been planned for future investigation is based on evaluating the influence of volume conduction on the analysis of functional connectivity. In this last part of the thesis, for this reason, some preliminary analysis on the MEG dataset relevant for this future research is discussed.

In particular, with the assumption that this type of data is affected by volume conduction, the PLI have been designed to provide a possible solution to this problem: finding the true connectivities which are cou-

pled at non-zero phase lag whose interactions are considered to be mainly biased to volume conduction phenomena [135]. Since the PLI, as described in the Appendix A, is a modified type of phase synchronisation, its application can be directly compared to the previous MPC index. As stressed in the Conclusion chapter, further tools of source reconstruction would be tested in the future to address this problem.

6.2.1 MEG dataset

MPC

The extraction of the phase synchronisation in the sensor space is firstly evaluated using the MPC index as was the case of the epilepsy data in Section 6.1. This analysis is performed over the MEG time series already preprocessed as described in Section 5.1 during the single channel analysis.

For each time series of the dataset, the Hilbert transform is computed on the broadband signals (0 – 48Hz). Since each time series contains only 1562 points, edge effects due to this transformation to the phase domain are not negligible. Therefore, in contrast with epileptic datasets, prior to the Hilbert transform in order to avoid these edge effects, it has been suggested in [101] to: firstly, taper each time series using a cosine half wave (Hamming window); secondly, after the Hilbert transform 10% (150 samples) of the instantaneous phase values should be discarded on each side. From the phase time series, the MPC can be computed as explained in Appendix A.

The phase synchronisation is computed for each single patient and for each single trial produces the real and symmetric similarity matrix \mathbf{D} . Therefore, since the recording from each subject is performed over 141 MEG channels, $141(141 - 1)/2 = 9870$ values per each trial are available. This number accounts for the number of unique edges between each pair of channels across the MEG sensor space (the upper or lower triangular part of \mathbf{D}). In practice, after this operation for each group of patients, a number of 322×9870 values for each eyes condition is computed. As previously discussed, the interest of this thesis is not to make any assumption on a particular patient. Therefore, in order to reduce the dimensionality of the data, for each channel of the MEG an average (simple arithmetic mean) is taken across trials: for each group of patients a set of 9870 values of synchronisation for each eyes condition is computed.

In Figure 6.8, a summary view of the analysis of the MEG datasets using the MPC index is shown. Figure 6.8 displays the case of the eyes closed only, since the eyes open condition shows the same qualitative plot. Figure 6.8(a) presents a scatter plot with 9870 points: each point is defined by the mean value of the MPC index averaged across trials, as discussed before, against the channel-to-channel physical distances. In practice, it is possible to consider each colour of the scatter plot as the distribution $p(MPC, Distance)$ of an average patient in the three groups. In the Figures 6.8(b), 6.8(c), 6.8(d), the plots of Figure 6.8(a) are separated in the corresponding group of patients for a better visualisation. Figure 6.8 shows clearly the dependence of the phase synchronisation as a function of the distance. In practice, channels that are close to each other (lower distances) are strongly synchronized while channels far apart, are weakly synchronized. This pattern of synchronisation may be a genuine property of the brain network: closer areas are likely to be more synchronized. Nevertheless, as reported in [108; 107; 106], a similar pattern of functional connectivity may be a product of spurious synchronisation. In these articles, simulations of realistic brain

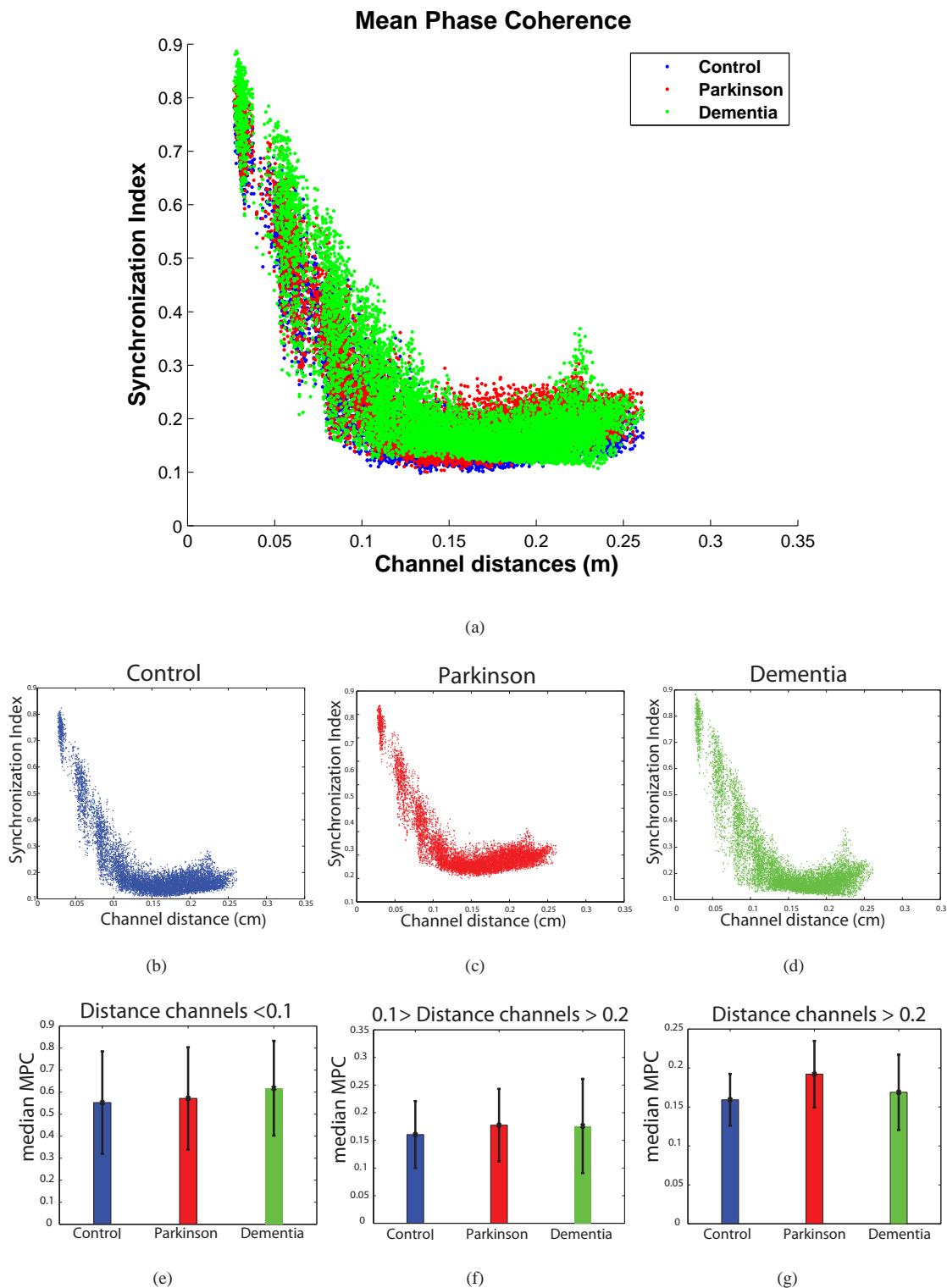


Figure 6.8: Plots that shows the analysis of MEG datasets for the eyes closed condition using the MPC index. The scatterplots show a strong dependence between distance and synchronisation which may be caused by volume conduction effects as noticed in (b),(c) and (e). The histograms in (f), (g) and (h) display the increase of medium and long range synchronisation for the Parkinson’s patients compared with the other groups.

models made by uncorrelated elements have shown that the shape of Figure 6.8 can be produced by volume conduction only. Figures 6.8(e), 6.8(f), 6.8(g) show the distribution of the value of the MPC for short, medium and long range connectivity. The subdivisions made are subjective and are not connected to any

particular topological reason. Nevertheless, the purpose of these plots is to show qualitatively the pattern of synchronisation at different connectivity ranges. From an inspection of these plots, it is shown that at medium and long range the synchronisation of the Parkinson's is higher than the Control and Dementia groups.

PLI and discussion

The treatment of the data for the PLI follows the same protocol of analysis as described by the MPC: firstly, the Hilbert transform is computed in all the time series segments available; secondly the PLI is calculated on the resultant phase series as specified in Appendix A; finally, the averaging of the PLI is performed across trials for each channel. Figure 6.9 shows the result of this computation in a similar fashion of Figure 6.8. Some points of interest visible from these plots are important to mention for future investigations:

- Firstly, in Figure 6.9(a) the scatterplots for each group of subjects do not display the typical decaying behaviour due to volume conduction as in Figure 6.8(a). Instead, *the scatter plots are independent of the channel distances*. This fact may be the result of the penalisation of volume conduction effects by the PLI.
- Secondly, it is possible to notice by a visual inspection that the application of the PLI *provides a better discriminative power between the group of subjects*. In fact, the scatter plot of the dementia patients at all lengths have an average higher value of the PLI comparing to Parkinson's and Control. The same observation is noticed between Parkinson's and Control but with less visible difference. It is not currently clear why this effect take place. It is possible that the PLI, by emphasising true interactions, helps to uncover this pattern of connectivity which is however present in the data.
- Thirdly and more interestingly, it is important to display in Figures 6.9(e),6.9(f),6.9(g) the qualitative separation of the scatter plot in terms of histograms. The three subjective length scales are presented as previously shown in Figure 6.8. In these plots it is possible to see that the difference between groups computed with the PLI is more substantial than with the MPC. More importantly, at medium and long range connectivity the synchronisation of the dementia patients have average higher values than normal Parkinson's in contrast with the qualitative results achieved with the previous MPC analysis.

The last result in particular is interesting in relation to some experimental findings which have been recently published in [16]. In this latter work, the synchronisation analysis of a study on Parkinson's and dementia patients performed using Synchronisation Likelihood (SL) [135] have shown in some frequency bands that the level of SL is Dementia < Parkinson's for medium to long range connectivities. While the analysis in this thesis using the MPC is technically different since it is applied to the broadband case, the conclusions are compatible with the work in [16]. This result as discussed in [16] was not expected by previous results in the literature (see references in [16]) for this particular disease but it is reminiscent of patients affected by Alzheimer disease. Therefore, from this PLI-MPC analysis of the MEG datasets an open question for future investigation emerges: Is the pattern of functional connectivity computed in the

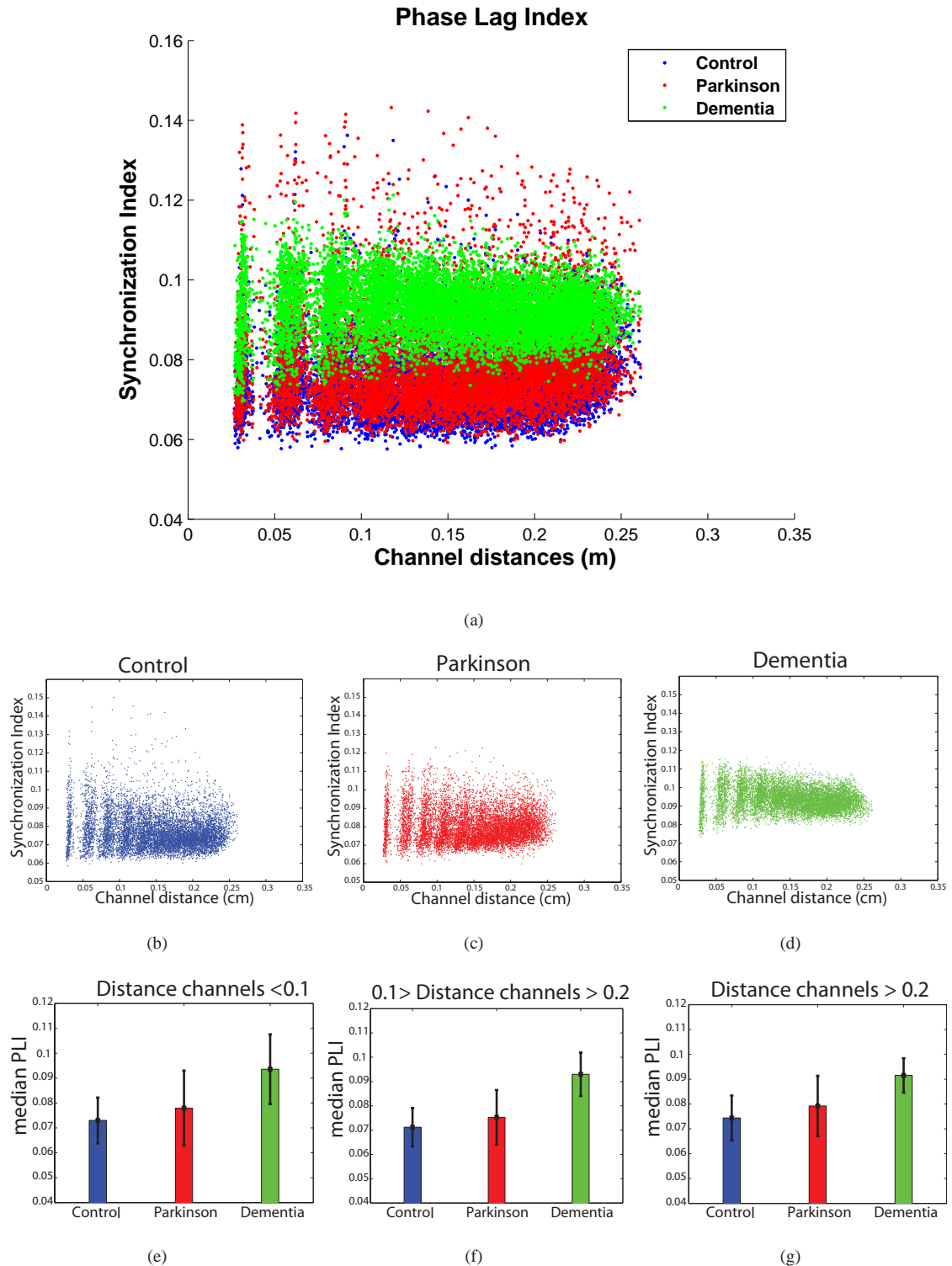


Figure 6.9: Plots showing the performance of the PLI in the MEG dataset. Firstly, the PLI is independent of the channel distance. Secondly, the PLI offers a better discrimination between groups of patients and it gives a different result to the MPC for medium to long range connectivity. A noticeable feature of the figures (a),(b),(c),(d) is the vertical grouping of some of the points towards the beginning of the X axis. This phenomena is the simple effect of the geometrical distance between the electrodots and is not result of some particular characteristic of the data: The first group is formed by the nearest neighbours channels while the other groups clustered at progressive distances.

medium to long range distance using MPC (and maybe SL) due to volume conduction effects?

6.3 Summary

The purpose of this chapter was to discuss experimentally the analysis of multivariate functional connectivity in real patient data. The chapter was divided in two parts.

In the first part, the investigation of bivariate synchronisation and causality was considered on the epilepsy data in order to extract the spatiotemporal evolution of seizures present within. Importantly, the analysis of causality confirmed for the iEEG dataset A and the photic epileptic dataset the evidence of the propagation of the seizure from the area containing the location of the focus. This result may help to confirm the validity of the Analogues-RBF Granger method for the analysis of epileptic data which is stated as the main objective of this chapter. While in the iEEG dataset B the same results cannot be found, this latter result may be explained by the fact that the seizure seems localised in a smaller region which does not propagate further in all the grid. In this case, both single channel and multivariate synchronisation measures seem to be more informative than causality for the discovery of this seizure dynamics.

The second part presented a preliminary investigation of the problem of volume conduction and the effects it may cause on the multivariate pattern of functional connectivity and some discussions. The PLI was recently proposed as a possible solution to this problem and here investigated in the collected datasets. The applications of the PLI and the comparison against the analysis of the MPC have shown, in the particular case of the MEG dataset, several differences. These latter results are considered in the future development of this thesis as material of further research addressed to the problem of volume conduction in EM signals.

7

Conclusion

7.1 General overview

In this thesis, the general problem of estimating synchronisation and causality phenomena from the data of an underlying latent complex system has been investigated. In particular, this thesis focussed on applications in the field of computational neuroscience. Novel signal processing techniques were developed to extract brain functional connectivity from a set of electromagnetic time series. The current trends of the relevant research for this problem have been reviewed and some new results have been derived and discussed which have not previously been reported in the specialised literature. As stated in the Introduction, this thesis is divided in three conceptual parts:

Modelling : The recent modelling framework of the brain using the paradigm of dynamical systems in complex networks and Weakly Coupled Dynamical Systems (WCDS).

Methods : Novel functional connectivity techniques of analysis which help to discover the effective connectivity in the brain have been implemented: a new single channel synchronisation measure and a novel Granger causality metric were investigated.

Experiments : These techniques have been tested in the analysis of two important brain pathologies, i.e. Epilepsy and Parkinson's disorders, and their functional analysis was further discussed.

7.1.1 Dynamical systems in complex network applied to neuroscience

The framework of dynamical systems in complex networks, as described in Chapter 1 and Chapter 2, is the most recent development in terms of modelling and data analysis to study brain mechanisms. Firstly, it is a mathematical approach which extends the lumped dynamical system models based on chaos theory frequently used during the last three decades of brain analysis. Secondly, it better supports the complicated hierarchical structure of the brain and the hypothesis of segregation and integration of its activities. Thirdly, it addresses the understanding of the functioning of the brain in term of interdependence, emergence and self-organised phenomena, i.e. effective connectivity.

From a **modelling perspective**, Chapter 2 discussed the specific class of problems considered in this thesis based on representing the dynamics of the neocortex at its mesoscopic level of description. While neurons are the elementary components of the neocortex, at the mesoscopic scale, macrocolumns are the most important elements (nodes) of the anatomical connectivity of the brain complex network. In fact, they are believed to be the fundamental processing units of the brain and they are considered the smallest finest neural structures perceived using electromagnetic techniques. While modelling large scale neocortical dynamics is not possible with today's knowledge, in this thesis we have considered a few synthetic examples which mimic the behaviour of these cortical networks: In Chapter 3 a chain of coupled non-identical Rössler Oscillators was employed while in Chapter 4 a series of linear and nonlinear bivariate WCDS were used. They cannot be regarded as realistic models of the neocortex. However, they still approximate some aspects of the brain activity which are useful in this thesis to test algorithms for interdependence analysis. Similar arguments and synthetic models have been used frequently in the computational neuroscience literature which validates our research approach.

From a **methodological perspective**, this framework drives the main aim of this thesis which addresses the problem of estimating the functional connectivity of the complex brain network, i.e. the pattern of interdependencies of the observable electromagnetic signals. In particular, it was discussed that the methodology of analysis is of an exploratory type: structural information of the brain was not available and the EM signals are the only accessible knowledge, i.e model free scenario. For this reason, three classes of interdependence methods were mentioned in this project thesis as fundamental types of relationships useful for the understanding of the connectivity of brain patterns and for their interpretation:

- a univariate measure of synchronisation in a single channel,
- a symmetric metric of synchronisation in multichannels,
- a multivariate directional metric of causality or information in multichannels.

These aspects of functional connectivity are meant to capture different emergent phenomena of the underlying brain dynamics. In this thesis, specifically, a novel development of single channel synchronisation and a new metric of information flow were studied as reported in Chapter 3 and Chapter 4, respectively. Two symmetric measures of phase synchronisation, i.e. the Mean Phase Coherence and Phase Lag Index were employed during the data analysis and discussed alongside the problem of volume conduction as a

preliminary data analysis.

From an **experimental perspective**, real patient datasets from two important neurological disorders were presented in order to discuss problems of functional connectivity and to test the usefulness of the methods developed. As reported in the thesis, these datasets are considered here only as possible examples rather than novel cases of study: the methodological part of the thesis has priority with respect to the experimental side which however is considered for future applications.

- Epilepsy is the most common neurological disorder which is due to abnormal synchronisation of the underlying neural network. Two datasets have been collected from a hospital database previously recorded by subdural EEG grids implanted in the neocortex of two patients and used for clinical examinations. They are examples of focal epilepsy which means that the pathological activity starts from a single location in the brain. Another dataset from a patient affected by focal epilepsy was considered in the first part of the project and used during the causality investigation. While structural deficits of the anatomical connectivity is a possible cause of this pathology, these datasets are considered in this thesis from a dynamic perspective: to study the spatiotemporal feature extraction of the spread of the seizures.
- A MEG dataset of Parkinson's and Parkinson's related dementia was considered because it is an example of a pathology where structural deficiencies of the underlying cortical network are responsible for the malfunctioning of the brain. These faults are believed to be visible at the sensor level where functional connectivity techniques can be of valid use.

7.1.2 Assessing local synchronisation using single EM channel

A univariate statistic was proposed in Chapter 4 with the main aim of estimating synchronisation on a local region of the brain network, the activity of which is captured by a single electrode. The principal idea of this algorithm is based on the dimensionality estimation of the manifold of the underlying neural dynamics. The dimensionality of this manifold is related to the degree of freedom and the synchronisation of the underlying system. Few possible existing techniques have been considered which have been combined to offer a novel automatic measure of the complexity: C_{eM} . Complexity and synchronisation are inversely proportional concepts. Simulation and experimental results have confirmed the validity of this new measure.

In Chapter 4, the simulation study of a lattice of 50 Rössler oscillators was considered in order to mimic the behaviour of a local neocortical structure. The C_{eM} successfully discriminates different synchronisation regimes simulated by this synthetic example. Secondly, this index rejects the presence of noise corrupting the observed signals. As discussed in the final part of Chapter 4, in this way, C_{eM} is not affected by the problem of variation of the SNR in the case of Gaussian observational noise.

Experimentally, this single channel metric in Chapter 5 was tested against the iEEG and the MEG datasets. In epilepsy, this measure of synchronisation is important to spot local anomalies which can be

used to find, for instance, the location of the focus. The moving windows analysis of the iEEG datasets has provided encouraging results in this direction. The first trace (Datasets A) is compatible with a gradual transition from the interictal to the ictal state. C_{eM} can detect subtle changes of the state of a few electrodes prior to the clinical seizure. It tracks the increasing synchronisation on the route to the ictal state and the subsequent desynchronisation in the post-ictal stage compatible with the findings in the literature. The second iEEG (Dataset B) is a long recording containing many short epileptic episodes. With a moving window analysis we could not find any clear changes prior to these events. This seems to be congruous with a type of epilepsy having an abrupt shift between interictal to ictal state. Therefore, we applied a different method of processing to this iEEG, based on the averaging of C_{eM} across each single seizure. This procedure has increased the contrast between the period before and after the pathological events. With this type of epilepsy we noticed that C_{eM} displayed spurious peaks during the transition interictal/ictal which was shown to be a problem for the C_{eM} algorithm. This phenomenon, while emphasising the moment of the seizure, did not provide the correct identification of the complexity value during the transition. Despite this, C_{eM} shows some channels having lower complexity consistent with the location of the seizure of the patient and it shows how the complexity changes over the grid during and after the seizure.

In the Parkinson's example, C_{eM} detected some underlying structural mechanisms of the Parkinson's pathology consistent with the literature [14; 139; 138]. In particular, this measure demonstrated a clear differentiation between the three groups of subjects and between eyes open and eyes close conditions in some part of the brain (occipital and parietal). These findings are compatible with some recent results in the literature [14; 139; 138].

7.1.3 Functional synchronisation

As a third topic in order of importance in this thesis, in Chapter 6 the analysis of phase synchronisation was computed on the MEG and the iEEG datasets. While the focus of this thesis is primarily given by novel single channel and causality arguments, the main reason to consider this analysis is given by the following motivations:

- Phase synchronisation is a metric of time correlation between multivariate time series which, in contrast to the univariate measure, is useful to compute the strength of the coupling at medium to large range distances. In practice, in this thesis, both single and multivariate synchronisation algorithms provided the complete view of the functional interaction of the underlying brain substrate. This was shown in the iEEG datasets where, for instance, phase synchronisation seemed to provide further confirmation about the location of the focus and the extension of its range of action.
- As shown during the simulations in Chapter 4, a high value of synchronisation can produce spurious estimation of the true directionality in the data. For this reason, in a general framework of functional connectivity, estimating synchronisation should always precede an analysis of directionality in order to test the strength of the coupling in the data and avoid false causality discovery.
- In Chapter 6 phase synchronisation was discussed as an open issue together with the problem of vol-

ume conduction which may affect the analysis of multivariate functional connectivity applied to EM signals. The PLI, a measure of phase synchronisation which was proposed in the literature to be less biased to volume conduction, was applied to the MEG dataset alongside the traditional MPC. The analysis of synchronisation in the particular case of MEG data has shown different patterns of functional connectivity if the analysis was performed using the the PLI or the MPC. Since connectivity analysis is currently the main direction of research in order to obtain information about the brain, **how much would volume conduction influence this analysis?**

7.1.4 Analogues-RBF Granger causality

Chapter 4 proposed a novel technique in order to detect causality in multivariate data: the Analogues-RBF Granger causality metric. The Analogues-RBF technique is based on a machine learning extension of a simple predictor in state space known as the Lorenz method of Analogues. It is a possible maximum likelihood estimator of the deviation from Markov property which is a general nonlinear formulation of the concept of Granger causality. As for the previous single channel methods, during the thesis, synthetic and real patients datasets were provided to support the validity of this novel technique.

In Chapter 4, together with the theoretical background of this causality method, a series of synthetic examples have been proposed to test performance and verify behaviour. These simulations were considered in this thesis because they have already appeared in the computational neuroscience literature as possible toy models to check the validity of causality algorithms. The analysis of causality shows that the Analogues-RBF method successfully estimated the strength of the simulated coupling in these examples and its synthetic directionality. Moreover, Chapter 4 discussed the problem of tuning the Granger metric since it is not parameter free. An approach of cross-validation was considered and investigated using the previous simulated examples.

In Chapter 6 the analysis of causality using the Analogues-RBF Granger causality metric was performed on real EEG physiological datasets. The MEG dataset was not taken into consideration for this analysis since a causality investigation was not particularly interesting from the disorder perspective.

In the case of the photic epilepsy dataset, the analysis of causality showed firstly an increase of directional activity between the period with photic stimulation than the period without it. Secondly and more importantly, the results displayed that the direction of the flow goes from the occipital to the frontal part of the brain. This is intuitively correct since it is arguable that the input of the photic stimulation produces the occurrence of the seizure in the visual cortex before generalising over all the brain region.

In the case of iEEG dataset A there is an increase of causality connectivity during the transition from the interictal to ictal state. From a qualitative analysis of the direction of the flow, it is shown that the epileptic focus previously found by the complexity C_{eM} measure, was the source of the causal propagation of the pathological activity in the whole intracranial region. This fact is intuitively correct. During the ictal to interictal, while some possible significant causality links were found, the flow did not appear to point back to the focus. It is arguable that after the seizure the region is subject to a state of disorder which therefore

does not show any preferable causality directions while trying to get back to the normal interictal activity.

In the most difficult case of the iEEG dataset B, while there was an increase of significant causality links in the region which contained the focus, no clear directionality was found in the estimated flow. This dataset contains short ictal periods and it is possible that the algorithm of causality cannot find any identifiable directional interactions. While further investigation is needed, these results displayed that the single channel synchronisation was shown to be more useful than the multivariate ones in this epileptic dataset in order to infer the underlying connectivity in the region.

7.2 Discussions and future developments

The framework of dynamical systems in complex networks is a recent and still largely unexplored area of research which has the enormous potential to bring new practical and theoretical insights to the understanding of brain mechanisms. This recent sub-field of applied mathematics is a natural evolution of the last three decades of brain signal processing using dynamical systems and nonlinear time series analysis. Despite several breakthroughs that have been achieved using these tools, many intriguing questions remain open. In this thesis, a few problems were successfully addressed regarding the early processing stage of a complex network framework. Due to the limited time other issues were left unanswered for future investigations. Starting from the conclusion of this project, in the following, a few potential directions are proposed.

Volume conduction and inverse problem functional connectivity

As emphasized during the thesis, one of the major open questions in this thesis left for future investigation is given by the effect of the volume conduction on the analysis of multivariate functional connectivity. This thesis, in fact, discussed methods of functional connectivity from the signals $\{\mathbf{x}_i\}_{i=1}^L$ at the sensor space which are intrinsically influenced by this problem. In Section 6.2, a few preliminary results were discussed using a modified metric of phase synchronisation, the PLI. The latter had reported different results in the analysis of the MEG data.

The PLI as well as techniques such the imaginary part of the coherence are methods which perform analysis directly on the sensor level signals $\{\mathbf{x}_i\}_{i=1}^L$ penalising components which are due to volume conduction effects. Another possible direction, debated in the literature, is based on computing the functional connectivity in the source space instead of the sensor space. Firstly, a method of source localisation is needed to solve the EM inverse problem which extracts the position and the activity of the neural sources from $\{\mathbf{x}_i\}_{i=1}^L$, i.e. $\{\hat{\mathbf{q}}\}_{i=1}^n$. Secondly, the functional connectivity between $\{\mathbf{q}\}_{i=1}^n$ can be estimated with the methods discussed in this thesis. In practice, in the ideal protocol of analysis described in Figure 6.1 a source localisation algorithm is included during the preprocessing block while the rest of the diagram remains unaltered.

If the reconstructed sources are reliable, the connectivity among $\{\mathbf{q}\}_{i=1}^n$ reflects the true communications between the real brain sources. However, as a criticism [135], from a model free scenario functional connectivity at the source level is biased towards the ill-posed nature of the inverse problem (number of

channels \ll number of sources). It seems necessary, in order to increase the reliability of the analysis, that a successful estimation of connectivity in source space should be performed together with extra structural information about the location of the brain activity. Data fusion methods between electromagnetic and structural imaging techniques (MRI and fMRI) have been recently investigated in the literature [7]. The solution of the latter problem can thus provide further directions for studying connectivity in the brain with electromagnetic techniques. In the datasets used in this thesis, the lack of any structural information about their origin was an obstacle for any preliminary analysis in this direction.

Functional network analysis

This thesis contains some of the early stages of a multivariate analysis of the brain, i.e. bivariate synchronization and causality, which are useful in order to understand medium to long range connectivities. This piece of information has the advantage of retrieving the communication between different functional areas of the brain as requested by modern neuroscientific studies. Single channel measures such as the one presented in this thesis, being local features are incapable of obtaining this type of information.

However, despite this theoretical advantage, multivariate measures are biased towards a more difficult analysis: reasoning with its complicated patterns of multivariate functional connectivity remains a big problem. For instance, visualizing in a clear informative manner both synchronization and causality connectivities is not as direct as using a single channel metric as dictated by the exponential explosion of the number of links with the increase of the number of electrodes.

Thus, while from the actual state of research a single channel analysis seems to be considered more straightforward for clinical and research purposes, multivariate techniques need to be further developed to take advantage of its information. One of the reasons to introduce the framework of complex networks is the recent interest in statistical tools of investigation based on graph and spectral matrix theory [6] which goes in the direction of solving the previous problems. These techniques would enter, as depicted in Figure 6.1, in the next step of analysis than the material discussed in this thesis. Several of these tools have been applied and are becoming popular for brain connectivity studies [119]. Therefore, during future investigations of specific neuroscientific problems, these statistics could be employed in order to extract useful information about the underlying state of the brain to reason with the complicated patterns of multivariate functional connectivity.

Metrics validation

Another important issue of this thesis current and future development is the validation of the methods proposed. In practice: how can we be certain that the findings obtained during the analysis are neuropsychological significant?

The main approach, taken during the processing of the EEG/MEG in this work, was to cross-validate our results with the help of an external expert or using ad-hoc datasets. The iEEGs were considered from a database of possible epilepsy datasets where the seizures position, duration and type could be identified by an expert and by previous clinical records. In the case of photic epilepsy, the data were presented with ON-OFF stimuli in order to trigger the seizure and presegment the recordings. For the MEG the subject

were divided in groups: correct identification of a patient group can be used as a positive argument in favor of this thesis metrics. This approach is thus qualitative but it is helpful to establish if the methods extracts meaningful neuropsychological results, i.e. empirically significant findings. Therefore, if the results are consistent with the expert opinion than the methods can be further utilize.

A more quantitative approach, which is important to consider, consists on checking if the results of synchronization and causality are statistically significant, i.e. supported by a statistical test and/or a confidence interval. In the case of bivariate causality and synchronization the standard test discussed in the literature based on surrogate analysis was presented in Section 4.2.4. It is not clear from the literature at the moment how a surrogate test can be extended to the the global network. This issue may better be addressed during the future investigation of functional network statistics as defined in the previous subsection and depends on the particular global metric adopted. Similarly, for the single channel metric this thesis does not developed a statistical test for the analysis of epilepsy but still relies only on the external expertize to check if the drop of complexity is somehow related to the seizure. It is not clear how to designed a surrogate test since the statistical property of this measure needs to be fully understood. In the case of Parkinson, the amount of trials in the datasets are enough in order to use a Wilcoxon rank-sum test.

In general, a the quantitative approach requires either a good understanding of the underlying system (provided by a model) or by having lots of data cross-validated by an expert in order to build up an empirical statistics. Considering the complexity of the underlying brain system and the technological limitation of the measuring process the former is currently difficult to achieve. The latter form of validation is thus the most viable solution for future development of this thesis.

Practical applications

Despite the fact that the previous chapters contain both methodological and experimental analysis, this thesis focused mainly on the demonstration of the applicability of novel algorithms of functional connectivity. The epilepsy and Parkinson's datasets were considered as possible methodological examples rather than cases of study used to build new knowledge about these disorders. The methodological experience acquired during this project is a step forward for the long term and natural direction of our research, i.e. consider a more detailed and driven investigation of these two pathologies.

Epilepsy is still a major open problem in neuroscience despite many years of research have been spent on this topic and several tools have been developed (see [100] for a recent review on the state of epilepsy research with major focus on seizure forecasting). The long term plan and the open dream of the research is seizure prediction. The methods in this thesis may be used for this purpose if the metrics studied will be confirm as significant predictive features. It is necessary, in order to learn some basic understanding of this disorder and the methods we developed, to collect more data than the one provided in this thesis. More data is needed as discussed previously to learn the statistical behavior of this thesis metrics. However, while intracranial recordings are an outstanding source of data, this typology of recordings are difficult to collect. For research for the Parkinson's disorder the size of the dataset collected should not be a problem since several studies have already been published and thus they have passed the quality standards required by the international community.

It is important to underline that for practical application, the single channel synchronization seems a more mature tool for the investigation of real datasets. However, the problem of statistical validation, especially for single trial event like the epilepsy datasets, need to be addressed. The more ambitious use of the bivariate metrics presented in this study is slowed down by some the issues we have discussed: computational load can be intensive, the results are difficult to interpret, the problem of volume conduction can produce spurious results. These arguments are more evident for the causality measure than the bivariate synchronization. At the moment, after experiencing with this thesis material, it is difficult to propose a causality metric for practical applications. Causality analysis other than being computational slower than synchronization are currently validate only empirically by looking a the graph of directional connectivities. In our opinion a causality method cannot be used rigorously, at the moment, in clinical or accademic research.

7.3 Final consideration

To conclude, this thesis has discussed some novel methodologies of exploratory data analysis for the processing of connectivity between multivariate time series justified by the framework of complex systems. We believed that in neuroscience, these methods are useful to find the dynamics of the communication between brain areas as measured by EM recording techniques. In fact, both simulation of synthetic models and experimental data analysis on real patients recordings have shown some positive results that confirm the validity of these methods. For future perspective, we consider to further develop these methods for both clinical and accademic application. Finally, the roadmap for future improvement and application of these methods was briefly considered by addressing the volume conduction problem.

A

Phase Synchronisation

Phase synchronisation is a symmetric metric in the space of time series, which seeks dynamical relationships between the properties of the signals called *phase*. As a particular instance of Definition 1 in the introduction, two signals $x(t)$ and $y(t)$ are phase synchronised if the following phase locking condition [116] applies

$$\varphi_{n,m}(t) = |n\phi_x(t) - m\phi_y(t)| \leq \varepsilon, \quad (\text{A.1})$$

where $\phi_x(t)$ and $\phi_y(t)$ are the instantaneous phases of $x(t)$ and $y(t)$. ε is usually a small term. Equation A.1 is a particular case of Definition 1 in the Introduction.

Equation A.1 is the general expression which describes the case of the $n : m$ synchronisation regime [116]. During the thesis, only the case of $1 : 1$, simply denoted as $\varphi(t)$, is considered since it is the most common choice in neurophysiology applications [114]. In order to exploit the relationship in Equation A.1, the following methodological procedure is usually employed:

- Estimate the instantaneous phases $\phi_x(t)$ and $\phi_y(t)$ of the two signals using the Hilbert transform.
- Compute a statistic which checks if the difference of phases stays bound as described by the expression in Equation. A.1.

As a possible extra step, it is common to employ an hypothesis testing framework as discussed for the Granger causality metric, in order to validate the previous statistics (see [2] for a review).

A.1 Instantaneous phase

Following the literature [114; 87], the computation of the instantaneous phase $\phi_x(t)$ of the signal $x(t)$ (the same procedure applies to $y(t)$) can be performed in two ways: either using the Hilbert transform or by the Wavelet transform. In this thesis, only the former is used to compute the the instantaneous phase.

The Wavelet transform technique is based on the following convolution

$$W_x(t) = \int_{-\infty}^{\infty} \Psi(t')x(t'-t)dt' = A_x(t)e^{i\phi_x(t)}, \quad (\text{A.2})$$

and the instantaneous phase can be computed by

$$\phi_x(t) = \arctan \frac{\text{Im } W_x(t)}{\text{Re } W_x(t)}, \quad (\text{A.3})$$

where $\Psi(\cdot)$ is the *wavelet kernel* function which define the previous convolution. The following Morlet wavelet is often considered:

$$\Psi(t) = \frac{e^{i\omega_0 t} - e^{-i\frac{\omega_0^2 \sigma_t^2}{2}}}{e^{\frac{t^2}{2\sigma_t^2}}}, \quad (\text{A.4})$$

where ω_0 and σ_t are two parameters, i.e. the center frequency and the bandwidth, which define the shape of the kernel function.

The Hilbert transform is computed through the analytical signal of $x(t)$ given by:

$$H_x(t) = x(t) + \tilde{x}(t) = A_x(t)e^{i\phi_x(t)}, \quad (\text{A.5})$$

where $\tilde{x}(t)$ is the Hilbert transform of the signal $x(t)$ given by the following

$$\tilde{x}(t) = \frac{1}{\pi} P.V. \int_{-\infty}^{\infty} \frac{x(t')}{t-t'} dt' \quad (\text{A.6})$$

with *P.V.* indicating the Cauchy principal value. Using Equation A.5 it is possible to compute the instantaneous phase by

$$\phi_x(t) = \arctan \frac{\tilde{x}(t)}{x(t)}. \quad (\text{A.7})$$

Both Hilbert and Wavelet transforms have been the subject of recent investigation which have been shown to produce similar results. The main difference consists in the filtering abilities of the two techniques: The Wavelet kernel provides a natural bandpass filter around the frequency of interest ω_0 while the Hilbert transform has a unit gain across the power spectrum. The Hilbert transform is thus considered a broadband technique to recover the instantaneous phase. For this reason, there has been an ongoing debate on the significance associated to the outcome of the instantaneous phase computed with the Hilbert transform. Our decision is based on the fact that it is most commonly used and more importantly it has the advantage of not being dependent on the choice of the particular kernel function.

The practical computation of the Hilbert transform is typically associated in the literature with an approach based on the Fourier transform. This algorithm is given by the following formula:

$$\tilde{x}(t) = -i\text{FT}^{-1}[\text{FT}[x(t)]\text{sign}(\omega)], \quad (\text{A.8})$$

where FT and FT^{-1} stand for the Fourier and inverse Fourier transform. In practice, as reported from [114], the Hilbert transform algorithm which codes the previous Equation A.8 is given by

- Compute the FFT of the input sequence $\{x_i\}_{i=1}^n$ and store the result in a vector $\{\hat{x}_i\}_{i=1}^n$,
- Create a vector $\{h_i\}_{i=1}^n$ such as

$$h_i = \begin{cases} 1 & \text{for } i = 1, (n/2) + 1, \\ 2 & \text{for } i = 2, 3, \dots, (n/2), \\ 0 & \text{for } i = (n/2) + 2, \dots, n. \end{cases} \quad (\text{A.9})$$

- Compute the pairwise product $z_i = h_i \hat{x}_i$,
- Calculate the inverse FFT of $\{z_i\}_{i=1}^n$ and return the first n elements of the result.

A.2 Mean Phase Coherence

Using the expression in Equation A.1, it is possible to check if the instantaneous phase difference is bounded which confirms that the signals are mutually synchronized. However, due to the randomness in real data, the investigation of $\varphi(t)$ may suffer from different problems: Firstly, $\varphi(t)$ may present sudden phase slips of 2π . For this problem, instead of $\varphi(t)$, it is better to use the wrapped phase $\tilde{\varphi}(t) = \varphi(t) \bmod(2\pi)$ which accounts for these jumps. Secondly, $\tilde{\varphi}(t)$ is no longer a deterministic quantity but instead it can be considered as a random periodic variable with support $[-\pi, \pi]$. In this probabilistic case, the boundeness condition in Eq. A.1 has to be replaced by a quantitative statistical measure.

Different methods have been proposed to check this property (see [114] for a review). In this thesis we consider the approach based on directional statistics formalized by the Mean Phase Coherence index (MPC). The latter is also known in the literature as the Phase Locking Value (PLV). $\tilde{\varphi}(t)$ is modelled by a Von Mises distribution which is the equivalent of a Gaussian distribution for a random variable with periodic support [99]. In practice, the MPC index measures the strength of the phase synchronisation as defined by the peakedness of the $\tilde{\varphi}(t)$ distribution. The MPC index is thus given by

$$MPC = \left| \frac{1}{N} \sum_{j=1}^N e^{i\tilde{\varphi}(t)} \right|. \quad (\text{A.10})$$

From the above value, it is possible to see that MPC is bounded between 0 and 1. By definition [99], the $MPC = 1 - CV$ where CV is denoted as the *circular variance* of the $\tilde{\varphi}(t)$ distribution.

A.3 Phase Lag Index

The phase lag index is a further metric of phase synchronisation which is designed to take care of phenomena of volume conduction and active reference electrodes [135]. As for the previous MPC index, the PLI is derived by the instantaneous phase distribution $\varphi(t)$. The PLI is defined as follow:

$$PLI = \left| \frac{1}{N} \sum_{j=1}^N \text{sign}[\tilde{\varphi}(t)] \right|, \quad (\text{A.11})$$

where $\text{sign}(x) = x/|x|$ is the sign operator defined as,

$$\text{sign}(x) = \begin{cases} -1 & x < 0, \\ 0 & x = 0, \\ 1 & x > 0. \end{cases} \quad (\text{A.12})$$

Within the formulation in Equation A.11, the PLI can take values between 0 and 1 as in the case of the MPC. However, by construction, the PLI is an index which is designed to be more sensitive by the asymmetry of the phase distribution. In practice, the basic idea behind the PLI index is that a single strong source propagates its effects at the same time to different electrodes. It is thus more likely that this source produces signals coupled at a zero phase synchronisation since its effects on the scalp are practically instantaneous. The PLI penalizes phenomena of this type, emphasizing phase differences at non zero lags, i.e. from not instantaneous coherent sources.

As discussed in [135], it is possible that some meaningful interactions might be still the product of zero lag phase synchronisation, i.e. two sources far apart completely synchronised at scalp level. The author explains, justifying the use of the PLI, that the danger of the possible loss of this piece of information is less important than the misinterpretation of the synchronisation pattern caused by volume conduction. From the preliminary results in Chapter 6 this may be the case: specific pattern in the data may be hidden by volume conduction.

As reported in [135], the PLI has shown to be able to deal with problems of volume conduction in the case of simulated data (coupled of oscillators dynamical systems) as well as for experiments with EEG and MEG data. These results were compared with interdependence tools of analysis such as the previous MPC index and the imaginary part of the coherence [104]. The latter measure was previously developed, to solve the volume conduction problem from scalp level EM measurements in the same fashion as for the PLI. For both indexes, the PLI has shown to be more effective than these latter two methods to estimate the underlying synchronisation from sensor level data hidden by volume conduction. For this reason the PLI is considered here for the exploratory analysis of MEG data in Chapter 6.

Bibliography

- [1] L.A. Aguirre and C. Letellier, *Observability of multivariate differential embeddings*, Journal of Physics A **38** (2005), no. 28, 6311–6326.
- [2] C. Allefeld and J. Kurths, *Testing for phase synchronization*, International Journal of Bifurcation and Chaos **14** (2004), no. 2, 405–416.
- [3] L.A.N. Amaral and J.M. Ottino, *Complex networks*, European Physical Journal B **38** (2004), 147–162.
- [4] N. Ancona, D. Marinazzo, and S. Stramaglia, *Radial basis function approach to nonlinear Granger causality of time series*, Physical Review E **70** (2004), no. 5, 056221.
- [5] A. Arenas, A. Diaz-Guilera, J. Kurths, Y. Moreno, and C. Zhou, *Synchronization in complex networks*, Physical Report **469** (2008), 93–153.
- [6] F.M. Atay, T. Bilykoglu, and J. Jost, *Network synchronization: Spectral versus statistical properties*, Physica D **224** (2006), no. 1-2, 35–41.
- [7] S. Baillet, J. C. Mosher, and R. M. Leahy, *Electromagnetic brain mapping*, Signal Processing Magazine **18** (2001), no. 6, 14–30.
- [8] D.S. Bassett and E. Bullmore, *Small-world brain networks*, Neuroscientist **12** (2006), no. 6, 512–523.
- [9] D. Bihan, J. Mangin, C. Poupon, C.A. Clark, S. Pappata, N. Molko, and H. Chabriat, *Diffusion tensor imaging: Concepts and applications*, Journal of Magnetic Resonance Imaging **13** (2001), no. 4, 534–546.
- [10] C. Bishop, *Neural networks for pattern recognition*, Oxford University Press, 1996.
- [11] ———, *Pattern recognition and machine learning*, Information Science and Statistics, Springer-Verlag New York Inc., 2006.
- [12] S. Boccaletti, J. Kurths, G. Osipov, D.L. Valladares, and C.S. Zhou, *The synchronization of chaotic systems*, Physics Reports **366** (2002), 1–101.
- [13] S. Boccaletti, D.L. Valladares, L.M. Pecora, H.P. Geffert, and T. Carroll, *Reconstructing embedding spaces of coupled dynamical systems from multivariate data*, Physical Review E **65** (2002), no. 3, 035204.

- [14] J.L.W. Bosboom, D. Stoffers, C. J. Stam, B. W. van Dijk, J. Verbunt, H. W. Berendse, and E. Ch Wolters, *Resting state oscillatory brain dynamics in Parkinson's disease: an MEG study*, *Clinical Neurophysiology* **117** (2006), no. 11, 2521–2531.
- [15] J.L.W. Bosboom, D. Stoffers, C.J. Stam, H.W. Berendse, and E.Ch. Wolters, *Cholinergic modulation of MEG resting-state oscillatory activity in Parkinson's disease related dementia*, *Clinical Neurophysiology* **120** (2009), no. 5, 910–915.
- [16] J.L.W. Bosboom, D. Stoffers, E.C. Wolters, C. J. Stam, and H. W. Berendse, *MEG resting state functional connectivity in Parkinson's disease related dementia*, *Journal Neural Transmission* **116** (2009), no. 2, 193–202.
- [17] M. Breakspear and C. J. Stam, *Dynamics of a neural system with a multiscale architecture*, *Philosophical Transactions of the Royal Society of London. Series B: Biological sciences* **360** (2005), no. 1457, 1051–1074.
- [18] M. Breakspear and J. R. Terry, *Nonlinear interdependence in neural systems: motivation, theory, and relevance*, *International Journal of Neuroscience* **112** (2002), no. 10, 1263–1284.
- [19] S. Bressler and J. Kelso, *Cortical coordination dynamics and cognition*, *Trends in Cognitive Sciences* **5** (2001), no. 1, 26–36.
- [20] D.S. Broomhead and G.P. King, *Extracting qualitative dynamics from experimental data*, *Physica D* **20** (1986), no. 2-3, 217–236.
- [21] R. Brown and L. Kocarev, *A unifying definition of synchronization for dynamical systems*, *Chaos: An Interdisciplinary Journal of Nonlinear Science* **10** (2000), no. 2, 344–349.
- [22] G. Buzsáki, *Rhythms of the brain*, Oxford University Press, 2006.
- [23] L. Cao, A. Mees, and K. Judd, *Dynamics from multivariate time series*, *Physica D* **121** (1998), no. 1-2, 75–88.
- [24] E. Casagrande, A. Hadjipapas, and D. Lowe, *An extension of the method of analogues using radial basis function to assess Granger causality in biomedical data*, *Proceedings of Computational Intelligence in Medicine and Healthcare*, 2007.
- [25] E. Casagrande, A. Hadjipapas, and D. Lowe, *Detecting dynamical interdependence and generalized synchronisation using the Lorenz method of analogues*, *Proceedings of International Workshop on Nonlinear Dynamics and Synchronization* (K. Kyamakya, ed.), Shaker Verlag, 2008, pp. 146–153.
- [26] Y. Chen, G. Rangarajan, J. Feng, and M. Ding, *Analyzing multiple nonlinear time series with extended Granger causality*, *Physics Letters A* **324** (2004), 26–35.
- [27] M. Chávez, Richard A Martinerie, and M. Le Van Quyen, *Statistical assessment of nonlinear causality: application to epileptic EEG signals*, *Journal of Neuroscience Methods* **124** (2003), no. 2, 113–128.

- [28] A. Cichocki and S. Amari, *Adaptive blind signal and image processing*, 1 ed., Wiley, 2002.
- [29] D. S. Coffey, *Self-organization, complexity and chaos: the new biology for medicine*, *Nature Medicine* **4** (1998), no. 8, 882–885.
- [30] T.H. Cormen, C.E. Leiserson, R.L. Rivest, and C. Stein, *Introduction to algorithms*, 2nd ed., The MIT Press, 2001.
- [31] T.M. Cover and J.A. Thomas, *Elements of information theory*, 2nd ed., Wiley Series in Telecommunications and Signal Processing, Wiley-Interscience, 2006.
- [32] C. Diks and J. DeGoede, *A general nonparametric bootstrap test for Granger causality*, *Global analysis of dynamical systems* (H. Broer, B. Krauskopf, and G. Vegter, eds.), IoP Publishing, London, 2001, pp. 391–403.
- [33] M. Ding, S. L. Bressler, W. Yang, and H. Liang, *Short-window spectral analysis of cortical event-related potentials by adaptive multivariate autoregressive modeling: data preprocessing, model validation, and variability assessment*, *Biol Cybern* **83** (2000), no. 1, 35–45.
- [34] M. Ding, Y. Chen, and S.L. Bressler, *Granger causality: Basic theory and application to neuroscience*, *Handbook of Time Series Analysis*, Wiley-VCH Verlag, Aug 2006.
- [35] J. Engel and International League Against Epilepsy (ILAE), *A proposed diagnostic scheme for people with epileptic seizures and with epilepsy: report of the ILAE task force on classification and terminology*, *Epilepsia* **42** (2001), no. 6, 796–803.
- [36] P. Faure and H. Korn, *Is there chaos in the brain? I. Concepts of nonlinear dynamics and methods of investigation*, *Comptes Rendus de l'Académie des Sciences - Series III - Sciences de la Vie* **324** (2001), no. 9, 773–793.
- [37] Andrew A. Fingelkurts, Alexander A. Fingelkurts, and Seppo Kähkönen, *Functional connectivity in the brain—is it an elusive concept?*, *Neuroscience & Biobehavioral Reviews* **28** (2005), no. 8, 827–836.
- [38] R.S Fisher, W. van Emde Boas, W. Blume, C. Elger, P. Genton, P. Lee, and J. Engel, *Epileptic seizures and epilepsy: definitions proposed by the international league against epilepsy (ILAE) and the international bureau for epilepsy (IBE)*, *Epilepsia* **46** (2005), no. 4, 470–472.
- [39] M. F. Folstein, S. E. Folstein, and P. R. McHugh, *Mini-mental state. a practical method for grading the cognitive state of patients for the clinician*, *Journal of Psychiatric Research* **12** (1975), no. 3, 189–198.
- [40] R.S.J. Frackowiak, K.J. Friston, C. Frith, R. Dolan, C.J. Price, S. Zeki, J. Ashburner, and W.D. Penny, *Human Brain Function*, 2nd ed., Academic Press, 2003.
- [41] W.A. Freiwald, P. Valdes, J. Bosch, R. Biscay, J.C. Jimenez, L.M. Rodriguez, V. Rodriguez, A.K. Kreiter, and W. Singer, *Testing non-linearity and directedness of interactions between neural groups in the macaque inferotemporal cortex*, *Journal of Neuroscience Methods* **94** (1999), no. 1, 105–119.

- [42] O. Friman, *Adaptive analysis of functional MRI data*, Ph.D. thesis, Linköping Universitet, 2003.
- [43] K. Friston, *Functional and effective connectivity in neuroimaging: A synthesis*, Human Brain Mapping **2** (1994), no. 1-2, 56–78.
- [44] ———, *The labile brain. I. neuronal transients and nonlinear coupling*, Philosophical Transactions of the Royal Society of London. Series B: Biological sciences **355** (2000), 215 – 236.
- [45] ———, *The labile brain. II. transients, complexity and selection*, Philosophical Transactions of the Royal Society of London. Series B: Biological sciences **355** (2000), 237 – 252.
- [46] ———, *The labile brain. III. transients and spatio-temporal receptive fields*, Philosophical Transactions of the Royal Society of London. Series B: Biological sciences **355** (2000), 253 – 265.
- [47] ———, *Beyond phrenology: What can neuroimaging tell us about distributed circuitry?*, Annual Review of Neuroscience **25** (2002), no. 1, 221–250.
- [48] S.P. Garcia and J.S. Almeida, *Multivariate phase space reconstruction by nearest neighbor embedding with different time delays*, Physical Review E **72** (2005), no. 2, 027205.
- [49] R. Germuska, *Complexity analysis of electroencephalographic data*, Master’s thesis, Aston University, 2000.
- [50] J. Geweke, *Inference and causality in economic time series models*, Handbook of Econometrics (Z. Griliches and M.D. Intriligator, eds.), vol. 2, Elsevier, 1 ed., 1984, pp. 1101–1144.
- [51] J. Geweke, R. Meese, and W. Dent, *Comparing alternative tests of causality in temporal systems : Analytic results and experimental evidence*, Journal of Econometrics **21** (1983), no. 2, 161–194.
- [52] M. Ghil, M.R. Allen, M.D. Dettinger, K. Ide, D. Kondrashov, M.E. Mann, A.W. Robertson, A. Saunders, Y. Tian, F. Varadi, and P. Yiou, *Advanced spectral methods for climatic time series*, Reviews of Geophysics **40** (2002), no. 1, 1003.
- [53] J.F. Gibson, J.D. Farmer, M. Casdagli, and S. Eubank, *An analytic approach to practical state space reconstruction*, Physica D **57** (1992), no. 1-2, 1–30.
- [54] N. Golyandina, V. Nekrutkin, and A. Zhigljavsky, *Analysis of time series structure: SSA and related techniques*, Chapman & Hall/CRC, 2001.
- [55] B. Gourevitch, R. Bouquin-Jeannes, and G. Faucon, *Linear and nonlinear causality between signals: methods, examples and neurophysiological applications*, Biological Cybernetics **95** (2006), no. 4, 349–369.
- [56] C.W.J. Granger, *Investigating causal relations by econometric models and cross-spectral methods*, Econometrica **37** (1969), no. 3, 424–38.
- [57] ———, *Testing for causality : A personal viewpoint*, Journal of Economic Dynamics and Control **2** (1980), no. 1, 329–352.

- [58] ———, *Essays in econometrics*, Cambridge Books, Cambridge University Press, 2001.
- [59] C. M. Gray, *The temporal correlation hypothesis of visual feature integration: still alive and well*, *Neuron* **24** (1999), no. 1, 31–47, 111–25.
- [60] L. Györfi and D. Schäfer, *Nonparametric prediction*, *Advances in Learning Theory: Methods, Models and Applications* (J.A.K. Suykens, G. Horváth, S. Basu, C. Micchelli, and J. Vandevallé, eds.), IOS Press, NATO Science Series, 2003, pp. 339–354.
- [61] A. Hadjipapas, *Synchronization processes in nonlinear systems and their relation to cortical oscillatory dynamics*, Ph.D. thesis, Aston University, 2005.
- [62] A. Hadjipapas, E. Casagrande, A. Nevado, G.R. Barnes, G.Green, and I.E Holliday, *Can we observe collective neuronal activity from macroscopic aggregate signals?*, *Neuroimage* **44** (2009), no. 4, 1290–1303.
- [63] A. Hadjipapas, A. Hillebrand, I.E. Holliday, K.D. Singh, and G.R. Barnes, *Assessing interactions of linear and nonlinear neuronal sources using MEG beamformers: a proof of concept*, *Clinical Neurophysiology* **116** (2005), no. 6, 1300–1313.
- [64] M. Hämmäläinen, R. Hari, R.J. Ilmoniemi, J. Knuutila, and O.V. Lounasmaa, *Magnetoencephalography: theory, instrumentation, and applications to noninvasive studies of the working human brain*, *Reviews of Modern Physics* **65** (1993), no. 2, 413–497.
- [65] S. Haykin, *Neural networks and learning machines*, Pearson Prentice Hall, 2009.
- [66] N. Hazarika and D. Lowe, *A neural-network extension of the method of analogues for iterated time series prediction*, *Neural Networks for Signal Processing VIII*, 1998. Proceedings of the 1998 IEEE Signal Processing Society Workshop, Aug-2 Sep 1998, pp. 458–466.
- [67] Craig Hiemstra and Jonathan D. Jones, *Testing for linear and nonlinear Granger causality in the stock price-volume relation*, *Journal of Finance* **49** (1994), no. 5, 1639 – 1664.
- [68] K. Hlavackova-Schindler, M. Palus, M. Vejmelka, and J. Bhattacharya, *Causality detection based on information-theoretic approaches in time series analysis*, *Physics Reports* **441** (2007), no. 1, 1–46.
- [69] HMCO, *The American Heritage, Dictionary of the English Language*, 4th ed., vol. 2006, Houghton Mifflin, 2000.
- [70] K.D. Hoover, *Causality in Macroeconomics*, Cambridge Univ. Press, 2001.
- [71] B. Horwitz, *The elusive concept of brain connectivity*, *Neuroimage* **19** (2003), no. 2, 466–470.
- [72] E. Huigen, A. Peper, and C. Grimbergen, *Investigation into the origin of the noise of surface electrodes*, *Medical and Biological Engineering and Computing* **40** (2002), no. 3, 332–338.
- [73] L. D. Iasemidis, *Epileptic seizure prediction and control*, *IEEE Transactions on Biomedical Engineering* **50** (2003), no. 5, 549–558.

- [74] E. M. Izhikevich, *Which model to use for cortical spiking neurons?*, IEEE Transactions on Neural Networks **15** (2004), no. 5, 1063–1070.
- [75] I.T. Jolliffe, *Principal Component Analysis*, 2nd ed., Springer, 2002.
- [76] K. Judd and A. Mees, *Embedding as a modeling problem*, Physica D **120** (1998), no. 3-4, 273–286.
- [77] S. Kalitzin, J. Parra, D.N. Velis, and F.H. Lopes da Silva, *Enhancement of phase clustering in the EEG/MEG gamma frequency band anticipates transitions to paroxysmal epileptiform activity in epileptic patients with known visual sensitivity*, IEEE Transactions on Biomedical Engineering **49** (2002), no. 11, 1279–1286.
- [78] ———, *Enhancement of phase clustering in the EEG/MEG gamma frequency band anticipates transitions to paroxysmal epileptiform activity in epileptic patients with known visual sensitivity*, IEEE Transactions on Biomedical Engineering **49** (2002), 1279–1286.
- [79] E.R. Kandel, *Principles of neural science*, McGraw-Hill Education, 2000.
- [80] K. Kaneko, *Overview of coupled map lattices*, Chaos **2** (1992), 279–282.
- [81] N. Kannathal, Min Lim Choo, U. Rajendra Acharya, and P. K. Sadasivan, *Entropies for detection of epilepsy in EEG*, Computer Methods and Programs in Biomedicine **80** (2005), no. 3, 187–194.
- [82] H. Kantz and T. Schreiber, *Nonlinear time series analysis*, Cambridge University Press, 2003.
- [83] A.Ya. Kaplan, A.A. Fingelkurts, A.A. Fingelkurts, S.V. Borisov, and B.S. Darkhovsky, *Nonstationary nature of the brain activity as revealed by EEG/MEG: methodological, practical and conceptual challenges*, Signal Processing **85** (2005), no. 11, 2190–2212.
- [84] S.J.A. Kelso, *Dynamic patterns: The self-organization of brain and behavior (complex adaptive systems)*, The MIT Press, 1995.
- [85] B. Kolb and I. Whishaw, *An introduction to brain and behavior*, 2nd ed., Worth Publishers, 2005.
- [86] H. Korn and P. Faure, *Is there chaos in the brain? II. Experimental evidence and related models*, Comptes Rendus Biologies **326** (2003), no. 9, 787–840.
- [87] T. Kreuz, F. Mormann, R.G. Andrzejak, A. Kraskov, K. Lehnertz, and P. Grassberger, *Measuring synchronization in coupled model systems: A comparison of different approaches*, Physica D **225** (2007), no. 1, 29–42.
- [88] D. Kugiumtzis, *State space reconstruction parameters in the analysis of chaotic time series - the role of the time window length*, Physica D **95** (1996), no. 1, 13–28.
- [89] D. Kugiumtzis and N. Christophersen, *State space reconstruction: Method of delays vs singular spectrum approach*, Tech. report, University of Oslo, 1997.
- [90] D. Kugiumtzis, O.C. Lingjærde, and N. Christophersen, *Regularized local linear prediction of chaotic time series*, Physica D **112** (1998), no. 3-4, 344 – 360.

- [91] J. Lachaux, L. Pezard, L. Garnero, C. Pelte, B. Renault, F.J. Varela, and J. Martinerie, *Spatial extension of brain activity fools the single-channel reconstruction of EEG dynamics*, *Human Brain Mapping* **5** (1997), no. 1, 26–47.
- [92] L. Lee, L.M. Harrison, and A. Mechelli, *A report of the functional connectivity workshop*, *Neuroimage* **19** (2003), no. 2, 457–465.
- [93] C. Letellier, L. Aguirre, and J. Maquet, *How the choice of the observable may influence the analysis of nonlinear dynamical systems*, *Communications in Nonlinear Science and Numerical Simulation* **11** (2006), no. 5, 555–576.
- [94] F.H. Lopez da Silva, W. Blanes, S. N. Kalitzin, J. Parra, P. Suffczynski, and D. N. Velis, *Dynamical diseases of brain systems: different routes to epileptic seizures*, *Biomedical Engineering, IEEE Transactions on* **50** (2003), no. 5, 540–548.
- [95] F.H. Lopez da Silva, W. Blanes, S.N. Kalitzin, J. Parra, P. Suffczynski, and D.N. Velis, *Epilepsies as dynamical diseases of brain systems: basic models of the transition between normal and epileptic activity*, *Epilepsia* **44 Suppl 12** (2003), 72–83.
- [96] D. Lowe, *Radial Basis Function networks*, *The Handbook of Brain Theory and Neural Network* (A. Arbib, ed.), MIT Press, Cambridge, MA, USA, 1998, pp. 779–782.
- [97] D. Lowe and C.J. James, *Extracting multisource brain activity from a single channel*, *Artificial Intelligence in Medicine* **28** (2003), 89–104.
- [98] W.W. Lytton, *Computer modelling of epilepsy*, *Nature Reviews Neuroscience* **9** (2008), no. 8, 626–637.
- [99] K.V. Mardia and P.E. Jupp, *Directional statistics*, 2 ed., Wiley Blackwell, 1999.
- [100] F. Mormann, R.G. Andrzejak, C.E. Elger, and K. Lehnertz, *Seizure prediction: the long and winding road.*, *Brain* **130** (2007), no. 2, 314–333.
- [101] F. Mormann, K. Lehnertz, P. David, and C.E. Elger, *Mean phase coherence as a measure for phase synchronization and its application to the EEG of epilepsy patients*, *Physica D* **144** (2000), no. 3-4, 358–369.
- [102] V.B. Mountcastle, *Introduction. computation in cortical columns*, *Cerebral Cortex* **13** (2003), no. 1, 2–4.
- [103] I.T. Nabney, *Netlab algorithms for pattern recognition*, Springer-Verlag, 2004.
- [104] G. Nolte, O Bai, L. Wheaton, Z. Mari, S. Vorbach, and M. Hallett, *Identifying true brain interaction from EEG data using the imaginary part of coherency*, *Clinical Neurophysiology* **115** (2004), no. 10, 2292–2307.
- [105] P.L. Nunez, *Neocortical dynamics and human EEG rhythms*, Oxford University Press, 1995.

- [106] ———, *Electric fields of the brain: The neurophysics of EEG*, Oxford University Press, 2005.
- [107] P.L. Nunez, R.B. Silberstein, Z. Shi, M.R. Carpenter, R. Srinivasan, D.M. Tucker, S.M. Doran, P.J. Cadusch, and R.S. Wijesinghe, *EEG coherency II: Experimental comparisons of multiple measures*, *Clinical Neurophysiology* **110** (1999), no. 3, 469–486.
- [108] P.L. Nunez, R. Srinivasan, A.F. Westdorp, R.S. Wijesinghe, D.M. Tucker, R.B. Silberstein, and P.J. Cadusch, *EEG coherency. I: Statistics, reference electrode, volume conduction, Laplacians, cortical imaging, and interpretation at multiple scales*, *Electroencephalography and Clinical Neurophysiology* **103** (1997), no. 5, 499–515.
- [109] G.V. Osipov, A.S. Pikovsky, M.G. Rosenblum, and J. Kurths, *Phase synchronization effects in a lattice of nonidentical Rossler oscillators*, *Physical Review E* **55** (1997), no. 3, 2353–2361.
- [110] Z.A. Ozdemir and E. Cakan, *Non-linear dynamic linkages in the international stock markets*, *Physica A* **377** (2007), no. 1, 173–180.
- [111] N.H. Packard, J.P. Crutchfield, J.D. Farmer, and R.S. Shaw, *Geometry from a time series*, *Physical Review Letters* **45** (1980), no. 9, 712–716.
- [112] J. Pearl, *Causality : Models, reasoning, and inference*, Cambridge University Press, 2000.
- [113] L.M. Pecora, L. Moniz, J. Nichols, and T.L. Carroll, *A unified approach to attractor reconstruction*, *Chaos: An Interdisciplinary Journal of Nonlinear Science* **17** (2007), 013110.
- [114] E. Pereda, R.Q. Quiroga, and J. Bhattacharya, *Nonlinear multivariate analysis of neurophysiological signals*, *Progress in Neurobiology* **77** (2005), 1–37.
- [115] G. Pfurtscheller and F.H. L. da Silva, *Event-related EEG/MEG synchronization and desynchronization: basic principles*, *Clinical Neurophysiology* **110** (1999), no. 11, 1842–1857.
- [116] A. Pikovsky, M. Rosenblum, and J. Kurths, *Synchronization : A universal concept in nonlinear sciences*, Cambridge University Press, 2003.
- [117] A.S. Pikovsky, M.G. Rosenblum, and J. Kurths, *Synchronization in a population of globally coupled chaotic oscillators*, *Europhysics Letters* **34** (1996), 165–170.
- [118] D.N. Politis and J.P. Romano, *The stationary bootstrap*, *Journal of the American Statistical Association* **89** (1994), no. 428, 1303–1313.
- [119] S.C. Ponten, F. Bartolomei, and C.J. Stam, *Small-world networks and epilepsy: Graph theoretical analysis of intracerebrally recorded mesial temporal lobe seizures*, *Clinical Neurophysiology* **118** (2007), no. 4, 918–927.
- [120] R.Q. Quiroga, J. Arnhold, and P. Grassberger, *Learning driver-response relationships from synchronization patterns*, *Physical Review E* **61** (2000), no. 5, 5142–5148.
- [121] R.Q. Quiroga, A. Kraskov, T. Kreuz, and P. Grassberger, *On the performance of different synchronization measures in real data: a case study on EEG signals*, *Physical Review E* **65** (2002), 041903.

- [122] A. L. Roskies, *The binding problem.*, *Neuron* **24** (1999), no. 1, 7–9, 111–25.
- [123] M. Roth, E. Tym, C.Q. Mountjoy, F.A. Huppert, H. Hendrie, S. Verma, and R. Goddard, *CAMDEX. a standardised instrument for the diagnosis of mental disorder in the elderly with special reference to the early detection of dementia*, *The British Journal of Psychiatry* **149** (1986), 698–709.
- [124] N.F. Rulkov, M.M. Sushchik, L.S. Tsimring, and H.D.I. Abarbanel, *Generalized synchronization of chaos in directionally coupled chaotic systems*, *Physical Review E* **51** (1995), no. 2, 980–994.
- [125] T. Sauer, J. A. Yorke, and M. Casdagli, *Embedology*, *Journal of Statistical Physics* **65** (1991), no. 3-4, 579–616.
- [126] H. Scheer, T. Sander, and L. Trahms, *The influence of amplifier, interface and biological noise on signal quality in high-resolution eeg recordings*, *Physiological Measurement* **27** (2006), no. 2, 109.
- [127] S.J. Schiff, P. So, T. Chang, R.E. Burke, and T. Sauer, *Detecting dynamical interdependence and generalized synchrony through mutual prediction in a neural ensemble*, *Physical Review E* **54** (1996), no. 6, 6708–6724.
- [128] T. Schreiber, *Measuring information transfer*, *Physical Review Letters* **85** (2000), no. 2, 461–464.
- [129] B.F. Shneker and N.B. Fountain, *Epilepsy*, *Disease a Month* **49** (2003), no. 7, 426–478.
- [130] C.A. Sims, *Money, income, and causality*, *American Economic Review* **62** (1972), no. 4, 540–52.
- [131] O. Sporns, *Networks analysis, complexity, and brain function*, *Complexity* **8** (2002), no. 1, 56–60.
- [132] O. Sporns, G. Tononi, and G.M. Edelman, *Theoretical neuroanatomy and the connectivity of the cerebral cortex*, *Behavioural Brain Research* **135** (2002), no. 1-2, 69–74.
- [133] O. Sporns and J.D. Zwi, *The small world of the cerebral cortex*, *Neuroinformatics* **2** (2004), no. 2, 145–162.
- [134] C.J. Stam, *Nonlinear dynamical analysis of EEG and MEG: Review of an emerging field*, *Clinical Neurophysiology* **116** (2005), 2266–2301.
- [135] C.J. Stam, G. Nolte, and A. Daffertshofer, *Phase Lag Index: Assessment of functional connectivity from multi channel EEG and MEG with diminished bias from common sources*, *Human Brain Mapping* **28** (2007), no. 11, 1178–1193.
- [136] C.J. Stam and J.C. Reijneveld, *Graph theoretical analysis of complex networks in the brain*, *Nonlinear Biomedical Physics* **1** (2007), no. 1, 1–19.
- [137] C.J. Stam and B.W. van Dijk, *Synchronization likelihood: an unbiased measure of generalized synchronization in multivariate data sets*, *Physica D* **163** (2002), no. 3, 236–251.
- [138] D. Stoffers, J L.W Bosboom, J.B. Deijen, E.C. Wolters, C.J. Stam, and H.W. Berendse, *Increased cortico-cortical functional connectivity in early-stage Parkinson’s disease: an MEG study*, *Neuroimage* **41** (2008), no. 2, 212–222.

- [139] D. Stoffers, J.L.W. Bosboom, J.B. Deijen, E.C. Wolters, H.W. Berendse, and C.J. Stam, *Slowing of oscillatory brain activity is a stable characteristic of Parkinson's disease without dementia*, *Brain* **130** (2007), no. Pt 7, 1847–1860.
- [140] F. Takens, *Detecting strange attractors*, *Lecture Notes in Mathematics* (D.A. Rand and L.S. Yang, eds.), vol. 898, Springer, 1981.
- [141] J. Theiler, *On the evidence for low-dimensional chaos in an epileptic electroencephalogram*, *Physics Letters A* **196** (1995), 335–341.
- [142] U. Triacca, *Is Granger causality analysis appropriate to investigate the relationship between atmospheric concentration of carbon dioxide and global surface air temperature?*, *Theoretical and Applied Climatology* **81** (2005), no. 3, 133–135.
- [143] J. Vrba and S.E. Robinson, *Signal processing in magnetoencephalography*, *Methods* **25** (2001), no. 2, 249–271.
- [144] D.J. Watts and S.H. Strogatz, *Collective dynamics of small-world networks*, *Nature* **393** (1998), no. 6684, 440–442.
- [145] A.S. Weigend and N.A. Gershenfeld (eds.), *Time series prediction: Forecasting the future and understanding the past*, Santa Fe Institute, 1994.
- [146] W.L. Woon, *Analysis of magnetoencephalographic data as a nonlinear dynamical system*, Ph.D. thesis, Aston University, 2002.
- [147] C.W. Wu, *Synchronization in complex networks of nonlinear dynamical systems*, World Scientific Publishing Company, 2007.
- [148] L. Zhou, C. Zemanova, G. Zamora, C.C. Hilgetag, and J. Kurths, *Hierarchical organization unveiled by functional connectivity in complex brain networks*, *Physical Review Letters* **97** (2006), no. 23, 238103.
- [149] A.M. Zoubir and D.R. Iskander, *Bootstrap techniques for signal processing*, Cambridge University Press, Cambridge, U.K., 2004.